materials

Special Issue Reprint

Advanced Stainless Steel

From Making, Shaping, Treating to Products

Edited by
Chao Chen and Wangzhong Mu

mdpi.com/journal/materials

MDPI

Advanced Stainless Steel—from Making, Shaping, Treating to Products

Advanced Stainless Steel—from Making, Shaping, Treating to Products

Guest Editors

Chao Chen
Wangzhong Mu

MDPI

Basel • Beijing • Wuhan • Barcelona • Belgrade • Novi Sad • Cluj • Manchester

Guest Editors

Chao Chen
College of Materials Science and Engineering
Taiyuan University of Technology
Taiyuan
China

Wangzhong Mu
Department of Materials Science and Engineering
KTH Royal Institute of Technology
Stockholm
Sweden

Editorial Office
MDPI AG
Grosspeteranlage 5
4052 Basel, Switzerland

This is a reprint of the Special Issue, published open access by the journal *Materials* (ISSN 1996-1944), freely accessible at: https://www.mdpi.com/journal/materials/special_issues/2B4236U0WR.

For citation purposes, cite each article independently as indicated on the article page online and as indicated below:

Lastname, A.A.; Lastname, B.B. Article Title. *Journal Name* **Year**, *Volume Number*, Page Range.

ISBN 978-3-7258-5703-6 (Hbk)
ISBN 978-3-7258-5704-3 (PDF)
https://doi.org/10.3390/books978-3-7258-5704-3

Contents

About the Editors

Chao Chen

Chao Chen is an Associate Professor at the College of Materials Science and Engineering, Taiyuan University of Technology. He completed his PhD in Materials Science and Engineering at the KTH Royal Institute of Technology in 2015. He is a member of the Academic Committee on Metallurgical Reaction Engineering of the Chinese Society for Metals, and a member of the National Academic Committee on Metallurgical Processes and Theories of the Metallurgical Physical Chemistry Division of the Chinese Society for Metals. His research interests include research on key technologies for the production of special steel stainless steel; computational fluid dynamics (CFD) simulations of complex fluid flows in industrial processes; physical simulation and mathematical modeling of metallurgical processes; and the preparation and application of catalysts for hydrogen production from electrolyzed water.

Wangzhong Mu

Wangzhong Mu is an Associate Professor at the Royal Institute of Technology (KTH), Department of Materials Science and Engineering, and a Visiting Professor at Key Lab EPM, Northeastern University. He received both a Docent (Assoc. Prof./Reader) qualification and a Ph.D. degree from KTH. Moreover, he has worked at McMaster University (Canada), Tohoku University (Japan), and Ferritico AB (Sweden). He is in close collaboration with the Max Planck Institute of Sustainable Materials (Dusseldorf, Germany), Hanyang University (Korea), Montan University Leoben (Austria), etc. His research interests include (i) particle behaviors in metals, (ii) sustainable metallurgy, (iii) artificial intelligence (AI)-based material design, etc. He has served as a PI for over 15 national-level and EU-level research grants, published over 70 peer-reviewed journal articles, and contributed over 20 plenary/keynote/invited lectures to international conferences.

materials

MDPI

Editorial

Advanced Stainless Steel—From Making, Shaping, Treating to Products

Chao Chen [1,*], Zhixuan Xue [1] and Wangzhong Mu [2,3,*]

[1] College of Materials Science and Engineering, Taiyuan University of Technology, Taiyuan 030024, China; 2024510282@link.tyut.edu.cn
[2] Key Laboratory of Electromagnetic Processing of Materials (Ministry of Education), School of Metallurgy, Northeastern University, Shenyang 110819, China
[3] Department of Materials Science and Engineering, KTH Royal Institute of Technology, Brinellvägen 23, SE-100 44 Stockholm, Sweden
* Correspondence: chenchao@tyut.edu.cn (C.C.); wmu@kth.se (W.M.)

Abstract

Stainless steels have undergone more than a century of continuous development, during which various advanced grades—such as lean duplex, super austenitic, and high-nitrogen stainless steels—have been introduced. Despite remarkable progress, the manufacturing of stainless steel remains a complex process that spans multiple critical stages, including stainless steelmaking, solidification and casting, continuous casting, heat treatment, electroslag and vacuum arc remelting, as well as both hot and cold rolling operations. Ensuring excellent corrosion resistance and mechanical performance of the final products continues to be a central focus of research and production. The current Special Issue (SI) entitled '*Advanced Stainless Steel—from Making, Shaping, Treating to Products*' has collected eight research papers focusing on various aspects of steel production, e.g., inclusions in steelmaking and continuous casting processes, continuous casting processes and the quality of stainless steel casting, heat treatment, corrosion of steels, and fatigue of steels. This summary aims to contribute to the state-of-the-art of the development of steel production.

Keywords: stainless steel; steelmaking; inclusions; continuous casting; heat treatment; corrosion; fatigue

1. Introduction

In the 1820s, scientists Pierre Berthier, Stoddard, and Faraday noted that chromium-containing iron was more corrosion-resistant against certain acids than its non-chromium counterpart [1]. Their alloys, however, were not true stainless steel. This era is widely attributed to the Englishman Harry Brearley, who in 1913 developed and analyzed the first authentic stainless steel, with a composition of 12.8% chromium and 0.24% carbon [1].

Owing to their superior combination of corrosion resistance and mechanical strength, stainless steels are extensively applied in engineering fields such as petrochemical industries, machines, railway systems, and aerospace applications. In modern classifications, stainless steels are generally divided into austenitic, ferritic, martensitic, and duplex categories [2,3]. Moreover, continuous alloy design and processing optimization have led to the emergence of new grades, including lean duplex, super austenitic, and high-nitrogen variants, which further expand the performance envelope of stainless steels. There are some recent book chapters [2], monographs [3], and review papers [4–8] that summarize the recent developments in stainless steels.

To name a few of the novel applications of stainless steels, the super austenitic stainless steel has been a hot research topic [9–16] nowadays due to its difficulty in continuous casting and precipitation controls. In addition, the 316 group stainless steel is tailored and applied in the in-core and out-of-core components of Generation-IV fast reactors [17–19], nuclear power pipeline systems [20,21], and low magnetic scenes [22,23], for example, medical materials [24,25] and mobile phone frames [26–28]. The stainless steel foils are another application in the communication industry [29]. Recent composite materials are made by ultra-thin stainless steel foils and carbon fiber reinforced polymer (CFRP) [30,31]. These advanced lightweight materials are promising for aircraft. In addition, composite plates made by stainless steel and titanium alloy or other steel grades are studied and produced in many areas [32–34]. A novel potential functional application of stainless steels is the bifunctional water electrolysis electrode [35,36], which is under development.

The current production process of stainless steel is basically as follows [37,38]: blast furnace→hot metal pretreatment→converter steelmaking→ladle furnace and/or vacuum oxygen degassing→tundish→continuous casting→hot rolling→pickling and annealing→cold rolling. Alternatively, the electric arc furnace (EAF) process can replace the steps before converter steelmaking [39]. In addition, some special melting methods, such as electric slag remelting and vacuum arc remelting, are used in the production of special stainless steels [21].

For the Argon Oxygen Decarburization (AOD) [40–42] and Vacuum Oxygen Degassing (VOD) [43] furnace operations, the technologies are very mature. The special design of the tundish for stainless steel is summarized in ref [44,45]. The design of the submerged entry nozzle (SEN) for stainless steel production is still an ongoing work [46]. Working roll modification is another hot research topic for rolling stainless steels [47,48].

The production of stainless steel is still a challenging process with respect to the non-metallic inclusions [49–54] and casting defects [55–57]. The inclusions formation thermodynamics [58], as well as nozzle clogging during the production of various stainless steel grades, for example, high silicon [59,60], Ti stabilized [61,62], and rare earth metal treated [63–65], are problems to be solved. The relationship between corrosion and inclusions in stainless steel is studied [66,67]. Solidification structure refining [68] for ferritic stainless steels, residual ferrite in austenitic stainless steels [69], and phase precipitation in duplex and super austenitic stainless steels [26,70–72] are the issues with respect to casting defects. The heat treatment of stainless steels [73–75] as well as the mechanical properties, corrosion resistance [76–80] of the product are all important issues.

2. An Overview of Published Articles

Manuscripts on many subjects regarding (stainless) steel production were submitted for the current Special Issue (SI). After the peer-review process, eight papers were finally accepted for publication. The papers cover the topics of inclusions in steelmaking and continuous casting processes, continuous casting processes and the quality of stainless steel casting, heat treatment, corrosion of steels, and fatigue of steels. A detailed description of each contribution is provided in Table 1.

Contribution 1 [81] established a three-dimensional segmented coupling model to analyze continuous casting billets under the simultaneous influence of final and mold electromagnetic stirring (F-EMS and M-EMS). Model accuracy was verified by comparing carbon segregation behavior in billets with and without electromagnetic stirring through industrial trials. Results demonstrated that both F-EMS and M-EMS generate tangential molten steel flow, which modifies the solidification dynamics and solute distribution inside the billet.

Table 1. Summary of the published contributions in this Special Issue.

No. of Contribution	Research Area	Focus	Type of Research
1 [81]	Continuous casting	Model comparison on the performance of combined mold and final electromagnetic stirring (M-EMS, F-EMS)	Numerical model study
2 [82]	Inclusions modification	Effect of the addition of Ce in U75V steel on the inclusion precipitation and mechanical properties	Experimental study
3 [83]	Fatigue of steel specimen	The low-cycle fatigue of S420M steel under undeformed and pre-strained conditions	Experimental study
4 [84]	Inclusions in continuous casting slab	A full section comparative analysis of the inclusions in a high-titanium steel	Experimental study
5 [85]	Continuous casting and heat treatment of stainless steel	Residual ferrite distribution in 304L austenitic stainless steel slab and the effect of heat treatment on it	Experimental study
6 [86]	Corrosion of stainless steel	Predict the corrosion behavior of austenitic stainless steels (316L, 904L, and AL-6XN) under various environmental conditions	Experimental study and artificial neural network models
7 [87]	Corrosion of steel	Formation of akaganeite in atmospheric corrosion induced by NaCl deliquescence	Experimental study
8 [88]	Fatigue of steel	Fatigue tests on Q500qENH weathering steel V-groove welded joints and finite element model study	Experimental study and numerical model study

Contribution 2 [82] investigated the precipitation behavior of Ce inclusions in steel melt and predicted their evolution using thermodynamic calculations. It was found that varying Ce levels alter the precipitation sequence of rare earth inclusions, where the formation of CeO_2, Ce_2O_3, and $CeAlO_3$ is increasingly suppressed with higher Ce contents. The addition of Ce also refined the grain size and pearlite lamellae of U75V steel. Mechanical testing indicated that when Ce content is controlled below 0.0042%, the tensile strength and impact toughness of U75V steel are both enhanced.

Contribution 3 [83] analyzed the low-cycle fatigue behavior of S420M steel under different loading states, including undeformed and pre-strained specimens. Under strain-controlled fatigue, S420M steel exhibited no cyclic stabilization phase. After the initial deformation, significant variations in cyclic behavior were observed from hysteresis loop parameters. The fatigue life of pre-strained samples differed from that of unstrained ones, showing dependence on the applied loading conditions.

Contribution 4 [84] focused on inclusion characteristics in high-titanium steel casting billets (0.4% Ti, 0.004% N) by means of industrial sampling and comparative cross-sectional analysis at central and quarter thickness positions. Results showed that accelerating cooling rates and lowering titanium levels effectively delayed TiN precipitation, thereby suppressing the formation of coarse TiN inclusions in high Ti steels.

Contribution 5 [85] explored the distribution and evolution of residual ferrite in 304L austenitic stainless steel continuous casting slabs. Along the thickness direction at the

slab's width center, ferrite content exhibited an "M"-type distribution—approximately 3% near edges and up to 13% at the center. Thermodynamic evaluation indicated an FA solidification mode. The impact of heat treatment processes on the ferrite content was also investigated. Optimal heat treatment at 1250 °C for 48 min followed by air cooling minimized ferrite content while maintaining the characteristic "M"-shaped distribution.

Contribution 6 [86] applied statistical modeling methods, including linear regression and artificial neural networks (ANNs), to predict the corrosion response of austenitic stainless steels (316L, 904L, and AL-6XN) under varying environmental factors. The considered parameters included temperature (30–90 °C), chloride ion concentration (20–40 g/L), and pH (2–6). The detailed analysis of variance (ANOVA) confirmed that the Pitting Resistance Equivalent Number (PREN, 24–45) exerted the most significant influence on the critical pitting potential, followed sequentially by temperature, pH, and chloride concentration.

Contribution 7 [87] explored the formation of akaganeite during atmospheric corrosion induced by NaCl deliquescence through laboratory simulations. The deliquescence of NaCl particles produced local electrolyte droplets, within which corrosion occurred independently. Akaganeite was detected within 12 h of exposure, while lepidocrocite and magnetite, as early corrosion products, facilitated its formation. Moreover, the extent of salt deposition was identified as a crucial factor influencing macroscopic akaganeite accumulation.

Contribution 8 [88] performed multi-factor coupled constant-amplitude fatigue tests on Q500qENH weathering steel V-groove welded joints and established an equivalent finite element model to analyze interdependent parameters under coupled conditions. The results demonstrated that stress level had the most pronounced impact on fatigue behavior, followed by corrosion duration and ambient temperature. Simulation findings further indicated that low temperatures improved the fatigue life of slightly corroded specimens by approximately 20%, though progressive damage occurred before reaching peak service performance.

3. Summary

The current Special Issue (SI), *Advanced Stainless Steel—from Making, Shaping, Treating to Products*, collects the research contributions on the topics of inclusions in steelmaking and continuous casting processes, continuous casting processes optimization and the quality of stainless steel castings, heat treatment, corrosion of steels, and fatigue of steels. Both experimental, numerical simulation, and artificial neural network model studies on the stainless steel production topics were reported in different papers. As a pity, review papers on this topic are not presented in this SI. We may organize a second Volume II SI with the identical topic to invite and collect more contributions regarding different topics of stainless steel production.

Author Contributions: Writing—original draft preparation, C.C. and Z.X.; writing—review and editing, Z.X., W.M., and C.C. All authors have read and agreed to the published version of the manuscript.

Acknowledgments: C.C. and W.M. would like to express our deep appreciation to all the authors who contributed valuable work to publish in the current Special Issue, all the anonymous reviewers who provided professional opinions to support the peer review process, the diligent Materials Editorial Office, and the Special Issue editor.

Conflicts of Interest: The authors declare no conflicts of interest.

References

1. Lai, J.K.L.; Lo, K.H.; Shek, C.H. *Stainless Steels: An Introduction and Their Recent Developments*; Bentham Science Publishers: Sharjah, United Arab Emirates, 2012; p. 4. [CrossRef]
2. San-Martin, D.; Celada-Casero, C.; Vivas, J.; Capdevila, C. Stainless steels. In *High-Performance Ferrous Alloys*; Rana, R., Ed.; Springer Nature: Cham, Switzerland, 2021; pp. 459–566. [CrossRef]
3. Li, J.M.; Liang, J.X.; Liu, Y.P. *Chinese Stainless Steel*; Metallurgical Industry Press: Beijing, China, 2021; pp. 3–5. (In Chinese)
4. Lo, K.H.; Shek, C.H.; Lai, J.K.L. Recent developments in stainless steels. *Mater. Sci. Eng. R Rep.* **2009**, *65*, 39–104. [CrossRef]
5. Patra, S.; Agrawal, A.; Mandal, A.; Podder, A.S. Characteristics and Manufacturability of Duplex Stainless Steel: A Review. *Trans. Indian Inst. Metals* **2021**, *74*, 1089–1098. [CrossRef]
6. Liu, Z.B.; Liang, J.X.; Yang, Z.; Wang, X.H.; Sun, Y.Q.; Wang, C.J.; Yang, Z.Y. Progress of application and research on high strength stainless steel. *China Metall.* **2022**, *32*, 42–53. (In Chinese) [CrossRef]
7. Liu, W.Q.; Wang, L.J.; Zhang, F.C.; Zhao, A.M.; Li, J.M. Review on development and second phase regulation of super austenitic stainless steel. *J. Iron Steel Res.* **2023**, *35*, 907–927. (In Chinese) [CrossRef]
8. Liu, S.; Guo, H.J. A short review of antibacterial Cu-bearing stainless steel: Antibacterial mechanisms, corrosion resistance, and novel preparation techniques. *J. Iron Steel Res. Int.* **2024**, *31*, 24–45. [CrossRef]
9. Ren, J.; Zhang, Y.; Yang, S.; Ma, J.; Zhang, C.; Jiang, Z.; Li, H.; Han, P. Effect of Boron Addition on the Oxide Scales Formed on 254SMO Super Austenitic Stainless Steels in High-Temperature Air. *Metals* **2023**, *13*, 258. [CrossRef]
10. Yang, S.; Ma, J.Y.; Chen, C.; Zhang, C.L.; Ren, J.Y.; Jiang, Z.H.; Fan, G.W.; Han, P.D. Effects of B and Ce Grain Boundary Segregation on Precipitates in Super Austenitic Stainless Steel. *Metals* **2023**, *13*, 326. [CrossRef]
11. Yan, X.; Xu, P.; Han, P.; Dong, N.; Wang, J.; Zhang, C. The Effect of B on the Co-Segregation of C-Cr at Grain Boundaries in Austenitic Steels. *Metals* **2023**, *13*, 1044. [CrossRef]
12. Liao, L.; Zhao, Z.; Zhang, W.; Li, J.; Chen, Y.; Pan, L. Unveiling Hot Deformation Behavior and Dynamic Recrystallization Mechanism of 654SMO Super-Austenitic Stainless Steel. *Metall. Mater. Trans. A* **2023**, *54*, 2554–2575. [CrossRef]
13. Tian, H.; Wang, J.; Liu, Z.; Han, P. Effect of Nitrogen on the Corrosion Resistance of 6Mo Super Austenitic Stainless Steel. *Metals* **2024**, *14*, 391. [CrossRef]
14. Liu, Z.Q.; Wang, J.; Chen, C.; Tian, H.Y.; Han, P.D. Effect of boron on the solidification characteristics and constitutive equation of S31254 superaustenitic stainless steel. *Steel Res. Int.* **2024**, *95*, 2400050. [CrossRef]
15. Chen, F.; Bai, K.; Wang, Y.; Liu, C.; Mu, W.; Zhang, H.; Ni, H. Effect of Ce on the Segregation and Secondary-Phase Precipitation During the Solidification of S31254 Super-Austenitic Stainless Steel. *Metall. Mater. Trans. B* **2024**, *55*, 2097–2114. [CrossRef]
16. Xu, S.G.; He, J.S.; Zhang, R.Z.; Zhang, F.C.; Wang, X.T. Static recrystallization behaviors and mechanisms of 7Mo super-austenitic stainless steel with undissolved sigma precipitates during double-stage hot deformation. *J. Iron Steel Res. Int.* **2024**, *31*, 475–487. [CrossRef]
17. Chen, S.H.; Xie, A.; Lv, X.L.; Chen, S.H.; Yan, C.G.; Jiang, H.C.; Rong, L.J. Tailoring Microstructure of Austenitic Stainless Steel with Improved Performance for Generation-IV Fast Reactor Application: A Review. *Crystals* **2023**, *13*, 268. [CrossRef]
18. Xie, A.; Chen, S.H.; Chen, S.H.; Jiang, H.C.; Rong, L.J. Austenite decomposition behavior adjacent to δ-ferrite in a Si-modified Fe-Cr-Ni austenitic stainless steel during thermal aging at 550 °C. *Acta Mater.* **2024**, *272*, 119948. [CrossRef]
19. Chen, S.H.; Wang, Q.Y.; Jiang, H.C.; Rong, L.J. Effect of δ-ferrite on Hot Deformation and Recrystallization of 316KD Austenitic Stainless Steel for Sodium-Cooled Fast Reactor Application. *Acta Metall. Sin.* **2024**, *60*, 367–376. (In Chinese) [CrossRef]
20. Li, X.; Gao, F.; Jiao, J.H.; Cao, G.M.; Wang, Y.; Liu, Z.Y. Influences of cooling rates on delta ferrite of nuclear power 316H austenitic stainless steel. *Mater. Charact.* **2021**, *174*, 111029. [CrossRef]
21. Wang, Y.; Chen, C.; Ren, R.J.; Xue, Z.X.; Wang, H.Z.; Zhang, Y.Z.; Wang, J.X.; Wang, J.; Chen, L.; Mu, W.Z. Ferrite formation and decomposition in 316H austenitic stainless steel electro slag remelting ingot for nuclear power applications. *Mater. Charact.* **2024**, *218*, 114581. [CrossRef]
22. Kumar, A.; Ganesh, P.; Sharma, V.K.; Manekar, M.; Gupta, R.K.; Singh, R.; Singh, M.K.; Mundar, G.; Kaul, R. Development of Low-Magnetic-Permeability Welds of 316L Stainless Steel. *Weld. J.* **2021**, *100*, 323. [CrossRef]
23. Chen, L.; Wang, Y.; Li, Y.F.; Zhang, Z.R.; Xue, Z.X.; Ban, X.Y.; Hu, C.H.; Li, H.X.; Tian, J.; Mu, W.Z.; et al. Effect of Nickel Content and Cooling Rate on the Microstructure of as Cast 316 Stainless Steels. *Crystals* **2025**, *15*, 168. [CrossRef]
24. Mani, G.; Feldman, M.D.; Patel, D.; Agrawal, C.M. Coronary stents: A materials perspective. *Biomaterials* **2007**, *28*, 1689–1710. [CrossRef]
25. Bharani Chandar, J.; Lenin, N.; Rathinasuriyan, C. Exploring surface integrity Experimental investigation into abrasive waterjet deep hole drilling on ss 316L for biomedical applications. *J. Alloys Metall. Syst.* **2024**, *8*, 100109. [CrossRef]
26. Chu, H.Y.; Shiue, R.K.; Cheng, S.Y. The Effect of Homogenization Heat Treatment on 316L Stainless Steel Cast Billet. *Materials* **2024**, *17*, 232. [CrossRef]
27. Wang, Y.; Chen, L.; Mu, W.Z.; Zhang, Z.R.; Wang, J.; Chen, C. Solidification mode and residual ferrite characteristics of high nickel 316L stainless steel continuous casting billet. *Iron Steel* **2024**, *59*, 80–91. (In Chinese) [CrossRef]

28. Wang, Y.; Chen, C.; Yang, X.Y.; Zhang, Z.R.; Wang, J.; Li, Z.; Chen, L.; Mu, W.Z. Solidification modes and delta-ferrite of two types 316L stainless steels: A combination of as-cast microstructure and HT-CLSM research. *J. Iron Steel Res. Int.* **2025**, *32*, 426–436. [CrossRef]
29. Zhao, J.W.; Xie, Q.Z.; Ma, L.N.; Zhou, C.L.; Jiang, Z.Y.; Liao, X.; Ma, X.G. Effect of rolling schedules on ridging resistance of ultra-thin ferritic stainless steel foil. *J. Iron Steel Res. Int.* **2025**, *32*, 198–214. [CrossRef]
30. Chen, L.; Cao, Z.R.; Wang, J.; Wang, T.; Wang, Z.G.; Zhang, Y.J.; Ma, B.; Jiang, Y.Q. Study on static load performance of FMLs based on ultra-thin stainless-steel foils and cross-ply thin CFRP. *J. Manuf. Process.* **2024**, *119*, 425–435. [CrossRef]
31. Chen, L.; Zhu, W.; Zhang, Q.; Zhang, Y.J.; Zhao, C.C.; Wang, T.; Huang, Q.X. Influence of surface modification on the interfacial properties of ultra-thin steel foils and CFRP co-curing without adhesive film: A comparative study of different techniques. *Compos. Part B Eng.* **2025**, *301*, 112517. [CrossRef]
32. Zhu, L.; Sun, C.Y.; Wang, B.Y.; Zhou, J. Cross wedge rolling deformation law and bonding mechanism of 304 stainless steel/Q235 carbon steel bimetallic shaft. *J. Iron Steel Res. Int.* **2024**, *31*, 2423–2437. [CrossRef]
33. Hao, P.J.; Liu, Y.M.; Zhang, Y.Y.; Wang, T.; Huang, Q.X. Effect of heating temperature on microstructure and properties of Ti/steel clad plates with corrugated interfaces. *J. Iron Steel Res. Int.* **2024**, *31*, 2997–3006. [CrossRef]
34. Guo, X.W.; Ren, Z.K.; Wu, H.; Chai, Z.; Zhang, Q.; Wang, T.; Huang, Q.X. Effect of annealing on microstructure and synergistic deformation of 304/TC4 composite plates with corrugated interface. *J. Iron Steel Res. Int.* **2025**, *32*, 2434–2451. [CrossRef]
35. Hou, C.; Xue, L.; Li, J.; Ma, W.; Wang, J.; Dai, Y.; Chen, C.; Dang, J. Unlocking the potential of lattice oxygen evolution in stainless steel to achieve efficient OER catalytic performance. *Acta Mater.* **2024**, *277*, 120176. [CrossRef]
36. Hou, C.; Xue, L.; Zhou, L.; Chen, C.; Lv, X.; Dang, J. Efficient stainless steel-based bifunctional water electrolysis electrode: Activating the OPM mechanism in OER and enhancing HER performance. *Acta Mater.* **2025**, *297*, 121361. [CrossRef]
37. Ramaswamy, V. Modern Developments in Stainless Steel Making. In *Advances in Stainless Steels*; Raj, B., Ed.; CRC press: Boca Raton, FL, USA, 2009; pp. 383–395.
38. Das, S.K.; Mehrotra, S.P.; Godiwalla, K.M. Technological Advances in Refining and Processing of Stainless Steel—A Brief Overview. In *Advances in Stainless Steels*; Raj, B., Ed.; CRC press: Boca Raton, FL, USA, 2009; pp. 431–451.
39. Conejo, A.N. *Electric Arc Furnace: Methods to Decrease Energy Consumption*; Springer Nature: Singapore, 2024; p. 699.
40. Pitkälä, J.; Holappa, L.; Jokilaakso, A. Nitrogen Control in Production of N-Alloyed Stainless Steels in AOD Converter: Application of Sieverts' Law. *Metall. Mater. Trans. B* **2024**, *55*, 524–536. [CrossRef]
41. Chanouian, S.; Pitkälä, J.; Larsson, H.; Ersson, M. Modeling Decarburization in the AOD Converter: A Practical CFD-Based Approach With Chemical Reactions. *Metall. Mater. Trans. B* **2024**, *55*, 480–494. [CrossRef]
42. Singha, P. Refining Contribution at Hotspot and Emulsion Zones of Argon Oxygen Decarburization: Fundamental Analysis Based upon the FactSage-Macro Program Approach. *Metall. Mater. Trans. B* **2024**, *55*, 2181–2193. [CrossRef]
43. Yang, W.; Wang, L.; Zhang, W.; Li, J. Deep Neural Network Prediction Model of Hydrogen Content in VOD Process Based on Small Sample Dataset. *Metall. Mater. Trans. B* **2022**, *53*, 3124–3135. [CrossRef]
44. Schade, J. Tundish Design and Practice Issues in the Production of Specialty Steels. In *Continuous Casting, Volume Ten Tundish Operations*; Baker, M.A., Ed.; Iron & Steel Society: Warrendale, PA, USA, 2003; p. 282.
45. Chen, C.; Cheng, G.; Sun, H.; Wang, X.; Zhang, J. Optimization of flow control devices in a stainless steel tundish. *Adv. Mater. Res.* **2012**, *476*, 156–163. [CrossRef]
46. Pang, J.C.; Qian, G.Y.; Pang, S.; Ma, W.H.; Cheng, G.G. Design of a submerged entry nozzle for optimizing continuous casting of stainless steel slab. *J. Iron Steel Res. Int.* **2023**, *30*, 2229–2241. [CrossRef]
47. Li, P.C.; Wang, T.; Zhao, C.C.; Liu, Q.; Huang, Q.X. Effect of ceramic work rolls on surface roughness of rolled SUS304 ultra-thin strips. *J. Iron Steel Res. Int.* **2024**, *31*, 1704–1718. [CrossRef]
48. Zhang, Z.Q.; Liao, X.; Ren, Z.K.; Wang, Z.H.; Liu, Y.X.; Wang, T.; Huang, Q.X. Effect of two-pass rolling of textured roll and polished roll on surface topography and mechanical properties of 316L stainless steel ultra-thin strip. *J. Iron Steel Res. Int.* **2025**, *32*, 186–197. [CrossRef]
49. Park, J.H.; Kang, Y. Inclusions in stainless steels—A review. *Steel Res. Int.* **2017**, *88*, 1700130. [CrossRef]
50. Kim, W.Y.; Nam, G.J.; Kim, S.Y. Evolution of Non-Metallic Inclusions in Al-Killed Stainless Steelmaking. *Metall. Mater. Trans. B* **2021**, *52*, 1508–1520. [CrossRef]
51. Liu, Q.; Zhan, Z.; Gao, M.; Xing, L.; Yin, Y.; Zhang, J. Investigation of Evolution of Inclusions in 15-5PH Stainless Steel During Hot Compression Using 3D X-Ray Microscopy. *Metall. Mater. Trans. B* **2023**, *54*, 2852–2863. [CrossRef]
52. Liu, C.S.; Li, F.K.; Zhang, H.; Li, J.; Wang, Y.; Lu, Y.Y.; Xiong, L.; Ni, H.W. Mechanisms of interfacial reactions between 316L stainless steel and MnO–SiO_2 oxide during isothermal heating. *J. Iron Steel Res. Int.* **2023**, *30*, 1511–1523. [CrossRef]
53. Quan, Q.; Zhang, Z.X.; Qu, T.P.; Li, X.L.; Tian, J.; Wang, D.Y. Physical and numerical investigation on fluid flow and inclusion removal behavior in a single-strand tundish. *J. Iron Steel Res. Int.* **2023**, *30*, 1182–1198. [CrossRef]
54. Zhao, M.; Shi, C.; Li, L.; Yan, W. Crystallization and Structure Characteristics of CaO–SiO_2–Al_2O_3–MgO–CaF_2 Melts Representing the Slag Inclusions in Stainless Steel. *Metall. Mater. Trans. B* **2025**, *56*, 4593–4602. [CrossRef]

55. Lindenberg, H.U.; Knackstedt, W.; Koehler, H.J.; Biesterfeld, W.; Unger, K.D.; Thielmann, R. Metallurgie des Stranggießens nichtrostender Stähle. *Stahl Eisen* **1984**, *104*, 227–234. (In German)
56. Wolf, M. Strand Surface Quality of Austenitic Stainless Steels: Part I—Macroscopic Shell Growth and Ferrite Distribution. *Ironmak. Steelmak.* **1986**, *13*, 248–257.
57. Ciuffini, A.F.; Di Giovanni, F.; Mombelli, D. Utilizzo di un sistema di ispezione ottica automatica atto al rilevamento dei difetti di colata continua basato su algoritmi di Machine Learning per l'analisi dell'incidenza delle marche di oscillazione su bramme di acciaio inossidabile austenitico AISI 316L e 316LI. *La Metall. Ital.* **2022**, *59*, 59–68. Available online: https://www.aimnet.it/eng/prodotto.php?id=730&idc=11 (accessed on 30 September 2025). (In Italian).
58. Yan, Y.; Shang, G.H.; Zhang, L.P.; Li, S.Y.; Guo, H.J. A deoxidation thermodynamic model for 304 stainless steel considering multiple-components coupled reactions. *J. Iron Steel Res. Int.* **2024**, *31*, 74–91. [CrossRef]
59. Bi, Y.; Karasev, A.V.; Jönsson, P.G. Evolution of Different Inclusions during Ladle Treatment and Continuous Casting of Stainless Steel. *ISIJ Int.* **2013**, *53*, 2099–2109. [CrossRef]
60. Dou, G.X.; Guo, H.J.; Guo, J.; Peng, X.C.; Chen, Q.Y. Effect of slag composition on kinetic behavior of deep deoxidation of 5 wt.% Si high-silicon austenitic stainless steel. *J. Iron Steel Res. Int.* **2024**, *31*, 1873–1885. [CrossRef]
61. Yin, X.; Sun, Y.H.; Yang, Y.D.; Bai, X.F.; Barati, M.; Mclean, A. Formation of inclusions in Ti-stabilized 17Cr austenitic stainless steel. *Metall. Mater. Trans. B* **2016**, *47*, 3274–3284. [CrossRef]
62. Fu, J.W.; Qiu, W.X.; Nie, Q.Q.; Wu, Y.C. Precipitation of TiN during solidification of AISI 439 stainless steel. *J. Alloys Compd.* **2017**, *699*, 938–946. [CrossRef]
63. Bi, Y.; Karasev, A.V.; Jönsson, P.G. Three Dimensional Evaluations of REM Clusters in Stainless Steel. *ISIJ Int.* **2014**, *54*, 1266–1273. [CrossRef]
64. Nabeel, M.; Karasev, A.; Jönsson, P.G. Formation and Growth Mechanism of Clusters in Liquid REM-alloyed Stainless Steels. *ISIJ Int.* **2015**, *55*, 2358–2364. [CrossRef]
65. Zhao, L.; Yang, J.C.; Fu, X.Y. Effect of Ce content on modification behavior of inclusions and corrosion resistance of 316L stainless steel. *Materials* **2025**, *18*, 69. [CrossRef]
66. Hu, J.Z.; Li, S.; Zhang, J.; Ren, Y.; Zhang, L.F. Pitting corrosion initiated by SiO_2–MnO–Cr_2O_3–Al_2O_3-based inclusions in a 304 stainless steel. *J. Iron Steel Res. Int.* **2024**, *31*, 2281–2293. [CrossRef]
67. Li, F.K.; Liu, C.S.; Wang, Y.; Zhang, H.; Li, J.; Lu, Y.Y.; Xiong, L.; Ni, H.W. Effect of inclusion and microstructure transformation on corrosion resistance of 316L stainless steel after isothermal heat treatment. *J. Iron Steel Res. Int.* **2025**, *32*, 2133–2151. [CrossRef]
68. Park, J.H. Effect of inclusions on the solidification structures of ferritic stainless steel: Computational and experimental study of inclusion evolution. *Calphad* **2011**, *35*, 455–462. [CrossRef]
69. Chen, C.; Cheng, G.G. Delta-ferrite distribution in a continuous casting slab of Fe-Cr-Mn austenitic stainless steel. *Metall. Mater. Trans. B* **2017**, *48*, 2324–2333. [CrossRef]
70. Li, Y.; Zou, D.; Li, M.; Tong, L.; Zhang, Y.; Zhang, W. Effect of cooling rate on δ-Ferrite formation and sigma precipitation behavior of 254SMO super-austenitic stainless steel during solidification. *Metall. Mater. Trans. B* **2023**, *54*, 3497–3507. [CrossRef]
71. Chen, X.; Qiao, T.; Cheng, G.; Bao, D.; Pan, J. Sigma-Phase Distribution in 2507 Super Duplex Stainless Steel Continuous Casting Slabs. *Steel Res. Int.* **2024**, *95*, 2300433. [CrossRef]
72. Chu, H.Y.; Wu, M.C.; Shiue, R.K.; Cheng, S.Y. Investigating the sigma formation in homogenization treatment of the 309L stainless cast billet. *J. Mater. Res. Technol.* **2025**, *35*, 2354–2368. [CrossRef]
73. Zhang, Y.; Liu, X.; Wang, C.J.; Liu, C. Effect of heat treatment on microstructure and mechanical properties of selective laser-melted PH13-8Mo stainless steel. *J. Iron Steel Res. Int.* **2024**, *31*, 945–955. [CrossRef]
74. Zhang, J.; Hu, Z.F.; Zhang, Z. EBSD parameter assessment and constitutive models of crept HR3C austenitic steel. *J. Iron Steel Res. Int.* **2023**, *30*, 772–781. [CrossRef]
75. Song, Y.; Li, Y.; Lu, J.; Hua, L.; Gu, Y.; Yang, Y. Strengthening and toughening mechanisms of martensite-bainite microstructure in 2 GPa ultra-high strength steel during hot stamping. *Sci. China Technol. Sci.* **2025**, *68*, 1520201. [CrossRef]
76. Wang, T.H.; Wang, J.; Bai, J.G.; Wang, S.J.; Chen, C.; Han, P.D. The effect of boron addition on the dissolution and repair behavior of passive film on S31254 superaustenitic stainless steels immersed in H_2SO_4 solution. *J. Iron Steel Res. Int.* **2022**, *29*, 1012–1025. [CrossRef]
77. Dai, Z.X.; Jiang, S.L.; Ning, L.K.; Xu, X.D.; Li, S.; Duan, D.L. Effect of friction on corrosion behaviors of AISI 304 and Cr26Mo1 stainless steels in different solutions. *J. Iron Steel Res. Int.* **2023**, *30*, 2541–2556. [CrossRef]
78. Dong, C.; Qu, S.; Fu, C.M.; Zhang, Z.F. Failure analysis of crevice corrosion on 304 stainless steel tube heat exchanger. *J. Iron Steel Res. Int.* **2023**, *30*, 1490–1498. [CrossRef]
79. Gao, W.B.; Gu, Y.; Han, Q.L.; Gu, X.Y.; Guan, W.; Zhao, S.B.; Li, W.H. Corrosion and passivation behavior of sensitized SAF 2507 super-duplex stainless steel in hot concentrated seawater. *J. Iron Steel Res. Int.* **2025**, *32*, 3026–3045. [CrossRef]
80. Xing, Y.C.; Sun, Z.B.; Han, Y.Q.; Zhang, D.X. Influence of alternating magnetic field on corrosion and microstructure of 2205 duplex stainless steel welded joints. *J. Iron Steel Res. Int.* **2025**, *32*, 1341–1355. [CrossRef]

81. Feng, Z.; Zhang, G.; Li, P.; Yan, P. Numerical Simulation of Fluid Flow, Solidification, and Solute Distribution in Billets under Combined Mold and Final Electromagnetic Stirring. *Materials* **2024**, *17*, 530. [CrossRef]
82. Feng, G.; Ren, L.; Yang, J. Study on Influence of Rare Earth Ce on Micro and Macro Properties of U75V Steel. *Materials* **2024**, *17*, 579. [CrossRef]
83. Mroziński, S.; Piotrowski, M.; Egner, H. Effect of Testing Conditions on Low-Cycle Fatigue Durability of Pre-Strained S420M Steel Specimens. *Materials* **2024**, *17*, 1833. [CrossRef]
84. Zhang, M.; Li, X.; Guo, Z.; Sun, Y. Research on the Size and Distribution of TiN Inclusions in High-Titanium Steel Cast Slabs. *Materials* **2025**, *18*, 3527. [CrossRef]
85. Xue, Z.; Yang, K.; Li, Y.; Pei, C.; Hou, D.; Zhao, Q.; Wang, Y.; Chen, L.; Chen, C.; Mu, W. The Influence of Heat Treatment Process on the Residual Ferrite in 304L Austenitic Stainless Steel Continuous Casting Slab. *Materials* **2025**, *18*, 3724. [CrossRef]
86. Jung, K.-H.; Kim, S.-J. Statistical and ANN Modeling of Corrosion Behavior of Austenitic Stainless Steels in Aqueous Environments. *Materials* **2025**, *18*, 4390. [CrossRef]
87. Xiao, H.; Zhang, H.; Guo, Y.; Hao, H.; Chang, H.; Li, Y. Formation of Akaganeite in Atmospheric Corrosion of Carbon Steel Induced by NaCl Particles in an 85% RH Environment. *Materials* **2025**, *18*, 4462. [CrossRef]
88. Song, S.; Qin, G.; Lan, T.; Li, Z.; Xing, G.; Liu, Y. Study on Multi-Factor Coupling Fatigue Properties of Weathering Steel Welded Specimens. *Materials* **2025**, *18*, 4551. [CrossRef]

materials

MDPI

Article

Numerical Simulation of Fluid Flow, Solidification, and Solute Distribution in Billets under Combined Mold and Final Electromagnetic Stirring

Zhenhua Feng [1], Guifang Zhang [1,*], Pengchao Li [1,2] and Peng Yan [1,*]

[1] Faculty of Metallurgy and Energy Engineering, Kunming University of Science and Technology, Kunming 650093, China; fengzhenhua666@126.com (Z.F.); 13696392999@163.com (P.L.)
[2] Linyi Iron and Steel Investment Group Special Steel Co., Ltd., Linyi 276000, China
* Correspondence: guifangzhang65@163.com (G.Z.); yanp_km@163.com (P.Y.); Tel.: +86-137-0871-6748 (G.Z.); Tel.: +86-186-8732-0090 (P.Y.)

Abstract: In this study, a three-dimensional segmented coupled model for continuous casting billets under combined mold and final electromagnetic stirring (M-EMS, F-EMS) was developed. The model was verified by comparing carbon segregation in billets with and without EMS through plant experiments. The findings revealed that both M-EMS and F-EMS induce tangential flow in molten steel, impacting solidification and solute distribution processes within the billet. For M-EMS, with operating parameters of 250A-2Hz, the maximum tangential velocity (velocity projected onto the cross-section) was observed at the liquid phase's edge. For F-EMS, with operating parameters of 250A-6Hz, the maximum tangential velocity occurred at $f_l = 0.7$. Furthermore, F-EMS accelerated heat transfer in the liquid phase, reducing the central liquid fraction from 0.93 to 0.85. M-EMS intensified the washing effect of molten steel on the solidification front, resulting in the formation of negative segregation within the mold. F-EMS significantly improved the centerline segregation issue, reducing carbon segregation from 1.15 to 1.02. Experimental and simulation results, with and without EMS, were in good agreement, indicating that M+F-EMS leads to a more uniform solute distribution within the billet, with a pronounced improvement in centerline segregation.

Keywords: numerical simulation; billets; electromagnetic stirring; fluid flow; carbon segregation

1. Introduction

Electromagnetic stirring (EMS) is a widely used metallurgical process in continuous casting processes. It utilizes electromagnetic forces to stir molten steel, improving the fluidity of the steel, promoting the uniform distribution of solute elements, refining the solidification structure of the cast billet, and ultimately achieving better metallurgical results, in turn, enhancing production efficiency and product quality [1]. EMS is generally categorized into different types based on its installation location, including mold electromagnetic stirring (M-EMS), strand electromagnetic stirring (S-EMS), and final electromagnetic stirring (F-EMS). Each type of EMS has distinct metallurgical effects. Therefore, it is crucial to investigate the impact of combined EMS on the metallurgical behavior of billets to improve their quality.

Many studies based on production experiments have demonstrated that M-EMS primarily serves to refine grain structure and, to some extent, alleviate central segregation issues in strands. Wu et al. [2] investigated the influence of M-EMS on the solidification structure of strands, and their findings indicate that increasing electromagnetic torque can refine grain size, expand the equiaxed grain zone, and improve central segregation issues. Regarding the effects of F-EMS, several production experiments have shown a significant improvement in central segregation issues [3,4], and it also offers some improvement in addressing central shrinkage concerns [5]. In addition, the experimental study by Falkus

et al. [6] showed that casting parameters such as casting speed also have a very obvious impact on macrosegregation.

Due to the high temperature and opacity constraints of the continuous casting process, the flow, heat transfer, and species transfer processes of molten steel cannot be directly observed through experimental methods. Therefore, numerical simulation methods serve as an ideal tool to investigate the impact of EMS on the metallurgical behavior of continuous casting strands. Since the 1960s, Flemings and his colleagues [7–9] have conducted pioneering research, discovering the significance of convection in the mushy zone during alloy solidification and deriving fundamental equations describing macrosegregation induced by interdendritic flow. Mehrabian et al. [10] developed a macrosegregation model considering the influence of shrinkage and thermal buoyancy on liquid flow, treating the solid–liquid two-phase region as a porous medium and calculating the flow velocity of interdendritic liquid using Darcy's Law. The model made assumptions of numerical values for temperature gradients and solidification rates due to the absence of solving the energy transfer equation. Fuji et al. [11] attempted to solve the momentum and energy equations in the solid–liquid two-phase region but did not couple the transport phenomena between the two-phase region and the solid region, and they specified the location of the solid–liquid interface. In the early 1980s, Ridder et al. [12] reported the first macrosegregation model that explained the coupling flow between the mushy zone and the liquid region. They solved the coupled equations given by Darcy's Law, the energy equation in the mushy zone, the Local Solute Redistribution Equation (LSRE), and the momentum and energy equations in the fully liquid region. The predicted macrosegregation patterns showed good agreement with experimental measurements. Based on these theories and models, many researchers have investigated macrosegregation behavior in various alloy systems [13–15]. Bennon et al. [16] studied dendrite erosion in the mushy zone and the formation of channel-type "A" segregation using a continuum model, achieving predictive capabilities by fully coupling the solute conservation equation with the energy and momentum conservation equations. Hebditch [17] examined the influence of interdendritic liquid density changes during solidification using Pb–Sn and Sn–Zn alloys and identified interdendritic convection as the primary mechanism for macrosegregation formation. The studies mentioned above mainly focused on macrosegregation in ingots, which is more complex compared to the transport behavior and formation mechanism of macrosegregation in the continuous casting system.

Many scholars have established corresponding models for different phenomena in the continuous casting process. Grundy et al. [18] proposed that hard secondary cooling significantly reduces macrosegregation through numerical simulation methods. Rajiah et al. [19] proposed that macrosegregation happens as a result of the breakage of columnar dendrites in the low ductility region of steel between zero ductile temperature (ZDT) and zero strength temperature (ZST). Melo et al. [20] calculated Secondary Dendrite Arm Spacing and second-phase particles were included, and the measured values are in good agreement with the calculated values. Mramor et al. [21] used the Reynolds-Averaged Navier–Stokes (RANS) model to predict the solute distribution within the crystallizer at different casting temperatures. The results indicated that lower casting temperatures favor a more uniform distribution of solutes. Moreover, in their study [22], a comparison was made between the Large Eddy Simulation (LES) model and the two-equation Low Re $k-\varepsilon$ turbulence RANS model in terms of temperature, velocity, and computational times. The LES model successfully captures the transient nature of vortices, a feature that RANS-type turbulence models struggle to address. However, it is important to note that the computational cost of LES models is significantly higher compared to RANS models. Wu et al. [23] studied the solute migration process in the vicinity of the mold, and the results of this model indicate a significant influence of M-EMS on dendritic growth and solute transport during the initial solidification process of molten steel. The research suggests that the addition of M-EMS leads to a thinner solidification shell at the outlet of the mold, and

due to the enhanced scouring effect of molten steel on the solidification front, it results in negative segregation. This was also proposed in the work of Kihara et al. [24].

The combined effects of M+F-EMS are also documented. Zhang et al. [25] employed a 2D–3D hybrid model to describe the influence of M+F-EMS on macrosegregation behavior in billets. In the regions of M-EMS and F-EMS, a three-dimensional model was used, while a two-dimensional model using the slicing method was applied in the secondary cooling zone. The study results reveal that the macrosegregation behavior of carbon, sulfur, manganese, and phosphorus in the mold is very similar. As the distance from the surface of the strand increases, the degree of solute segregation changes from positive to negative. Due to the significant challenge in simulating computational efficiency and convergence using geometric models of the same size as the continuous casting machine, there are fewer reports on using full three-dimensional models to describe the metallurgical effects of combined EMS. Wang et al. [26] established a curved three-dimensional model for the macrosegregation of billets with M+F-EMS. The model neglects the effect of thermal solute buoyancy, and it has been reported that the calculation time for this model is approximately 50 days. Dong et al. [27] developed a three-dimensional model that ignores the curvature of the continuous casting machine. Although the difference in geometric models may lead to inaccurate results, the study also demonstrated the positive impact of M-EMS+F-EMS on improving the solute distribution in strands.

This study, following the geometry of a continuous casting machine in use at a steel plant, constructed a segmented three-dimensional multiphysics coupling model for the curved continuous casting of billets. The primary objective was to investigate the influence of M+F-EMS on the internal fluid dynamics, heat transfer, solidification, and solute distribution in billet. Subsequently, the production experiments were conducted at the steel plant under two EMSs and non-EMS conditions. The results of these experiments were used to validate the model, particularly with regard to carbon segregation in the experimental billets.

2. Model Description

2.1. Assumptions

(1) Molten steel is considered to be an incompressible Newtonian fluid, and all thermophysical properties are assumed to be uniform and isotropic [27].
(2) The continuous casting process is assumed to be in a steady-state or quasi-steady-state condition. This means that within the computational domain, physical parameters such as flow state, temperature distribution, and solute distribution do not vary with time or vary periodically.
(3) The effects of mold taper and vibration, as well as phenomena like solidification shrinkage and bulging, are neglected. It is assumed that the shape of the cast billet remains constant throughout the entire continuous casting process.
(4) Low Reynolds number turbulence models are employed to simulate the flow field, in accordance with previous studies [27,28].
(5) This study does not account for the electromagnetic heat generated by EMS on the cast billet.
(6) Due to the similar segregation behaviors of solute elements such as phosphorus, sulfur, and manganese in steel, this study specifically focuses on the macrosegregation behavior of carbon. Additionally, interactions between different elements are disregarded.

2.2. Governing Equations

2.2.1. Fluid Flow

The fluid flow can be described by the following governing equations:

$$\nabla \cdot (\rho \boldsymbol{u}) = 0 \tag{1}$$

where ρ represents the density of the mixture, kg/m^3, and $\boldsymbol{u}$ represents the velocity of the mixture, m/s.

$$\nabla\cdot(\rho\boldsymbol{u}\boldsymbol{u}) = \nabla\cdot(\mu_{\text{eff}}\nabla\boldsymbol{u}) - \nabla p + \rho g + F_{mag} + F_b + S_D \tag{2}$$

where p represents the pressure, Pa. g stands for the acceleration due to gravity, which, in this study, is set to 9.81 m/s^2. F_{mag} denotes the electromagnetic force, and its description is provided in the electromagnetic governing equations. μ_{eff} represents the effective viscosity, which is calculated as the sum of the laminar viscosity coefficient μ and the turbulent viscosity coefficient μ_T. The value of the turbulent viscosity coefficient μ_T can be determined using the following equation:

$$\mu_T = \rho C_\mu \frac{k}{\varepsilon^2} \tag{3}$$

where C_μ is an empirical constant with a value of 0.09. k represents the turbulent kinetic energy, m^2/s^2. ε stands for the turbulent dissipation rate, m^2/s^3.

In Equation (2), F_b represents the thermal and solutal buoyancy and can be calculated using the following formula:

$$F_b = \rho g\left[\beta_T\left(T - T_{ref}\right) + \beta_C\left(C - C_{ref}\right)\right] \tag{4}$$

where β_T denotes the thermal expansion coefficient, 1/K. T represents the temperature, K. T_{ref} is the reference temperature, assumed as the liquidus temperature in this study. β_c stands for the solutal expansion coefficient, 1/wt.%. C signifies the carbon concentration, 1/wt.%. C_{ref} is the reference carbon concentration, representing the initial carbon content in the molten steel.

In this study, the enthalpy-porosity technique is employed to treat the mushy zone as a porous medium. In Equation (2), S_D represents the Darcy source term and can be computed using the following formula:

$$S_D = \frac{(1-\alpha)^2}{\alpha^3 + \xi} A_{mush}\left(\boldsymbol{u} - \boldsymbol{u_p}\right) \tag{5}$$

where α denotes the liquid phase fraction. ξ is a very small positive number, chosen to ensure that the denominator is not zero (in this study, it takes a value of 0.001). $\boldsymbol{u_p}$ represents the casting speed, m/s. A_{mush} stands for the mushy zone constant, and its value can be calculated using the following formula [29]:

$$A_{mush} = \frac{180}{\lambda_2^2} \tag{6}$$

$$\lambda_2 = \begin{cases} (169.1 - 720.9\cdot C_C)\cdot C_R & 0 < C_C < 0.15 \\ 143.9\cdot C_R^{-0.3616}\cdot C_C^{(0.5501 - 1.996 C_C)} & 0.15 < C_C \end{cases} \tag{7}$$

where λ_2 represents the secondary dendrite arm spacing, μm. C_R stands for the cooling rate, °C/s; in this work, the cooling rate was calculated by taking the difference between the cross-sectional average temperature at the solidification endpoint and the pouring temperature, divided by the time taken to reach the solidification endpoint and the value is 0.7 °C/s in this work. C_C represents the carbon content, wt.%.

In this study, the low Reynolds number turbulent k–ε model is employed, where the turbulent kinetic energy k and turbulent dissipation rate ε in Equation (3) are determined using the following expressions:

$$\rho(\boldsymbol{u}\cdot\nabla)k = \nabla\cdot\left[\left(\mu + \frac{\mu_T}{\sigma_k}\right)\nabla k\right] + P_k - \rho\varepsilon \tag{8}$$

$$\rho(\boldsymbol{u}\cdot\nabla)\varepsilon = \nabla\cdot\left[\left(\mu + \frac{\mu_T}{\sigma_\varepsilon}\right)\nabla\varepsilon\right] + C_{\varepsilon 1}\frac{\varepsilon}{k}P_k - C_{\varepsilon 2}\rho\frac{\varepsilon^2}{k} \tag{9}$$

where P_k represents the turbulent kinetic energy generated due to the mean velocity gradient, m^2/s^2. σ_k is the Prandtl number for turbulent kinetic energy k, with a value of 1.0 in this study. σ_ε is the Prandtl number for turbulent dissipation rate ε, set to 1.3 in this study. $C_{\varepsilon 1}$ and $C_{\varepsilon 2}$ are empirical constants in the low Reynolds number turbulent k–ε model, taking values of 1.44 and 1.92, respectively, in this study.

2.2.2. Electromagnetism

In this study, the frequency domain method is used to calculate the electromagnetic fields generated by M and F-EMS. In the frequency domain, the relationship between electric field and magnetic induction intensity is converted by Fourier transform into the following equations:

Faraday's Law of Electromagnetic Induction:

$$\nabla \times \boldsymbol{E} = -j\omega \boldsymbol{B} \tag{10}$$

where $\boldsymbol{E}$ represents the electric field strength, N/C. j represents the imaginary unit. ω represents the angular frequency, rad/s. $\boldsymbol{B}$ represents the magnetic flux density, T.

Gauss's Law for Magnetic Fields:

$$\nabla \cdot \boldsymbol{B} = 0 \tag{11}$$

Ampere's Law with Maxwell's Addition:

$$\nabla \times \boldsymbol{H} = \mathbf{J} + j\omega \varepsilon_r \boldsymbol{E} \tag{12}$$

where $\boldsymbol{H}$ represents the magnetic field strength, A/m. $\boldsymbol{J}$ represents the current density, A/m^2.

Without considering the influence of molten steel flow on the magnetic field, Ohm's Law can be simplified to the following form:

$$\boldsymbol{J} = \sigma \boldsymbol{E} \tag{13}$$

where σ represents the electrical conductivity, S/m.

The constitutive equation for the above formulae is:

$$\boldsymbol{B} = \mu \boldsymbol{H} \tag{14}$$

where μ represents the magnetic permeability, H/m.

The relative permeability of iron core is set to 1000, the relative permeabilities of air, strand, copper mold, and coil are set to 1, the electric conductivity of strand is set to 7.14×10^5 S/m, and the electric conductivity of copper mold is set to 3.18×10^7 S/m.

The time-averaged Lorentz force generated by EMS can be calculated using the following formula:

$$F_{mag} = \frac{1}{2} Re(\boldsymbol{J} \times \boldsymbol{B}^*) \tag{15}$$

where Re represents the real part of a complex number and $\boldsymbol{B}^*$ is the complex conjugate of the magnetic induction vector $\boldsymbol{B}$.

2.2.3. Heat Transfer and Solidification

In the continuous casting system, the energy conservation equation during the solidification process of billets is expressed as follows:

$$\nabla \cdot (\rho \boldsymbol{u} H) = \nabla \cdot (k_{\text{eff}} \nabla T) \tag{16}$$

where H represents the total enthalpy, J/kg. k_{eff} denotes the effective thermal conductivity, W/(m·K). H and k_{eff} can be expressed by the following formulae, respectively:

$$H = h_{\text{ref}} + \int_{T_{\text{ref}}}^{T} c_p dT + f_l L \tag{17}$$

$$k_{\text{eff}} = \begin{cases} k_{T,s} & T \le T_s \\ k_{T,s} f_s + k_{T,l} f_l & T_s < T < T_l \\ k_{T,l} + \frac{\mu_T}{Pr_t} & T > T_l \end{cases} \tag{18}$$

where h_{ref} represents the enthalpy at the reference temperature, J/kg. c_p is the specific heat capacity of steel, J/(kg·K). L is the latent heat of steel, J/kg. Pr_t is the turbulent Prandtl number. f_l and f_s are the liquid and solid phase fractions, and they can be calculated using the following formulae [30]:

$$f_l = 1 - f_s = \begin{cases} 0 & T \le T_s \\ \frac{T - T_s}{T_l - T_s} & T_s < T < T_l \\ 1 & T_l \le T \end{cases} \tag{19}$$

where T_{l} is the liquidus temperature, set as a constant in this study at 1788 K and T_{s} is the solidus temperature, also set as a constant in this study at 1738 K.

2.2.4. Solute Transport

In this study, the following equations are used to describe the carbon transport process within the billet:

$$\begin{aligned} \nabla\cdot(\rho \boldsymbol{u} C) = \nabla\cdot\left[\rho\left(D_l + \tfrac{\mu_T}{Sc_t}\right)\nabla\cdot C\right] + \nabla\cdot[\rho f_s D_s \nabla\cdot(C_s - C)] + \nabla \\ \cdot[\rho f_l D_l \nabla\cdot(C_l - C)] - \nabla\cdot[\rho(\boldsymbol{u} - \boldsymbol{u}_{\text{cast}})(C_l - C)] \end{aligned} \tag{20}$$

where C is the carbon concentration, wt.%. Sc_t is the turbulent Schmidt numbers, set to 1. D_s is the diffusion coefficient of carbon in the solid phase, m^2/s. C_s is the carbon concentration in the solid phase, wt.%. D_l is the diffusion coefficient of carbon in the liquid phase, m^2/s. C_l is the carbon concentration in the liquid phase, wt.%. C_s and C_l can be expressed by the following equations:

$$C_l = \frac{C}{1 + f_s(k_C - 1)} \tag{21}$$

$$C_s = \frac{k_c C}{1 + f_s(k_C - 1)} \tag{22}$$

where k_c is the equilibrium distribution coefficient for carbon.

3. Computational Procedure

3.1. Geometry and Meshing

This study employed COMSOL Multiphysics 5.6 (COMSOL, Inc., Burlington, VT, USA) and SOLIDWORKS 2018 (Dassault Systèmes SOLIDWORKS Corp., Waltham, MA, USA) to establish a three-dimensional geometric model of a bent continuous casting billet. The geometric model of the continuous casting billet was created using COMSOL Multiphysics. The three-dimensional geometric models of M-EMS and F-EMS were constructed using SOLIDWORKS. These models were exported in the .igs file format and imported into COMSOL. The positions of M-EMS and F-EMS in COMSOL were adjusted based on the installation locations in the steel plant. The F-EMS was aligned parallel to the cross-section of the cast billet at its installation location. The curved three-dimensional model was established according to the dimensions of a 10-strand continuous casting machine used in

a specific steel plant. The model utilizes a straight-type SEN at the mold inlet, consistent with the practical production setup. The SEN has an inner diameter of 0.026 m, an outer diameter of 0.09 m, and is submerged to a depth of 0.11 m. The installation positions of the stirrers and other geometric parameters are detailed in Table 1.

Table 1. Three-dimensional geometric model parameters.

Parameters	Value
Billet cross-sectional dimensions	200 mm × 200 mm
Continuous casting machine arc radius	12 m
Mold effective length	0.8 m
SEN inner diameter	0.026 m
SEN outer diameter	0.09 m
SEN depth	0.11 m
Mold thickness	0.01 m
Vertical distance from M-EMS to meniscus	0.45 m
Vertical distance from F-EMS to meniscus	9.23 m

This study divides the three-dimensional multiphysics coupled model into three computational domains based on the flow and solute transport phenomena in different regions during the continuous casting process. The geometric model division method is illustrated in Figure 1. The mold region and Zone 1 of the secondary cooling zone are grouped as Domain 1. This is due to the consideration of the effect of M-EMS and the jet action of molten steel entering the mold at a high speed from the submerged entry nozzle (SEN), leading to the formation of forced convection in this area. Domain 2 is defined by dividing Zone 2 to Zone 5 of the secondary cooling zone and a portion of the air-cooling zone. This division is motivated by the fact that after the molten steel exits the forced convection zone, its flow is mainly driven by gravity in this region, where convection is primarily induced by thermal and solutal buoyancy. Including a portion of the air-cooling zone in Domain 2 is to optimize computational resources and enhance efficiency since significant computational resources are required for magnetic field and electromagnetic force calculations. The outlet of Domain 2 is set approximately 1 m away from the length of F-EMS to conserve computational resources. Domain 3 is designated for the F-EMS action region, focusing on the forced convection effect induced by F-EMS.

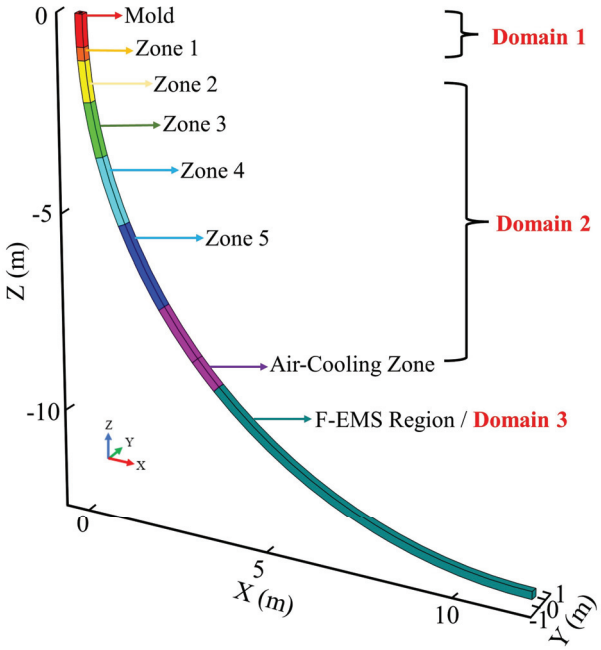

Figure 1. Schematic of computational domain division.

The segmented model is computed by sequentially solving three domains, where the physical quantities (including components of velocity in X, Y, Z denoted as u, v, w, as well as turbulent model variables k and ε, temperature T, and solute concentration C) at the outlet of the preceding domain serve as the boundary conditions for the inlet of the subsequent domain. The steady-state method is employed for fluid flow, heat transfer, solidification, and solute transport behaviors of the billet without EMS. When EMS is introduced, a frequency domain method is initially used to calculate the electromagnetic field and electromagnetic forces. Subsequently, a frequency domain steady-state method is employed to calculate the fluid flow, heat transfer, solidification, and solute transport behaviors influenced by EMS. All simulation computations are conducted using COMSOL Multiphysics.

Due to the curvature of the model, the direction and magnitude of the casting speed vary with position. As is evident from Figure 1, the cast billet is symmetric about the Y-axis. Therefore, the casting speed does not have a component along the Y-axis ($\boldsymbol{u}_{\mathrm{cast-Y}} = 0$). The components of the casting speed along the X-axis and Z-axis are calculated by the following equations:

$$\boldsymbol{u}_{\mathrm{cast-X}} = \boldsymbol{u}_{\mathrm{cast}} \cdot sin\theta \tag{23}$$

$$\boldsymbol{u}_{\mathrm{cast-Z}} = \boldsymbol{u}_{\mathrm{cast}} \cdot cos\theta \tag{24}$$

$$\theta = \arcsin\left(\frac{s}{R}\right) \tag{25}$$

where $\boldsymbol{u}_{\mathrm{cast-X}}$ is the component of the casting speed along the X-axis, m/s. $\boldsymbol{u}_{\mathrm{cast-Z}}$ is the component of the casting speed along the Z-axis, m/s. θ is the angle between the position and the meniscus. s is the vertical distance from this position to the meniscus, equal to the absolute value of the Z-axis coordinate of the position, m. R is the straight-line distance from the position to the center of the curved continuous casting machine, m.

Figure 2 displays the geometric model and meshing of the regions affected by M-EMS and F-EMS. M-EMS comprises 12 coils, divided into six groups, with each group carrying current in the same phase. The phase difference between each group is 120°. F-EMS consists of 6 coils and, thus, no grouping is needed. The three-phase current input method is the same as that of M-EMS. Hexahedral meshing is employed for both the billet and the electromagnetic stirrer. However, when calculating the magnetic field generated by EMS, meshing is applied to the surrounding air domain. Due to the complexity of the geometric model, adaptive tetrahedral meshing is used for meshing the air domain and the copper mold. The total number of meshes for the three computational domains is approximately 3.5 million, and the installation positions of M-EMS and F-EMS are listed in Table 1.

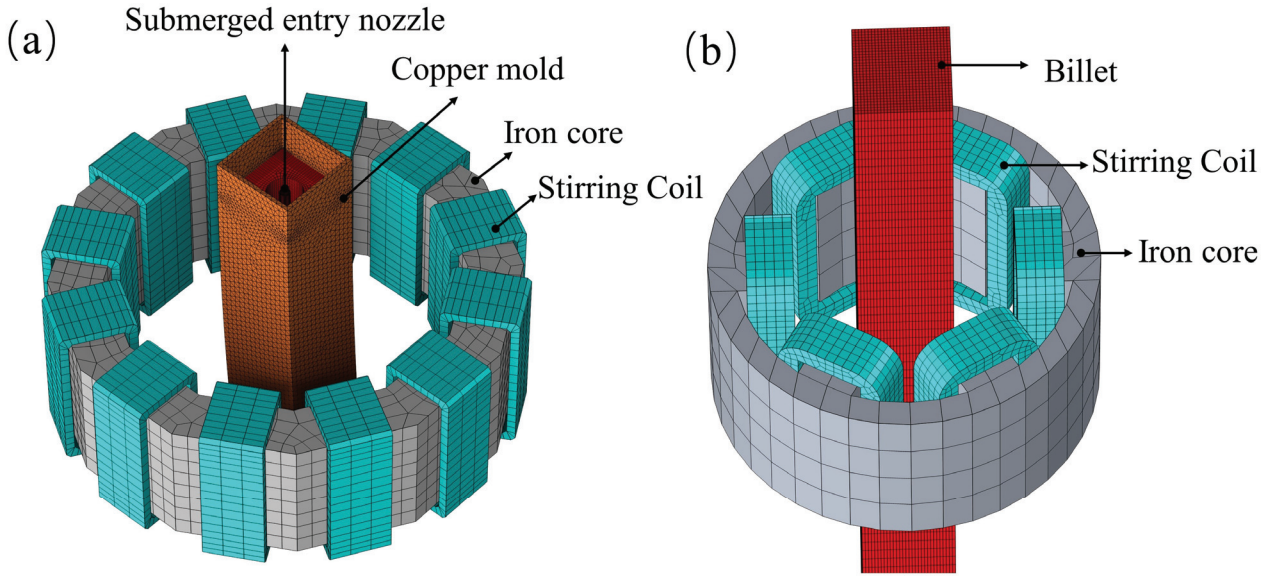

Figure 2. Mesh division of (**a**) M-EMS region; (**b**) F-EMS region.

3.2. Boundary Conditions

3.2.1. Inlets and Outlets

According to the calculation method of the segmented model, the entrance boundary conditions for Domain 2 and Domain 3 are the physical quantities at the outlet of the previous computational domain. Therefore, it is only necessary to provide the boundary conditions at the entrance of Domain 1. The entrance of Domain 1 is the upper end of the SEN, and the values of the physical quantities required for the turbulence model at this location can be calculated using the following formulae:

$$\boldsymbol{u}_0 = \frac{4S^2}{\pi d^2}\boldsymbol{u}_{\text{cast}} \tag{26}$$

$$k_0 = 0.01 \cdot {\boldsymbol{u}_0}^2 \tag{27}$$

$$\varepsilon_0 = \frac{{k_0}^{1.5}}{d} \tag{28}$$

where S^2 is the cross-sectional area of the cast billet, m. d is the diameter of the SEN, m. $\boldsymbol{u}_{\text{cast}}$ is the casting speed, m/s. The molten steel temperature at the inlet is set to the pouring temperature, with a value of 1813 K. The carbon concentration of the steel at the inlet is set to 0.20 wt.%. The casting speed in all three computational domains is set to 1.4 m/min.

The outlets of all three computational domains are uniformly set to a fully developed flow, meaning that the normal gradients of all variables are set to zero.

3.2.2. Walls

The surface of the strand is designated as a slip boundary condition in the fluid flow calculations. In the heat transfer computations, the surface is subjected to heat flux coefficient conditions. Specifically, in the heat transfer calculations within the mold segment, the wall heat flux q_m is determined using the following formula:

$$q_m = \rho_w c_w W_m \frac{\Delta T_w}{A_m} \tag{29}$$

where ρ_w represents the density of the cooling water, kg/m^3. c_w denotes the specific heat capacity of the cooling water, J/(kg·K). W_m stands for the flow rate of the cooling water in the mold, L/min. ΔT_w signifies the temperature difference between the inlet and outlet of the cooling water, K. A_m represents the contact area between the billet and the mold, m^2.

The heat flux in the secondary cooling zone is set as q_s and is determined by the following formula:

$$q_s = h_s\left(T_{surf} - T_w\right) \tag{30}$$

where T_{surf} represents the surface temperature of the cast billet, K. T_w is the temperature of the cooling water, K. h_s is the heat transfer coefficient. The magnitude of h_s is correlated with the cooling water flow rate for each segment of the secondary cooling zone and is calculated using the following formula [31]:

$$h_s = 116 + 10.44{W_s}^{0.851} \tag{31}$$

where W_s denotes the cooling water flow rate in the secondary cooling zone, L/min. The lengths and cooling water flow rates for each segment of the secondary cooling zone are listed in Table 2.

The heat flux in the air-cooling zone is set as q_a, and its magnitude is determined by the following formula:

$$q_a = \varepsilon_s \sigma\left(T_{surf}^4 - T_{amb}^4\right) \tag{32}$$

where T_{amb} represents the ambient temperature, K. ε_s is the emissivity of the strand and σ is the Stefan–Boltzmann constant.

Table 2. Lengths and water flow rate for each segment in the secondary cooling zone.

	Zone 1	Zone 2	Zone 3	Zone 4	Zone 5
Length (m)	0.3	1.0	1.3	1.5	1.5
Water flow rate (L/min)	43.9	38.4	23.3	17.8	13.7

3.2.3. Thermal Properties

The subject of this study is billets with a cross-sectional dimension of 200 mm × 200 mm produced by a 10-strand continuous casting machine in a steel plant. The steel grade is 20# and its chemical composition is listed in Table 3. The thermal properties' parameters used in the simulation calculations are presented in Table 4.

Table 3. Chemical composition of 20# steel.

Element	C	Si	Mn	S	P	Cr
Concentration (wt.%)	0.17–0.23	0.17–0.30	0.35–0.65	<0.035	<0.035	<0.25

Table 4. Properties of 20# steel.

Parameter	Symbol	Value
Thermal conductivity of liquid phase (W/(m·K))	$k_{T,l}$	38
Thermal conductivity of solid phase (W/(m·K))	$k_{T,s}$	40
Density of the billet (kg/m^3)	ρ	7100
Viscosity (Pa·s)	μ	0.0035
Initial solute concentration of carbon (wt.%)	C_0	0.20
Latent heat (kJ/kg)	L	270
Solute expansion coefficient (1/wt.%)	β_C	0.011
Thermal expansion coefficient (1/K)	β_T	1.0×10^{-4}
Diffusion coefficient in the liquid phase (cm^2/s)	D_l	0.0761exp(−134,557.44/RT)
Diffusion coefficient in the solid phase (cm^2/s)	D_s	0.0052exp(−11,700/RT)
Equilibrium distribution coefficient for carbon	k_C	0.34
Specific heat of the liquid phase (J/(kg·K))	$c_{p,l}$	828.33
Specific heat of the solid phase (J/(kg·K))	$c_{p,s}$	722
Emissivity of the strand	ε_s	0.8

4. Results and Discussions

4.1. Model Validation

To validate the coupled model established in this study, carbon segregation experiments were conducted on the 10-strand continuous casting machine equipped with M-EMS and F-EMS in a steel plant. The production parameters of the steel plant are listed in Table 5.

Table 5. Experimental production parameters.

Parameter	Value
Pouring temperature (K)	1808–1818
Casting speed (m/min)	1.3–1.4
Pouring carbon content (wt.%)	0.19–0.21
M-EMS operating parameters (A-Hz)	250-2
F-EMS operating parameters (A-Hz)	250-6

This study conducted a comparison between the measured and numerically calculated magnetic field magnitudes for M and F-EMS, as illustrated in Figure 3. Figure 3a and b, respectively, depict the comparison between the measured values and numerical simulation results of magnetic induction magnitudes at different distances from the center along the

central axis of M and F-EMS. The operating parameters for M-EMS were set at 200A-3Hz, and for F-EMS at 250A-8Hz. The Tesla meter model HT201 was used for measuring magnetic induction intensity. The results indicate a good agreement between the calculated and measured values, validating the reliability of the magnetic field model employed in this study. It is important to note that both numerical simulations and experimental measurements were conducted under the condition of no billet passing through.

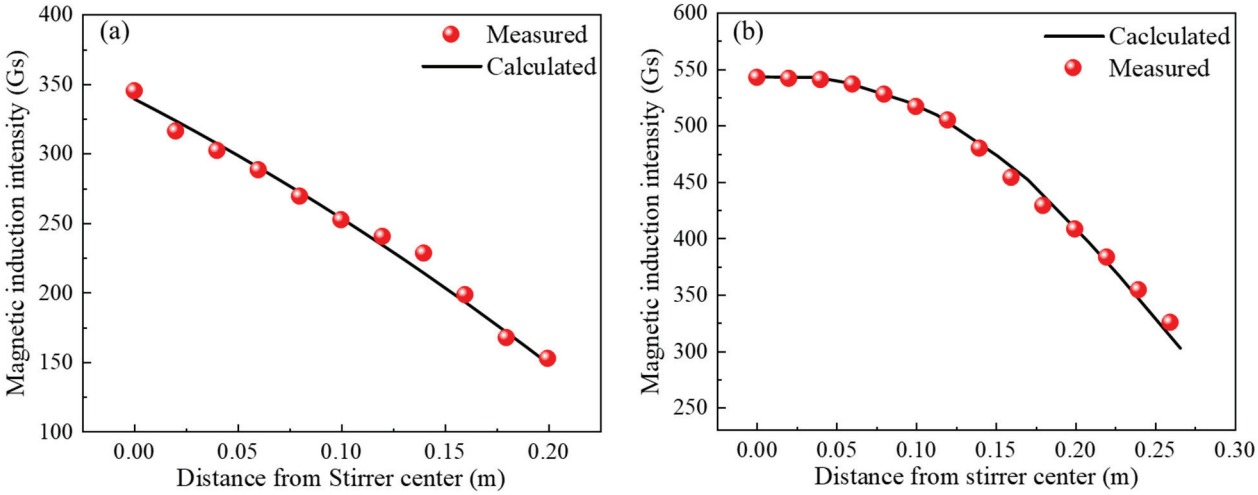

Figure 3. Comparison of measured and calculated magnetic induction intensity: (**a**) M-EMS; (**b**) F-EMS.

This study conducted a simulation calculation of carbon segregation in the billet without employing EMS and compared the results with experimental data. Figure 4 illustrates the experimental sampling method, macrostructure photographs of the trial billet, simulation outcomes, and the comparison between experimental and simulation results. In the carbon segregation experiment, shavings were collected through drilling after the complete solidification of the billet. The sampling took place just after the straightening section of the continuous casting machine (after Z = −12 m). Subsequent carbon analysis was performed using a carbon–sulfur analyzer (EMIA Pro, Horiba Inc., Osaka, Japan). A 4 mm-diameter drill bit was employed to create holes on the cross-section of the billet at nine points (1 to 4, 6 to 9, with distances from the billet edge at 5 mm, 25 mm, 50 mm, and 75 mm, where 5 denotes the center), as illustrated in Figure 4a. The segregation degree "r" was used in this study to represent the extent of carbon segregation, with its value determined by the following formula:

$$r = \frac{c}{c_0} \tag{33}$$

where c represents the carbon concentration at the point, wt.%. c_0 stands for the average carbon concentration at each sampling point in the experiment and is the initial carbon concentration in the molten steel in the simulation, wt.%. When $r > 1$, it indicates positive segregation, and when $r < 1$, it indicates negative segregation.

In the absence of EMS, Figure 4b presents the macrostructure image of the experimental billet sample after being immersed in a 1:1 hydrochloric acid–water solution at 60 °C for 10 min. Examination of the billet's macrostructure reveals a typical solidification pattern, featuring an outermost chilled zone, an inner coarser columnar zone, and a central equiaxed zone [32]. Notably, a subtle point segregation is discernible at the billet's central position. The carbon segregation distribution after complete solidification, as simulated, is illustrated in Figure 4c. The figure demonstrates the development of negative segregation in the corners and edges of the billet, consistent with the chilled zone depicted in Figure 4b. Additionally, a subtle positive segregation is observed in the subsurface. Significantly, there

is a prominent occurrence of positive segregation in the central part, corresponding to the central equiaxed zone shown in Figure 4b. Figure 4d presents a comparison between simulation and experimental results, with the horizontal axis denoting the distance from the center of the billet and the vertical axis representing the segregation degree. The simulated sampling line aligns with the experimental one. At the center of the billet, the experimental measurement of the carbon segregation degree is 1.15, while the simulated segregation degree is 1.13, resulting in an error of less than 2%. Furthermore, the results at other measurement points exhibit good concordance with the simulation. Therefore, it can be concluded that the three-dimensional coupled model established in this study is accurate.

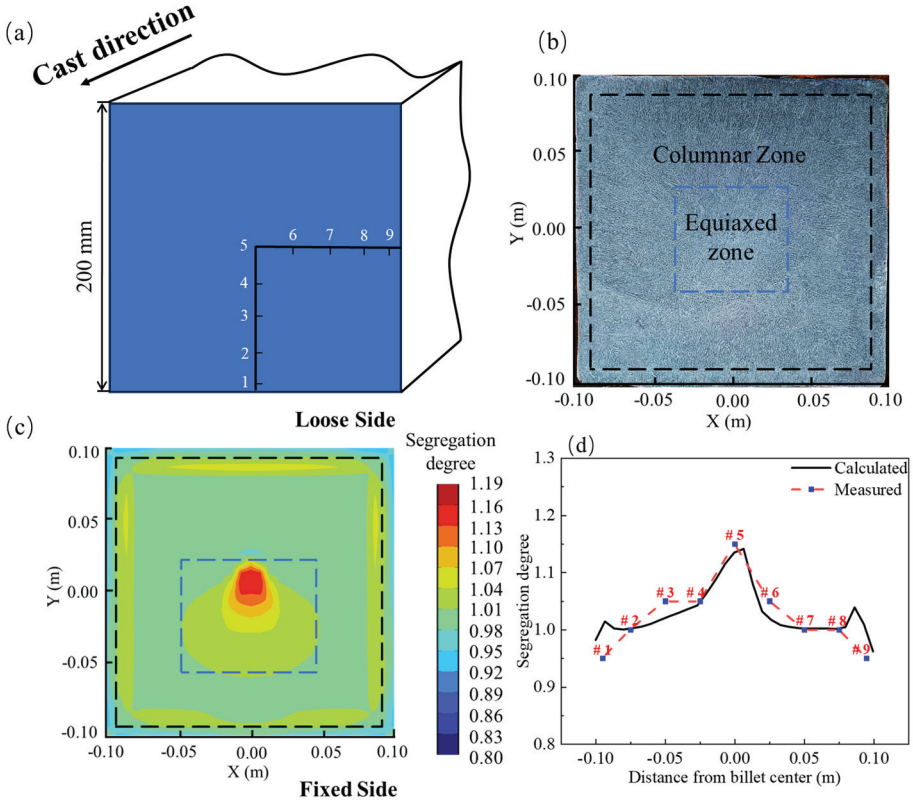

Figure 4. Model validation: (**a**) sampling method; (**b**) macrostructure image; (**c**) simulated carbon distribution; (**d**) comparison of simulated and experimental results.

4.2. Fluid Flow and Solidification

The simulation results depicting the flow field and liquid fraction distribution in the M-EMS operating region are presented in Figure 5. In the absence of M-EMS, when molten steel enters the mold from the SEN, a distinct circulation movement is formed below due to the jet effect. A portion of the molten steel moves upward along the initial solidifying shell and flows back along the casting direction upon reaching the meniscus. This creates a smaller circulation around the meniscus, solidifying shell, and outer wall of the SEN. This region exhibits poorer fluidity compared to the area below the SEN, constituting a typical "dead zone" beneath the meniscus [33]. Most of the molten steel flows along the casting direction at the bottom of the circulation formed by the impact of the jet. The curved model leads to an asymmetric flow, with the depth of impact for molten steel on the fixed side being approximately 400 mm, while on the loose side, it is approximately 500 mm, as shown in Figure 5a. Simultaneously, the difference in the degree of scouring of the solidification front on the fixed and loose sides results in uneven solute distribution. Figure 5b displays the three-dimensional streamline distribution with M-EMS operating parameters at 250A-2Hz. Under the stirring effect, molten steel forms a noticeable rotational flow in the mold, primarily in the region below the SEN to the mold

exit. The flow in the dead zone undergoes little change, preventing molten steel fluctuations at the meniscus that could lead to slag entrapment. Therefore, the installation position of M-EMS can be considered reasonable. The liquid fraction distributions at Z = −0.11 m (SEN outlet), Z = −0.45 m (M-EMS center), and Z = −0.80 m (mold exit) are also shown in both Figure 5a,b. Under the strong cooling conditions in the mold, a thin solidifying shell has already formed at the SEN outlet. As the position descends, the thickness of the solidifying shell gradually increases. It is noteworthy that with the addition of M-EMS, the shape of the liquid phase pool also shifts in alignment with the direction of the rotating flow.

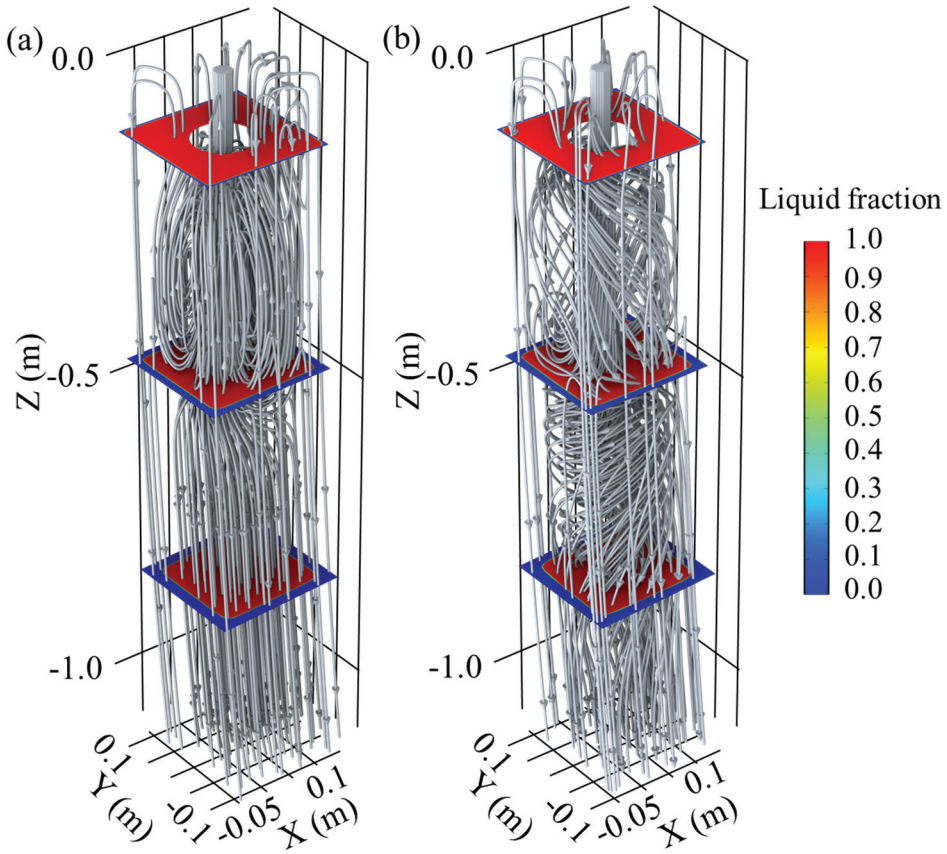

Figure 5. Effect of M-EMS on fluid flow and solidification: 3D stream-line distribution (**a**) without M-EMS; (**b**) M-EMS at 250A-2Hz.

In the presence and absence of M-EMS, the tangential velocity (velocity projected onto the cross-section) and the shape of the liquid phase at the M-EMS center cross-section (Z = −0.45 m) and the mold outlet (Z = −0.8 m) are shown in Figure 6. In this study, the region where $f_l > 0.7$ is considered as the liquid phase, $f_l < 0.3$ as the solid phase, and other regions as the mushy zone. The red line in the figure represents the contour line of $f_l > 0.7$, indicating the shape of the liquid phase. At Z = −0.45 m, without M-EMS, the tangential velocity is mainly generated by the circulating flow formed by the jet effect, as shown in Figure 6a. When M-EMS operates at 250A-2Hz, the stirring effect of M-EMS and the jet effect of the SEN are both strong. The distribution of tangential velocity is irregular despite the trend of rotational flow, as shown in Figure 6b. The distribution of tangential velocity at the Z = −0.80 m cross-section is illustrated in Figure 6c,d. It is observed that the shape of the liquid phase has undergone a significant shift, rotating clockwise with the direction of the rotational flow. The magnitude of the tangential velocity shows a clear pattern on this cross-section, being the largest at the edges of the solidification front and smaller at the corners and the center. This phenomenon is attributed to the higher solidification resistance at the corners, lower electromagnetic force at the center, and a continued strong tendency of steel liquid flow along the casting direction.

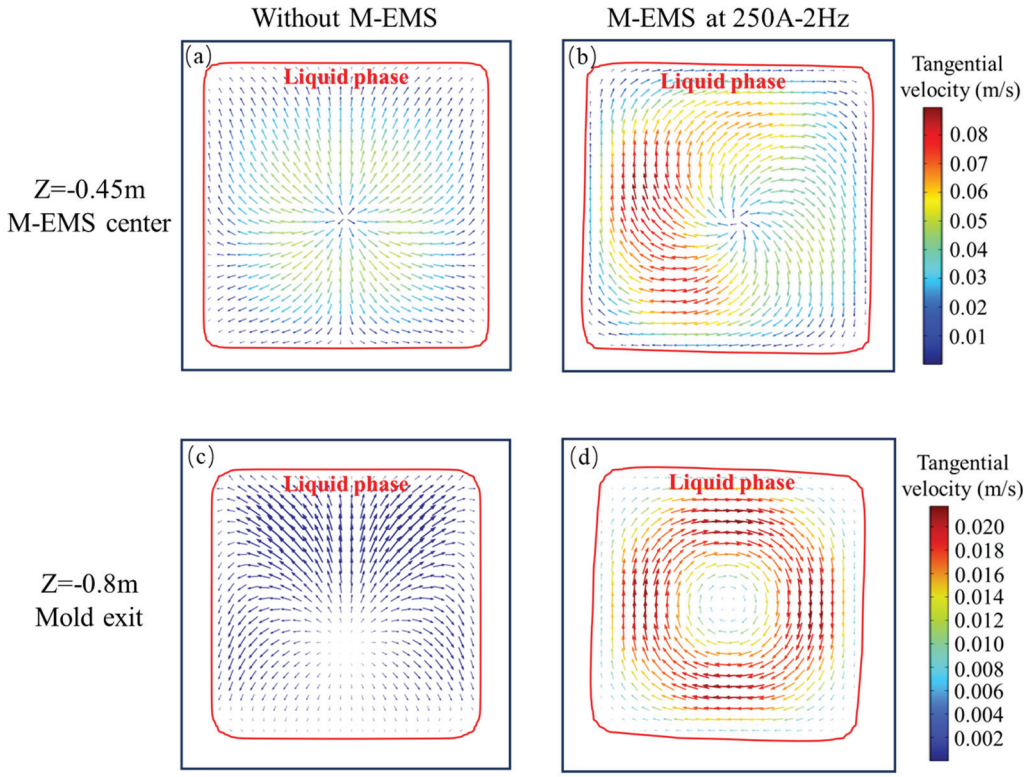

Figure 6. Vector plots on cross-sections: Z = −0.45 m (**a**) without M-EMS, (**b**) M-EMS at 250A-2Hz; Z = −0.8 m (**c**) without M-EMS, (**d**) M-EMS at 250A-2Hz.

Figure 7 illustrates the impact of F-EMS on the liquid fraction and tangential velocity, with results obtained under the operation of M-EMS at 250A-2Hz. In Figure 7a, the tangential velocity on the central cross-section with and without F-EMS is compared. It can be observed that without F-EMS, there is almost no rotational convection in the molten steel, resulting in a nearly zero tangential velocity. However, with F-EMS operating at 250A-6Hz, a significant rotational flow is generated in the molten steel in the solidification end, with a maximum tangential velocity of approximately 0.006 m/s. Figure 7b compares the influence of F-EMS on the distribution of liquid fraction. It is evident that the addition of F-EMS significantly reduces the central liquid fraction, decreasing from 0.93 without F-EMS to 0.85. This reduction is attributed to F-EMS promoting convection in the late stage of solidification, thereby accelerating heat dissipation. Figure 7c,d contrast the distribution of liquid fraction and the vector plot of tangential velocity on the Z = −9.23 m cross-section with and without F-EMS. Without F-EMS stirring, the convection in the molten steel in the late stage of solidification is mainly due to the action of thermal solutal buoyancy. In the vector plot on the right side in Figure 7c, weak circulation can be observed, where the magnitude of the tangential velocity is approximately 10^{-7} m/s. This is because the size of the molten steel in the late-stage liquid phase limits the development of flow, and the decreased steel temperature leads to a smaller thermal solutal buoyancy, resulting in weak convection at this location. Figure 7d shows the situation under F-EMS with operating parameters at 250A-6Hz. A clockwise rotational flow pattern is clearly visible on this cross-section, and the maximum tangential velocity occurs at the position of the solidification front (approximately $f_l = 0.7$). This phenomenon is attributed to the fact that both electromagnetic force and solidification resistance increase with the distance from the center of the billet. At $f_l = 0$, the solidification resistance reaches its maximum. Under the combined action of these two forces, this phenomenon occurs.

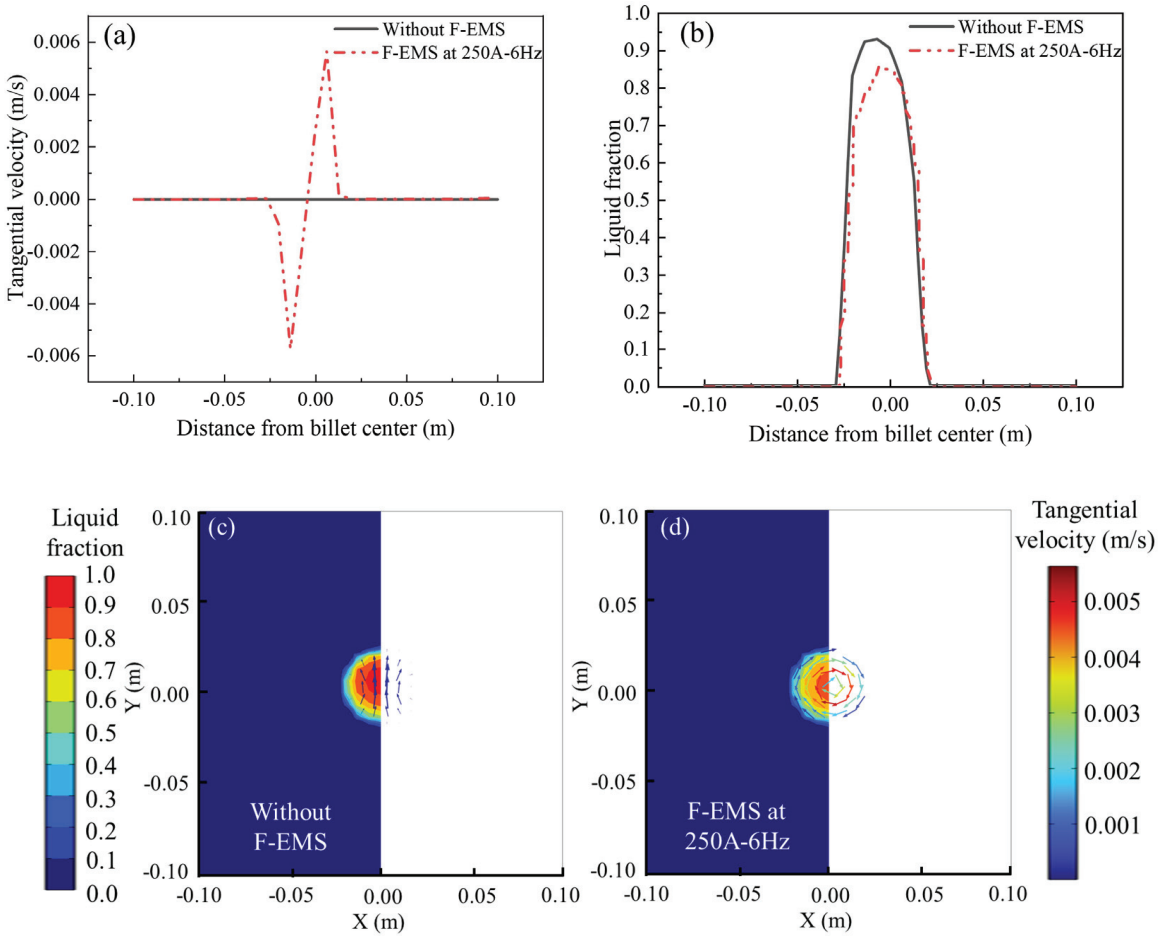

Figure 7. The influence of F-EMS on velocity and liquid fraction distribution: (**a**) tangential velocity; (**b**) liquid fraction; (**c**,**d**) contour plots of liquid fraction with and without F-EMS, along with vector plots of tangential velocity.

4.3. Solute Distribution

In the presence and absence of M-EMS, the carbon distributions on the central longitudinal section (Y = 0) of Domain 1 are shown in Figure 8. Without EMS, due to the lower solubility of carbon in the solid phase compared to the liquid phase, carbon is expelled into the molten steel. As a result, the initial solidifying shell has a lower carbon concentration, leading to a slight negative segregation, with a segregation index of approximately 0.92. In the subsurface, the combined effect of rising circulation and thermal solutal buoyancy causes higher carbon concentration steel to gather near Z = −0.3 m. As solidification progresses and the diffusion coefficient of carbon in the solid phase is small, a positive segregation layer is formed. The solute distribution in the curved model is asymmetrical, with stronger "washing effects" on the outer arc side compared to the inner arc side. Along the outer arc side, the positive segregation is reduced due to the washing effect of molten steel, resulting in a smaller positive segregation degree compared to the inner arc side, as shown in Figure 8a. When M-EMS operates at 250A-2Hz, the solute distribution undergoes changes. The positive segregation on the inner arc side is noticeably reduced. Due to the circulation formed by M-EMS, there is a slight negative segregation layer outside the positive segregation zone below the M-EMS installation position. The negative segregation index is approximately 0.95, as shown in Figure 8b. The positions of the M-EMS center and the mold exit are marked in Figure 8. The carbon distribution results on the cross-section of Domain 1 will be compared at these two positions.

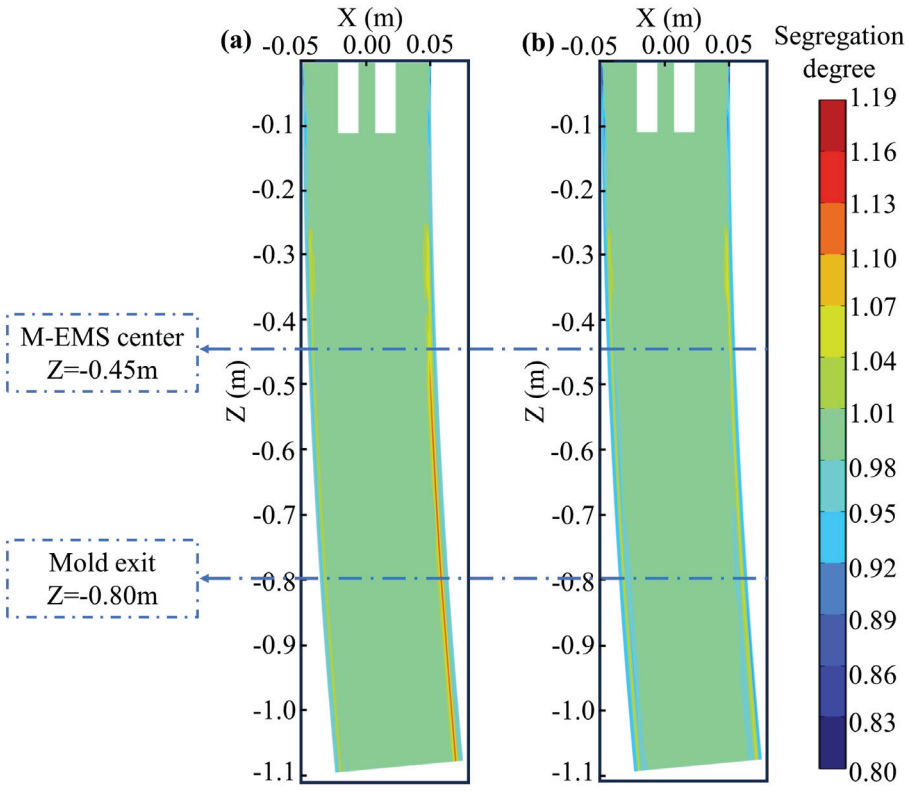

Figure 8. Carbon distribution on the longitudinal section of Domain 1: (**a**) without M-EMS; (**b**) M-EMS at 250A-2Hz.

The carbon distributions on the central section of M-EMS and the mold outlet section are depicted in Figure 9. The carbon distributions on the cross-section at Z = −0.45 m with and without M-EMS are illustrated in Figures 9a and 9b, respectively. In the absence of M-EMS, it is evident on this section that the degree of positive segregation is smaller on the fixed side compared to the loose side, as shown in Figure 9a, corresponding to Figure 8a. When M-EMS operates at 250A-2Hz, the flow pattern of the melt in the mold undergoes changes. The upward and lateral swirling flow leads to an increased degree of both positive and negative segregation, with severe segregation occurring near the corner, as depicted in Figure 9b. The comparison of the carbon segregation degree along the centerline of this cross-section is presented in Figure 9c, where negative values of X represent the side closer to the fixed side, and positive values are closer to the loose side. It can be observed from this figure that with the addition of M-EMS, the width of the positive segregation area on the loose side decreases, but a slight negative segregation appears near the solidification front, with a segregation degree of approximately 0.98. The carbon distribution on the cross-section at the mold outlet is depicted in Figure 9d,e. Without M-EMS, the carbon distribution pattern at the mold outlet is similar to that at Z = −0.45 m, but the degree of positive segregation is more severe, as shown in Figure 9d. After adding M-EMS, the positive and negative segregation degrees on this section are mitigated compared to Z = −0.45 m, as illustrated in Figure 9e. The comparison of the carbon segregation degree along the centerline of this cross-section is shown in Figure 9f. It is observed that the addition of M-EMS reduces the positive segregation, and the position of negative segregation corresponds to the flow direction, shifting clockwise. However, due to the effect of the swirling flow on the solidification front, a negative segregation layer forms in the mold, and it cannot be eliminated in the subsequent continuous casting process.

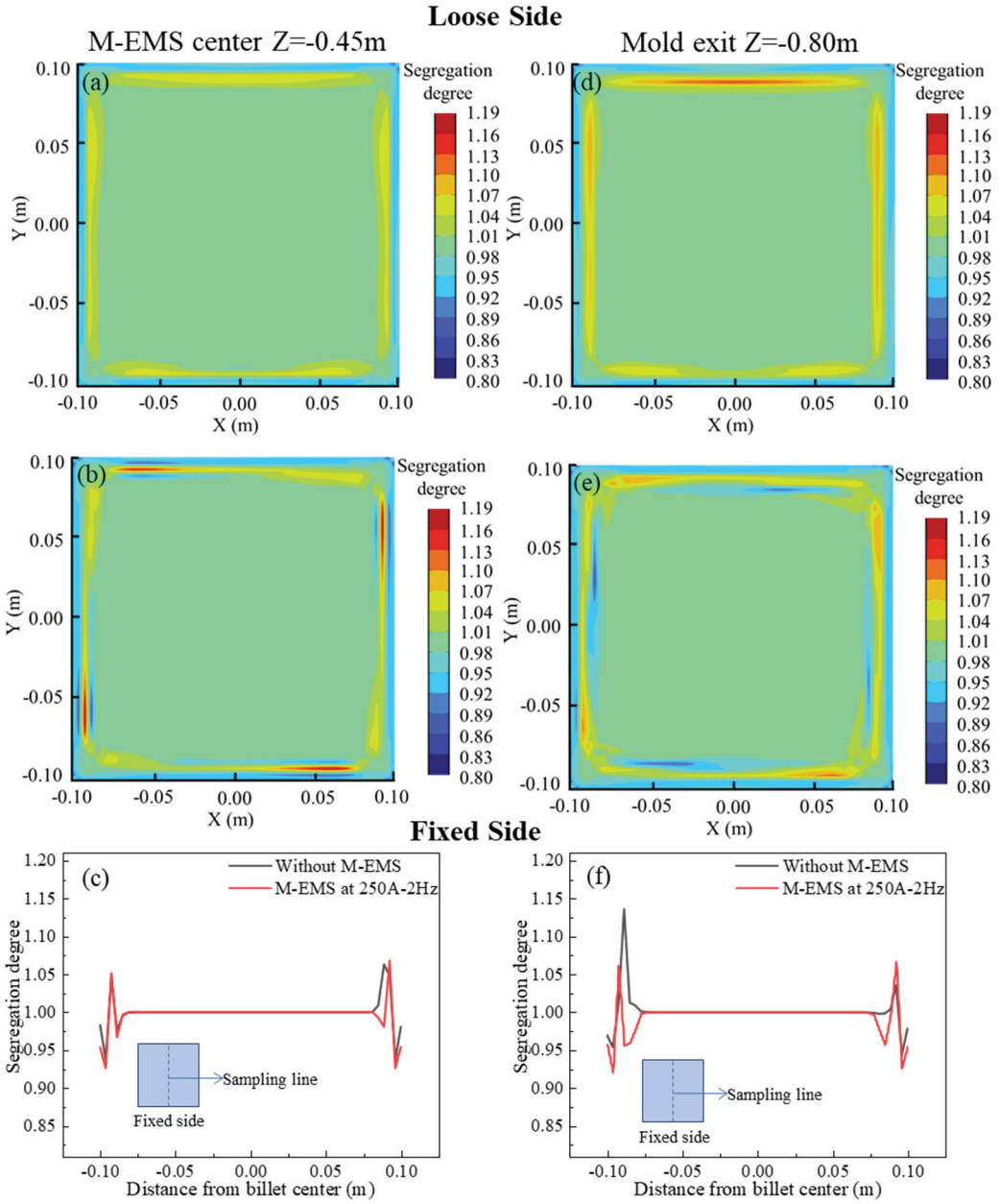

Figure 9. Carbon distribution on the cross-section: M-EMS center section (Z = −0.45 m) (**a**) without M-EMS; (**b**) with M-EMS; (**c**) carbon distribution along the centerline, mold exit (Z = −0.80 m); (**d**) without M-EMS; (**e**) with M-EMS; (**f**) carbon distribution along the centerline.

The carbon distributions near the F-EMS region are illustrated in Figure 10. Figure 10a shows that in the absence of EMS, carbon tends to accumulate significantly in the liquid phase pool during the final stages of solidification. After complete solidification, carbon in the central region cannot diffuse, resulting in severe central macrosegregation issues on the cross-section, as indicated by the carbon distribution cloud map after complete solidification in Figure 4c. Figure 10b depicts the carbon distribution cloud map on the longitudinal section when there is no M-EMS, and F-EMS operates at 250A-6Hz. It is evident that F-EMS significantly improves the solute distribution in the liquid phase pool during the final stages of solidification. The stirring effect from F-EMS contributes to a more uniform distribution of solute in the liquid phase pool. It is worth noting that F-EMS, as revealed in this study, has a pronounced improvement effect on central macrosegregation issues, which differs from the results obtained by Wang et al. [26]. This disparity can be attributed to the appropriate installation of F-EMS in this study at a position where carbon

solutes accumulate significantly. In Wang et al.'s study, the F-EMS action region was too forward (approximately Z = −10.2 m), while, based on their solute distribution results, the location where carbon accumulated significantly during the final stages of solidification was approximately Z = −15 m. This improper installation of F-EMS in Wang et al.'s study might have led to suboptimal stirring effects, allowing solutes to still accumulate significantly during the final stages of solidification, resulting in central macrosegregation.

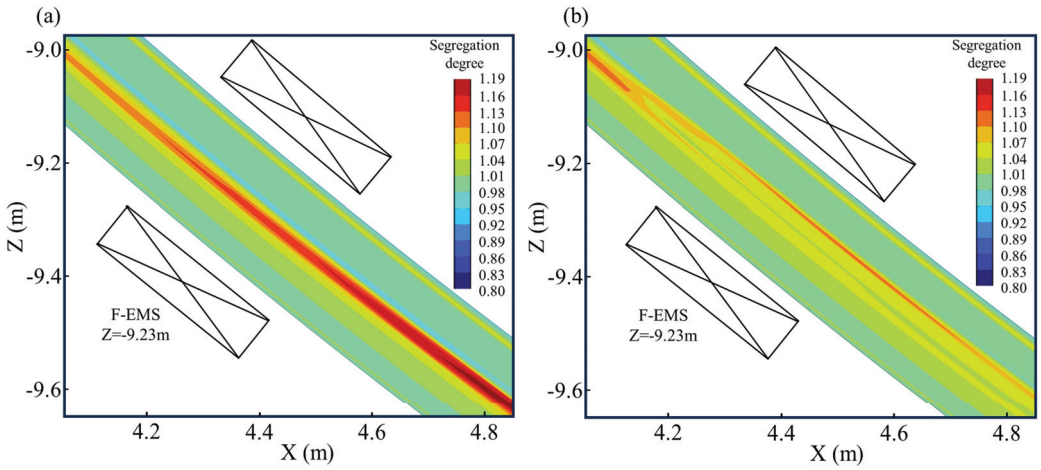

Figure 10. Effect of F-EMS on carbon distribution: (**a**) without F-EMS; (**b**) F-EMS at 250A-6Hz.

In the cross-section at Z = −11 m, where the billet has completely solidified, the carbon distributions under different EMS modes are illustrated in Figure 11. The parameters for M-EMS are set at 250A-2Hz, while F-EMS operates at 250A-6Hz. Figure 11a depicts the carbon segregation with only M-EMS. A noticeable center segregation issue persists, indicating that the effectiveness of M-EMS in addressing the center segregation problem is limited. Figure 11b shows the carbon distribution with only F-EMS. The introduction of F-EMS significantly reduces the carbon concentration in the central liquid pool, with even a slight negative segregation at the edges of the center. Figure 11c compares the carbon segregation indices under different agitation modes, with sampling locations consistent with those in Figure 11a,b. From the graph, it is evident that without EMS, the center segregation problem is most severe, with the maximum carbon segregation index along the sampling line reaching 1.15. With only M-EMS, besides changes in the carbon distribution within the initial solidification shell formed in the mold, there is a reduction in carbon concentration at the center, yielding a maximum carbon segregation index of approximately 1.11, a decrease of 0.04 compared to the case without EMS. In the case of only F-EMS, aside from a significant reduction in carbon concentration within the central liquid pool, there is no change in the carbon distribution at other locations. At this point, the carbon segregation index at the center is approximately 1.02, indicating a noticeable improvement in the center segregation problem. The impact of M+F-EMS on carbon segregation is presented in Figure 12.

Figure 12 illustrates the carbon segregation distribution in the billet when both M-EMS and F-EMS are operational, with M-EMS and F-EMS parameters set at 250A-2Hz and 250A-6Hz, respectively. In Figure 12a, the simulated carbon segregation after complete solidification shows the impact of M-EMS generating a negative segregation band and F-EMS improving the center segregation. The central liquid pool distribution is more uniform in comparison to Figure 11b. Experimental trials with M+F-EMS were conducted in a steel plant, with M-EMS operating at 250A-2Hz and F-EMS at 250A-6Hz, mirroring the simulation parameters. The macrostructure photograph of the test billet is presented in Figure 12b. The size distribution of the fine crystal zone at the billet edge, the intermediate columnar zone, and the central equiaxed zone are similar to the case without EMS. However, no significant point segregation is observed at the center. Using the same sampling method, the experimental carbon segregation results are compared with the simulation in Figure 12c.

The carbon segregation degree at the center in the experiment is 1.05, closely aligning with the simulated value of 1.02. The experimental and simulated results are in good agreement. Combining the findings from Figures 9 and 10, it is evident that M-EMS alters the carbon distribution in the initial solidification shell within the mold, generating a negative segregation band approximately 15 mm from the edge due to the effect of the circulation. M-EMS has a certain improvement effect on the center segregation issue. F-EMS significantly improves center segregation, and with M+F-EMS, the carbon distribution on the cross-section of the billet is more uniform than with only F-EMS.

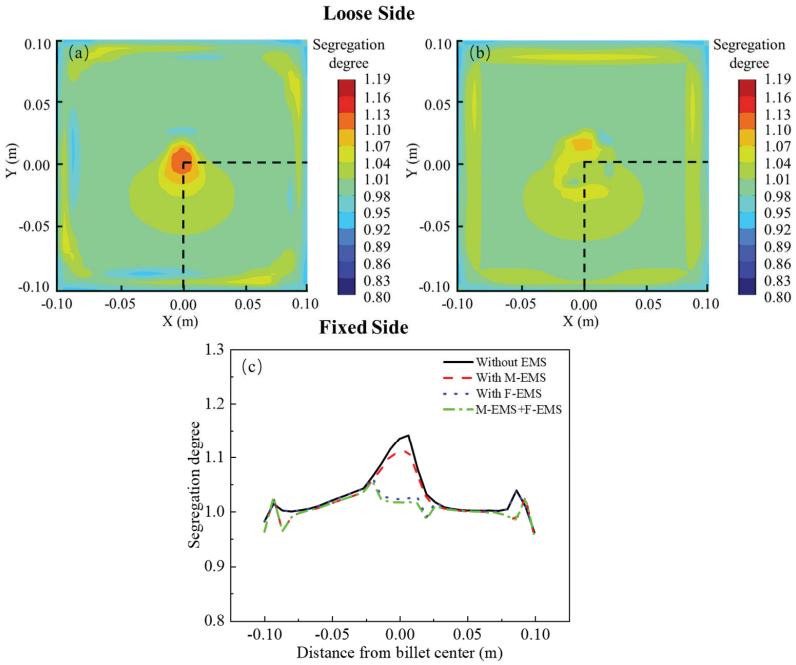

Figure 11. The effect of different EMS modes on carbon distribution: (**a**) M-EMS only; (**b**) F-EMS only; (**c**) comparison of segregation degree.

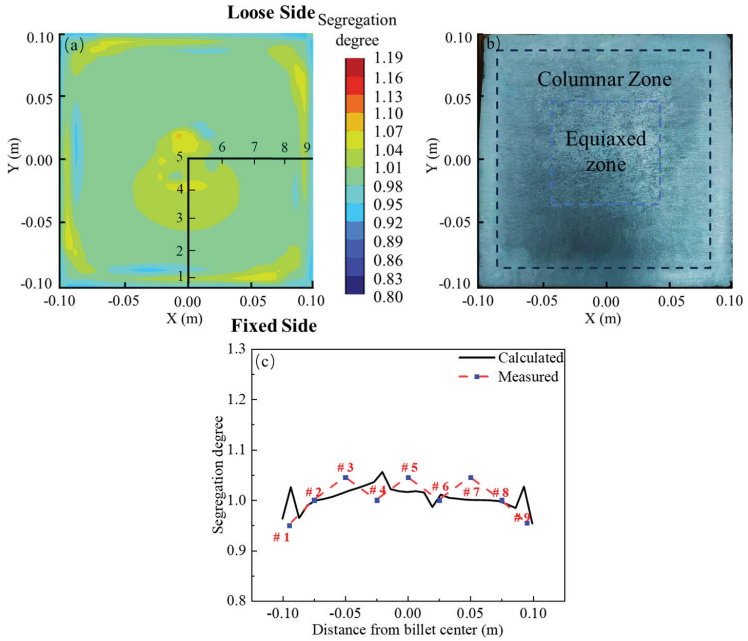

Figure 12. Carbon segregation under M+F-EMS: (**a**) simulation result; (**b**) macrostructure photo of the test billet; (**c**) comparison of simulation and experimental results.

5. Conclusions

(1) Both M-EMS and F-EMS induce tangential flow in molten steel, influencing the solidification and solute distribution processes within the billet. When M-EMS operates at 250A-2Hz, the maximum tangential velocity occurs at the periphery of the liquid pool, causing a rotational flow that deviates the shape of the liquid pool in the mold. For F-EMS operating at 250A-6Hz, the maximum tangential velocity is observed at $f_l = 0.7$, and F-EMS accelerates heat transfer in the liquid pool, reducing the central liquid fraction from 0.93 to 0.85.

(2) Both M-EMS and F-EMS alter the solute distribution within the billet. M-EMS, by increasing the tangential velocity of the steel, enhances the scouring effect of the molten steel on the solidification front, forming a negative segregation band in the mold. In comparison, F-EMS has a more pronounced effect on alleviating central segregation issues. When F-EMS operates at 250A-6Hz, the central carbon segregation is reduced from 1.15 to 1.02, demonstrating a more significant improvement.

(3) The model was validated through experiments in a steel plant. In the absence of EMS, both experimental and simulated results yielded a central carbon segregation of 1.15 and 1.13, respectively. With M+F-EMS in operation, the central carbon segregation decreased to 1.05 in experiments and 1.02 in simulations. Both experimental and simulated results indicate that M+F-EMS promotes a more uniform solute distribution in the cast billet, with a noticeable improvement in central segregation.

(4) Based on the simulation results, it can be inferred that the effect of M-EMS on improving central segregation is not significant, while F-EMS shows a remarkable improvement. In comparison with previous findings, it can be considered that the installation position of F-EMS might be closely related to the effectiveness of improving central segregation. Subsequent studies should delve deeper into the analysis of this issue.

Author Contributions: Investigation, Z.F.; Writing—review & editing, P.Y.; Project administration, validation, methodology, G.Z. and P.L. All authors have read and agreed to the published version of the manuscript.

Funding: This research was financially supported by [Hunan Zhongke Electric Co., Ltd.] grant number [HZ2021F0529A].

Data Availability Statement: The raw data supporting the conclusions of this article will be made available by the authors on request.

Conflicts of Interest: Author Pengchao Li was employed by the company Linyi Iron and Steel Investment Group Special Steel Co., Ltd. The remaining authors declare that the research was conducted in the absence of any commercial or financial relationships that could be construed as a potential conflict of interest.

References

1. Shakhov, S.I.; Vdovin, K.N. Electromagnetic Stirring in Continuous-Casting Machines. *Steel Transl.* **2019**, *49*, 261–264. [CrossRef]
2. Wu, H.; Wei, N.; Bao, Y.; Wang, G.; Xiao, C.; Liu, J. Effect of M-EMS on the Solidification Structure of a Steel Billet. *Int. J. Miner. Metall. Mater.* **2011**, *18*, 159–164. [CrossRef]
3. Qin, F. A Study on Parameters of F-EMS Process for Bearing Steel GCr15 240 Mm × 240 Mm Casting Bloom. *Spec. Steel* **2020**, *41*, 6.
4. Han, Y.; Yan, W.; Zhang, J.; Chen, J.; Chen, W.; Liu, Q. Comparison and Integration of Final Electromagnetic Stirring and Thermal Soft Reduction on Continuous Casting Billet. *J. Iron Steel Res. Int.* **2021**, *28*, 160–167. [CrossRef]
5. Li, X.; Zhang, Z.; Lv, M.; Fang, M.; Ma, S.; Li, D.; Xi, X. Effect of Mold Electromagnetic Stirring on Metallurgical Behavior in Ultrahigh Speed Continuous Casting Billet Mold. *Steel Res. Int.* **2023**, *94*, 2200796. [CrossRef]
6. Falkus, J.; Miłkowska-Piszczek, K.; Krajewski, P.; Ropka, T. Method of Verification of Carbon Segregation Ratio Determined with Experimental Methods. *Metals* **2020**, *10*, 499. [CrossRef]
7. Flemings, M.C.; Nereo, G.E. Macrosegregation. Pt. 1. *Trans. Metall. Soc. AIME* **1967**, *239*, 1449–1461.
8. Flemings, M.C.; Mehrabian, R.; Nereo, G.E. Macrosegregation. Pt. 2. *Trans. Metall. Soc. AIME* **1968**, *242*, 41–49.
9. Flemings, M.C.; Nereo, G.E. Macrosegregation. Pt. 3. *Trans. Metall. Soc. AIME* **1968**, *242*, 50–55.
10. Mehrabian, R.; Keane, M.; Flemings, M.C. Interdendritic Fluid Flow and Macrosegregation; Influence of Gravity. *Metall. Mater. Trans. B* **1970**, *1*, 1209–1220. [CrossRef]

11. Fujii, T.; Poirier, D.R.; Flemings, M.C. Macrosegregation in a Multicomponent Low Alloy Steel. *Metall. Trans. B* **1979**, *10*, 331–339. [CrossRef]
12. Ridder, S.D.; Kou, S.; Mehrabian, R. Effect of Fluid Flow on Macrosegregation in Axi-Symmetric Ingots. *Metall. Trans. B* **1981**, *12*, 435–447. [CrossRef]
13. Pickering, E.J. Macrosegregation in Steel Ingots: The Applicability of Modelling and Characterisation Techniques. *ISIJ Int.* **2013**, *53*, 935–949. [CrossRef]
14. Lesoult, G. Macrosegregation in Steel Strands and Ingots: Characterisation, Formation and Consequences. *Mater. Sci. Eng. A* **2005**, *413*, 19–29. [CrossRef]
15. Combeau, H.; Založnik, M.; Hans, S.; Richy, P.E. Prediction of Macrosegregation in Steel Ingots: Influence of the Motion and the Morphology of Equiaxed Grains. *Metall. Mater. Trans. B* **2009**, *40*, 289–304. [CrossRef]
16. Bennon, W.D.; Incropera, F.P. The Evolution of Macrosegregation in Statically Cast Binary Ingots. *Metall. Trans. B* **1987**, *18*, 611–616. [CrossRef]
17. Hebditch, D.J.; Hunt, J.D. Observations of Ingot Macrosegregation on Model Systems. *Metall. Mater. Trans. B* **1974**, *5*, 1557–1564. [CrossRef]
18. Grundy, A.N.; Münch, S.; Feldhaus, S.; Bratberg, J. Continuous Casting of High Carbon Steel: How Does Hard Cooling Influence Solidification, Micro- and Macro Segregation? *IOP Conf. Ser. Mater. Sci. Eng.* **2019**, *529*, 012069. [CrossRef]
19. Rajiah, S.; Sambandam, M.; Shanmugam, S.P.; Vikraman, S.; Taticherla, R. Inter-Columnar Macro-Segregation in Continuously Cast Steel; Characterization, Possible Reasons, and Consequences. *Trans. Indian Inst. Met.* **2021**, *74*, 1557–1568. [CrossRef]
20. Melo, G.M.S.D.; Costa, A.M.; Nascimento, A.A.; Oliveira, A.P.D.; Gorni, A.A.; Oliveira, G.L.P.D.; Rodriguez−Ibabe, J.M. MACRO AND MICROSEGREGATION ASSESSMENT METHOD FOR CONTINUOUS CASTING OF WIDE SLABS. In *Proceedings of the ABM Proceedings*; Editora Blucher: São Paulo, Brazil, 2023; pp. 1002–1015.
21. Mramor, K.; Vertnik, R.; Šarler, B. Numerical Modelling of Macrosegregation in Three-Dimensional Continuous Casting of Steel Billets. *IOP Conf. Ser. Mater. Sci. Eng.* **2023**, *1281*, 012029. [CrossRef]
22. Mramor, K.; Vertnik, R.; Šarler, B. Development of Three-Dimensional LES Based Meshless Model of Continuous Casting of Steel. *Metals* **2022**, *12*, 1750. [CrossRef]
23. Zhang, Z.; Wu, M.; Zhang, H.; Hahn, S.; Wimmer, F.; Ludwig, A.; Kharicha, A. Modeling of the As-Cast Structure and Macrosegregation in the Continuous Casting of a Steel Billet: Effect of M-EMS. *J. Mater. Process. Technol.* **2022**, *301*, 117434. [CrossRef]
24. Kihara, K.; Okada, N.; Saito, S.; Kawashima, K. Numerical Simulation of Macrosegregation in a Continuous Casting Mold with Electromagnetic Stirring. *ISIJ Int.* **2022**, *62*, 1862–1873. [CrossRef]
25. Sun, H.; Zhang, J. Study on the Macrosegregation Behavior for the Bloom Continuous Casting: Model Development and Validation. *Metall. Mater. Trans. B* **2014**, *45*, 1133–1149. [CrossRef]
26. Wang, Y.; Zhang, L.; Chen, W.; Ren, Y. Three-Dimensional Macrosegregation Model of Bloom in Curved Continuous Casting Process. *Metall. Mater. Trans. B* **2021**, *52*, 2796–2805. [CrossRef]
27. Dong, Q.; Zhang, J.; Yin, Y.; Nagaumi, H. Numerical Simulation of Macrosegregation in Billet Continuous Casting Influenced by Electromagnetic Stirring. *J. Iron Steel Res. Int.* **2022**, *29*, 612–627. [CrossRef]
28. Mathur, A.; He, S. Performance and Implementation of the Launder–Sharma Low-Reynolds Number Turbulence Model. *Comput. Fluids* **2013**, *79*, 134–139. [CrossRef]
29. Won, Y.-M.; Thomas, B.G. Simple Model of Microsegregation during Solidification of Steels. *Metall. Mater. Trans. A* **2001**, *32*, 1755–1767. [CrossRef]
30. Ha, M.Y.; Lee, H.G.; Seong, S.H. Numerical Simulation of Three-Dimensional Flow, Heat Transfer, and Solidification of Steel in Continuous Casting Mold with Electromagnetic Brake. *J. Mater. Process. Technol.* **2003**, *133*, 322–339. [CrossRef]
31. Brimacombe, J.K. Design of Continuous Casting Machines Based on a Heat-Flow Analysis: State-of-the-Art Review. *Can. Metall. Q.* **1976**, *15*, 163–175. [CrossRef]
32. Wang, Y.; Zhang, L.; Yang, W.; Ji, S.; Ren, Y. Effect of Mold Electromagnetic Stirring and Final Electromagnetic Stirring on the Solidification Structure and Macrosegregation in Bloom Continuous Casting. *Steel Res. Int.* **2021**, *92*, 2000661. [CrossRef]
33. Qiu, D.; Zhang, Z.; Li, X.; Lv, M.; Mi, X.; Xi, X. Numerical Simulation of the Flow Field in an Ultrahigh-Speed Continuous Casting Billet Mold. *Metals* **2023**, *13*, 964. [CrossRef]

materials

MDPI

Article

Study on Influence of Rare Earth Ce on Micro and Macro Properties of U75V Steel

Guangqian Feng, Lei Ren * and Jichun Yang

School of Materials and Metallurgy, Inner Mongolia University of Science and Technology (IMUST), Baotou 014010, China; 15379229582@163.com (G.F.); yangjichun1963@163.com (J.Y.)
* Correspondence: renlei19890817@163.com

Abstract: Non-metallic inclusions in steel have great influence on the continuity of the steel matrix and the mechanical properties of steel. The precipitation sequence of Ce inclusions in molten steel is predicted by thermodynamic calculations. The results show that Ce content will affect the precipitation sequence of rare earth inclusions in molten steel, and the formation of CeO_2, Ce_2O_3 and $CeAlO_3$ will be inhibited with the increase in Ce content. Our laboratory smelted the test steel without rare earth additive and the test steel with rare earth Ce additive (0.0008%, 0.0013%, 0.0032%, 0.0042%). It was found that the MnS inclusions and inclusions containing Al, Ca, Mg and Si oxides or sulfides in the steel after rare earth addition were modified into complex inclusions containing $CeAlO_3$ and Ce_2O_2S. The size of inclusion in steel was reduced and the aspect ratio of inclusion was improved. The addition of Ce also improved the grain size of U75V steel and significantly refined the pearlite lamellar spacing. After mechanical property testing of the test steel, it was found that when Ce is increased within 0.0042%, the tensile and impact properties of U75V steel are also improved.

Keywords: U75V steel; rare earth Ce; inclusions; mechanical property

1. Introduction

As an important component of railway tracks, heavy rail steel needs to withstand the huge pressure, impact and wear of the wheel, so more attention should be paid to its mechanical properties whilst ensuring the output of heavy rail steel [1,2]. As one of the important factors that reduces the mechanical properties of steel, the quantity, size, distribution and chemical composition of nonmetallic inclusions seriously affect the continuity of the steel matrix and lead to the decline of its mechanical properties [3–7]. In particular, plastic MnS inclusions easily grow into large-size long strip inclusions during the solidification process of liquid steel; this is the source of steel crack initiation [8]. During hot rolling, MnS inclusions deform and extend along the rolling direction, which increases the anisotropy of steel and seriously affects the tensile, impact, ductility and other properties of steel [9–12]. Improving the non-metallic inclusions in steel can effectively improve the mechanical properties of steel, and some studies have found that rare earth treatment can effectively improve the inclusions in steel.

Because of its unique electron layer structure, rare earth Ce is widely used for modifying inclusions in steel, improving solidification structure, microalloying and so on [13–19]. Rare earth elements have a strong affinity with harmful elements such as O and S in steel [20,21]. When rare earth Ce is added to steel, high-melting-point rare earth inclusions such as $CeAlO_3$ and Ce_2O_2S will be generated first, which can effectively modify oxides or sulfides in steel. Such rare earth inclusions have the characteristics of small size, regular shape and dispersion [22], and they have little impact on the continuity of the steel matrix [23]. In addition, the thermal expansion coefficient of rare earth inclusions is closer to that of the steel matrix, which can effectively improve the mechanical properties of steel [24]. Z. Adabavazeh et al. [25] found that rare earth inclusions such as Ce_2O_2S

and $CeAlO_3$ appeared in Commercial SS400 steel after a small amount of rare earth Ce was added. With the increase in rare earth Ce content, the $CeAlO_3$ inclusions disappeared, and most of the steel was rare earth oxides and rare earth oxygen sulfides. After adding a small amount of rare earth, the small and medium size inclusions in Commercial SS400 steel increase and the large-size inclusions decrease. However, with the increase in Ce content, the inclusion size increases again due to the collision and aggregation of inclusions. Zhao Qingbo et al. [26] found that the addition of rare earth Ce could refine the grain of medium manganese steel and improve its comprehensive properties. Previous studies have found that the addition of rare earth Ce has a positive effect on a variety of steels, such as IF steel and medium manganese steel. As far as U75V steel is concerned, long irregular MnS inclusions in steel cause considerable harm to the mechanical properties of U75V steel. The use of rare earth treatment can reduce the activity of S in the molten steel, affect the combination of Mn and S and reduce the formation of pure MnS inclusions under supersaturated conditions. However, the addition of excessive rare earth will lead to a sharp increase in the number of rare earth inclusions, and the collision and aggregation in the molten steel will lead to the formation of large-size inclusions. Therefore, the content of rare earth should be attended to when treating the inclusions in the rare earth steel.

Taking U75V heavy rail steel as the experimental object, this study studies the influence of Ce content on the composition, size, distribution and microstructure of MnS and other non-metallic inclusions in U75V heavy rail steel, and it explores the changes in the mechanical properties of U75V steel before and after adding rare earth Ce. It is expected that this study can provide some reference for the application of rare earth in heavy rail steel.

2. Experimental Method

2.1. Preparation of Experimental Steel

The experimental U75V steel was smelted in a ZG-0.02 20 Kg vacuum induction furnace; the structure diagram is shown in Figure 1, and the raw material composition of the experimental steel is shown in Table 1. The smelting steps of the experimental steel are as follows: (1) The iron rod required for smelting the test steel is placed into the crucible, and the rare earth Ce, ferrosilicon, ferromanganese and ferrovanadium alloys are placed into the secondary charging device. (2) In order to eliminate the impact of impurities in the air, the vacuum furnace is vacuumed first and then filled with high purity argon. (3) After aeration, heating is carried out; the initial power is 5 Kw and then increased at a rate of 3 Kw/20 min until the iron rod is completely melted. (4) After the iron rod has been completely melted for 5 min, the secondary feeding is carried out, and the rare earth and alloy are added. After waiting for about 10 min, the rare earth and alloy are fully melted and evenly mixed with the liquid steel, the heating device is turned off and the steel is produced after the ingot is cooled. (5) In order to eliminate the uneven stress of casting, we retain the dense part of the ingot and roll it.

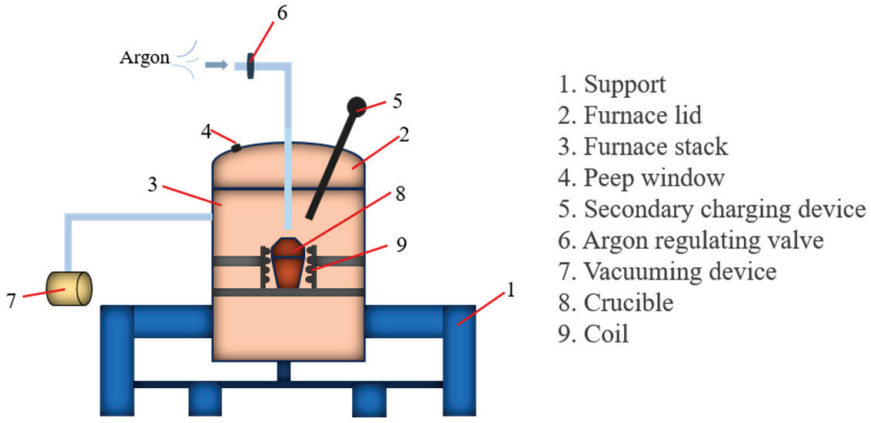

Figure 1. Structure diagram of vacuum induction furnace.

Table 1. Chemical composition of raw materials used for smelting U75V heavy rail steel (mass fraction%).

Calcined Petroleum Coke	Ferrosilicon	Ferromanganese	Ferrovanadium	Ferrocerium	Pure Iron
[%C] = 98.5 [%Volatiles] = 1.5	[%Si] = 72.53 [%C] = 0.12 [%P] = 0.03 [%S] = 0.02 [%Fe] = 27.3	[%Mn] = 97.15 [%C] = 0.07 [%P] = 0.04 [%S] = 0.04 [%Fe] = 2.7	[%V] = 46 [%C] = 0.17 [%P] = 0.06 [%S] = 0.01 [%Fe] = 53.76	[%Ce] = 30 [%Fe] = 70 [%C] $\leq$ 0.01	[%Fe] = 99.99

The O content of the test steel was measured using an ON-3000 oxygen and nitrogen analyzer (Ncs Testing Technology Co., Ltd., Beijing, China), the Ce content of rare earth was determined by an ion spectroscopy–mass spectrometer (ICP-MS), and the other components were detected using a Labspark1000 direct reading spectrometer (Ncs Testing Technology Co., Ltd., Beijing, China). The composition of the experimental steel is shown in Table 2; it conforms to the national standard and has certain reliability. The sampling and processing diagram of the sample is shown in Figure 2. The processed sample was polished until the surface was smooth and without scratches, and the sample was observed by a FEI-QUANTA400 scanning electron microscope (FEI, Hillsboro, OR, USA) and analyzed by its energy spectrum.

Table 2. Chemical compositions of experiment steels (mass fraction%).

Sample Numbers	C	Si	Mn	V	S	P	O	Ce
S1	0.798	0.660	0.980	0.061	0.013	<0.005	0.00365	0
S2	0.791	0.716	1.009	0.0068	0.01	0.037		0.0008
S3	0.832	0.713	0.978	0.062	0.011	0.003	0.00331	0.0013
S4	0.785	0.673	1.017	0.069	0.012	0.007		0.0032
S5	0.831	0.709	0.913	0.046	0.007	0.006		0.0042

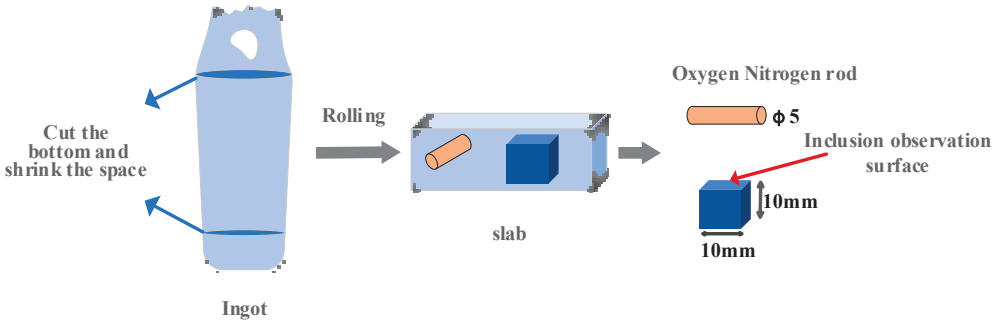

Figure 2. Sampling and processing diagram of ingot.

2.2. Thermodynamic Calculation

The Wagner model based on the change of Gibbs free energy is used to calculate the formation of Ce inclusion; the components used in the calculation are shown in Table 3. According to the composition of U75V steel in Table 3, the thermodynamic relationship between O, S, Al and Ce in liquid steel is discussed, so as to explore the possibility of Ce inclusion formation. In this calculation, 1 mol of cerium is taken as the standard, and the Gibbs free energy of each reaction of U75V steel at different temperatures is calculated according to the above model. The possible chemical reactions and standard Gibbs free energy are shown in Table 4 [27,28]. The interaction coefficients of various elements in liquid steel at 1600 °C are shown in Table 5 [20,27,29]. The interaction coefficients of each element in liquid steel at 1650 °C and 1550 °C are deduced by using a quasi-normal solution model. The theoretical values calculated by this model are close to the experimental values and within the allowable error range of thermodynamic calculation. The calculation method is shown in Equation (1). In order to ensure the full reaction of Ce-containing oxygen sulfide

and sulfide in molten steel, the ratio of oxygen to sulfur in the calculation for Ce-containing inclusions is 0.1 < O/S < 0.2.

Table 3. U75V steel composition for calculation.

C	Si	Mn	V	S	P	Ca	Al	O	Ce
0.75	0.6	0.8	0.06	0.02	0.02	0.001	0.001	0.003	0.0025
0.75	0.6	0.8	0.06	0.02	0.02	0.001	0.001	0.0028	0.006
0.75	0.6	0.8	0.06	0.02	0.02	0.001	0.001	0.0026	0.008
0.75	0.6	0.8	0.06	0.02	0.02	0.001	0.001	0.0024	0.012
0.75	0.6	0.8	0.06	0.02	0.02	0.001	0.001	0.002	0.014

Table 4. Gibbs free energy of rare earth inclusions generated by reaction in liquid steel [27,28].

Reaction	$\Delta G^{\theta}/(\mathbf{J\ mol^{-1}})$
$[Ce] + 3/2[O] = 1/2Ce_2O_3(s)$	$-715560 + 180T$
$[Ce] + 2[O] = CeO_2(s)$	$-852720 + 249.96T$
$[Ce] + [S] = CeS(s)$	$-422100 + 120.38T$
$[Ce] + 3/2[S] = 1/2Ce_2S_3(s)$	$-536420 + 163.86T$
$[Ce] + 4/3[S] = 1/3Ce_3S_4(s)$	$-497670 + 146.3T$
$[Ce] + [O] + 1/2[S] = 1/2Ce_2O_2S(s)$	$-675700 + 165.5T$
$[Ce] + [Al] + 3[O] = CeAlO_3(s)$	$-1366460 + 364T$

Table 5. Interaction coefficient e_i^j of various elements in liquid steel at 1600 °C [20,27,29].

	C	Si	Mn	V	S	P	Ca	Al	O	Ce
O	−0.45	−0.013	−0.021	−0.3	−0.133	0.07	−313	−3.85	−0.02	−12.1
Al	0.091	0.0056	−0.02	0.025	0.03	0.033	−0.047	0.045	−6.6	−0.43
Ce	0.091	-	-	−0.33	1.77	1.77	-	−2.25	−106	−0.006

The Gibbs free energy of each reaction, as generated by rare earth inclusions in U75V steel under different rare earth contents and presented in Tables 4 and 5, is calculated according to the combination of Equations (1)–(4):

$$e^j_{i\ (T)} = (\frac{2538}{T} - 0.355)e^j_{i\ (1873)} \quad (1)$$

$$\lg f_i = \sum_{j=1}^{n} e_i^j w[j] \quad (2)$$

$$a_i = f_i w[i] \quad (3)$$

$$\Delta G = \Delta G^{\theta} + RT \ln K \quad (4)$$

where $e^j_{i\ (T)}$ is the interaction coefficient of element j on i at T(K) temperature, and f_i is the activity coefficient of element i; e_i^j is the interaction coefficient of element j on i at 1600 °C; $w[i]$ (wt%) is the mass fraction of element i; a_i is the activity of element i, and the activity product of pure matter is 1; R is the gas constant ($\mathrm{J{\cdot}mol^{-1}{\cdot}K^{-1}}$), where K is the ratio of the product activity product to the reactant activity product.

3. Results and Discussion

3.1. Thermodynamic Calculation of Ce-Containing Inclusions

3.1.1. Precipitation Sequence of Ce-Containing Inclusions at 1600 °C

In order to predict the formation of rare earth inclusions in steel, the Wagner model was used to calculate the Gibbs free energy of the reaction of various rare earth inclusions in steel with different Ce contents at 1600 °C, and the calculation results are shown in Figure 3. It can be seen that the ΔG of each reaction is less than zero at 1600 °C, indicating that

under the above smelting conditions, each reaction in Table 4 can spontaneously proceed. In addition, with the increase in Ce content, the Gibbs free energy of CeO_2 and $CeAlO_3$ decreases first and then increases. Under the condition of a certain Al content, when Ce < 0.0075%, the Gibbs freedom of $CeAlO_3$ is the lowest, and the inclusion of $CeAlO_3$ will be first formed in the molten steel. When Ce > 0.0075%, the Gibbs freedom of Ce_2O_2S is the lowest, and the inclusion of Ce_2O_2S is first formed in the molten steel. The sequence of precipitation of Ce inclusions at 1600 °C is shown in Table 6. It has been determined that U75V steel mainly contains MnS inclusions and Al_2O_3 inclusions [30]. After rare earth Ce is added at steelmaking temperature, Ce will first form Ce_2O_2S and $CeAlO_3$ containing other Ce inclusions with O, S, Al and other elements in the steel. With the decrease in temperature, there may be Ce inclusions and Ca, Al and Si complex inclusions in the steel; such inclusions have a regular appearance and small size, and the addition of rare earth Ce can play a certain role in modifying the inclusions in U75V steel.

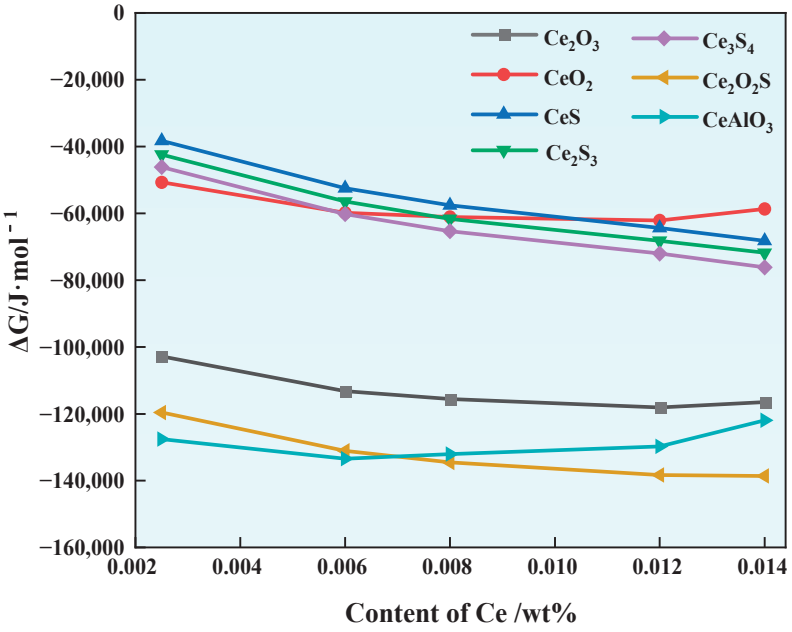

Figure 3. Gibbs free energy generated by Ce inclusion in steel with different Ce contents at 1600 °C.

Table 6. Precipitation and evolution sequence of rare earth inclusions at 1600 °C.

Al	Ce	Precipitation Sequence of Ce-Containing Inclusions
0.0010%	0.0025–0.0058%	$CeAlO_3 > Ce_2O_2S > Ce_2O_3 > CeO_2 > Ce_3S_4 > Ce_2S_3 > CeS$
	0.0058–0.0075%	$CeAlO_3 > Ce_2O_2S > Ce_2O_3 > Ce_3S_4 > CeO_2 > Ce_2S_3 > CeS$
	0.0075–0.0078%	$Ce_2O_2S > CeAlO_3 > Ce_2O_3 > Ce_3S_4 > CeO_2 > Ce_2S_3 > CeS$
	0.0078–0.0102%	$Ce_2O_2S > CeAlO_3 > Ce_2O_3 > Ce_3S_4 > Ce_2S_3 > CeO_2 > CeS$
	0.0102–0.014%	$Ce_2O_2S > CeAlO_3 > Ce_2O_3 > Ce_3S_4 > Ce_2S_3 > CeS > CeO_2$

3.1.2. Effect of Temperature and Ce Content on the Formation of Ce-Containing Inclusions

In order to investigate the stability of Ce inclusions during temperature reduction, the Gibbs free energies of the reactions at 1650 °C, 1600 °C and 1550 °C for the formation of rare earth inclusions were calculated. The results show that the ΔG of the reaction between Ce-containing oxygen sulfide and Ce-containing sulfide decreases with the increase in the Ce range from 0.0025% to 0.014%, and the ΔG of the formation of such rare earth inclusions decreases with the decrease in temperature. The results show that CeS, Ce_2S_3, Ce_3S_4 and Ce_2O_2S inclusions can exist stably in steel under an increase in Ce content and decrease in temperature, and the calculation results are shown in Figure 4.

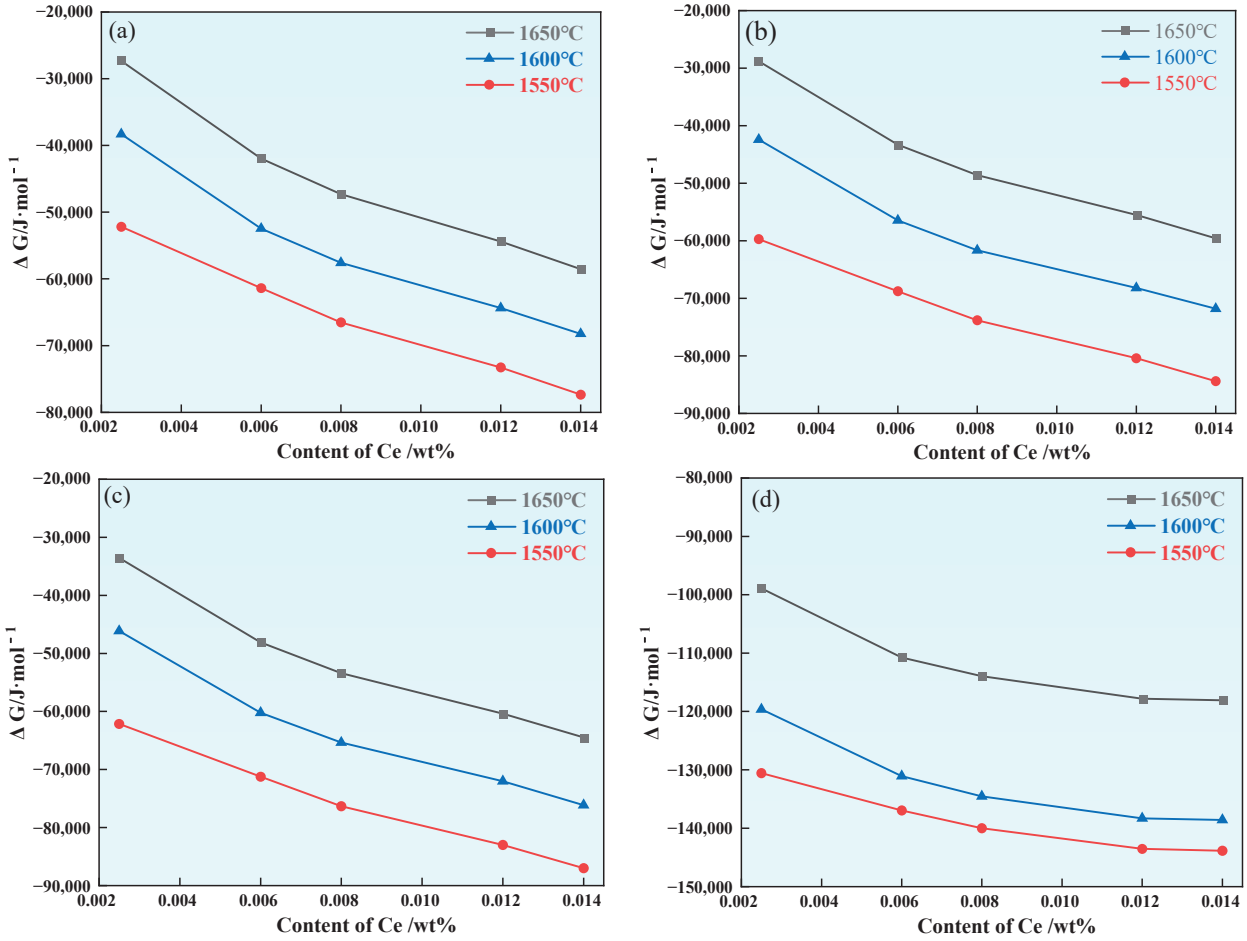

Figure 4. Effect of changes in Ce content on ΔG generated by CeS, Ce_2S_3, Ce_3S_4 and Ce_2O_2S inclusions during cooling: (**a**) CeS, (**b**) Ce_2S_3, (**c**) $Ce_3S_4$and (**d**) Ce_2O_2S.

As the range of Ce increases from 0.0025% to 0.014%, the ΔG generated by CeO_2, Ce_2O_3 and $CeAlO_3$ inclusions in U75V steel decreases first and then increases, indicating that excessive Ce will inhibit the formation of these three types of rare earth inclusions as the temperature drops. This indicates that the decrease in temperature does not affect the formation of CeO_2, Ce_2O_3 and $CeAlO_3$ inclusions, and the calculation results are shown in Figure 5.

As the most common inclusion in U75V steel, MnS inclusions seriously affect the continuity and mechanical properties of the steel matrix. This calculation aims to explore the modification of MnS inclusions by rare earth, so the S content is set to be high in calculation. After the addition of rare earth Ce, it will first react with O, S, Al and other elements in the steel to form Ce_2O_2S and $CeAlO_3$ inclusions. With the increase in Ce content, Ce and S will further react to produce rare earth sulfide, so CeS, Ce_2S_3, Ce_3S_4 and Ce_2O_2S inclusions will statically exist in the steel when the Ce content increases, as shown in Figure 4. Due to a series of deoxidation processes before smelting U75V steel, the O content in the steel is low. The Ce_2O_3 inclusions generated in steel further react with S to form Ce_2O_2S inclusions; the reaction process is shown in Equation (5). With the progress of the reaction, the unstable $CeAlO_3$ in steel reacts with Ce and S elements, and the reaction process is shown in Equation (6) [28].

$$Ce_2O_3(s) + [S] = Ce_2O_2S(s) + [O] \qquad \Delta G^{\theta} = 77360 - 28.48T \tag{5}$$

$$CeAlO_3 + [Ce] + [S] = Ce_2O_2S + [O] + [Al] \qquad \Delta G^{\theta} = 12870 - 32T \tag{6}$$

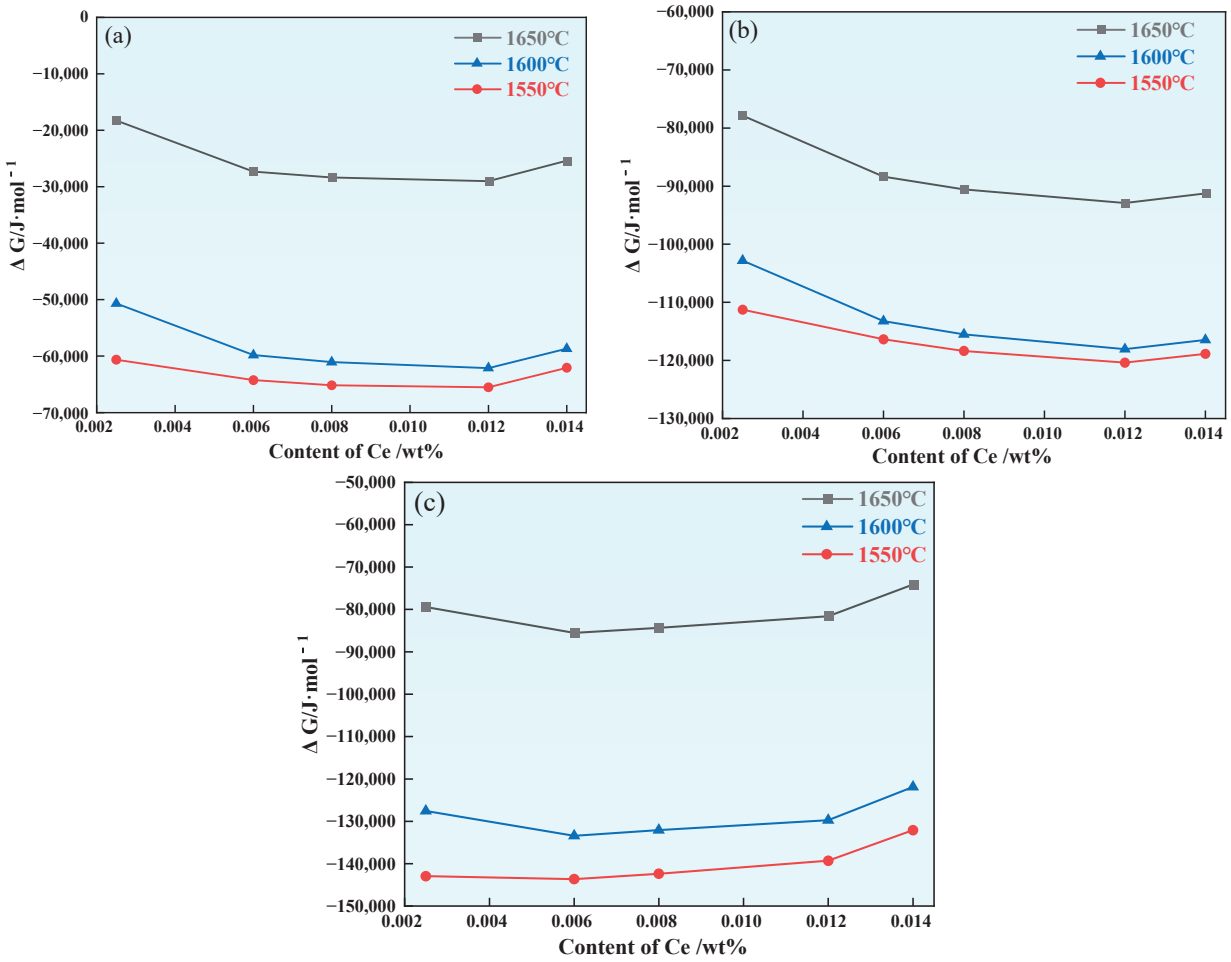

Figure 5. Effects of changes in Ce content on ΔG generated by CeO_2, Ce_2O_3 and $CeAlO_3$ inclusions during cooling: (**a**) CeO_2, (**b**) Ce_2O_3 and (**c**) $CeAlO_3$.

According to Equations (1)–(6), it can be calculated that at 1600 °C, when the Ce content is 0.0025%, the ΔG of Equations (5) and (6) are −35,001 J/mol and −112,001 J/mol, respectively. When the Ce content is 0.014%, the ΔG of Equations (5) and (6) is −45,512 J/mol and −154,513 J/mol, respectively. The calculation results show that $CeAlO_3$ and Ce_2O_3 inclusions tend to be unstable with the increase of Ce in the range of 0.0025–0.014%, as shown in Figure 5b,c. Since the reaction of CeO_2 in molten steel is uncertain, it is further analyzed here.

3.2. Inclusions in Steel

3.2.1. Morphology and Composition of Inclusions

In Sample S1 without rare earth additive, the main inclusions were large and irregular pure MnS (Figure 6a) and complex inclusions containing Al, Si, Ca, Mn, S, O and other elements, as shown in Figure 6b–d. Such MnS inclusions are distributed in the steel structure, just as there are many very low strength voids in the steel, and the MnS inclusions will be significantly extended after rolling. In the process of steel use, when subjected to external force, the gap formed by the extension of inclusions will increase with the deformation of the steel matrix, thereby forming cracks in the steel or producing anisotropy of the material properties, thereby shortening the service life of the steel and causing premature failure of the steel [31]. In addition to pure MnS, a part of MnS is deposited on the surface of the oxide or sulfide inclusions to form irregular composite inclusions, as shown in Figure 6c.

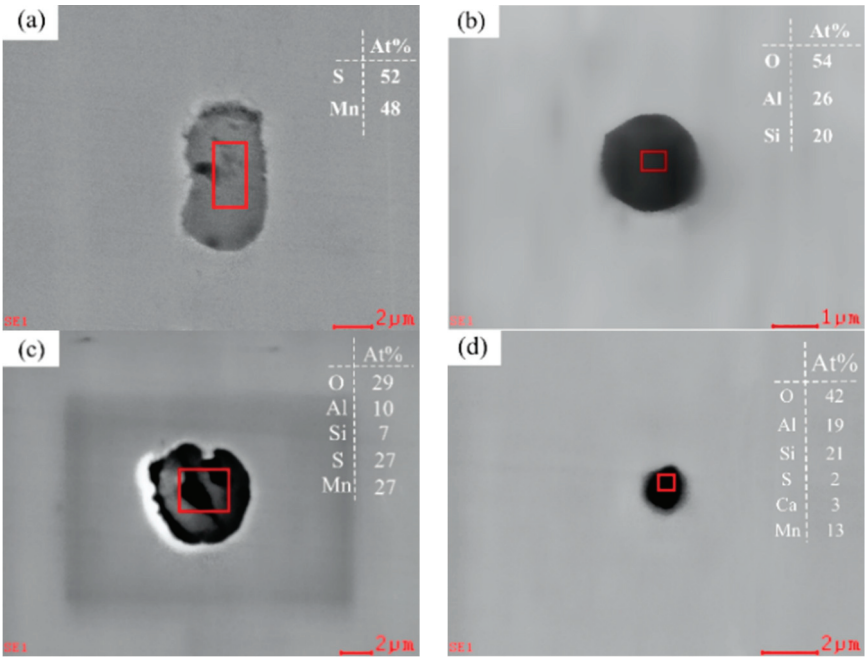

Figure 6. Inclusion species and morphology in Sample S1: (**a**) MnS, (**b**) Si-Al-O, (**c**) Al-Si-O + MnS and (**d**) Al-Si-Ca-Mn-S-O.

Compared with the samples without rare earth Ce, most of the pure MnS inclusions in Samples S2–S5 with rare earth Ce added to the steel changed from large and irregular to spherical, as shown in Figure 7a. In addition, rare earth complex inclusions containing Ce, Mg, Al, Si, Ca, O, S and other elements appeared in the samples with rare earth additives. According to the thermodynamic calculation results in Figure 3, $CeAlO_3$ inclusions will first be formed in steel when the Ce content is low, as shown in Figure 7b–d. Compared with pure MnS inclusions, these three types of rare earth complex inclusions have a higher melting point, are not easy to deform during hot rolling, have good adaptability to the steel matrix, have a good shape and distribution, reduce the stress concentration and promote the improvement of steel properties. In addition, S-Ti-V-Ce inclusions also appear in the steel, as shown in Figure 7e. The shape of rare earth inclusions with high V and Ti content is irregular. Pure (Ti, V) inclusions have high hardness and do not change their appearance with the change of the steel matrix; thus, they are non-deformable inclusions, which easily produce micro-cracks in the steel after rolling [32]. After rare earth Ce modification treatment, the integration degree of such inclusions with the steel matrix can be enhanced, and the stress concentration and micro-cracks in the steel can be reduced. After the modification of rare earth Ce, the integration degree of such inclusions with the steel matrix can be enhanced, and the stress concentration and micro-cracks of the steel can be reduced. It is worth noting that in addition to the inclusion containing V and Ti, the shape of pure MnS and other rare earth inclusions is relatively regular, all are spherical or spheroid, and the ductility is low in the rolling process, which has little influence on the comprehensive properties of steel [21].

In addition, double-layer complex inclusions containing Ce were found in Sample S3 with rare earth additives, as shown in Figure 8a. Double-layer complex inclusions containing Ce inclusions were found in Sample S4, as shown in Figure 8b. These two types of double-layer inclusions have a regular morphology and smaller size than those without the rare earth additive. With the increase in Ce content, complex inclusions containing $CeAlO_3$ wrapped by $MgO\text{-}CeAlO_3$ were found in Sample S5, as shown in Figure 8c. It is noteworthy that Al-Ca-Ce-O-S double-layered composite inclusions were found in Sample S5, as shown in Figure 8d. According to the calculation results of Figure 5c and Equation (6), it is not difficult to find that with the increase in Ce content, some $CeAlO_3$ inclusions will react

with S, O and other elements to form Ce_2O_2S inclusions [25], and according to the energy spectrum atom percentage in Figure 8d, it can be deduced that the core part of the inclusion is a complex inclusion containing Ce_2O_2S. The low Ce content may be the reason for the absence of Ce_2O_2S inclusions in Samples S2–S4.

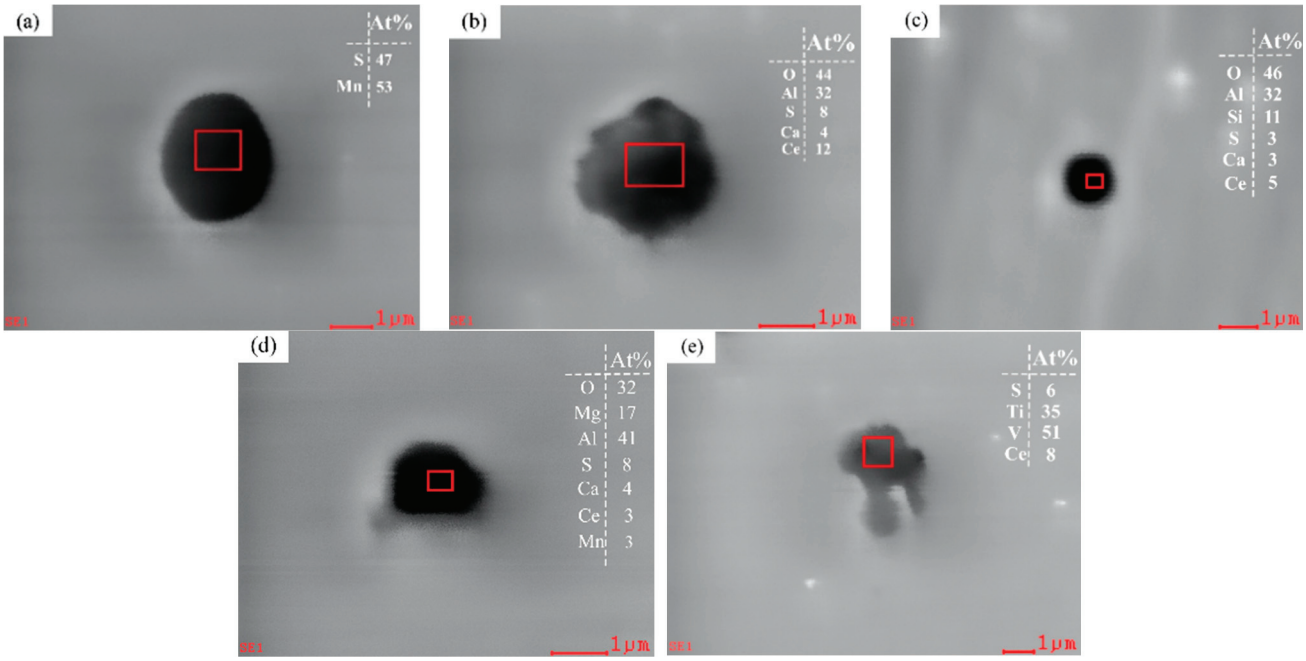

Figure 7. Inclusion in U75V after the addition of rare earth: (**a**) MnS, (**b**) Al-Ca-S-O-$CeAlO_3$, (**c**) Al-Si-Ca-S-O-$CeAlO_3$, (**d**) Mg-Al-Ca-Mn-O-S-$CeAlO_3$, and (**e**) S-Ti-V-Ce.

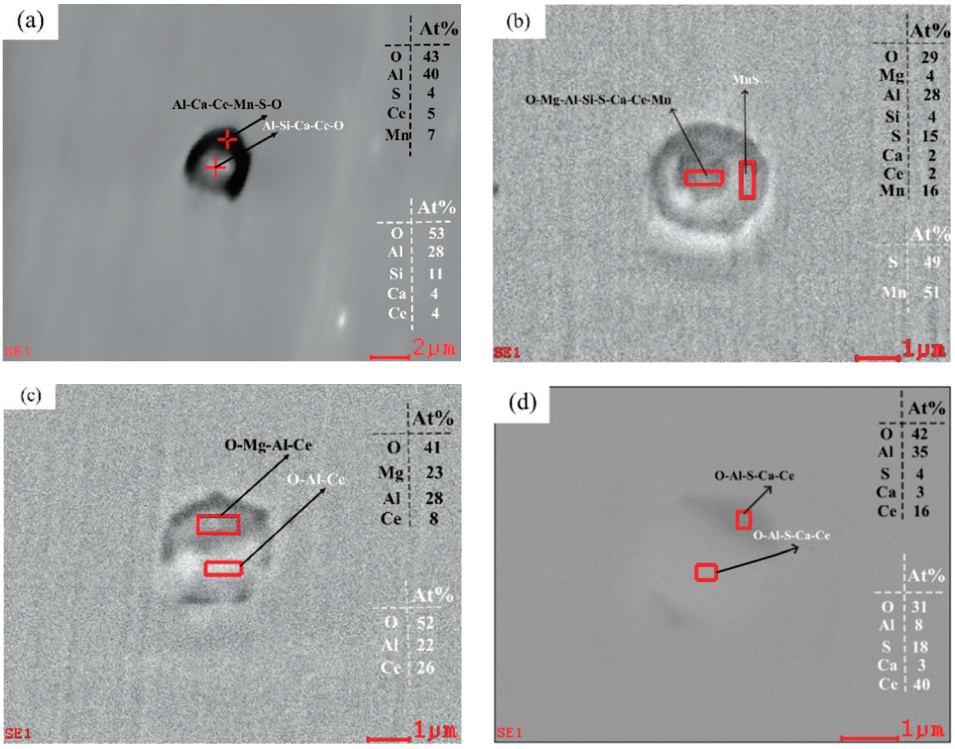

Figure 8. Compound inclusions in U75V after the addition of rare earths: (**a**) Al-Ca-Mn-S-O-$CeAlO_3$ + Al-Si-Ca-O-$CeAlO_3$ inclusions in S3, (**b**) MnS + Mg-Al-Si-Ca-Mn-O-S-$CeAlO_3$ inclusions in S4, (**c**) MgO-$CeAlO_3$ + $CeAlO_3$ inclusions in S5and (**d**) Al-Ca-S-O-$CeAlO_3$ + Al-Ca-O-S-Ce_2O_2S inclusions in S5.

3.2.2. Changes of Inclusion Species in Steel

With the increase in Ce content, the change in inclusions in U75V steel is as shown in Figure 9. From the figure, we can see that there are MnS inclusions with irregular morphologies and compound inclusions containing Al, Si, Ca, Mn, S, O and other elements in steel without rare earth additive. The inclusion containing $CeAlO_3$ is formed first after rare earth is added into the steel, and the shape of pure MnS in Samples S2–S5 containing Ce changes from irregular to more regular and spherical. When the Ce content increased to 0.0032%, the double-layer structure inclusions containing $CeAlO_3$ inclusions appeared in the steel, and when the Ce content further increased to 0.0042%, the composite inclusions containing Ce_2O_2S began to appear in the steel. We found that most of the inclusions in the samples containing rare earth Ce existed in spherical or sphere-like shapes. It is worth noting that when the rare earth content in the steel is less than 0.0042%, MnS inclusions do not disappear, but MnS and complex inclusions containing rare earth elements appear, and the melting point of Ce_2O_2S inclusions is higher than that of MnS, so they precipitate before MnS in the solidification process. The activity of S in the molten steel is reduced to some extent, the combination of Mn and S is affected, and the formation of pure MnS inclusions under supersaturation is reduced.

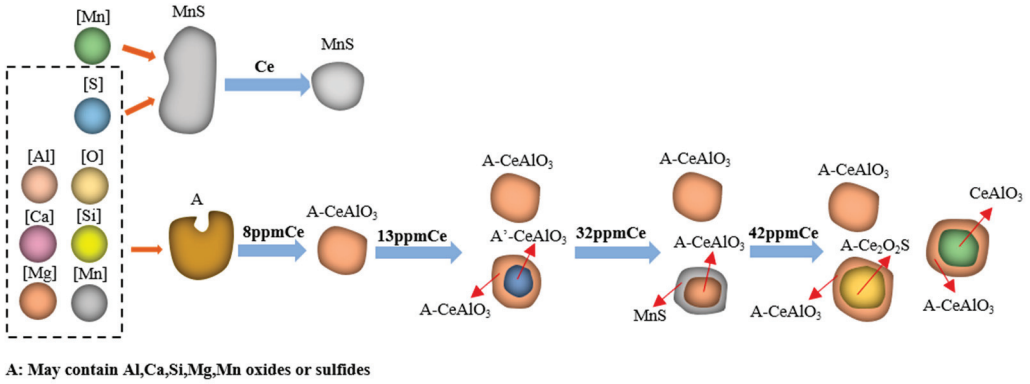

Figure 9. Change diagram of inclusions in U75V steel after adding rare earth Ce.

3.3. Statistics of Inclusions Size and Aspect Ratio in Steel

3.3.1. Average Inclusion Size and Aspect Ratio

In order to quantitatively characterize inclusions in steel, the average size and aspect ratio of inclusions in different samples were calculated. The statistics of average size changes of inclusions are shown in Figure 10a. The average size of inclusions in Sample S1 is 4.78 μm. The average size of inclusions in S2 is 4.31 μm, which is about 10% lower than that in Sample S1. The average size of inclusions in Sample S3 is 3 μm, which is about 37% lower than that in Sample S1. The average size of inclusions in Sample S4 is 3.39 μm, which is about 30% less than that in Sample S1. The average inclusion size of Sample S5 is reduced to 2.46 μm, which is about 49% less than that of Sample S1. The comparison of inclusions in Samples S1–S5 shows that with the increase in rare earth content, the average size of inclusions in steel decreases by 10% to 49%, and the average size of inclusions in Sample S5 containing 0.0042% rare earth Ce is the smallest.

The statistics of the average aspect ratio of inclusions in different samples are shown in Figure 10b. The average aspect ratio of inclusions in Sample S1 is 1.38. The average aspect ratio of inclusions in Sample S2 is 1.33, which is about 3.6% lower than that in Sample S1. The average aspect ratio of inclusions in Sample S3 is 1.25, which is about 9.5% lower than that in Sample S1. The average aspect ratio of inclusions in Sample S4 is 1.21, which is about 12.3% lower than that in Sample S1. The average aspect ratio of inclusions in Sample S5 is 1.5, which is increased by 0.12 compared with Sample S1. The average aspect ratio of inclusions in Samples S1–S5 was compared and it was found that the average aspect ratio of inclusions in steel first decreased and then increased with the increase of rare earth content, and the aspect ratio of Sample S4 was closest to 1. It also shows that the addition

of rare earth Ce not only changes the composition of inclusions but also refine the size of inclusions in steel and improve the appearance of inclusions.

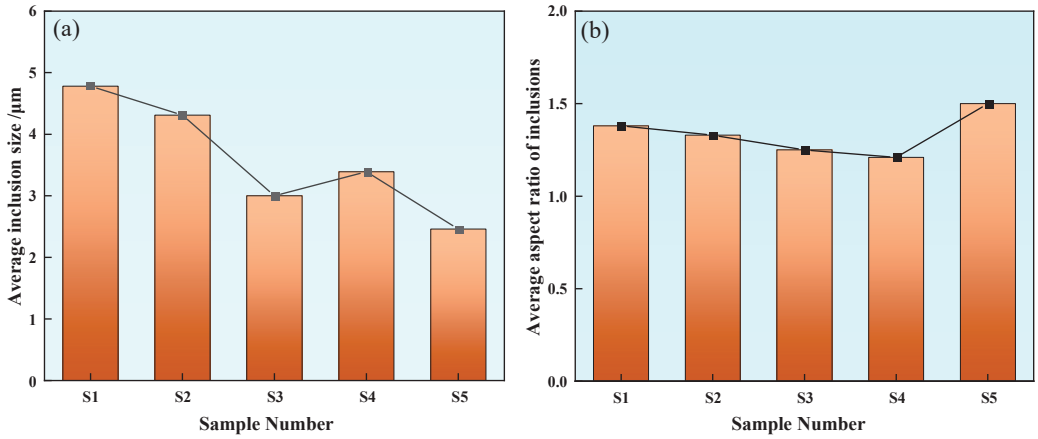

Figure 10. Average inclusion size and average aspect ratio: (**a**) average inclusion size and (**b**) average aspect ratio of inclusions.

3.3.2. Inclusion Size Distribution

Figure 11 shows the average size distribution of inclusions in samples with different rare earth Ce contents. In Sample S1 without rare earth treatment, the inclusion size distribution ranges from 1 to 12 μm, and the size distribution range is large. The inclusion size range of 1–2 μm accounts for about 25%, and the inclusion size range of less than 5 μm accounts for 51%, as shown in Figure 11a. The average size and proportion of inclusions in Sample S2 are shown in Figure 11b. The size of inclusions in Sample S2 containing 0.0008% rare earth Ce is distributed within 1–8 μm, and the proportion of inclusions in the range 2–3 μm is about 23%, and inclusions above 10 μm disappear. The size distribution of inclusions in Sample S3 is shown in Figure 11c. It can be seen that the size of inclusions in Sample S3 is basically less than 5 μm, among which the inclusions with a size of 2–3 μm occupy the highest proportion. The inclusions in Samples S4 and S5 were mainly distributed in the range of 1–6 μm, and the proportion of inclusions smaller than 5 μm was 92%, which was significantly higher than that of Sample S1, as shown in Figure 11d,e. With the increase of rare earth content, the effect of rare-earth-refining inclusions becomes more obvious. The modification of non-metallic inclusions such as MnS in steel by rare earth elements is the main reason for the size refinement of inclusions, but there are still a small amount of large-size inclusions in the samples containing rare earth. The reason may be that the lower rare earth content fails to completely modify the inclusions such as MnS and Al_2O_3 in steel, so there is still the possibility of large-size inclusions in steel.

However, excess rare earth will enhance the ability of rare earth elements to combine with other inclusions and generate a large number of rare earth inclusions—resulting in an increased probability of collision and the aggregation of inclusions—and further increase the size of inclusions. In this paper, the proportion of small and medium-sized inclusions in other samples containing rare earth elements is significantly higher than that in Sample S1 without rare earth element additives.

3.3.3. Statistics of Average Size and Aspect Ratio of MnS Inclusions

Among all kinds of inclusions in U75V heavy rail steel, MnS inclusions have the greatest impact on the continuity, strength, toughness and mechanical properties of the steel matrix during steel processing, so the average size and aspect ratio changes of MnS inclusions are analyzed separately. The statistics of average size changes of MnS inclusions in different samples are shown in Figure 12a. The average size of MnS inclusions in Sample S1 is 8 μm. The average size of inclusions in Sample S2 is 4.74 μm, which is about 41% lower than that in Sample S1. The average inclusion size of Sample S3 is 2.62 μm,

which is about 67% lower than that of Sample S1. The average inclusion size of Sample S4 is 4.63 μm, which is about 42% lower than that of Sample S1. The average inclusion size of Sample S5 is reduced by about 62%. Compared with the MnS inclusion size of U75V steel without rare earth treatment, it is found that the MnS inclusion size in steel is greatly reduced by different rare earth contents.

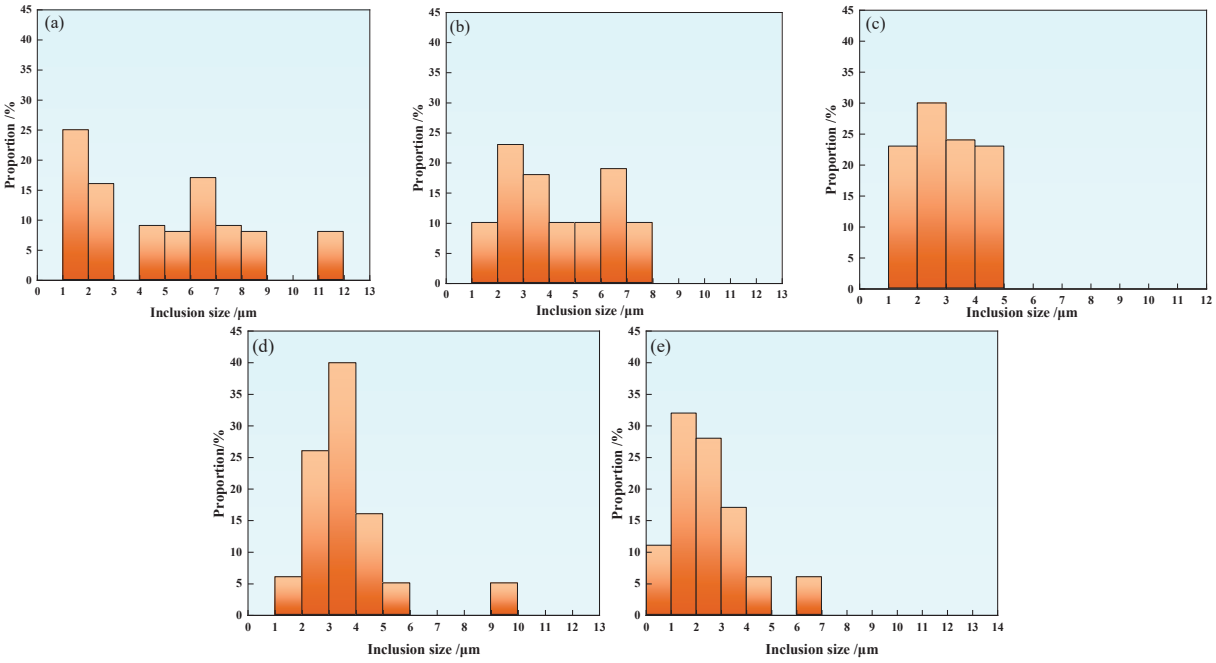

Figure 11. Size distribution of inclusions in U75V steel: (**a**) S1, (**b**) S2, (**c**) S3, (**d**) S4 and (**e**) S5.

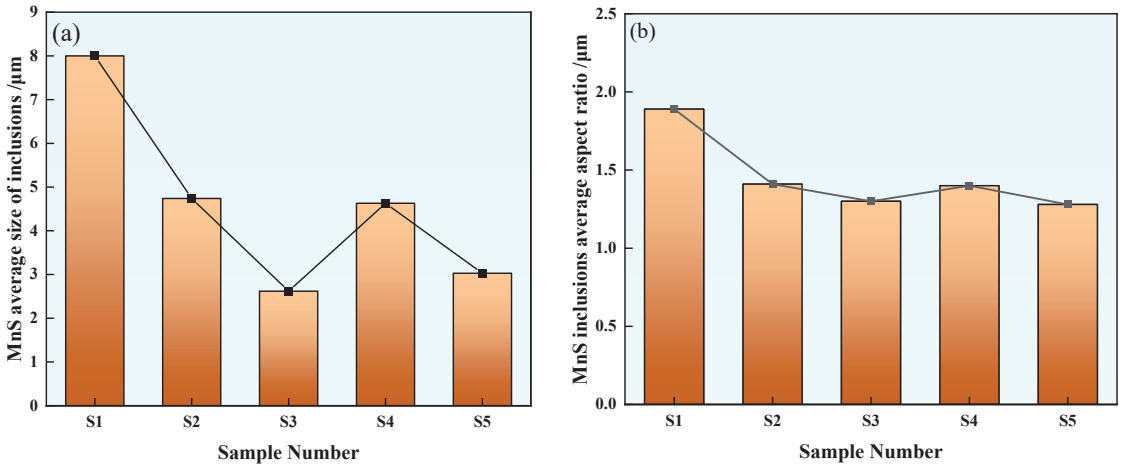

Figure 12. Average size and average aspect ratio of MnS inclusions: (**a**) average size and (**b**) average aspect ratio.

The statistical variation of the average aspect ratio of MnS inclusions in different test steels is shown in Figure 12b. The average aspect ratio of MnS inclusions in Sample S1 is 1.89. The average aspect ratios of inclusions in S2, S3, S4 and S5 samples are 1.41, 1.3, 1.4 and 1.28, respectively. Compared with Sample S1, it is found that the aspect ratio of MnS inclusions decreases in the range of 25–32% after the addition of rare earth Ce to steel, and the decrease effect of MnS inclusions in Sample S5 containing 0.0042% rare earth Ce is the most obvious.

3.4. Effect of Rare Earth on Microstructure in U75V Steel

3.4.1. Effect of Rare Earth Ce on Grain Size and Pearlite Lamellae Spacing of U75V Steel

Scanning electron microscopy was used to observe the macro structures in different samples after heating to 1200 °C for 1 h and water cooling, as shown in Figure 13. It can be seen from Figure 13a–d that the grain size of the steel after adding rare earth decreases.

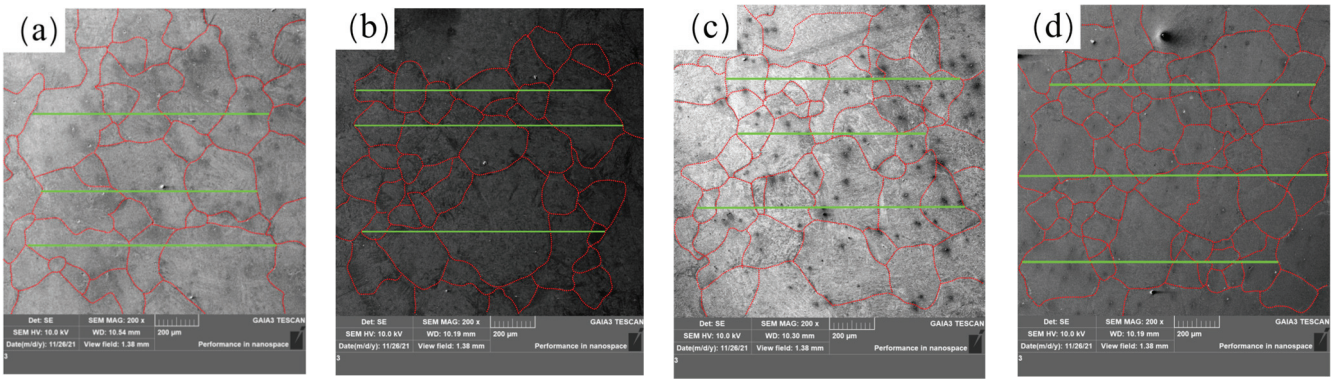

Figure 13. U75V steel grain size: (**a**) S1, (**b**) S2, (**c**) S4 and (**d**) S5.

The pearlite structure was observed by emission scanning electron microscopy, as shown in Figure 14. From Figure 14a–d, it can be seen that the layer is clearly refined after the addition of rare earth. In order to further represent the changes of grain size and pearlite lamellae spacing, Image-J 1.53a software was used to measure the grain size and pearlite lamellar layer. Eight fields of view were selected for each statistical sample, and the average value was obtained after measurement by the trans-sectional method. The measurement results are shown in Figure 15. The grain size of Sample S1 without rare earth Ce is 232 μm. With the increase in rare earth content in experimental steel, the grain sizes of Samples S2, S4 and S5 decrease to 174 μm, 162 μm and 153 μm, respectively. The grain size of Sample S5 containing 0.0042% rare earth Ce is the smallest. Compared with Sample S1 without rare earth Ce, it is reduced by about 35%. Due to the active chemical properties of Ce, the inclusion containing Ce formed after rare earth was added to the steel can act as a heterogeneous nucleating agent, which can inhibit the grain growth and optimize the structure of the steel. After the addition of rare earth Ce in the steel, the grains are continuously refined, which means that there are more grain boundaries, which can absorb more impact or tensile energy, slow down the expansion of steel cracks and improve the mechanical properties of steel [33]. The pearlite lamellae spacing of Sample S1 without rare earth Ce was 0.87 μm, and the pearlite lamellae spacings of S2, S4 and S5 samples after rare earth Ce was added were reduced to 0.53 μm, 0.43 μm and 0.22 μm, respectively, among which the pearlite lamellae spacing of Sample S5 containing 0.0042% rare earth Ce was the smallest. Compared with the Sample S1 without Ce, it was reduced by about 75%. It can be seen that Ce has an obvious thinning effect on grain size and pearlite lamellae spacing.

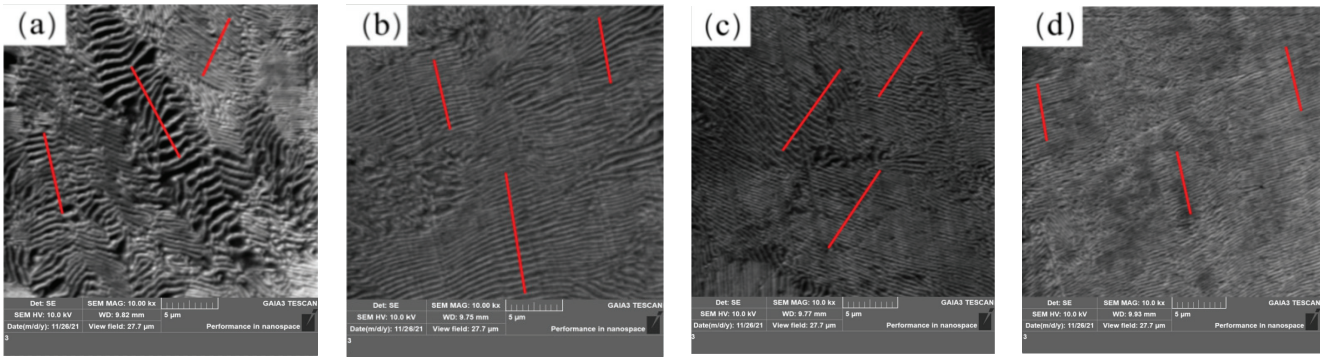

Figure 14. U75V steel pearlite lamellar spacing: (**a**) S1, (**b**) S2, (**c**) S4 and (**d**) S5.

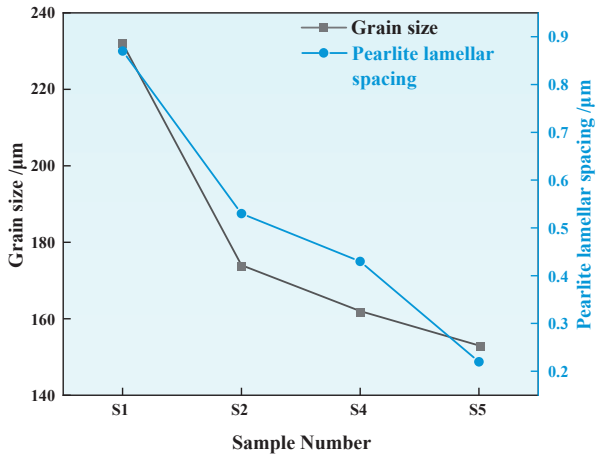

Figure 15. Average grain size and average pearlite lamellae spacing statistics of U75V steel.

3.4.2. Effect of Rare Earth Ce on Grain Boundary Precipitates of Experimental Steel

The purification of grain boundaries and the form and distribution of rare earth inclusions in steel are important factors affecting the mechanical properties of steel. Therefore, scanning electron microscopy was used to observe precipitates near the grain boundaries, and the results are shown in Figure 16. Most of the precipitates from Sample S1 are MnS precipitates, as shown in Figure 16a. After the addition of rare earth, the composite precipitates containing Al-Mg-O-S-$CeAlO_3$ and $CeAlO_3$-Ce_2O_2S were precipitated near the grain boundary, as shown in Figure 16b–d. The consumption of S elements in liquid steel by rare earth Ce effectively reduces the segregation of MnS precipitates at the grain boundary, which is conducive to the improvement of steel properties.

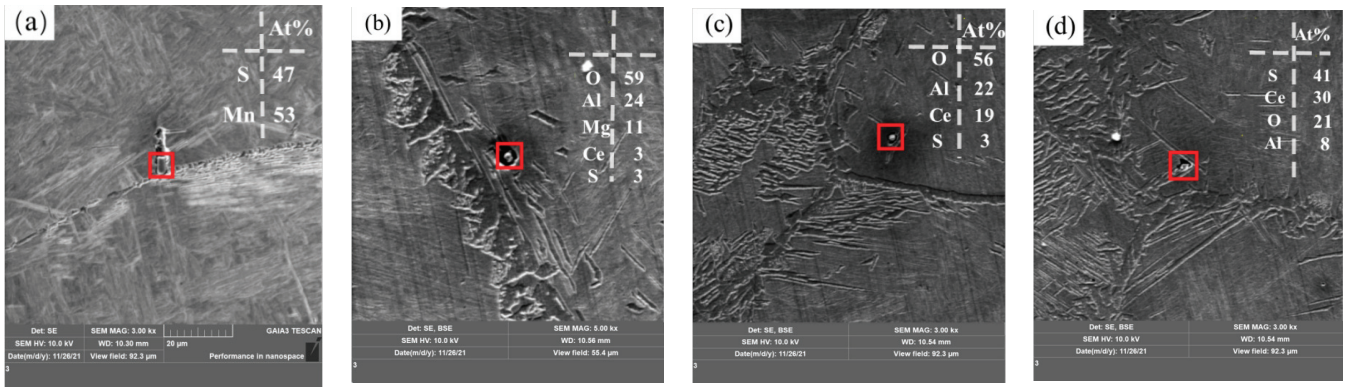

Figure 16. Grain boundary precipitates: (**a**) MnS, (**b**) Mg-Al-O-S-$CeAlO_3$ and (**c**,**d**) $CeAlO_3$-Ce_2O_2S.

3.5. Effect of Rare Earth Ce on Mechanical Properties of U75V Steel

3.5.1. Impact Properties

Impact experiments were conducted on samples with different rare earth contents, and the results are shown in Figure 17. The impact energy of Sample S1 without rare earth elements was 5.9 J at 20 °C; the impact energies of Samples S2, S4 and S5 with rare earth element additives were 9.5 J, 5.9 J and 6.8 J at 20 °C, respectively; and the impact energy of Samples S2 and S5 at room temperature was improved. The impact energy of Sample S1 is 5.6 J at −20 °C, and the impact energies of Samples S2, S4 and S5 with rare earth additive were 7.2 J, 4.8 J and 6.8 J at −20 °C, respectively. The impact energy of Sample S1 was 4.8 J at −40 °C, and the impact energy of Sample S2 and S5 increased to 7.4 J at −40 °C after the addition of rare earth. The impact energy of Sample S1 was 3.9 J at −60 °C, and the impact energy of Samples S2, S4 and S5 increased to 7.2 J, 4.8 J and 5.4 J at −60 °C after the addition of rare earth Ce. As can be seen from Figure 17, the addition of rare earth can improve the impact performance of U75V steel, especially in different degrees under low-temperature

conditions, which has good reference significance for railway construction in extremely cold areas.

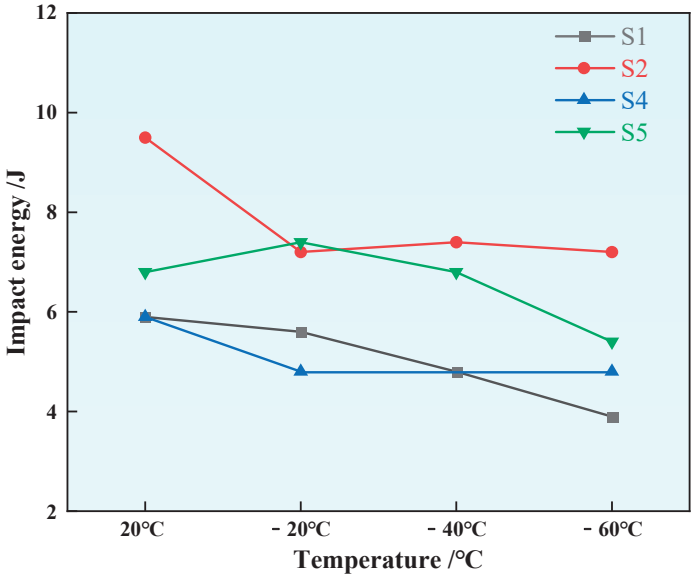

Figure 17. Impact energy of U75V steel at different temperatures.

In order to analyze the reasons for the improvement of impact performance, we observed and analyzed the fracture morphology and the inclusion from the impact fracture. Scanning electron microscopy was used to observe the fracture morphology, as shown in Figure 18. From the fracture morphology, it can be found that the fracture morphology of Sample S1 without rare earth Ce appears to be step and river, and the tear edge is large, which is a typical brittle fracture, as shown in Figure 18a,b. After the addition of rare earth Ce, the fracture morphology of the impact sample is stepped, but the fault layer tends to be gradual, the tear edge decreases and the presence of small dimples is observed, as shown in Figure 18c,d. This shows that the impact characteristics of steel change from brittle fracture to ductile fracture with the increase in rare earth Ce content in steel.

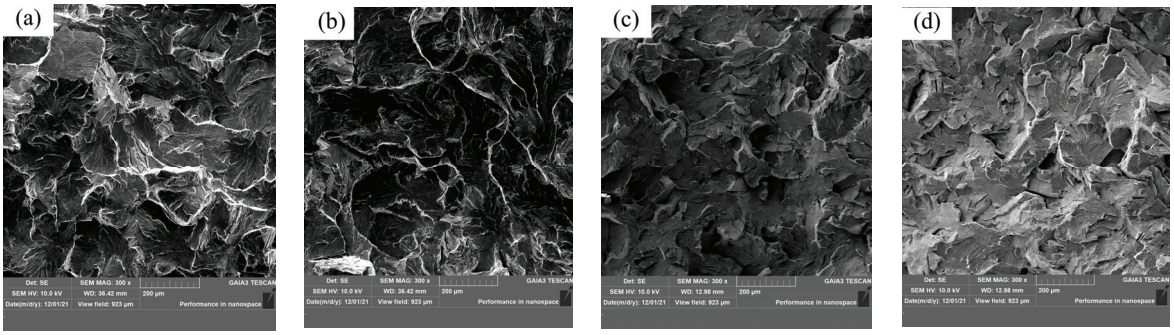

Figure 18. Impact fracture morphology: (**a**,**b**) without rare earths and (**c**,**d**) with rare earths.

Figure 19 shows the analysis of inclusions at the impact fracture. The inclusions in the impact fracture of Sample S1 without rare earth Ce are mostly MnS inclusions or MnS-Ti-V composite inclusions, as shown in Figure 19a,b. Because MnS inclusions are plastic inclusions, the deformation is large when subjected to external force, and the mechanical properties of the steel are easily reduced seriously. However, the inclusions containing (V,Ti) have high hardness, and it is difficult to change the appearance of inclusions with the change of the steel matrix, which easily produces stress concentration of the steel during use, causing the steel to produce micro-cracks. Therefore, the analysis shows that the existence of these two types of inclusions causes the impact performance of steel to decrease to a large extent. As shown in Figure 19c,d, the inclusion in the fracture of the

sample after the addition of rare earth is transformed from MnS and MnS-Ti-V inclusions to inclusions containing rare earth Ce, and rare earth elements play the role of modified inclusions. Because rare earth inclusions are not easily deformed compared with MnS inclusions, and the thermal expansion coefficient of rare earth inclusions is similar to that of the steel matrix, rare earth inclusions can reduce the stress concentration caused by impact load and delay the initiation and expansion of cracks during the impact process when cracks expand to inclusions, thereby effectively improving the impact performance of steel at normal and low temperatures [34].

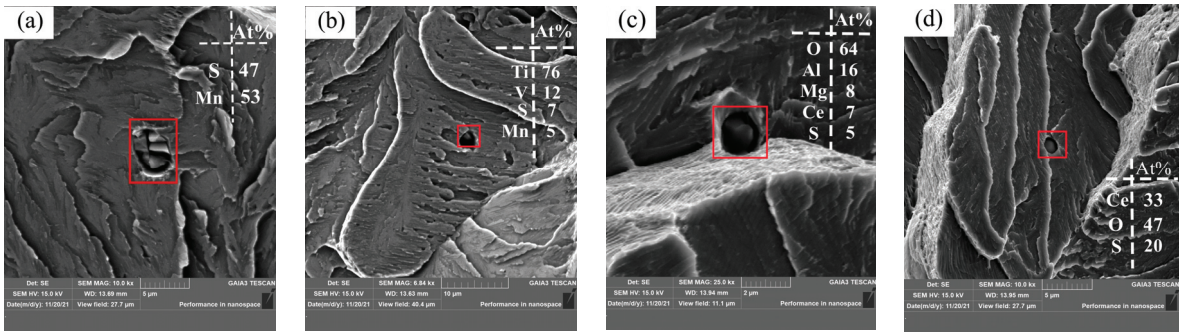

Figure 19. Inclusion at impact fracture: (**a**,**b**) without rare earths and (**c**,**d**) with rare earths.

3.5.2. Tensile Properties

Figure 20 shows the yield strength and tensile strength of the U75V steel sample before and after adding rare earth. The yield strength of Sample S1 was 600 MPa, and the yield strength of Sample S2 after adding 0.0008% rare earth Ce was 642 MPa, which is about 7% higher than that of Sample S1. The yield strength of Sample S4 after adding 0.0032% Ce was 701 MPa, which is about 16.8% higher than that of Sample S1. The yield strength of Sample S5 steel after adding 0.0042% rare earth Ce was 711 MPa, which is about 18.5% higher than that of Sample S1.

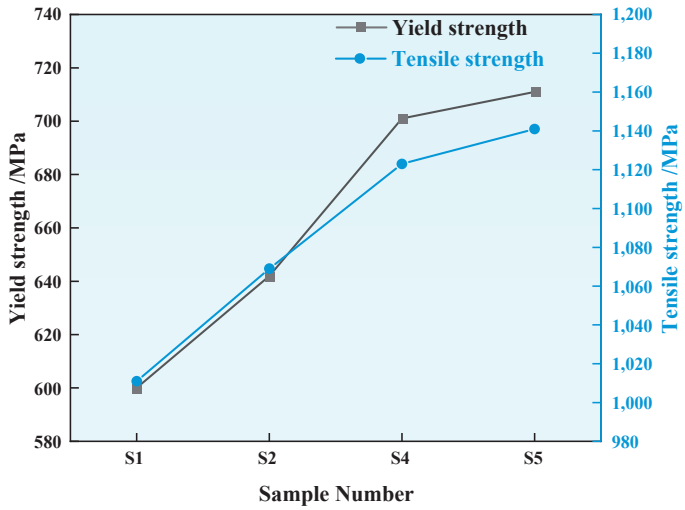

Figure 20. Yield strength and tensile strength of U75V steel.

The tensile strength of Sample S1 was 1011 MPa, and the tensile strength of Sample S2 after adding 0.0008% rare earth Ce was 1069 MPa, which is about 5.7% higher than that of Sample S1. The tensile strength of Sample S4 after adding 0.0032% rare earth Ce was 1123 MPa, which is about 11.1% higher than that of Sample S1. The tensile strength of Sample S5 after adding 0.0042% rare earth Ce was 1141 MPa, which is about 12.9% higher than that of S1. The analysis of the experimental results shows that with the increasing

of rare earth content within 0.0042%, both the yield strength and tensile strength of U75V steel are increased correspondingly.

Scanning electron microscopy was used to observe the morphology of the tensile specimen fracture and analyze the inclusion, and the tensile fractures are shown in Figure 21. The tensile fracture morphology of Sample S1 without rare earth Ce is step and river, which is a typical brittle fracture, as shown in Figure 21a. After the addition of different rare earth contents, obvious dimples were generated in the tensile fracture of the sample, and the tear edges became smaller, as shown in Figure 21b–d. This shows that the change from brittle fracture to ductile fracture is beneficial to the improvement of tensile properties, which is consistent with the experimental results.

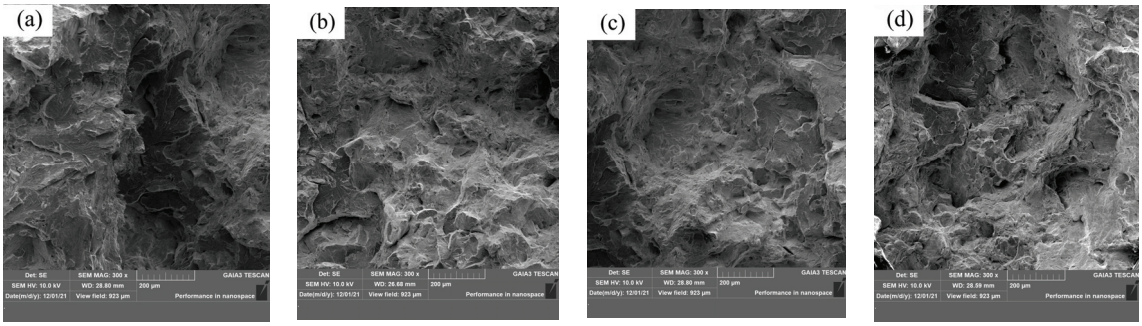

Figure 21. Tensile fracture morphology: (**a**) without rare earths and (**b**–**d**) with rare earths.

Figure 22 shows the analysis of inclusions in the fracture of the tensile sample. The results show that the inclusions of Sample S1 without rare earth Ce are mostly MnS inclusions and complex inclusions formed by MnS, Ti and V, as shown in Figure 22a,b. The inclusion in the tensile fracture after the addition of rare earth Ce was modified into a complex inclusion containing rare earth Ce, as shown in Figure 22c,d. It has been suggested that inclusions are an important factor affecting the mechanical properties of steel. Rare earth inclusion is generally not the cause of crack growth, but sulfide is the direct cause of fatigue crack growth. This is because when the crack extends to the inclusion, the rare earth inclusion slows down the stress concentration, thereby preventing the crack growth [28,35]. Rare-earth inclusions have better fusion with the steel matrix than MnS inclusions and MnS-Ti-V complex inclusions. Rare-earth inclusions absorb a large amount of stress concentration before deformation and fracture of the tensile specimen, which causes the crack propagation of the tensile specimen under external loads to be slow [36].

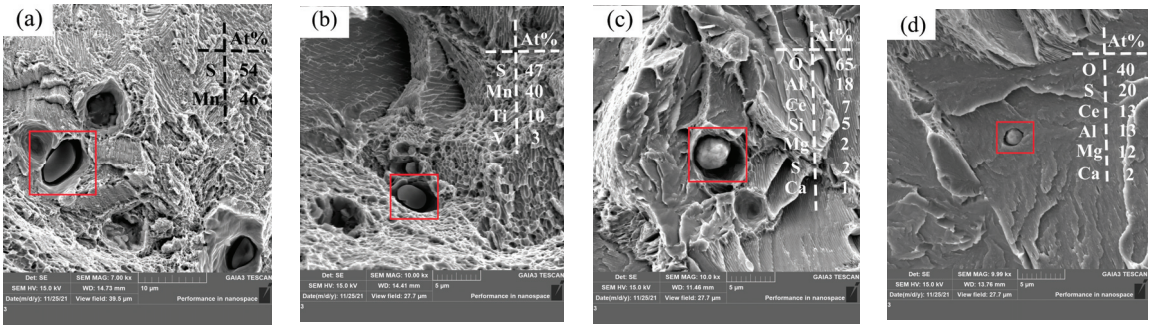

Figure 22. Inclusion at tensile fracture: (**a**,**b**) without rare earths and (**c**,**d**) with rare earths.

4. Conclusions

In this paper, the thermodynamic calculation of Ce-containing inclusions is first carried out to study the precipitation of Ce-containing inclusions in liquid steel. In the experimental part, the changes in the appearance, type and size of inclusions in U75V heavy rail steel before and after the addition of rare earth Ce are studied, and the macro-structure and pearlite lamination of U75V steel are also observed and analyzed. Finally, the influence of

rare earth Ce on the mechanical properties of U75V steel is studied, and the research results are as follows:

1. According to the thermodynamic calculation results of the Wagner model, the value is $0.1 < O/S < 0.2$; under the condition of a certain Al content, $CeAlO_3$ inclusion is first precipitated in U75V steel at 1600 °C when the Ce content is less than 0.0075%, and Ce_2O_2S inclusion is first precipitated in liquid steel when the Ce content is greater than 0.0075%. The precipitation stability of Ce inclusions is not affected by the decrease in temperature, but the formation of CeO_2, Ce_2O_3 and $CeAlO_3$ inclusions is inhibited by the increase in rare earth Ce.
2. U75V steel without rare earth Ce contains irregular MnS and complex inclusions containing Al, Si, Ca, Mn, S, O, etc. After the addition of rare earth Ce, the pure MnS in the steel decreases, and rare earth inclusions such as $CeAlO_3$ and Ce_2O_2S and other complex inclusions containing Al, Si, Ca, Mn, S, O and other elements appear. With the increase in Ce content, the sizes and aspect ratios of inclusions in the steel are reduced to some extent, and the addition of rare earth Ce has a certain thinning effect on pure MnS inclusions.
3. Rare earth Ce can effectively refine the grain size of U75V steel and significantly reduce the pearlite lamellae spacing. The analysis of precipitates near the grain boundary shows that rare earth elements can reduce the segregation of sulfide at the grain boundary.
4. The addition of rare earth Ce can improve the normal- and low-temperature impact performance of U75V steel; in particular, the improvement effect of low-temperature impact performance is obvious; this has certain practical significance in the application of rails in extremely cold weather. The experiment also found that with the increase in Ce content, the yield strength and tensile strength of U75V steel also increased.

Author Contributions: Formal analysis, L.R. and J.Y.; writing—original draft, G.F. and L.R.; writing—review & editing, L.R., G.F. and J.Y. All authors have read and agreed to the published version of the manuscript.

Funding: The authors are grateful for support from the National Natural Science Foundation of China (Grant No. 52264045), 2023 Young Science and Technology Talents Development Project (Young Science and Technology Talents NJYT23117) and the Fundamental Research Funds for Inner Mongolia University of Science & Technology (Grant No. 0406082229).

Institutional Review Board Statement: Not applicable.

Informed Consent Statement: Not applicable.

Data Availability Statement: Data are contained within the article.

Conflicts of Interest: The authors declare no conflict of interest.

References

1. Liu, C.J.; Huang, Y.H.; Jiang, M.F. Effects and Mechanisms of RE on Impact Toughness and Fracture Toughness of Clean Heavy Rail Steel. *J. Iron Steel Res. Int.* **2011**, *3*, 52–58. [CrossRef]
2. Cen, Y.D.; Ji, C.J.; Chen, L.; Chen, K.Y.; Ke, D.D. Microstructure Evolution of RE Rail Steel During Hot Deformation. *Metallogr. Microstruct. Anal.* **2023**, *12*, 545–556. [CrossRef]
3. Wang, S.J.; Shi, C.B.; Liang, Y.J.; Wan, X.X.; Zhu, X. Evolution and Formation of Non-metallic Inclusions During Electroslag Remelting of a Heat-Resistant Steel for Ultra-supercritical Power Plants. *Metall. Mater. Trans. B* **2022**, *53*, 3095–3114. [CrossRef]
4. Fuchs, D.; Tobie, T.; Stahl, K. Challenges in determination of microscopic degree of cleanliness in ultra-clean gear steels. *J. Iron Steel Res. Int.* **2022**, *29*, 1583–1600. [CrossRef]
5. Paul, S.K.; Chakrabarty, A.K.; Basu, S. Effect of Rare Earth Additions on the Inclusions and Properties of a Ca-Al Deoxidized Steel. *Metall. Mater. Trans. B* **1982**, *13*, 185–192. [CrossRef]
6. Kiviö, M.; Holappa, L. Addition of Titanium Oxide Inclusions into Liquid Steel to Control Nonmetallic Inclusions. *Metall. Mater. Trans. B* **2011**, *43*, 233–240. [CrossRef]
7. Imashuku, S.; Wagatsuma, K. Cathodoluminescence Analysis of Nonmetallic Inclusions in Steel Deoxidized and Desulfurized by Rare-Earth Metals (La, Ce, Nd). *Metall. Mater. Trans. B* **2019**, *51*, 79–84. [CrossRef]

8. Song, P.S.; Li, Y.Q.; Ren, Q.; Ren, Y.; Zhang, L.F. Effect of Al_2O_3 Content in Inclusions on the Precipitation of MnS During Cooling of a Heavy Rail Steel. *Metall. Mater. Trans. B* **2023**, *54*, 1468–1482. [CrossRef]
9. Tian, Q.R.; Wang, Z.F.; Zhang, X.Y.; Liu, N.F.; Xu, X.Y.; Fu, J.X. Formation Mechanism of Different Morphologies Inclusions in Tellurium-Containing Medium-Carbon-Microalloyed Steel. *Metall. Mater. Trans. B* **2023**, *54*, 3405–3415. [CrossRef]
10. Temmel, C.; Gunnar Ingesten, N.; Karlsson, B. Fatigue Anisotropy in Cross-Rolled, Hardened Medium Carbon Steel Resulting from MnS Inclusions. *Metall. Mater. Trans. A* **2006**, *37*, 2995–3007. [CrossRef]
11. Maciejewski, J. The Effects of Sulfide Inclusions on Mechanical Properties and Failures of Steel Components. *J. Fail. Anal. Prevent.* **2015**, *15*, 169–178. [CrossRef]
12. Hosseini, S.B.; Temmel, C.; Karlsson, B.; Ingesten, N.G. An In-Situ Scanning Electron Microscopy Study of the Bonding between MnS Inclusions and the Matrix during Tensile Deformation of Hot-Rolled Steels. *Metall. Mater. Trans. A* **2007**, *38*, 982–989. [CrossRef]
13. Bao, D.H.; Cheng, G.G.; Huang, Y.; Qiao, T. Effect of Rare Earth Ce on the Solidification Structure of Fe–18Cr–0.8Si Ferritic Stainless Steel. *Metall. Mater. Trans. B* **2023**, *54*, 944–958. [CrossRef]
14. Han, S.; Geng, R.; Lei, S.; Li, Y.; Wang, C. Effect of Cerium on Inclusion Modification in a Secondary-Hardening Steel. *Materials* **2023**, *16*, 3972. [CrossRef] [PubMed]
15. Tuttle, R.B. Study of Rare Earth Additions Effect on the Solidification and Properties of 4130 Steel. *J. Mater. Eng. Perform.* **2019**, *28*, 6720–6727. [CrossRef]
16. Torkamani, H.; Raygan, S.; Garcia-Mateo, C.; Rassizadehghani, J.; Palizdar, Y.; San-Martin, D. Evolution of Pearlite Microstructure in Low-Carbon Cast Microalloyed Steel Due to the Addition of La and Ce. *Metall. Mater. Trans. A* **2018**, *49*, 4495–4508. [CrossRef]
17. Bartlett, L.N.; Avila, B.R. Grain Refinement in Lightweight Advanced High-Strength Steel Castings. *Int. J. Metalcast* **2016**, *10*, 401–420. [CrossRef]
18. Torkamani, H.; Raygan, S.; Mateo, C.; Rassizadehghani, J.; Vivas, J.; Palizdar, Y.; San-Martin, D. The Influence of La and Ce Addition on Inclusion Modification in Cast Niobium Microalloyed Steels. *Metals* **2017**, *7*, 377. [CrossRef]
19. Cao, J.; Li, Y.; Lin, W.; Che, J.; Zhou, F.; Tan, Y.; Li, D.; Dang, J.; Chen, C. Assessment of Inclusion Removal Ability in Refining Slags Containing Ce_2O_3. *Crystals* **2023**, *13*, 202. [CrossRef]
20. Ren, Q.; Zhang, L.F. Effect of Cerium Content on Inclusions in an Ultra-Low-Carbon Aluminum-Killed Steel. *Metall. Mater. Trans. B* **2020**, *51*, 589–600. [CrossRef]
21. Pan, C.; Hu, X.J.; Lin, P.; Chou, K.C. Evolution of Inclusions after Cerium and Titanium Addition in Aluminum Deoxidized Fe-17Cr-9Ni Austenitic Stainless Steel. *ISIJ Int.* **2020**, *60*, 1878–1885. [CrossRef]
22. Yang, C.Y.; Luan, Y.K.; Li, D.Z.; Li, Y.Y. Effects of rare earth elements on inclusions and impact toughness of high-carbon chromium bearing steel. *J. Mater. Sci. Technol.* **2019**, *35*, 1298–1308. [CrossRef]
23. Smirnov, L.A.; Rovnushkin, V.A.; Dobuzhskaya, A.B.; Yunin, G.N.; Polevoi, E.V.; Boikov, D.V.; Spirin, S.A. Influence of rare-earth modification on the formation of nonmetallic inclusions in high-carbon steel. *Steel Transl.* **2017**, *46*, 805–813. [CrossRef]
24. Torkamani, H.; Raygan, S.; Garcia Mateo, C.; Rassizadehghani, J.; Palizdar, Y.; San-Martin, D. Contributions of Rare Earth Element (La,Ce) Addition to the Impact Toughness of Low Carbon Cast Niobium Microalloyed Steels. *Met. Mater. Int.* **2018**, *24*, 773–788. [CrossRef]
25. Adabavazeh, Z.; Hwang, W.S.; Su, Y.H. Effect of Adding Cerium on Microstructure and Morphology of Ce-Based Inclusions Formed in Low-Carbon Steel. *Sci. Rep.* **2017**, *7*, 46503. [CrossRef]
26. Zhao, Q.B.; Dong, R.F.; Lu, Y.F.; Yang, Y.; Wang, Y.R.; Yang, X. Effect of Trace Rare-Earth Element Ce on the Microstructure and Properties of Cold-Rolled Medium Manganese Steel. *Metals* **2023**, *13*, 116. [CrossRef]
27. Wang, H.; Bao, Y.P.; Zhi, J.G.; Duan, C.Y.; Gao, S.; Wang, M. Effect of Rare Earth Ce on the Morphology and Distribution of Al_2O_3 Inclusions in High Strength IF Steel Containing Phosphorus during Continuous Casting and Rolling Process. *ISIJ Int.* **2021**, *61*, 657–666. [CrossRef]
28. Geng, R.M.; Li, J.; Shi, C.B.; Zhi, J.G.; Lu, B. Effect of Ce-La on inclusion evolution in Al-killed high strength steel. *Metall. Res. Technol.* **2020**, *117*, 616–624. [CrossRef]
29. Feng, H.; Lu, P.C.; Li, H.B.; Jiang, Z.H. Effect of Mg Pretreatment and Ce Addition on Cleanliness and Inclusion Evolution in High-Nitrogen Stainless Bearing Steels. *Metall. Mater. Trans. B* **2022**, *53*, 864–876. [CrossRef]
30. Bai, G.J.; Yang, J.C.; Liang, W.J. Evaluation and Analysis of the Influence of Rare-Earth Ce on Inclusions in Heavy Rail Steel. *Metals* **2023**, *13*, 614. [CrossRef]
31. Zhuo, C.; Liu, R.; Zhao, Z.R.; Zhang, Y.L.; Hao, X.S.; Wu, H.J.; Sun, Y.H. Effect of Rare Earth Cerium Content on Manganese Sulfide in U75V Heavy Rail Steel. *Metals* **2022**, *12*, 1012. [CrossRef]
32. Sun, H.R.; Du, H.G.; Tong, K.K.; Liu, L.H.; Yan, Q.J.; Zuo, X.R. Influence of TiN Inclusions and Segregation Bands on the Mechanical Properties and Delayed Crack in Thick NM550 Wear-Resistant Steel. *Materials* **2023**, *16*, 5856. [CrossRef]
33. Guo, Z.S.; Li, Y.P.; Ma, J.Y.; Liang, X.H.; Li, H.B.; Zhang, S.C.; Han, P.D. Effect of Ce content on precipitation behavior in S31254 super austenitic stainless steel. *J. Alloy. Compd.* **2023**, *966*, 171254. [CrossRef]
34. Liu, X.J.; Yang, J.C.; Zhang, F.; Fu, X.Y.; Li, H.W.; Yang, C.Q. Experimental and DFT study on cerium inclusions in clean steels. *J. Rare Earth* **2021**, *39*, 477–486. [CrossRef]

35. Zhang, R.Z.; He, J.S.; Xu, S.G.; Zhang, F.C.; Wang, X.T. The roles of Ce and Mn on solidification behaviors and mechanical properties of 7Mo super austenitic stainless steel. *J. Mater. Res. Technol.* **2023**, *22*, 1238–1249. [CrossRef]
36. Wang, H.; Wang, A.Q.; Li, C.Y.; Yu, X.S.; Xie, J.P.; Liang, T.T.; Liu, C.L. Effects of rare earth metals on microstructure, mechanical properties, and pitting corrosion of 27% Cr hyper duplex stainless steel. *Rev. Adv. Mater. Sci.* **2022**, *61*, 873–887. [CrossRef]

materials

MDPI

Article

Effect of Testing Conditions on Low-Cycle Fatigue Durability of Pre-Strained S420M Steel Specimens

Stanisław Mroziński [1], Michał Piotrowski [1] and Halina Egner [2,*]

[1] Faculty of Mechanical Engineering, Bydgoszcz University of Science and Technology, Al. Kaliskiego 7, 85-796 Bydgoszcz, Poland; stmpkm@utp.edu.pl (S.M.); michal.piotrowski@pbs.edu.pl (M.P.)
[2] Faculty of Mechanical Engineering, Cracow University of Technology, Al. Jana Pawla II 37, 31-864 Kraków, Poland
* Correspondence: halina.egner@pk.edu.pl

Abstract: S420M steel subjected to strain-controlled low-cycle fatigue does not exhibit a period of cyclic properties stabilization. The maximum stress on a cycle continuously drops until fracture. For this reason, it is difficult to plan experimental research for different types of control in such a way that their results can be considered comparable. The aim of this paper is to present and discuss the results of tests conducted in various conditions of low-cycle fatigue of S420M steel specimens, both undeformed and pre-strained. In both loading conditions, after initial deformation, a significant change in the cyclic properties of steel described by the parameters of the hysteresis loop was observed. Also, the fatigue life of the pre-strained specimens appeared to be different from unstrained specimens and was affected by the test loading conditions. The reduction in life under controlled stress conditions was attributed to the increase in the extent of plastic deformation and stress and the occurrence of creep.

Keywords: low-cycle fatigue; durability prediction; experimental testing; pre-strain; cyclic properties

1. Introduction

Structural elements of many technical devices, such as elements of power plants, bridges, and wind farms, may be subjected to occasional significant static loads during operation, resulting, for example, from improper start-up, assembly, or shutdown due to seismic events. The effects of such unforeseen events (emergencies) in the form of initial deformations are usually disregarded in fatigue calculations, which are most often based on the data determined experimentally using as-received materials [1–6]. However, to properly design important technical objects that may be subject to occasional unforeseen events, it is necessary to have detailed knowledge about the construction material response to possible additional deformation, which may affect the course of material stabilization and material data used in fatigue calculations.

The impact of the initial deformation on the basic strength properties of engineering materials was discussed in many research papers in relation to both static and fatigue loading conditions. In papers [7–9], a beneficial effect of the initial deformation on the strength characteristics obtained as a result of carrying out static tensile tests was demonstrated for precipitation-strengthened stainless steel SUH660 [7], complex phase steel CP800 [8], and austenitic stainless steel AISI 304L [9]. However, such an improvement in basic strength parameters due to initial deformation was not observed for S420M steel [10].

As described in the literature, tests of the impact of initial deformation on the fatigue life were carried out under various cyclic loading conditions. Mnif et al. in [11] performed strain-controlled torsion fatigue tests (τ_{at} = const.) of brass alloy specimens and found that initial deformation results in a slight increase in fatigue life. Such an increase in the fatigue life and fatigue limit of specimens made of sheet metal used for car bodies, as a result of 10% of initial strain, was also noted in [12]. They carried out fatigue tests under conditions

of flat bending and controlled strain (ε_{at} = const.). On the other hand, a slight reduction in the fatigue life of SUH660 austenitic steel specimens after 10% pre-strain was found in [7] under the conditions of rotating–bending fatigue under controlled stress (σ_a = const.). The authors of [13] investigated the pre-strain-related changes in the fatigue limit of 0.1% (annealed) and 0.5% (quenched and tempered) carbon steel by using a rotating bending fatigue test. The changes were correlated with the surface parameters. Increasing surface hardness improved the fatigue limit of 0.1% carbon steel, while pre-cracks generated on the surface decreased the fatigue limit in the case of 0.5% carbon steel. The authors of [14] conducted fatigue tests of 27MnCr5 steel samples in three loading conditions: tension, bending, and torsion. The results were analyzed to investigate the influence of pre-strain on fatigue strength. All investigations showed an increase in fatigue strength caused by strain hardening.

Most of the research concerning the effect of initial deformation on the fatigue life takes into account tension–compression tests, either under conditions of controlled strain (ε_{at} = const.) [15–18] or stress (σ_a = const.) [19–22]. The authors of [15] observed that the initial deformation reduces fatigue life and leads to a new state of stabilization of the C45 steel. The authors of [16] investigated the fatigue behavior of pre-deformed TRIP 780 steel specimens. The authors found that initial deformation followed by tempering increases the durability of steel for cyclic strain amplitudes larger than 0.004. The authors of [17] analyzed the effect of initial strains of TRIP780 multiphase steel specimens applied at different temperatures (−20 °C, 0, and 80 °C). A slight dependence of fatigue life on the initial deformation temperature was found. Mroziński et al. in [10] considered the strain-controlled fatigue tests of S420M steel specimens after initial deformation and observed a slight increase in the fatigue life of pre-strained specimens. The largest increase in fatigue life was detected at the lowest strain levels. On the other hand, the authors of [18] analyzed the influence of initial strains on the durability of the 7050-T6 aluminum alloy. Based on the examination of the strain–life and energy–life graphs, it was found that increasing initial deformation decreases the fatigue life. The authors of [23] analyzed the influence of both cyclic and monotonic pre-strains of similar magnitude on the cyclic behavior of pure copper and 316L stainless steel. It appeared that the impact of cyclic and monotonic pre-strains was similar for the investigated range of plastic strain amplitudes. In both cases, strain-controlled fatigue tests on pre-strained specimens revealed reduced fatigue life in comparison with as-received specimens. Whittaker and Evans [24] investigated the effect of pre-strain on the fatigue properties of Ti834 in the strain-controlled tests. They discovered that at low pre-strain levels, the mechanical properties change minimally, and durability is not significantly affected. On the other hand, 8% or more pre-strain significantly influences the fatigue properties of Ti834 and reduces durability. The authors of [25] investigated the pre-strain inherited memory effect by experimentally testing three FCC metallic materials: OFHC pure copper, nickel–chromium alloy, and AISI 316L stainless steel. Tensile pre-strain levels corresponded to different strain-hardening stages, and a wide range of strain amplitudes was considered. Three memory regions have been distinguished depending on the cyclic plastic strain amplitude.

For stress-controlled fatigue tests, the initial straining most often causes a reduction in the fatigue life. Yang and Wang [19] reported the influence of pre-strain on the reduction in durability and change in cyclic properties of high-strength spring steel specimens. The impact of the initial strain on the durability depended on both the magnitude of the initial strain and the amplitude of the variable load applied after it. The influence of the magnitude of pre-strain on the reduction in durability was confirmed in [8]. The reduction in fatigue life due to initial strains was also found in [7,20,21]. In these studies, it was found that the most significant reduction in durability takes place at the level of the fatigue limit. The authors of [22], based on tests of specimens made of austenitic steel Z2CN18.10, found that tensile pre-strain improves durability, while for compressive pre-strain, the fatigue life is reduced.

Based on the analysis of numerous literature reports (cf also [26–32] and many others), it can be concluded that the impact of initial deformations on the fatigue life largely depends on the load conditions occurring after the initial deformation. In the case of stress-controlled cycles (σ_a = const.), a decrease in fatigue life is most often observed. In the case of strain-controlled conditions (ε_{at} = const.), the durability of the specimens may depend also on other factors, such as the type of material, amount of deformation, etc.

The research problem undertaken in the present paper is the quantitative assessment of the impact of loading conditions applied after initial deformation on the fatigue life of S420M steel specimens. S420M steel is very often used for welded elements that are subjected to very high static and fatigue loads. Typical applications for S420M steel are bridges, viaducts, long-span structures, high-rise buildings, and other responsible engineering structures. Due to frequent cases of overloads of these types of objects, tests are necessary to investigate how such events influence the durability of S420M steel elements. The experiments determining the basic strength parameters of both as-received and pre-strained S420M steel specimens in a static tensile test were already performed and described in [10]. It was shown that a pre-strain of S420M steel specimens of as much as 33% of the total elongation (A_5) does not reduce the basic strength parameters determined in the static tensile test. In the present research, low-cycle fatigue tests were carried out under conditions of controlled strain (ε_{at} = const.) and controlled stress (σ_a = const.). The analysis of hysteresis loops parameters and metallographic microstructure observations were performed to formulate the conclusions.

2. Materials and Methods

2.1. Experimental Methods

2.1.1. Test Specimens

The test samples were cut out of a S420M steel sheet with a thickness of 30 mm. Table 1 summarizes the chemical composition of S420M steel.

Table 1. Chemical composition of S420M steel (wt %).

Fe	C	Si	Mn	P	Cr	Al	Nb	Ti	V	W
98.0	0.125	0.215	1.45	0.0135	0.0208	0.0268	0.0288	0.013	0.0519	0.0150

Specimens were prepared according to the requirements of standards [33–35] (see Figure 1).

After measuring the specimen diameters, the R_a roughness measurements of the gauge part were carried out. Measurements were performed on a MarSurf XR 20 profilographometer, on three randomly selected specimens. The mean value R_a = 0.59 was obtained.

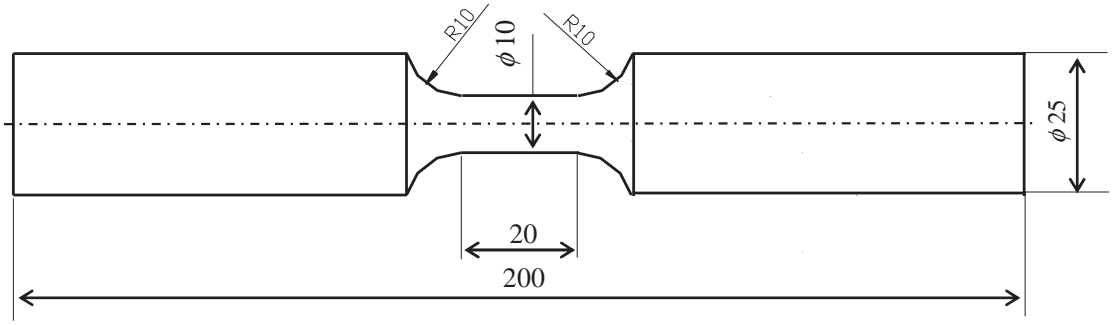

Figure 1. Test specimen (dimensions given in mm).

2.1.2. Low-Cycle Fatigue Tests

During the low-cycle tests, both undeformed specimens (as-received specimens) and pre-strained specimens (ε = 10%) were used. Fatigue tests were conducted for strain-

controlled conditions (ε_{at} = const.) and stress-controlled conditions (σ_a = const.) in accordance with the guidelines given in ASTM E606-92. The tests were performed on the Intron 8502 testing machine at the temperature T = 20 °C. Five levels of controlled total strain ε_{at}, and of controlled stress σ_a were applied in tests. Three as-received samples and three pre-strained samples were tested on each load level. Strain levels (ε_{at}) were adopted after analyzing the static tensile diagrams (see Figure 2), while stress levels σ_a were determined after low-cycle fatigue tests in the conditions ε_{at} = const. In the absence of a stabilization period, to establish comparable test conditions, stress amplitudes were assumed based on the middle cycle of each strain-controlled test (n/N = 0.5). The amplitudes of all fatigue tests are listed in Table 2.

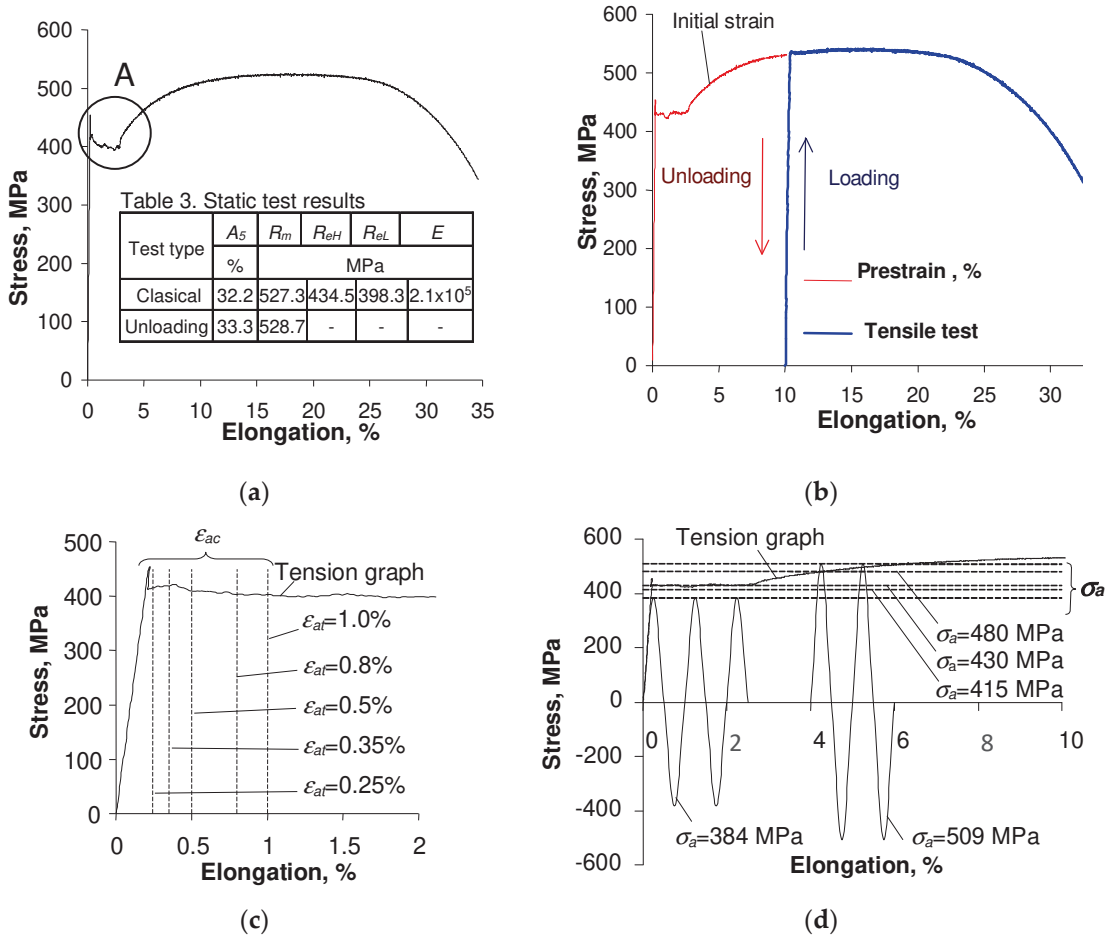

Figure 2. Tensile diagrams used for fatigue tests strain amplitude determination: (**a**) monotonic tests; (**b**) tension with unloading; (**c**) strain amplitude levels ε_{at} adopted in tests (enlarged section A of stress-strain curve shown in (**a**); (**d**) stress amplitude levels σ_a.

Table 2. Test parameters.

Level	T = 20 °C	
	ε_{at}, %, (ε_{at} = const.)	σ_a, MPa, σ_a = const.)
1	0.25	384
2	0.35	415
3	0.5	430
4	0.8	480
5	1.0	509

Instantaneous stresses during the cyclic loading were obtained as a quotient of the instantaneous values of forces loading the specimen and its initial cross-sectional area. The

frequency of the load during the tests was 0.2 Hz. The instantaneous values of the force loading the specimen and its deformation were recorded. Each load cycle was described with 200 points. The criteria for the end of the fatigue test were adopted in accordance with the approach given in the standard ASTM E606-92. Strains were measured by the use of a dynamic test extensometer (type 2630-110) mounted on the gauge part of the specimen, with a base of 10 mm and a measuring range of ±1 mm. The force was measured using a force gauge head (2518-113) with a measuring range of ±125 kN.

3. Results

3.1. Low-Cycle Fatigue Properties

The results of low-cycle fatigue tests were examined in the context of changes in the stress amplitude σ_a and plastic strain amplitude ε_{ap}, depending on whether the sample was as-received or pre-deformed.

To illustrate the phenomena observed during the tests, Figures 3 and 4 present exemplary hysteresis loops at two strain amplitude levels of the strain-controlled test (Figure 3) and one stress amplitude level of the stress-controlled experiment (Figure 4) obtained for an as-received specimen and a pre-deformed specimen. The loops were taken from three characteristic durability periods, i.e., the first cycle ($n = 1$), mid-life ($n/N = 0.5$), and the last cycle ($n/N = 1$).

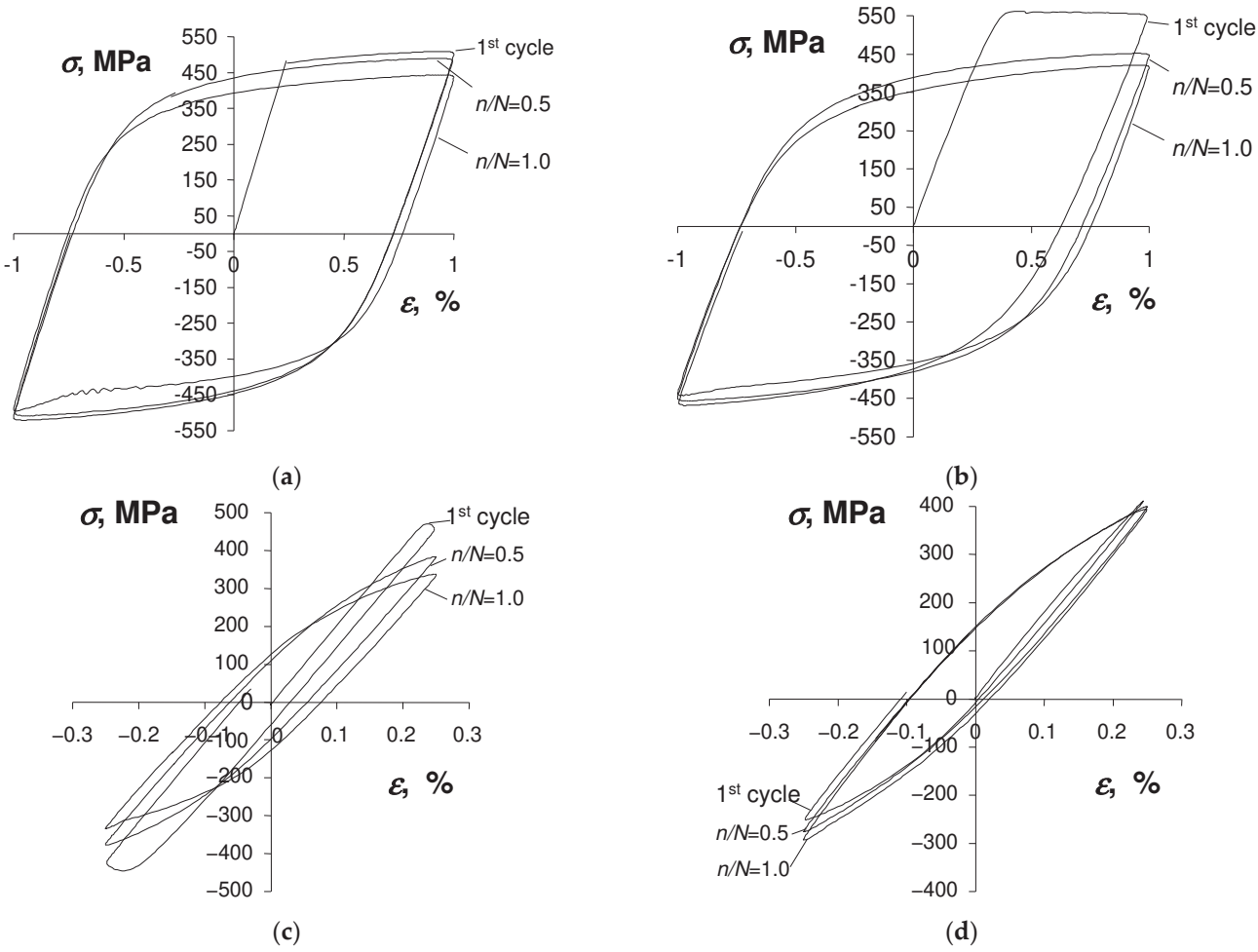

Figure 3. Hysteresis loops for strain-controlled test and strain amplitude levels: (**a**) ε_{at} = 1.0% (as-received specimen); (**b**) ε_{at} = 1.0% (pre-strained specimen); (**c**) ε_{at} = 0.25% (as-received specimen); (**d**) ε_{at} = 0.25% (pre-strained specimen).

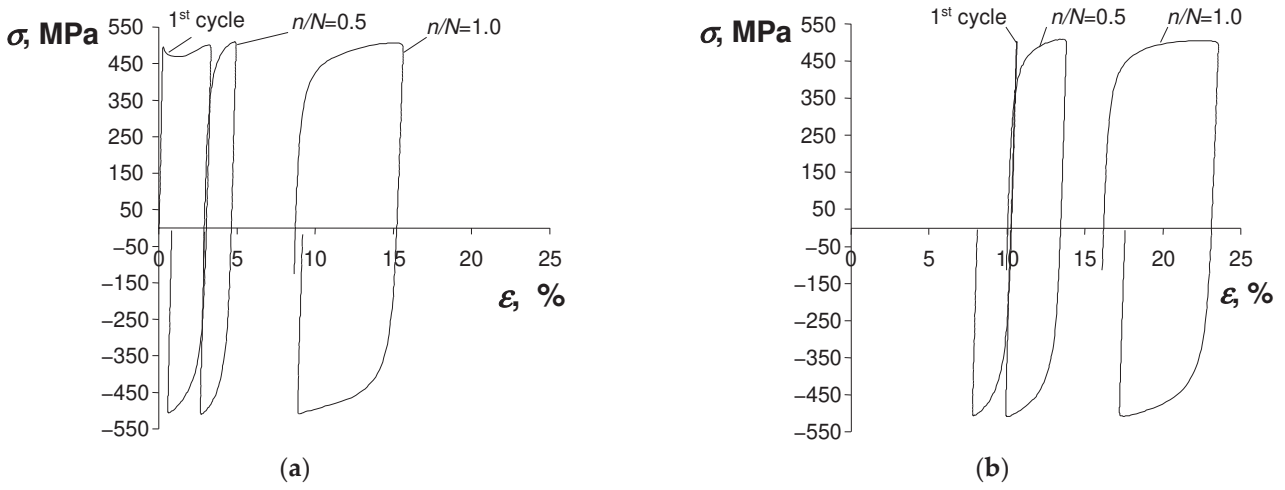

Figure 4. Hysteresis loops for stress-controlled test and stress amplitude level σ_a = 509 MPa: (**a**) as-received specimen; (**b**) pre-strained specimen.

The comparison of test results shown in Figures 3 and 4 confirmed that the hysteresis loop parameters of both as-received and pre-deformed specimens changed during the tests. Also, irrespective of the specimen, there is no clear stabilization period during the cyclic load, which significantly complicates the analysis of test results. As expected, during the tests under the conditions σ_a = const. (Figure 4), a pronounced creep is visible. It manifests itself in the shift of successive hysteresis loops in the direction of the horizontal axis. Creep takes place both in the tests of as-received and pre-deformed specimens. The magnitude of the loop displacement is influenced by the stress amplitude level σ_a, and increases with increasing stress. Assuming the range of plastic strain ε_{ap} in the as-received specimen and pre-strain specimen as a measure of changes in low-cycle properties, it can be concluded that in the conditions σ_a = const., these changes are definitely larger than those observed in the conditions ε_{at} = const. In order to illustrate changes in loop parameters, Figures 5 and 6 present exemplary comparative ε_{ap} charts for both as-received and deformed specimens at three levels of strain amplitude ε_{at}, and corresponding stress amplitude levels σ_a (see Table 2).

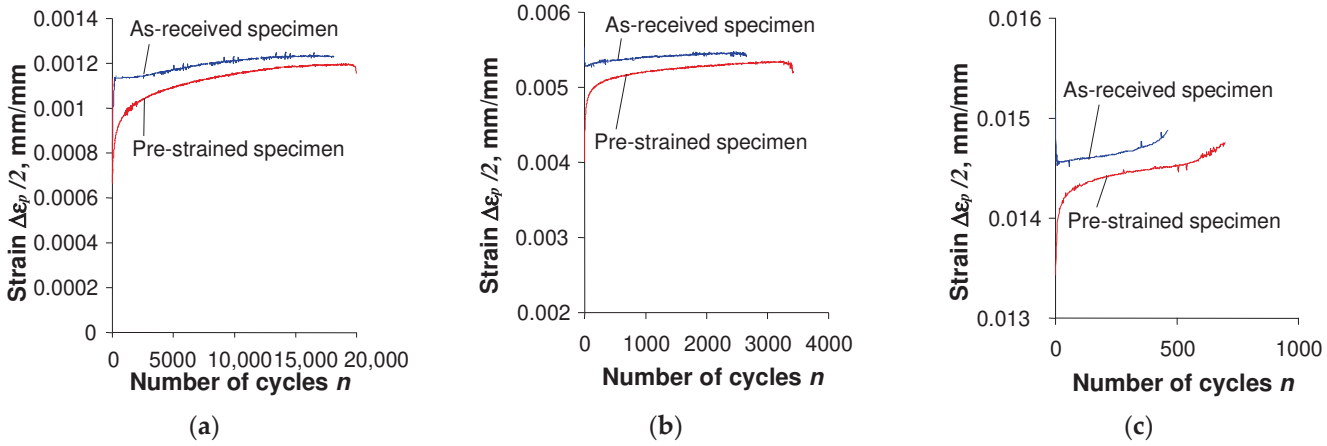

Figure 5. Influence of initial strain on $\Delta\varepsilon_p$ observed in strain-controlled tests: (**a**) ε_{at} = 0.25%; (**b**) ε_{at} = 0.5%; (**c**) ε_{at} = 1.0%.

Attention is drawn to the asymmetry of stresses and plastic deformations of specimens subjected to initial deformations at the deformation level ε_{at} = 0.25%. (Figure 2d). The analysis showed that the level of strain significantly influences the asymmetry of stress. The highest values of average stress σ_m were obtained at the strain level ε_{at} = 0.25%. No such

phenomenon was found when testing as-received samples (the value of σ_m was often close to the force measurement error). A detailed analysis of stress asymmetry in the conditions of controlled deformation is included in [10].

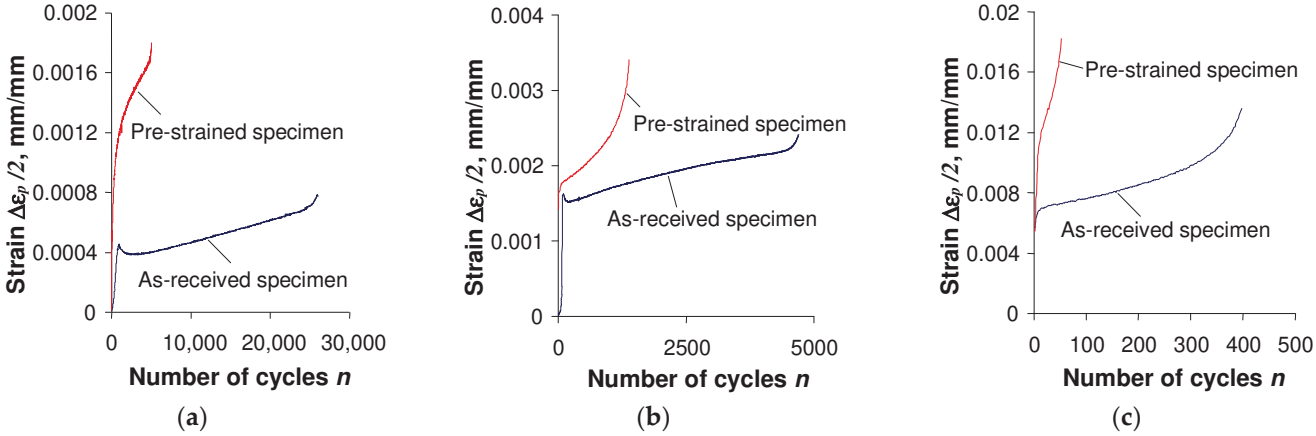

Figure 6. Influence of initial strain on $\Delta\varepsilon_p$ observed in stress-controlled tests: (**a**) σ_a = 384 MPa; (**b**) σ_a = 430 MPa; (**c**) σ_a = 509 MPa.

The analysis of Figures 5 and 6 shows that during cyclic loads, the plastic strain ε_{ap} of as-received specimens is significantly different from the corresponding plastic strain of pre-deformed specimens. Based on the comparative study of plastic strain ε_{ap}, it can be concluded that under the conditions ε_{at} = const. (Figure 5), after permanent pre-strain (ε = 10%), plastic strains are smaller than those observed during testing of as-received specimens. The situation is different when testing in conditions σ_a = const. Significantly higher strain values ε_{ap} were observed after permanent deformation at the same stress levels. The results of fatigue tests under various load conditions were developed in accordance with the standard [33].

The analytical dependency of stress amplitude σ_a on plastic strain amplitude ε_{ap}, is described by the equation of the form proposed in [33]:

$$log\sigma_a = logK' + n'log\varepsilon_{ap} \quad (1)$$

The values of σ_a and ε_{ap} hysteresis loop parameters were obtained by means of the least squares method, evaluating the coefficients and exponents of a simple regression described by Equation (1). The results of fatigue life were presented in the $2N_f - \varepsilon$ coordinate system. Fatigue graphs in the bi-logarithmic scale were approximated by the equation of the following form [33]:

$$\frac{\Delta\varepsilon_t}{2} = \frac{\Delta\varepsilon_e}{2} + \frac{\Delta\varepsilon_p}{2} = \frac{\sigma'_f}{E}\left(2N_f\right)^b + \varepsilon'_f\left(2N_f\right)^c \quad (2)$$

Test results were analyzed in terms of the impact of load conditions (σ_a = const. or ε_{at} = const.) and initial strains on the durability and low-cycle properties of S420M steel. It can be concluded that in the conditions σ_a = const. the fatigue life is slightly lower than the durability obtained in the conditions ε_{at} = const. To illustrate the results, Figure 7 shows fatigue diagrams described by Equation (2) and a stress–strain diagram described by Equation (1) for the as-received material.

Based on the above results, it was found that the differences in the fatigue life under the conditions σ_a = const. and ε_{at} = const. increase with the increase in strain (or stress) amplitude. These results confirm the conclusions presented in [6,7].

Pre-deformation of the specimens affects the low-cycle properties both in stress-controlled and strain-controlled test conditions. Figures 8 and 9 show diagrams illustrating

the results of tests carried out in accordance with [33] under conditions ε_{at} = const. and σ_a = const.

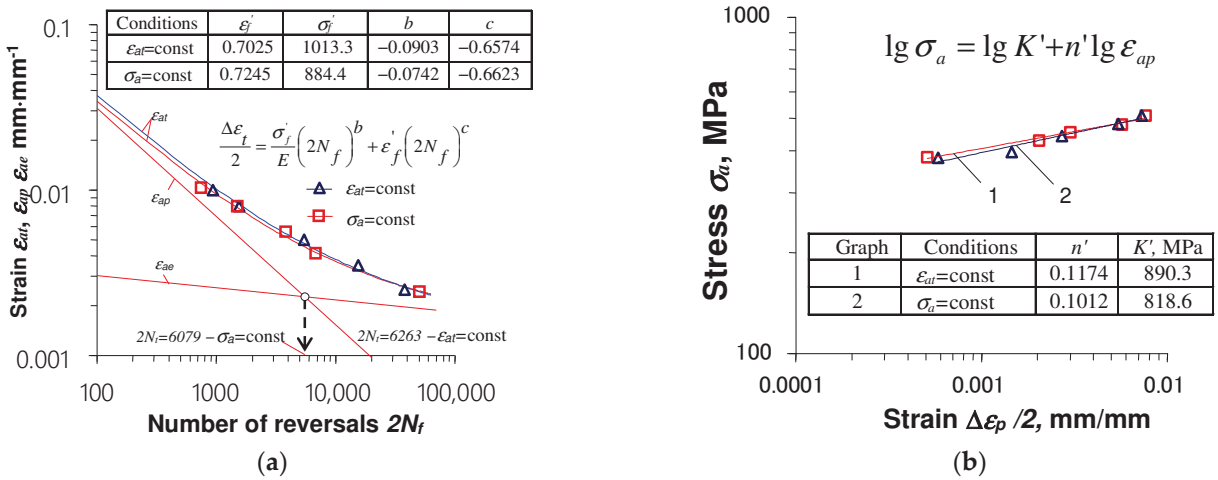

Figure 7. As-received material test results for ε_{at} = const. and σ_a = const.: (**a**) fatigue diagrams; (**b**) stress–strain diagrams.

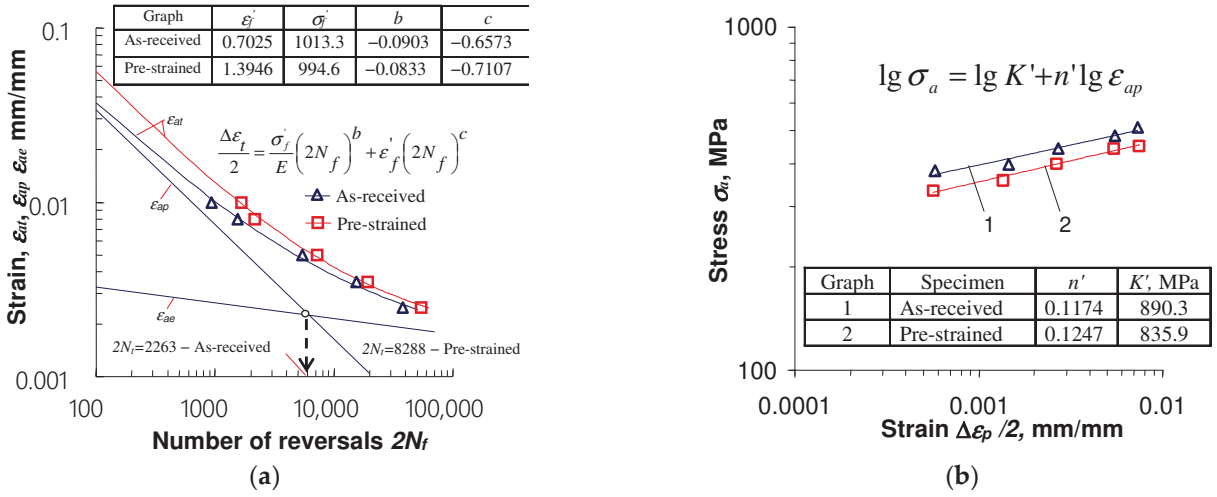

Figure 8. Results of tests performed under strain control ε_{at} = const.: (**a**) $\varepsilon = f\left(2N_f\right)$; (**b**) $\sigma_a = f\left(\varepsilon_{ap}\right)$.

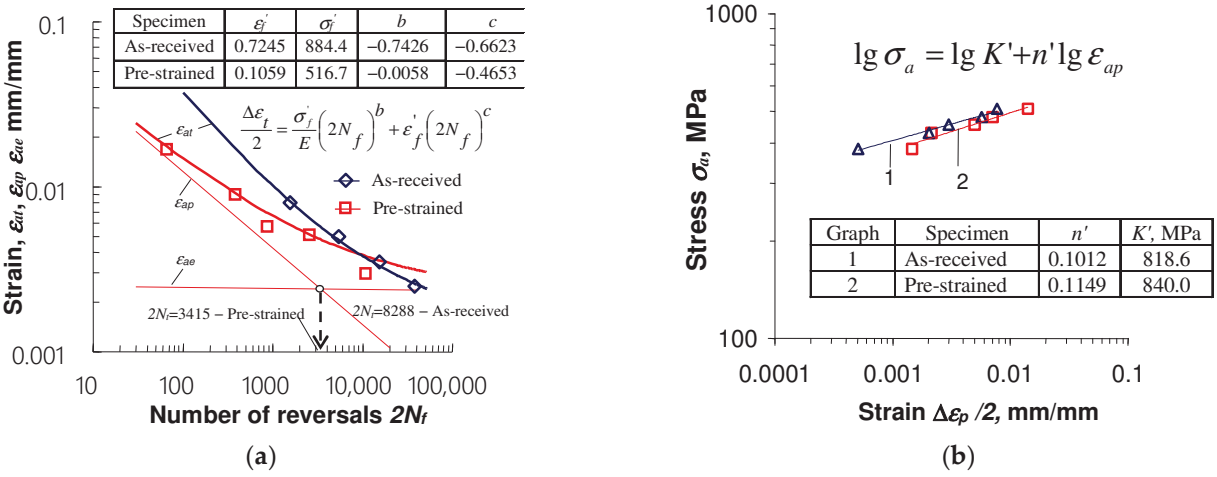

Figure 9. Results of tests performed under stress control σ_a = const.: (**a**) $\varepsilon = f\left(2N_f\right)$; (**b**) $\sigma_a = f\left(\varepsilon_{ap}\right)$.

Based on the test results in the conditions ε_{at} = const., it can be concluded that at the same strain amplitude levels ε_{at}, the number of cycles to failure of specimens subjected to initial deformation is always larger than that of as-received specimens. It is a consequence of the decrease in stress amplitude σ_a and plastic strain amplitude ε_{ap} caused by the initial straining of the specimens (Figure 5). The above conclusion is consistent with the material response observed during the fatigue tests of the TRIP multi-phase steel described in [16]. At lower strain amplitude ε_{at} levels, the increase in fatigue life of pre-strained specimens is more pronounced. With the increase in strain amplitude, the diversity of the obtained durability decreases. Detailed information on the impact of initial strains on the durability of S420M steel specimens under controlled strain conditions is described in [10] and will not be repeated here.

In the case of tests carried out under conditions of controlled stress σ_a = const., the durability of pre-deformed specimens is significantly lower than that of as-received specimens (Figure 9). The remarkably higher plastic strains ε_{ap} of pre-strained specimens at the same stress amplitude levels (Figure 6) result in the reduction in their durability.

The above results conclude that the basic fatigue characteristics of S420M steel as-received and pre-deformed specimens differ. For example, Figure 10 presents diagrams of cyclic strain approximated by the Ramberg–Osgood equation in the following form:

$$\varepsilon_{at} = \frac{\sigma_a}{E} + \left(\frac{\sigma_a}{K'}\right)^{\frac{1}{n'}} \tag{3}$$

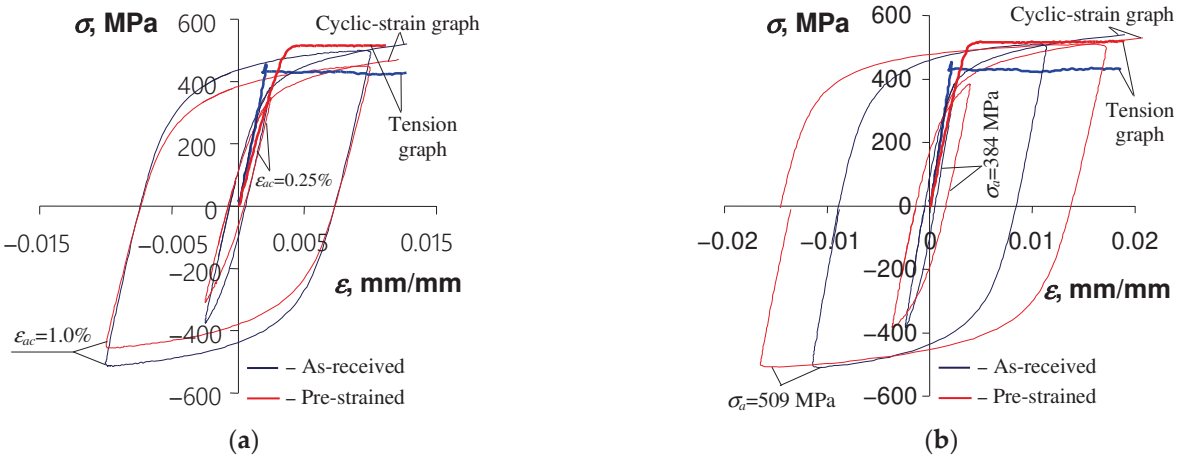

Figure 10. Effect of pre-strain on hysteresis loop characteristics: (**a**) ε_{at} = const., (**b**) σ_a = const.

The hysteresis loops at half-life ($n/N = 0.5$), obtained at two load levels, are shown in Figure 10 for comparison of pre-deformed and as-received specimens' cyclic properties. The loops obtained in the conditions of σ_a = const. (Figure 10b) were translated to the origin of the coordinate system.

The location of the cyclic deformation diagrams described by Equation (3) confirms the change in the cyclic properties of the S420M steel specimens as a result of the initial strain.

Based on the analysis of the mutual location of monotonic tension diagrams and cyclic diagrams for as-received specimens shown in Figure 10, it can be concluded that the cyclic properties of S420M steel, regardless of the type of load (ε_{at} = const. and σ_a = const.), depend on the level of deformation. In the range of deformations of approximately $\varepsilon_{at} > 0.5\%$, the steel is slightly strengthened. This is evidenced by the location of cyclic graphs above monotonic tensile graphs in this area. For strain levels $\varepsilon_{at} < 0.5\%$, as-received specimens are subject to softening. Such properties of as-received specimens were also confirmed in the work [10] on the basis of the analysis of the stress amplitude variation curves. In the case of pre-deformed specimens, the cyclic strain amplitude diagram described by Equation (3) is

placed below the static tensile diagram, which confirms that this material exhibits softening over the entire range of deformation.

Figure 11 shows comparative fatigue diagrams obtained for pre-deformed specimens under two types of loading schemes.

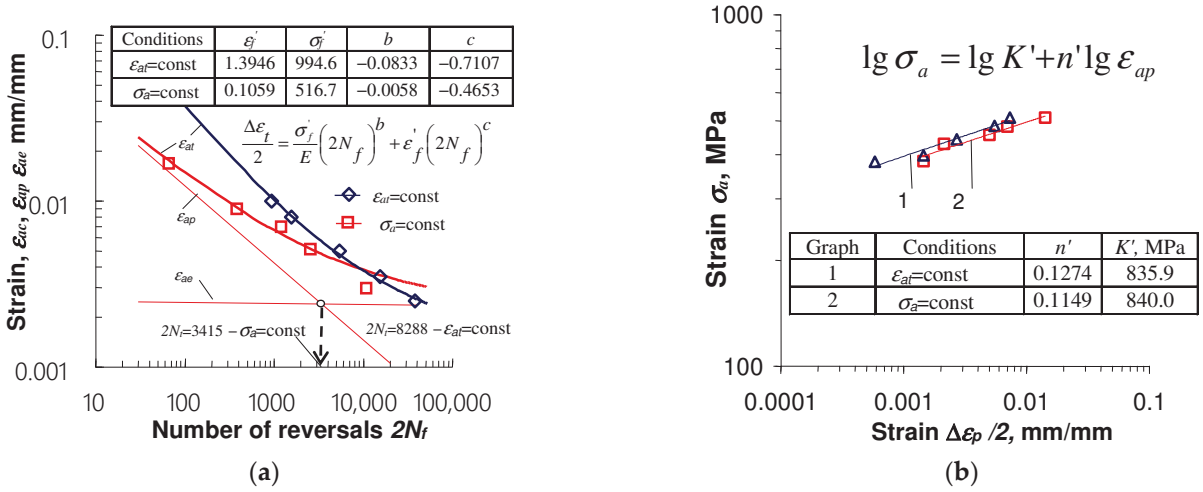

Figure 11. Effect of pre-strain on fatigue properties of S420M steel: (**a**) $\varepsilon = f\left(2N_f\right)$; (**b**) $\sigma_a = f\left(\varepsilon_{ap}\right)$.

Summarizing the results of tests for pre-deformed and as-received specimens, it can be concluded that the impact of pre-deformation on durability depends on the fatigue load conditions that take place after pre-straining. In the case of fatigue stress-controlled tests (σ_a = const.), a significant reduction in fatigue life takes place. The fatigue life obtained under these conditions is definitely lower than the durability observed in the strain-controlled (ε_{at} = const.) fatigue tests. This observation is of great practical importance. It indicates that disregarding the unfavorable effect of pre-straining on durability in conditions σ_a = const. may result in erroneous predictions of structural element durability.

3.2. Microstructural Observations

The microstructure of S420M steel in the as-received state, as well as its modification due to static tensile test, were described in [10].

To compare the influence of the test control scheme on the microstructure of non-pre-strained S420M steel, Figure 12 shows the microstructure of the steel after the fatigue test of the as-received specimen under the strain control ε_{at} = const. (Figure 12a) and stress control σ_a = const. (Figure 12b).

In the case of as-received specimens subjected to the cyclic strain-controlled load ε_{at} = const., a ferritic–pearlitic microstructure with characteristics similar to the material in the delivery condition was observed [10] near the fracture site (Figure 12a). The micro-damage in the specimen developed along the ferrite and pearlite grain boundaries and grew in the direction perpendicular to the axis of the specimen. Cracks that propagated parallel to the scrap surface were also detected. Fracture of the specimens subjected to stress-controlled cyclic load (σ_a = const.) occurred as a result of the nucleation of cracks parallel and perpendicular to the surface of the scrap in the pearlite areas. The propagation of cracks followed the grain boundaries with their local grain deformation (Figure 12b). Figure 13 presents an example of the microstructure obtained after fatigue tests of a pre-strained specimen at the strain amplitude level ε_{at} = 1.0% (Figure 13a), and the stress amplitude level σ_a = 509 MPa (Figure 13b). In the case of the strain-controlled test (Figure 13a)—the microstructure in the vicinity of the scrap surface was similar to the material in the delivery condition. The micro-damage nucleated on the side surface of the sample and spread both along the grain boundaries and inside the grains. Initially, cracks were observed parallel to the scrap surface, as in the case of samples made from the as-received material. In the

area of decohesion of the tested material, a strongly deformed, banded ferritic–pearlitic microstructure with grains elongated in the direction of the principal stress was observed. The microstructure also revealed the presence of quite numerous nucleating voids in the pearlitic areas as well as in the ferrite (Figure 13b).

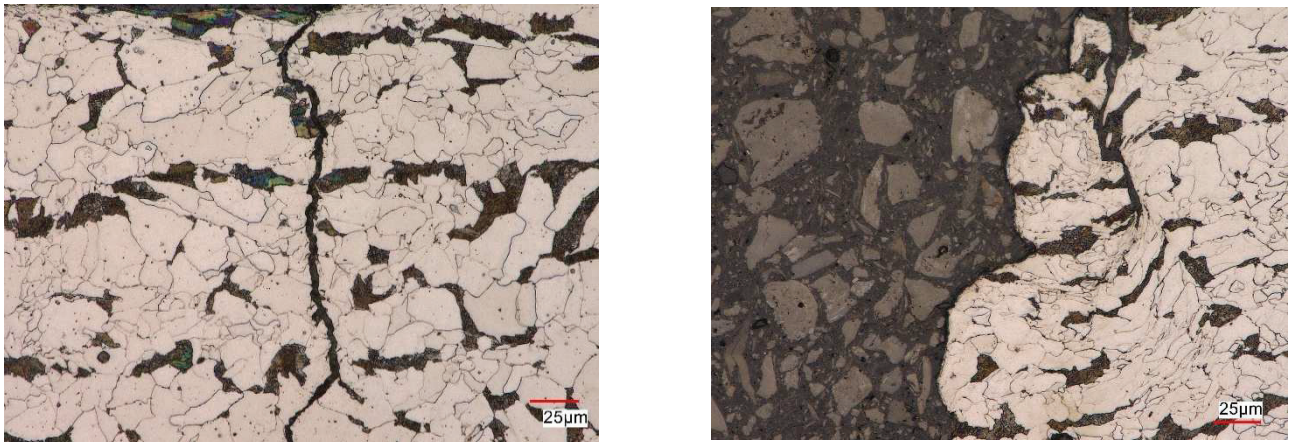

(**a**) (**b**)

Figure 12. S420M steel microstructure after fatigue test: (**a**) ε_{at} = const. − ε_{at} = 1.0%; (**b**) σ_a = const. − σ_a = 509 MPa.

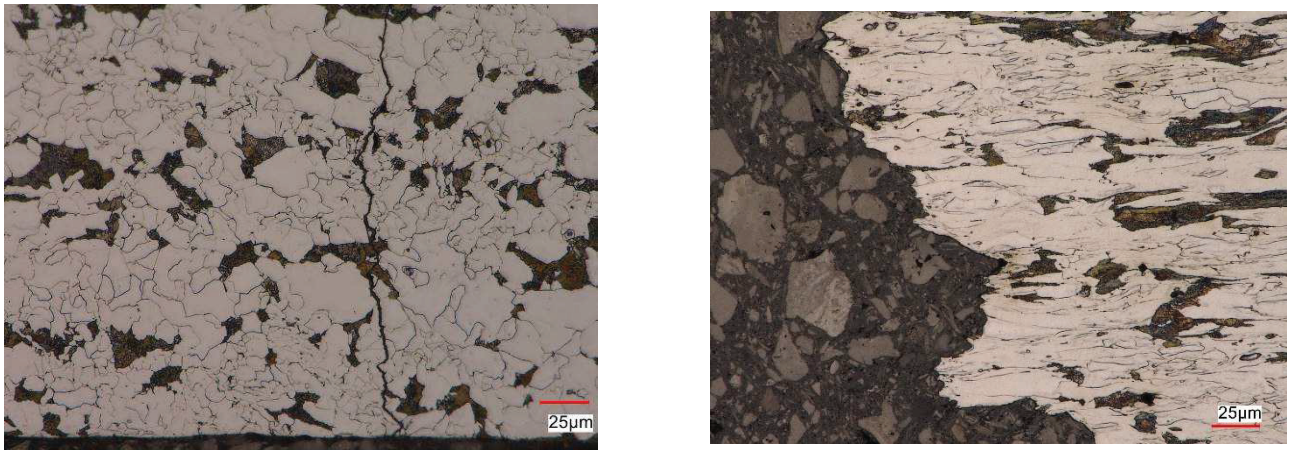

(**a**) (**b**)

Figure 13. S420M steel microstructure of pre-strained specimen (ε = 10%) after fatigue test: (**a**) ε_{at} = const. − ε_{at} = 1.0%; (**b**) σ_a = const. − σ_a = 509 MPa.

Figure 14 presents the microstructure of a pre-strained S420M steel specimen after fatigue tests for the strain-controlled case at the strain amplitude level ε_{at} = 0.35% (Figure 14a) and for stress-controlled scheme at the stress amplitude level σ_a = 384 MPa (Figure 14b).

For both test control schemes, a ferritic–pearlitic microstructure with characteristics similar to the material in the delivery state was observed near the surface of the scrap. In the regions near the surface of the scrap, cracks propagating in the directions parallel to the surface were revealed. The material damage occurred on the side surface of the specimen, where cracks of various depths were revealed, propagating along the grain boundaries perpendicularly to the axis of the specimen (Figure 14b). On the other hand, on the surface of the scrap, a ferritic–pearlitic microstructure was visible, locally deformed, and characterized by a revealed substructure. Studies of the microstructure of S420M steel showed that in most cases, regardless of the assumed deformation and stress parameters, the fracture of the steel was brittle. The nucleation of micro-cracks in these cases was observed on the side surfaces of the specimens, and the propagation took place both along

the boundaries and inside the grains. For micro-cracking preceded by plastic deformation (for the case σ_a = 509 MPa—initial deformation ε = 10%), material damage was associated with the appearance of micro-voids in the microstructure.

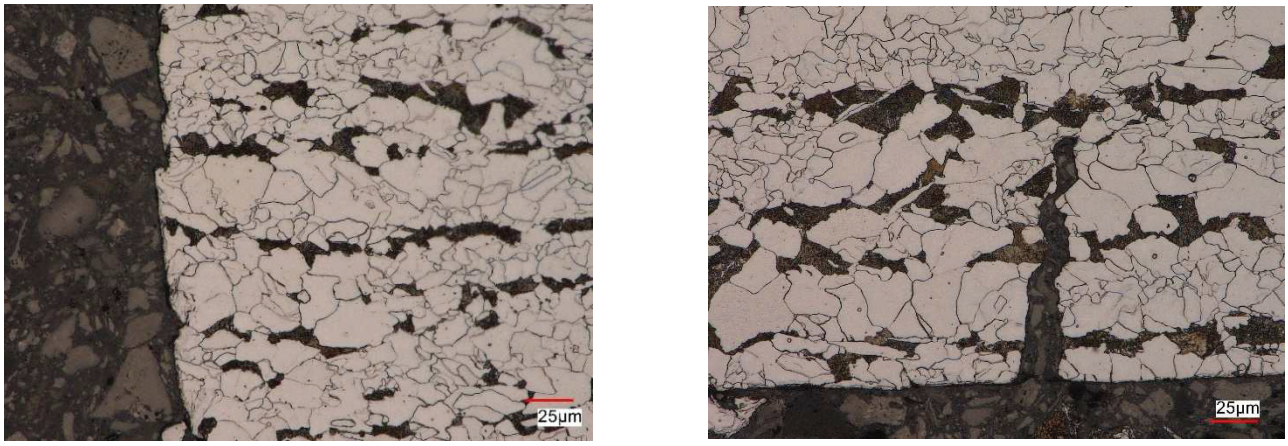

(**a**) (**b**)

Figure 14. S420M steel microstructure of pre-strained specimen (ε = 10%) after fatigue test: (**a**) ε_{at} = 0.35%, ε_{at} = const.; (**b**) σ_a = 384 MPa − σ_a = const.

4. Conclusions

The low-cycle fatigue tests of the S420M steel specimens performed within the present research allow for the formulation of the following conclusions:

1. Loading conditions (test control scheme) affect the fatigue life of both as-received and pre-strained specimens. The fatigue life obtained in the stress control conditions (σ_a = const.) is lower than the durability observed in the strain control conditions (ε_{at} = const.). One factor influencing the variation in durability is creep accompanying the cyclic load under stress control conditions. These results confirm findings published in [6,7].
2. Comparative analysis of the hysteresis loop basic parameters of the as-received and pre-deformed S420M steel specimens, obtained at the same strain and stress amplitude levels, reveals that pre-straining causes a significant change in the fatigue properties.
3. Initial deformation preceding variable load under ε_{at} = const. conditions causes a slight increase in fatigue life. It is caused by the reduction after permanent deformation of two basic parameters of the hysteresis loop, i.e., plastic strain $\Delta\varepsilon_p$, and stress amplitude σ_a.
4. Initial deformations of the specimens (ε = 10%) cause stress asymmetry and plastic deformation during variable loading under the conditions ε_{at} = const. The value of the average stress σ_m and plastic strain is influenced by the level of deformation, ε_{at}. The average stress σ_m reaches its highest values at the lowest level of deformation (ε_{at} = 0.25%).
5. Pre-straining preceding a cyclic load under controlled stress conditions (σ_a = const.) results in a reduction in fatigue life. It is caused by a much larger range of plastic deformations in pre-strained specimens in relation to as-received specimens.
6. The fatigue life calculations may be carried out only if the fatigue diagram and the loading program are known. It is also necessary to adopt a damage summation hypothesis, e.g., Palmgren–Miner. This issue was not considered in this paper. The presented research showed that initial deformations of the material might cause a change in its fatigue properties, described using a fatigue diagram. Neglecting this issue during fatigue calculations of pre-deformed structural elements and using only the characteristics determined for the as-received material may lead to significant errors in the durability assessments obtained from calculations.

Author Contributions: S.M.: Supervision, Conceptualization, Methodology, Investigation, Validation, Visualization, Writing—Original draft preparation. M.P.: Visualization, Investigation, Writing—Original draft preparation. H.E.: Methodology, Writing—Reviewing and Editing, Project administration, Funding acquisition. All authors have read and agreed to the published version of the manuscript.

Funding: This research received no external funding.

Institutional Review Board Statement: Not applicable.

Informed Consent Statement: Not applicable.

Data Availability Statement: Data are contained within the article.

Conflicts of Interest: The authors declare no conflicts of interest.

References

1. Tucker, L.E. *A Procedure for Designing Against Fatigue Failure of Notched Parts*; SAE Paper No 720265; Society of Automotive Engineers, Inc.: New York, NY, USA, 1972.
2. Mroziński, S. Energy-based method of fatigue damage cumulation. *Int. J. Fatigue* **2019**, *121*, 73–83. [CrossRef]
3. Jin, L.; Zhang, S.-L.; Wang, X.-X.; Yin, Q.-W.; Zhu, M.-L.; Xuan, F.-Z. Effect of aging on the low cycle fatigue performance of a low alloy steel. *Procedia Struct. Integr.* **2024**, *52*, 12–19. [CrossRef]
4. Mroziński, S.; Lipski, A. Method for processing of the results of low-cycle fatigue test. *Mater. Sci.* **2012**, *48*, 83–88. [CrossRef]
5. Sulich, P.; Egner, W.; Mroziński, S.; Egner, H. Modeling of cyclic thermo-elastic-plastic behaviour of P91 steel. *J. Theor. Appl. Mech.* **2017**, *55*, 595–606. [CrossRef]
6. Mroziński, S.; Lis, Z. Comparative Analysis of Methods for Determining Cyclic Properties of Metals, Experimental Mechanics of Solids, Materials Research Forum RLC. *Mater. Res. Proc.* **2019**, *12*, 139–145.
7. Wu, H.; Hamada, S.; Noguchi, H. Pre-strain effect on fatigue strength characteristics of SUH660 plain specimens. *Int. J. Fatigue* **2013**, *55*, 291–298. [CrossRef]
8. Sun, H.; Wei, K.; Yang, X.; Xiao, Z.; Wu, Y. Effects of pre-strain and annealing on the fatigue properties of complex phase steel CP800. *Int. J. Fatigue* **2020**, *131*, 105364. [CrossRef]
9. Kim, J.-H.; Park, W.-S.; Chun, M.-S.; Kim, J.-J.; Bae, J.-H.; Kim, M.-H.; Lee, J.-M. Effect of pre-straining on low-temperature mechanical behavior of AISI 304L. *Mater. Sci. Eng. A* **2012**, *543*, 50–57. [CrossRef]
10. Mroziński, S.; Lipski, A.; Piotrowski, M.; Egner, H. Influence of Pre—Strain on Static and Fatigue Properties of S420M Steel. *Materials* **2023**, *16*, 590. [CrossRef]
11. Mnif, R.; Elleuch, R.; Halouani, F. Effects of cyclic torsional prestraining and overstrain on fatigue life and damage behavior of brass alloy. *Mater. Des.* **2010**, *31*, 3742–3747. [CrossRef]
12. Berchem, K.; Hocking, M.G. The influence of pre-straining on the high-cycle fatigue performance of two hot-dip galvanised car body steels. *Mater. Charact.* **2007**, *58*, 593–602. [CrossRef]
13. Kang, M.; Aono, Y.; Noguchi, H. Effect of prestrain on and prediction of fatigue limit in carbon steel. *Int. J. Fatigue* **2007**, *29*, 1855–1862. [CrossRef]
14. Gerin, B.; Pessard, E.; Morel, F.; Verdu, C.; Mary, A. Beneficial effect of prestrain due to cold extrusion on the multiaxial fatigue strength of a 27MnCr5 steel. *Int. J. Fatigue* **2016**, *92*, 345–359. [CrossRef]
15. Mroziński, S.; Szala, J. An analysis of the influence of overloads on a fatigue life of 45-steel within the range of low–cycle fatigue. *J. Theor. Appl. Mech.* **1993**, *4*, 111–123.
16. Robertson, L.T.; Hilditch, T.B.; Hodgson, P.D. The effect of prestrain and bake hardening on the low-cycle fatigue properties of TRIP steel. *Int. J. Fatigue* **2008**, *30*, 587–594. [CrossRef]
17. Ly, A.L.; Findley, K.O. The effects of pre-straining conditions on fatigue behavior of a multiphase TRIP steel. *Int. J. Fatigue* **2016**, *87*, 225–234. [CrossRef]
18. Branco, R.; Costa, J.D.; Borrego, L.P.; Wuc, S.C.; Long, X.Y.; Antunes, F.V. Effect of tensile pre-strain on low-cycle fatigue behaviour of 7050-T6 aluminium alloy. *Eng. Fail. Anal.* **2020**, *114*, 104592. [CrossRef]
19. Yang, Z.; Wang, Z. Effect of prestrain on cyclic creep behaviour of a high strength spring steel. *Mater. Sci. Eng. A* **1996**, *210*, 83–93. [CrossRef]
20. Chiou, Y.-C.; Jen, Y.-M.; Weng, W.-K. Experimental investigation on the effect of tensile pre-strain on ratcheting behavior of 430 Stainless Steel under fully-reversed loading conditions. *Eng. Fail. Anal.* **2011**, *18*, 766–775. [CrossRef]
21. Wang, G. Effect of local plastic stretch on total fatigue life evaluation. In Proceedings of the ECF 15th European conference of fracture 2004, Stockholm, Sweden, 11–13 August 2004.
22. Wang, Y.; Yu, D.; Chen, G.; Chen, X. Effects of pre-strain on uniaxial ratcheting and fatigue failure of Z2CN18.10 austenitic stainless steel. *Int. J. Fatigue* **2013**, *52*, 106–113. [CrossRef]
23. Marnier, G.; Keller, C.; Taleb, L. Fatigue of OFHC pure copper and 316L stainless steel subjected to prior tensile and cyclic prestrains. *Int. J. Fatigue* **2016**, *91*, 204–2019. [CrossRef]
24. Whittaker, M.T.; Evans, W.J. Effect of prestrain on the fatigue properties of Ti834. *Int. J. Fatigue* **2009**, *31*, 1751–1757. [CrossRef]

25. Marnier, G.; Keller, C.; Taleb, L. Tensile prestrain memory effect on subsequent cyclic behavior of FCC metallic materials presenting different dislocations slip modes. *Int. J. Plast.* **2016**, *78*, 64–83. [CrossRef]
26. Zhu, Z.; Chai, G.; Zhang, J.; Li, X.; Huang, Y.; Zhang, J.; Yu, C.; Wang, Q. Origin of prestrain-induced cyclic-strain hardening: Multi-scale experimental characterizations and simulations of 7075 aluminum alloy. *Mater. Des.* **2024**, *238*, 112711. [CrossRef]
27. Mahato, J.K.; De, P.S.; Sarkar, A.; Kundu, A.; Chakraborti, P.C. Effect of prestrain and stress rate on Bauschinger effect of monotonically and cyclically deformed OFHC copper. *Procedia Eng.* **2014**, *74*, 368–375. [CrossRef]
28. De, P.S.; Kundu, A.; Chakraborti, P.C. Effect of prestrain on tensile properties and ratcheting behaviour of Ti-stabilised interstitial free steel. *Mater. Des.* **2014**, *57*, 87–97. [CrossRef]
29. Moço, R.F.; Cavalcante, F.G.; Donato, G.H.B. Effects of manufacturing plastic prestrains found on calendered and UOE pipes and pressure vessels on structural integrity assessments regarding fatigue crack growth and LBB. *Procedia Struct. Integr.* **2018**, *13*, 1915–1923. [CrossRef]
30. Le, Q.; Kang, H.; Kridli, G.; Khosrovaneh, A.; Yan, B. Modified strain-life equation to consider the effect of different prestrain paths for dual phase sheet steel. *J. Mater. Process. Technol.* **2009**, *209*, 3525–3531. [CrossRef]
31. Lanning, D.B.; Nicholas, T.; Haritos, G.K. Effect of plastic prestrain on high cycle fatigue of Ti–6Al–4V. *Mech. Mater.* **2002**, *34*, 127–134. [CrossRef]
32. Stöcker, C.; Zimmermann, M.; Christ, H.-J. Effect of precipitation condition, prestrain and temperature on the fatigue behaviour of wrought nickel-based superalloys in the VHCF range. *Acta Mater.* **2011**, *59*, 5288–5304. [CrossRef]
33. *ASTM E606-92*; Standard Practice for Strain—Controlled Fatigue Testing. ASTM International: West Conshohocken, PA, USA, 2004.
34. *ASTM E8*; Tension Testing of Metallic Material. ASTM International: West Conshohocken, PA, USA, 2004.
35. *ASTM E466-21*; Standard Practice for Conducting Force Controlled Constant Amplitude Axial Fatigue Tests of Metallic Materials. ASTM International: West Conshohocken, PA, USA, 2004.

materials

MDPI

Article

Research on the Size and Distribution of TiN Inclusions in High-Titanium Steel Cast Slabs

Min Zhang [1], Xiangyu Li [2], Zhijie Guo [1] and Yanhui Sun [1,*]

[1] Collaborative Innovation Center of Steel Technology, University of Science and Technology Beijing, Beijing 100083, China; b20200562@xs.ustb.edu.cn (M.Z.); d202210640@xs.ustb.edu.cn (Z.G.)
[2] College of Materials Science and Engineering, Taiyuan University of Technology, Taiyuan 030024, China; 2023520466@link.tyut.edu.cn
* Correspondence: sunyanhui@metall.ustb.edu.cn

Abstract

High-titanium steel contains an elevated titanium content, which promotes the formation of abundant non-metallic inclusions in molten steel at high temperatures, including titanium oxides, sulfides, and nitrides. These inclusions adversely affect continuous casting operations and generate substantial internal/surface defects in cast slabs, ultimately compromising product performance and service reliability. Therefore, stringent control over the size, distribution, and population density of inclusions is imperative during the smelting of high-titanium steel to minimize their detrimental effects. In this paper, samples of high titanium steel (0.4% Ti, 0.004% N) casting billets were analyzed by industrial test sampling and full section comparative analysis of the samples at the center and quarter position. Using the Particle X inclusions, as well as automatic scanning and analyzing equipment, the number, size, location distribution, type and morphology of inclusions in different positions were systematically and comprehensively investigated. The results revealed that the primary inclusions in the steel consisted of TiN, TiS, TiC and their composite forms. TiN inclusions exhibited a size range of 1–5 μm on the slab surface, while larger particles of 2–10 μm were predominantly observed in the interior regions. Large-sized TiN inclusions (5–10 μm) are particularly detrimental, and this problematic type of inclusion predominantly concentrates in the interior regions of the steel slab. A gradual decrease in TiN inclusion number density was identified from the surface toward the core of the slab. Thermodynamic and kinetic calculations incorporating solute segregation effects demonstrated that TiN precipitates primarily in the liquid phase. The computational results showed excellent agreement with experimental data regarding the relationship between TiN size and solidification rate under different cooling conditions, confirming that increased cooling rates lead to reduced TiN particle sizes. Both enhanced cooling rates and reduced titanium content were found to effectively delay TiN precipitation, thereby suppressing the formation of large-sized TiN inclusions in high-titanium steels.

Keywords: TiN; high-titanium steel; inclusions; continuous cast slabs

1. Introduction

As a commonly used alloying element, titanium is widely employed in various steels, including microalloyed steels, interstitial-free (IF) steels, and heat-resistant steels [1–4]. When added to steel, titanium atoms substitute for iron atoms in the iron crystal lattice, causing lattice distortion and impeding dislocation motion, thereby enhancing the strength

of the steel through solid solution strengthening. On the other hand, as a strong nitride-forming element, titanium reacts with nitrogen (N) in molten steel to form TiN precipitates. These precipitates inhibit grain growth by pinning grain boundaries, leading to grain refinement [5–7] and contributing to dispersion-strengthening and precipitation-strengthening effects [8–10].

Since the nitrogen content in steel is generally high, the addition of even small amounts of titanium can fulfil the precipitation conditions for TiN, leading to the formation of TiN inclusions [11–14]. TiN inclusions in steel typically appear as cubic particles with sharp edges, ranging in size from tens of nanometers to over ten micrometers. Besides existing as individual particles, TiN may also aggregate into large multi-particle clusters. The size of TiN inclusions depends on its precipitation location; those formed during solidification are generally micrometer-scale, while those precipitated in the solid phase are nanometer-scale [15–17]. Smaller TiN particles lead to favorable steel properties by refining grains and promoting heterogeneous nucleation [18], whereas larger TiN inclusions, due to their high hardness, non-deformability and sharp edges, can damage the continuity of the steel matrix and become fatigue crack initiation sites under stress, significantly harming steel performance [19]. Fu et al. demonstrated that TiN particles as small as 6 μm can severely reduce steel's fatigue life [20]. Liu et al. found that when the TiN particle size exceeds 4.9 μm, it induces microcrack propagation and causes toughness fluctuations in Ti-microalloyed steels [21]. Du et al. similarly confirmed that coarse TiN inclusions can serve as cleavage crack initiation sites [22]. Constantino Capurro's study of medium-carbon steel production revealed that while TiN content is low in molten steel, it increases significantly in continuous cast billets, primarily located in interdendritic regions [23]. Due to the high melting point (2950 °C) of TiN inclusions and their thermodynamically stability, they become hardly removable once formed in steel. Therefore, optimizing smelting processes to mitigate their detrimental effects is crucial during production. Research consistently demonstrates that elemental content and cooling rate predominantly influence TiN precipitation [24,25], and products with elevated Ti and N concentrations promote premature TiN formation, while reducing the content of these elements can delay precipitation. Accelerating cooling rates in the mold effectively suppresses TiN growth. Yan et al. revealed that both the Ti/N ratio and Ti-N concentrations of products affect TiN particle size, recommending maintaining the concentration of elemental products below that of TiN's solubility product at the solidus temperature with a Ti/N ratio under 3.42, essentially controlling Ti at minimal levels [26]. Tian et al. further established critical Ti/N contents and cooling rates for restricting the TiN particle size to below 6 μm, proposing a three-stage formation mechanism for aggregated TiN [27].

Researchers have investigated the precipitation behavior of TiN inclusions by integrating multiple factors including mass transfer, elemental segregation, and thermodynamics. Ma et al. revealed that in the solidification process of 20 CrMnTi steel containing 0.0072% N and 0.071% Ti, TiN formation occurs only when the solidification fraction exceeds 0.533 [25]. Liu et al. developed a coupled model based on the ChemAppPy platform to investigate the precipitation and growth behavior of TiN inclusions in Ti-containing microalloyed steels. The results demonstrate that, in steel with a 0.06% Ti content, TiN begins to precipitate at a solid fraction of 0.77. Increasing the Ti concentration leads to earlier TiN precipitation. When the cooling rate decreases from 10 K/s to 0.05 K/s, the predicted size of TiN inclusions increases significantly from 0.83 μm to 13.38 μm [28].

In actual production processes, varying cooling rates lead to different precipitation behaviors of TiN at different locations of the slab. Duan et al. found that different cooling rates resulted in significant differences in the average size and number density of TiN between the surface and center of ferritic stainless-steel rolled plates [29]. Que et al.

developed an integrated model combining heat transfer, thermodynamic, and kinetic principles to simulate the precipitation and growth of TiN inclusions in steel slabs. The modeling results showed that the average TiN inclusion size increased from 2.82 μm at the slab surface to 10.07 μm at the center. Experimental observations confirmed this trend, demonstrating a progressive decrease in TiN number density accompanied by a corresponding increase in average inclusion size from the surface to the center of the slab [30]. Wang et al. investigated the elemental variations and inclusion distribution in an enameled steel slab. The results revealed that nitrogen content peaked at the slab center and decreased toward the edges. The number density of TiN inclusions exhibited an initial increase followed by a decrease from the inner arc side to the outer arc side, with the largest TiN particle size observed at the slab center [31]. Gao et al.'s research results demonstrate that in titanium-bearing interstitial-free steel slabs, TiN inclusions begin to precipitate when the solid fraction (fs) reaches 0.646–0.68. The TiN–MnS complex inclusions are predominantly concentrated at the quarter-thickness position of the slab [32]. Wang et al. drew similar conclusions in Ti-microalloyed steel slabs, with the peak TiN precipitation occurring at the quarter-thickness position of the slab [33].

Existing studies on TiN inclusion size and precipitation behavior predominantly focus on microalloyed steels, while research on high-titanium steels (with a Ti content significantly exceeding that of microalloyed grades) remains notably scarce. There are even fewer systematic studies on TiN in high-titanium steel slabs. This paper investigates the size distribution of TiN inclusions in high-titanium steel slabs with a titanium content of 0.4% under current production conditions, with a particular focus on the detrimental large-sized TiN inclusions that critically compromise steel matrix integrity and mechanical properties. The analysis further identifies key elemental factors governing TiN growth kinetics, thereby providing theoretical foundations for controlling oversized inclusion formation and suppressing premature TiN precipitation during solidification.

2. Experimental Section

2.1. Materials

The high-titanium steel slabs used in the experiments were obtained from the continuous casting process at a steel plant. The production process of high-titanium steel has the following sequence: converter tapping → ladle refining → RH vacuum refining → continuous casting. To control nitrogen content in the high-titanium steel, an argon-blowing process was implemented in the tundish. Argon supply pipes were installed on the tundish cover, with continuous argon injection at 200 Nm^3/h during casting to displace air and maintain the atmospheric nitrogen content at below 1% in the tundish. The mold meniscus was protected by argon shielding. The casting speed was maintained between 0.8 and 1.1 m/min. The study involved sampling high-titanium steel cast slabs at two critical locations—the quarter-thickness position (midway between the surface and centerline) and the centerline—with 11 specimens collected from each region along a transverse line spanning from the edge to the center and back to the opposite edge. As shown in Figure 1, the billet quarter-thickness directions from top to bottom are numbered S1–S11, while the center positions are numbered Z1–Z11. The samples were sequentially ground using abrasive paper of varying grit sizes, followed by mechanical polishing with diamond suspensions to achieve a mirror-like finish. The main elemental content of t he high-titanium steel is presented in Table 1.

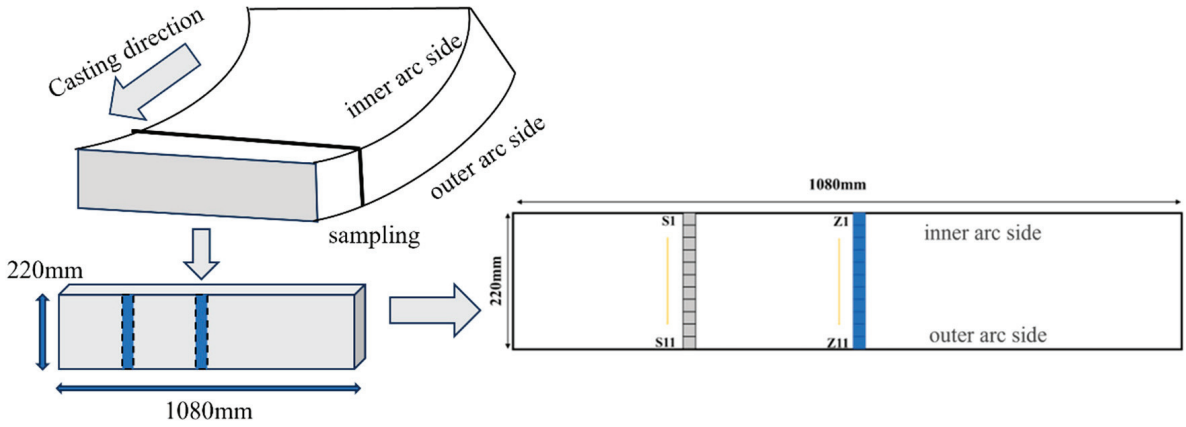

Figure 1. Schematic diagram of casting direction and billet sampling.

Table 1. The main elemental content of the high-titanium steel, mass%.

Element	C	N	Si	Mn	S	P	Mo	Ti	Al
Content	0.18	0.004	0.22	1.3	0.015	0.02	0.22	0.40	0.04

2.2. Analysis

The Reaction module of thermodynamic software Fact Sage 8.1 was employed to calculate the Gibbs free energy changes in three the titanium-containing inclusions (TiN, TiS and TiC) in the high-titanium steel within the temperature range of 1000 °C to 1600 °C, using the FactPS and FToxid databases.

The Particle X automated inclusion analysis system was used to analyze the size, composition, and number of inclusions in the steel, with an initial detection threshold of 1 μm and a scanning area of about 55 mm^2 per sample to ensure statistical reliability. The bulk composition of major alloying elements was detected using chemical ICP-AES methods, with a minimum accuracy of 5 ppm, while oxygen (O) and nitrogen (N) contents were measured using an inert gas fusion-based oxygen/nitrogen analyzer (TCH600).

3. Result and Discussion

3.1. Inclusion Analysis in Slab

3.1.1. Typical Inclusions in Slab

Figure 2 shows typical TiN inclusions at the quarter-thickness position of the slab. The inclusions exhibit three distinct morphologies: Figure 2a shows cubic particles with sharp edges; this TiN inclusion measured 8.7 μm in size, and this type of TiN inclusion was the most commonly observed in the slab. Figure 2b shows triangular particles with angular facets. Figure 2c shows large aggregated inclusions formed by the clustering of individual TiN particles, as evidenced by the preserved sharp edges and relatively regular morphology at the boundaries of these aggregates. This type of inclusion typically measures approximately 20 μm in size.

Figure 3 shows typical TiN inclusions at the center position of the slab. Figure 3a shows agglomerated large TiN inclusions measuring 8.07 μm with sharp edges. Figure 3b shows isolated cubic TiN particles measuring 7.36 μm showing a similar angular morphology. No morphological differences were observed between TiN inclusions at the center and quarter-thickness positions, with variations only in size distribution.

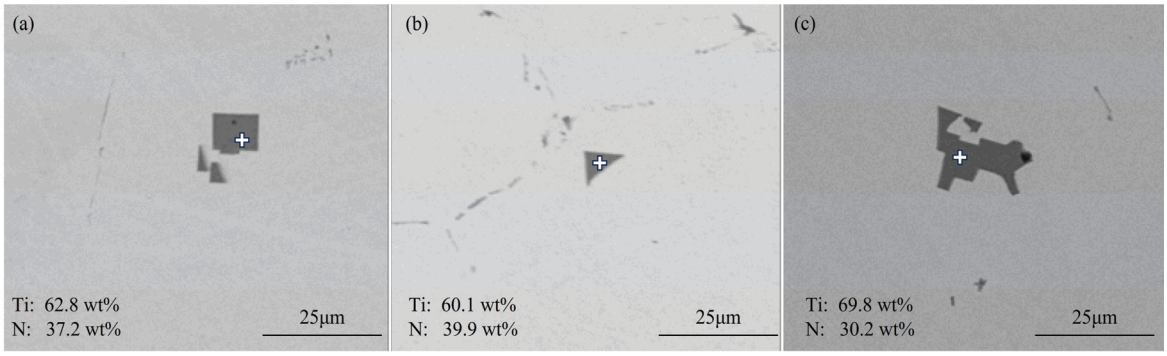

Figure 2. Typical TiN inclusions at the quarter-thickness position of the slab: (**a**) cubic particles with sharp edges; (**b**) triangular particles with angular facets; (**c**) clustered.

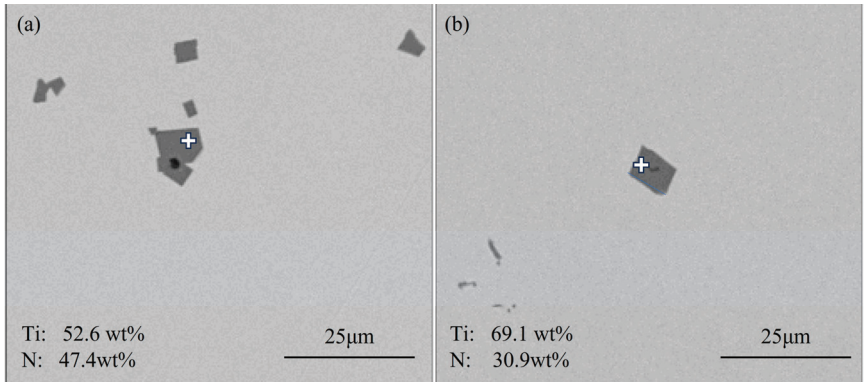

Figure 3. Typical TiN inclusions at the center of the slab: (**a**) agglomerated; (**b**) angular morphology.

Figure 4 shows typical TiS inclusions at the quarter-thickness position of the slab. Most TiS inclusions appeared as aggregated short rod-shaped particles, as shown in Figure 4b, while some agglomerated TiS inclusions exhibited irregular morphologies, as illustrated in Figure 4a.

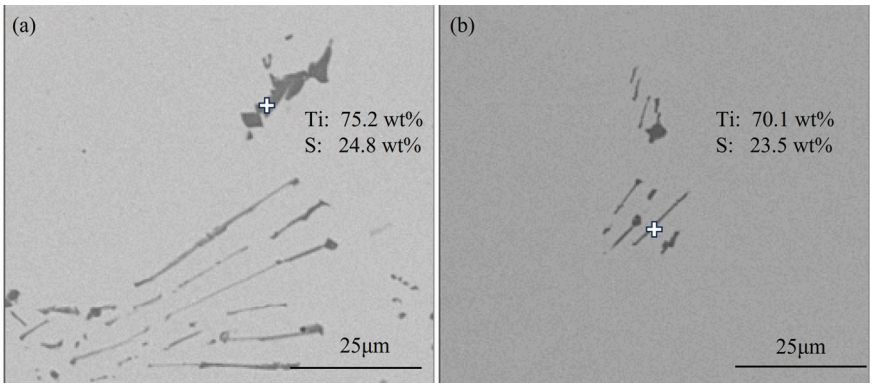

Figure 4. Typical TiS inclusions at the quarter-thickness position of the slab: (**a**) irregular morphologies; (**b**) aggregated short rod-shaped.

Figure 5 shows typical TiS inclusions at the center position of the slab. The TiS morphologies at the center of slab closely resemble those at the quarter-thickness position, primarily exhibiting elongated rod-shaped forms, as can be seen in Figure 5a, or short rod-shaped forms, along with irregular morphologies, as demonstrated in Figure 5b.

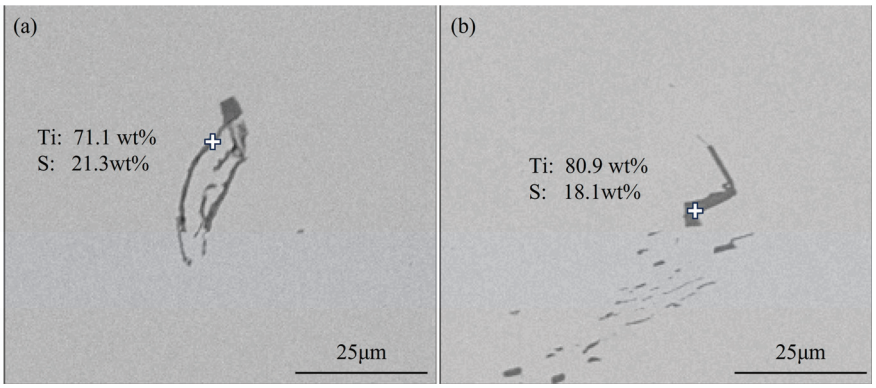

Figure 5. Typical TiS inclusions at the center of the slab: (**a**) short rod-shaped forms; (**b**) irregular morphologies.

The calculation results of the Gibbs free energy changes in the three titanium-containing inclusions are shown in Figure 6. According to the calculation results, at 1600 °C, the Gibbs free energy of all three types of inclusions was negative, indicating that under thermodynamic conditions, all three inclusions could precipitate. Among them, TiN consistently exhibited the lowest Gibbs free energy, suggesting that TiN inclusions are more likely to form. Furthermore, as the temperature decreased, the Gibbs free energy of TiN continued to decrease, demonstrating that the precipitation of TiN would persist.

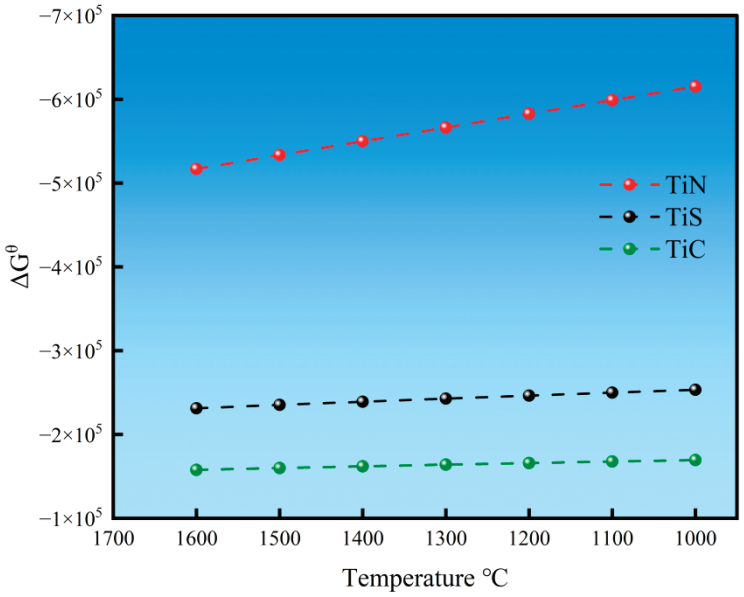

Figure 6. Gibbs free energy of titanium-containing inclusions.

3.1.2. Inclusion Distribution Across Slab Thickness

Figure 7 presents inclusion distribution maps and a size-classified composition analysis of inclusions from edge samples at both the quarter-thickness and center positions of the slab. Figure 7a applies to S1 and Figure 7b applies to Z1. For each sampling location, 1000 randomly selected inclusions were characterized and categorized by size into five ranges: 1–2 μm, 2–5 μm, 5–10 μm, 10–20 μm, and >20 μm. At the edge region of the slab's quarter-thickness position, the composition of most inclusions falls within the lower right corner of the diagram. This indicates that, apart from single-phase TiX (X = C,N,S) inclusions, the composite inclusions primarily consist of Ti (C,N) and TiN + TiS, with TiN being the dominant component in these complex inclusions. A small number of inclusions have compositions corresponding to TiS or TiC, with sizes ranging from 1 to 5 μm. In this

sample, the inclusion sizes are mainly distributed in two ranges: 1–2 μm and 2–5 μm, with a minority of inclusions measuring 5–10 μm. Notably, these larger inclusions (5–10 μm) also exhibit compositions located in the lower right corner of Figure 7a.

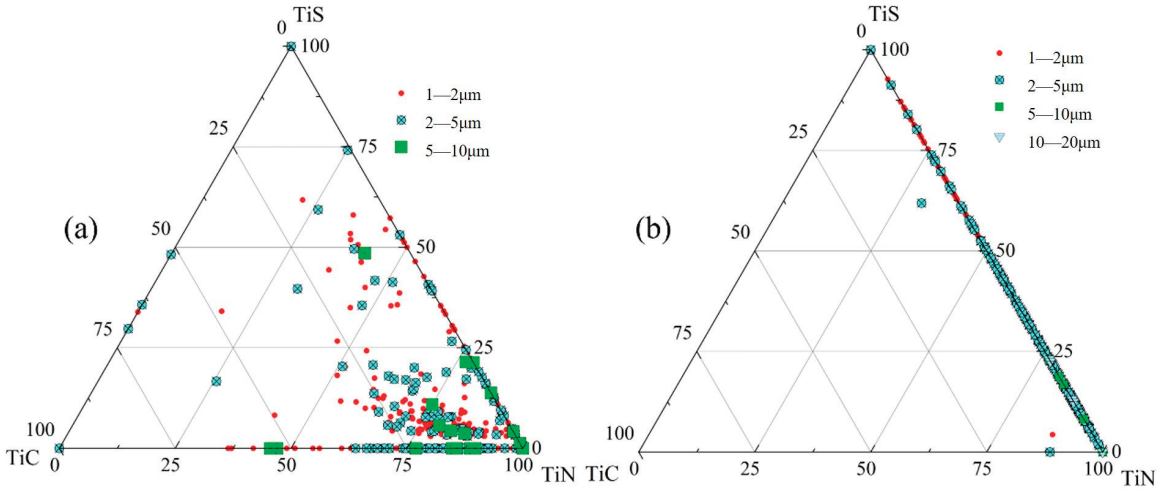

Figure 7. Inclusion distribution map of edge samples: (**a**) S1; (**b**) Z1.

The edge sample from the slab center exhibits inclusions, most measuring 2–5 μm, with their compositional data points almost exclusively distributed along the TiN-TiS phase line. At this location, apart from single-phase TiN and TiS inclusions, nearly all other inclusions consist of TiN + TiS composites.

The compositional distributions of inclusions in samples S3 and Z3 are presented in Figure 8. In sample S3 from the quarter-thickness of the slab, the compositional data points of complex inclusions are mainly distributed along the three edges of the ternary phase diagram. In this sample, apart from single-phase TiX (X = C,N,S) inclusions, the composite inclusions primarily consist of TiC + TiS and TiN + TiS, with a small amount of Ti (C,N), and the sizes of these inclusions are predominantly in the range of 1–2 μm. The TiC + TiS inclusions are predominantly 2–5 μm in size and contain a relatively higher TiS content. The TiN + TiS inclusions include a few large particles exceeding 20 μm.

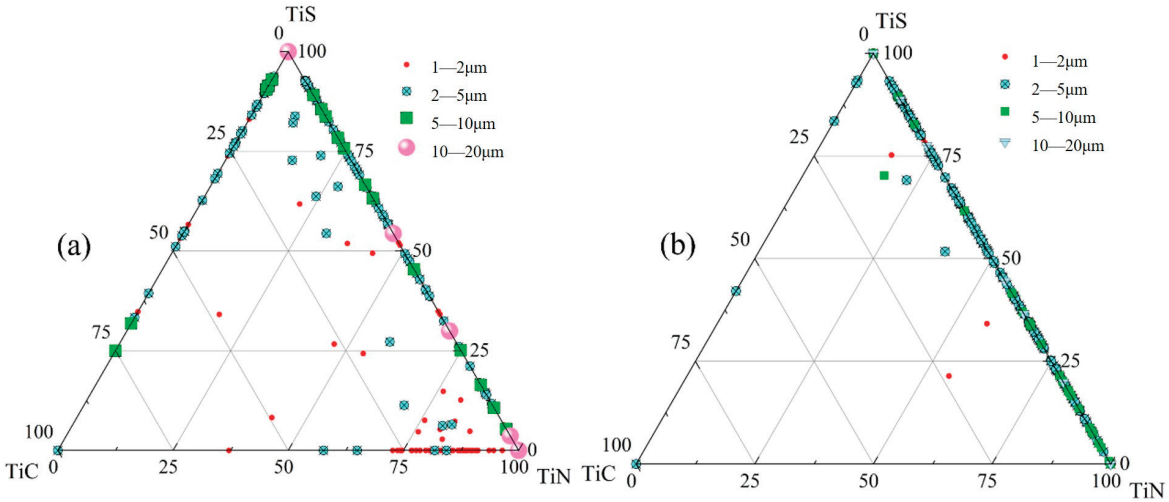

Figure 8. Inclusion distribution map of interior samples: (**a**) S3; (**b**) Z3.

In sample Z3 from the slab center, the inclusion composition points are primarily distributed at the TiN vertex, at the TiS vertex and along the TiS−TiN line, with a small number of single-phase TiC and TiC + TiS composite inclusions present. In this sample,

the 2–5 μm inclusions mainly consist of TiS, TiN and TiS + TiN, along with minor amounts of TiS + TiC and TiC. The composition points of 5–10 μm inclusions are predominantly located near the TiN side of the TiS-TiN line. All 10–20 μm inclusions are situated along the TiS—TiN line, with compositions of TiN, TiS and TiS + TiN.

The compositional distributions of inclusions in the centerline samples (S6 and Z6) from both the slab center and quarter-thickness positions are presented in Figure 9. At the center of the quarter-thickness position in the slab (S6), the compositional data points of inclusions are predominantly located along the TiS + TiN boundary, indicating that the primary inclusion phases in this sample are TiS + TiN composites. A minor fraction of data points are distributed along the TiS + TiC and TiC + TiN boundaries. Most 1–2 μm inclusions exhibit compositions clustered near the TiN side of the TiC-—TiN boundary. For 10–20 μm inclusions, while some data points correspond to pure TiS and TiN at the vertices, the majority align along the TiS + TiN line, confirming their composition as TiN, TiS, and TiN + TiS phases. The relatively few inclusions exceeding 20 μm in size show compositional coordinates either at the TiS/TiN vertices or along the TiS-—TiN boundary, demonstrating that these large inclusions consist exclusively of TiN, TiS, and TiN + TiS.

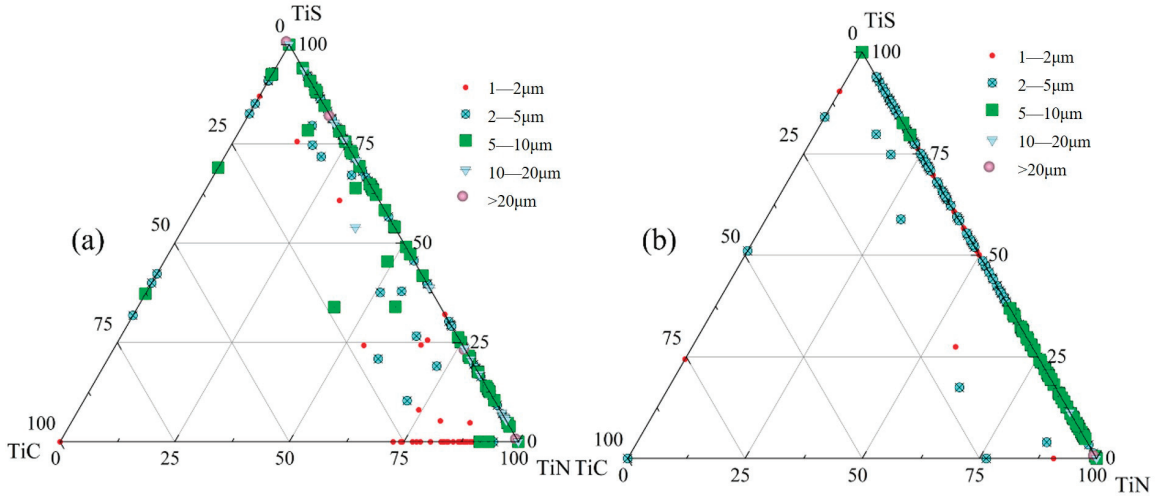

Figure 9. Inclusion distribution map of center samples: (**a**) S6; (**b**) Z6.

In sample Z6 from the slab center, the compositional data points of the inclusions are predominantly distributed along the TiS — TiN phase boundary. Specifically, the 5–10 μm inclusions are mainly concentrated on the TiN side of the TiS-TiN line, while the 10–20 μm inclusions are exclusively located on the TiN-rich side, with TiN content exceeding 90%. A small number of larger inclusions (>20 μm) are positioned closest to the TiN vertex, demonstrating a clear trend of increasing TiN content with inclusion size.

In this experiment, TiS, TiC, and TiN inclusions, as well as their composite inclusions, were observed. Choi [34] and Li [35], respectively, demonstrated that both TiN and TiS exhibit a pinning effect capable of inhibiting grain growth. TiS inclusions precipitate during solidification [36], and both TiS and Ti4 C_2 S_2 inclusions demonstrate good pitting resistance, with minimal impacts on the mechanical properties of steel [37]. TiC precipitates in the solid phase. As shown in Figures 8 and 9, in the high-titanium steel used in this experiment, the quantity of individual TiC and TiC-containing inclusions was significantly lower than that of TiN. Among the three types of titanium-containing inclusions, TiN has the most significant influence on steel performance and service life. Fine TiN particles can pin grain boundaries and inhibit grain coarsening, while large-sized TiN inclusions disrupt matrix continuity, leading to microcrack formation and deteriorating processing performance.

Therefore, the following analysis focuses on the size distribution and precipitation behavior of TiN inclusions in steel.

3.2. Size Distribution of TiN Inclusions

According to the statistical results of TiN inclusion sizes in samples from the quarter-thickness and center positions of the slab, Figures 10 and 11 were plotted. Figure 10 shows the size distribution of TiN inclusions at the quarter-thickness position of the slab, while Figure 11 presents the size distribution of TiN inclusions at the center position. The statistical results indicate that at the quarter-thickness position of the slab, the size of TiN inclusions is primarily in the range of 2–10 μm, whereas at the center position, TiN inclusions are all within 1–10 μm, with no large inclusions exceeding 10 μm.

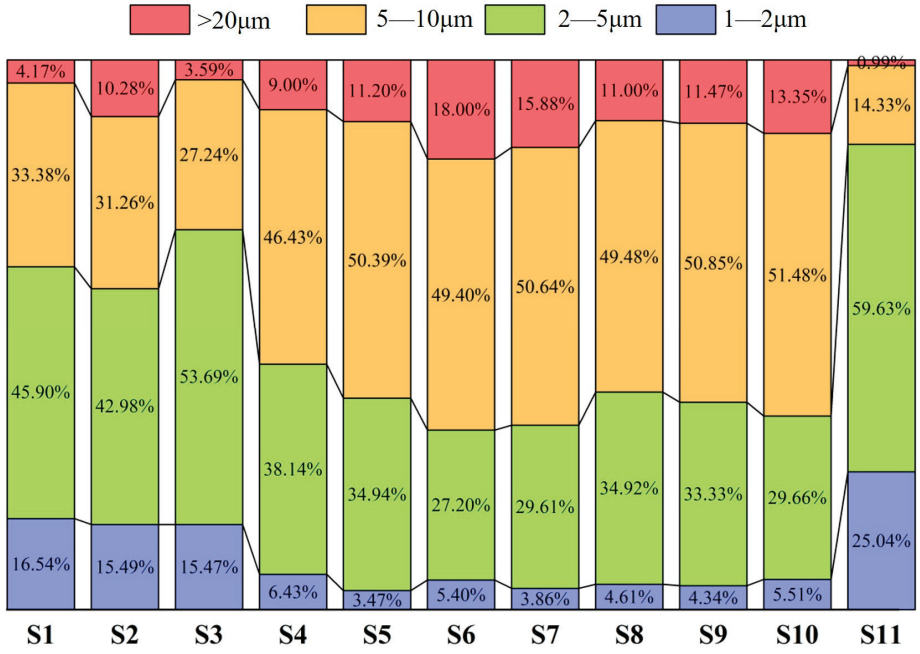

Figure 10. Size distribution of TiN inclusions at quarter-thickness position of slab.

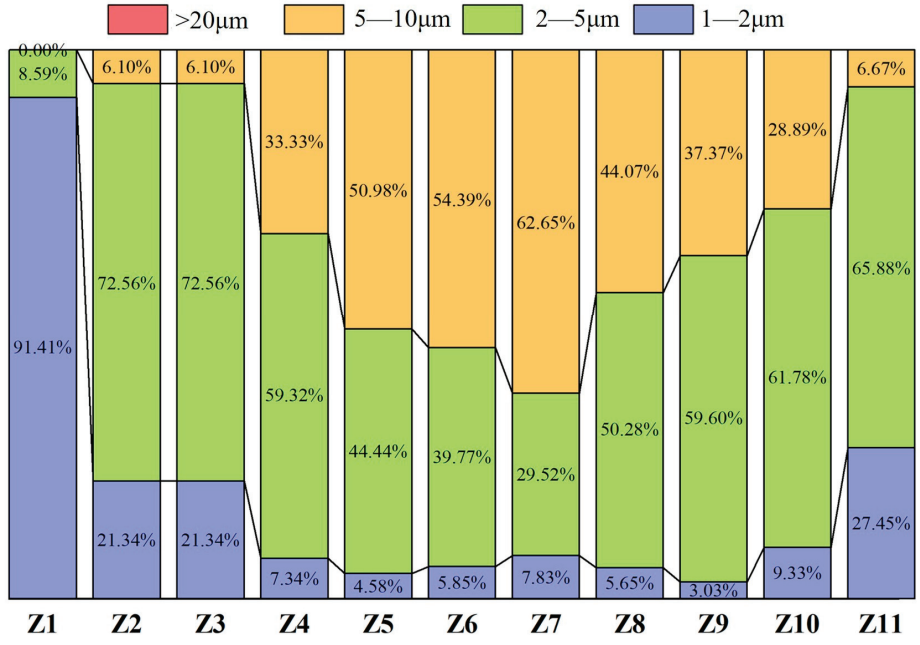

Figure 11. Size distribution of TiN inclusions at slab center.

A study by Que et al. [30]. demonstrated that in microalloyed steel containing 0.12% Ti, TiN inclusions were predominantly concentrated in the 0–2 μm and 2–4 μm size ranges, accounting for 33% and 20% of the total population, respectively. In contrast, larger TiN inclusions (6–8 μm and 8–10 μm) showed significantly lower proportions, each constituting less than 10%. The TiN distribution in Figures 10 and 11 is predominantly concentrated in the 2–10 μm range. This discrepancy with Que et al.'s results can be partially attributed to the higher Ti content (0.4% vs. 0.12%) in our high-titanium steel, which promoted earlier TiN precipitation and consequently led to larger inclusion sizes.

As shown in Figure 10, at the quarter-thickness position, 1–2 μm TiN inclusions accounted for a relatively high proportion near the edge, reaching 16.54% (S1) and 25.04% (S11). This is because the cooling rate near the edge was higher than that in the interior, leading to the precipitation of smaller TiN inclusions. This faster solidification limited the growth time, resulting in a higher proportion of fine TiN inclusions compared to that in the interior. In the inner samples, the proportion of 1–2 μm inclusions decreased to around 5%, with the lowest values observed in S5 (3.47%) and S7 (3.86%). For 2–5 μm TiN inclusions, the distribution trend was similar—the proportion was higher in edge samples, reaching 45.90% (S1) and 59.63% (S11). In the inner samples, the proportion decreased to approximately 35%, with the lowest values observed in S6 (27.20%) and S7 (29.61%). The distribution of 5–10 μm TiN inclusions followed an inverted "V" pattern, with a lower proportion near the edge (33.38% in S1 and 14.33% in S11) and a gradual increase toward the interior, reaching around 50%. Among the six samples from S5 to S10, the proportion of TiN inclusions with sizes ranging from 2 to 5 μm reached its maximum value, at approximately 50%. Additionally, a certain proportion of large TiN inclusions (>10 μm) were present at the quarter-thickness position. These large inclusions were formed by the aggregation of single-phase TiN particles. Their distribution trend was similar to that of 5–10 μm inclusions—the proportion was lowest near the edge (0.99% in S11) and increased toward the interior, reaching a maximum of 18%.

As shown in Figure 11, at the center position of the slab, the proportion of 1–2 μm TiN inclusions was relatively high in the edge samples, reaching 91.41% (Z1) and 27.45% (Z11). During the continuous casting process, water accumulation on the inner arc side resulted in asymmetric cooling intensity between the inner and outer arcs. The Z1 position located on the inner arc side experienced faster cooling rates, which promoted the precipitation of fine inclusions. This phenomenon may explain the anomalous abundance of small-sized (1–2 μm) TiN inclusions observed at the Z1 location. In the interior samples, the proportion of 1–2 μm inclusions exhibited a continuous decline, reaching its minimum value of 3.03% at Z9, similarly to the distribution observed at the quarter-thickness position. For 2–5 μm inclusions, the distribution exhibited a distinct "V" shape. Except for Z1, this size range dominated in the edge samples, accounting for 72.56% (Z2, Z3) and 65.88% (Z11). Toward the interior, the proportion gradually decreased, reaching a minimum of 29.52% (Z7) at the center. In contrast, 5–10 μm inclusions showed a reverse trend—they accounted for only 6.67% (Z11) at the edge but increased in concentration significantly in the interior, peaking at 62.65% (Z7) at the center.

Statistical analysis and comparison of the total size distribution of TiN inclusions were conducted for both the quarter-thickness position and center position of the slab. Through statistical analysis of the total TiN inclusions at both the slab center and quarter-thickness positions, along with the quantity of TiN inclusions within each size range, the proportional distribution of differently sized TiN inclusions at these two locations was determined. The size distributions of TiN inclusions at these two locations showed similar characteristics. As shown in Figure 12, inclusions in the 2–5 μm range accounted for the highest proportion, representing 42.25% of the inclusions at the quarter-thickness position

and 48.16% at the center position. The second most prevalent size range was 5–10 μm, constituting 27.04% at the quarter-thickness position and 28.43% at the center. Inclusions measuring 1–2 μm represented 20.78% and 23.33% of the inclusions at the quarter-thickness and center positions, respectively. Notably, the quarter-thickness position contained an additional 9.91% of TiN inclusions larger than 10 μm, while no such large inclusions were observed at the slab center.

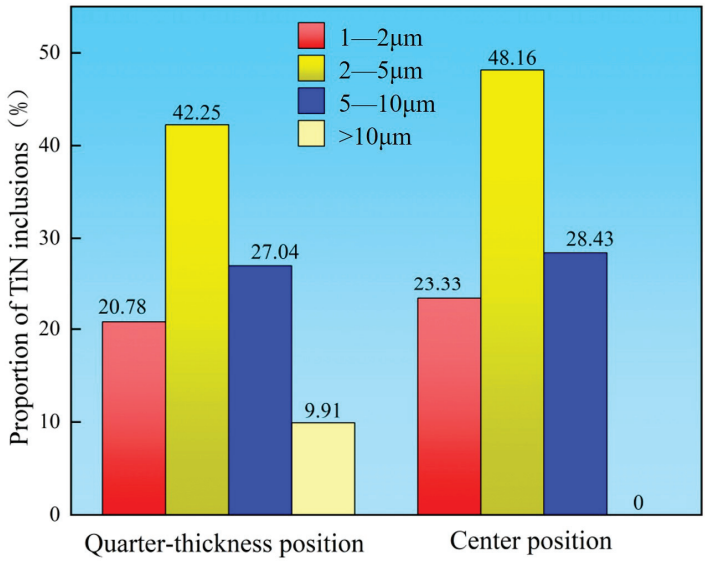

Figure 12. Size distribution of TiN inclusions.

Figure 13 presents the average sizes of TiN inclusions across different sampling positions at both locations. With the exception of edge samples at the center position, which showed smaller average sizes, inclusion dimensions at all other sampling positions generally ranged between 3 and 7 μm. Both locations exhibited an inverted "V" distribution pattern of average inclusion sizes: as sampling positions progressed from the edge toward the interior, the average size gradually increased, reaching maximum values of 7.09 μm (quarter-thickness position) and 5.78 μm (center position), respectively. Notably, the average inclusion sizes at the quarter-thickness position consistently exceeded those at the center position throughout all comparable sampling locations.

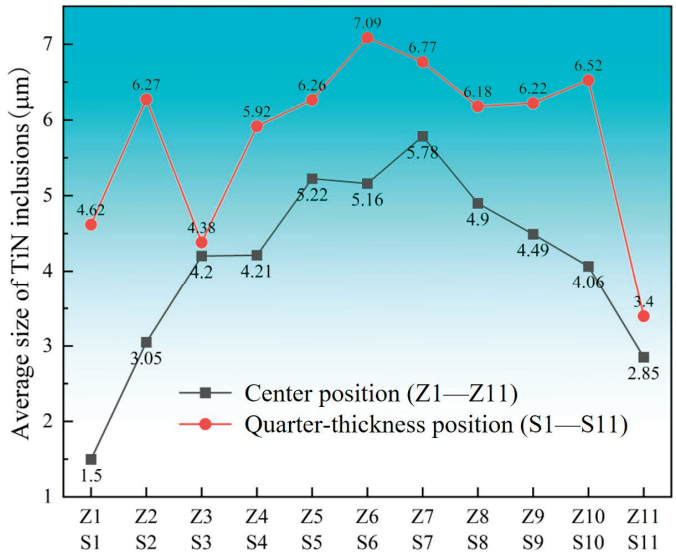

Figure 13. Average size of TiN inclusions at slab position and quarter-thickness position.

3.3. Number Density of TiN Inclusions

The number density of TiN inclusions in each sample in the quarter-thickness position and center position of the slab was statistically analyzed based on the count of TiN-containing inclusions within the scanned sample area and the scanning area size. As for Figure 14, a color-gradient map was generated to visualize the number density of TiN inclusions, where the color scale ranges from purple to red, indicating increasing number density (purple represents a low number density and red represents a high number density); the lowest number density is 12%, and the highest number density is 42%. Comparative analysis of the color patterns reveals distinct differences in TiN distribution between the quarter-thickness position and center position. The number density of TiN inclusions at the quarter-thickness position of the slab is generally higher than that at the center of the slab. The number density of TiN inclusions shows a consistent variation trend at both locations, with higher values observed in the edge samples and a gradual decrease observed in the interior samples. The most central sample exhibits the lowest number density of TiN inclusions. At the quarter-thickness position of the slab, the edge samples exhibited the highest TiN inclusion number densities of 40.05 mm^{-2} (S1) and 40.3 mm^{-2} (S11), while the lowest recorded density was 34.2 mm^{-2} (S7). At the center position of the slab, the edge samples showed the highest TiN inclusion number density, with samples Z1 and Z2 measuring 34.5 mm^{-2} and 41.3 mm^{-2}, respectively. The corresponding opposite specimens (Z10 and Z11) exhibited significantly lower inclusion densities of 24.2 mm^{-2} and 27.0 mm^{-2}, respectively, compared to Z1 and Z2. Notably, the three interior specimens (Z6–Z8) showed the lowest TiN inclusion densities, measuring 16.8 mm^{-2} (Z6), 15.8 mm^{-2} (Z7), and 13.4 mm^{-2} (Z8), respectively. Based on the statistical results, the number density of TiN inclusions at the quarter-thickness position of the slab was higher than that at the center position, indicating the presence of a greater quantity of TiN inclusions at the quarter-thickness location. The number density at the edge region was higher than that in the interior. This phenomenon may be attributed to the fact that the central region experienced the final solidification stage with a reduced temperature gradient, leading to a decreased nucleation driving force for TiN inclusions. Therefore, the number density of TiN inclusions gradually decreased from the slab edge to the interior.

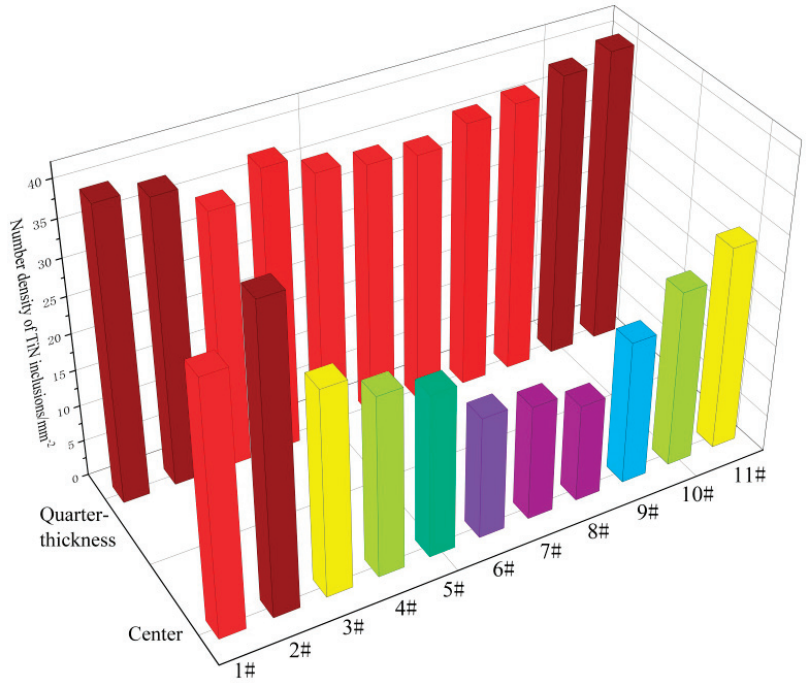

Figure 14. Variation in TiN inclusion content.

Both Que and Duan quantitatively analyzed the variations in TiN inclusion number density within Ti-microalloyed steel and Ti-stabilized ultra-pure ferritic stainless steel slabs [29,30], respectively. Their findings align with our experimental results, demonstrating a gradual decrease in inclusion number density from the surface layer to the interior region. This phenomenon is attributed to the fact that the slab surface had the fastest cooling rate and shortest solidification time.

3.4. Calculation of TiN Inclusion Precipitation

3.4.1. TiN Precipitation Temperature

The standard Gibbs free energy (ΔG^{θ}) for TiN precipitation is calculated as follows [29]:

$$[\mathrm{Ti}] + [\mathrm{N}] = \mathrm{TiN(s)} \tag{1}$$

$$\Delta G^{\theta} = -314800 + 114.35 \cdot T \tag{2}$$

$$\Delta G = \Delta G^{\theta} + RT\ln K \tag{3}$$

$$K = \frac{a_{TiN}}{a_{[N]} \cdot a_{[Ti]}} = \frac{a_{TiN}}{(f_{[N]} \cdot w_{[N]}) \cdot (f_{[Ti]} \cdot w_{[Ti]})} \tag{4}$$

In Equation (4), a denotes the activities of products and reactants, and w denotes the content of each element, with $w_{[Ti]}$ and $w_{[N]}$ being 0.4% and 0.002%, respectively. f is the activity coefficient; the activity coefficient f of each element in molten steel can be expressed in terms of the interaction coefficients, e, and the elemental content, w, as shown in Equation (5):

$$\lg f_i = \sum_{j=1}^{n} e_i^j \cdot w_{[j]} \tag{5}$$

By substituting the elemental contents from Table 1 and the interaction coefficients from Table 2 into Equation (5), the activities of nitrogen ($a_{[N]}$) and titanium ($a_{[Ti]}$), respectively, in the system were obtained To simplify the calculation, the activity of TiN (a_{TiN}) was set as 1, while the activity coefficients and contents of Ti and N were incorporated into Equation (4). When $\Delta G = 0$ in Equation (3), the calculated precipitation temperature of TiN was determined to be 1829.1 K (1556 °C).

Table 2. Interaction coefficients of elements at 1600 °C [38–40].

I	e_i^C	e_i^{Si}	e_i^P	e_i^S	e_i^{Al}	e_i^N	e_i^{Mn}	e_i^{Ti}
Ti	−0.165	0.05	−0.11	−0.006	0.035	−1.8	0.0043	0.013
N	0.13	0.047	0.045	0.007	−0.028	0	−0.02	−0.53
C	0.14	0.008	0.051	0.046	0.043	0.11	−0.012	
S	0.11	0.01	0.029	−0.028	0.035	0.01	−0.026	−0.072

The calculation formulas for the liquidus and solidus temperatures are given by Equations (6) and (7), respectively:

$$T_L = 1536 - 65w_{[C]} - 30w_{[P]} - 25w_{[S]} - 20w_{[Ti]} - 8w_{[Si]} - 5w_{[Mn]} - 2.7w_{[Al]} - 90w_{[N]} - 2w_{[Mo]} \tag{6}$$

$$T_S = 1538 - 175w_{[C]} - 280w_{[P]} - 575w_{[S]} - 40w_{[Ti]} - 20w_{[Si]} - 30w_{[Mn]} - 7.5w_{[Al]} - 5w_{[Mo]} \tag{7}$$

Substituting the elemental content of high-titanium steel into Equations (6) and (7), the liquidus temperature that can be obtained is 1431.37 °C (1704.5 K) and the solidus temperature is 1506.12 °C (1779.2 K). The precipitation temperature of TiN is higher than the liquidus temperature, indicating that in a high-titanium steel system with 0.4% Ti and 0.004% N, TiN inclusions begin to precipitate in the liquid phase. Assuming the liquidus

temperature remains constant at 1779.2 K and the nitrogen content in the molten steel is unchanged, the critical titanium content for TiN precipitation at the liquidus temperature is approximately 0.17%. Only when the Ti content is below 0.17% will TiN precipitate in the two-phase region. Similarly, assuming the solidus temperature remains at 1704.5 K with a constant nitrogen content, the critical titanium content for TiN precipitation at the solidus temperature is about 0.08%, and TiN will only precipitate in the solid-phase region when the Ti content falls below 0.08%. Comparing the critical Ti contents at different precipitation temperatures reveals that the precipitation temperature of TiN increases with a higher Ti content in the system. This demonstrates that increasing Ti content promotes earlier TiN precipitation, while reducing Ti content delays its formation.

During the solidification of molten steel, the segregation of solute elements leads to the enrichment of Ti and N in the liquid phase. This results in localized concentration products exceeding the equilibrium threshold required for TiN precipitation, thereby causing premature TiN formation. Consequently, the redistribution of solute elements (Ti and N) between the two phases must be considered. According to the law of mass conservation, the initial solute concentration (C_0) in the steel melt equals the sum of solute contents in both liquid and solid phases.

$$C_0 = f_s \cdot C_s + (1 - f_s) \cdot C_L \tag{8}$$

The solute partition coefficient (K) can be expressed as follows:

$$K = \frac{C_S}{C_L} \tag{9}$$

By substituting the solute partition coefficient K into Equation (8), the relationship between solute content in the liquid phase, C_L, and the solidification parameter, f, is obtained, as shown in Equation (10)

$$C_L = \frac{C_0}{1 + f_s\,(K - 1)} \tag{10}$$

During solidification, the activity product (Q_{TiN}) for TiN precipitation in the two-phase region is expressed as follows:

$$Q_{TiN} = (f_{Ti} \cdot w_{Ti}) \cdot (f_N \cdot w_N) \tag{11}$$

f_{Ti} and f_N represent the activity coefficients of Ti and N, respectively, with the initial contents of $w_{0\,[Ti]}$ = 0.4% and $w_{0[N]}$ = 0.004%. Substituting these parameters into the equation yields the relationship between the actual activity product, Q_{TiN}, and the solid fraction, fs. As shown in Figure 15, the actual activity product for TiN precipitation (Q_{TiN}) already exceeds the equilibrium activity product at the onset of solidification (fs = 0), indicating that TiN begins precipitating in the liquid phase prior to solidification. During solidification, the actual activity product Q_{TiN} continuously increases with progressive solid fraction (fs), persistently remaining above the equilibrium value throughout the process, thereby driving continuous TiN precipitation.

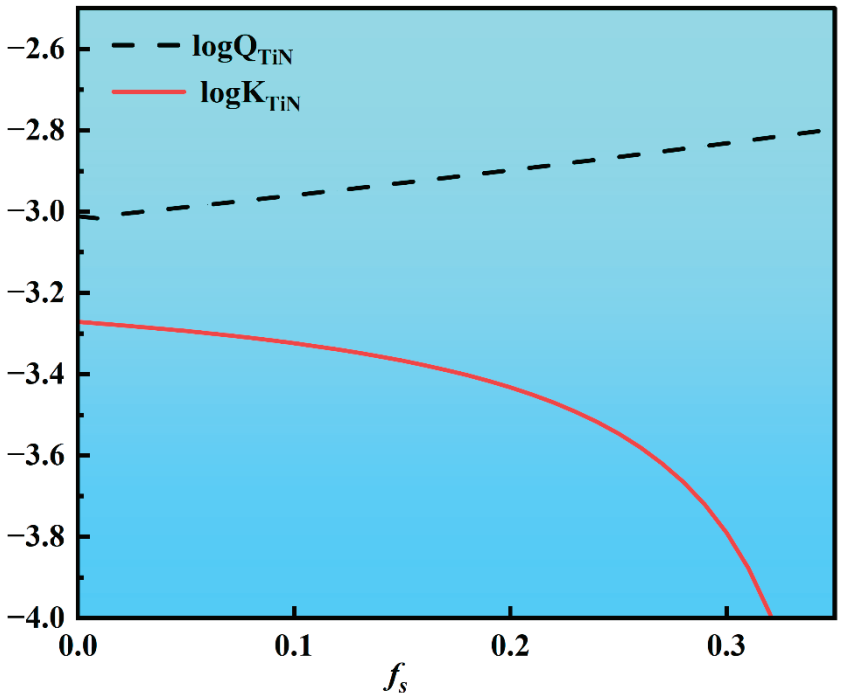

Figure 15. The relationship between the Q_{TiN} and K_{TiN} values of TiN precipitation with varying solid fractions.

3.4.2. Calculation of TiN Inclusion Precipitation Size

The calculation formula for the precipitation radius of TiN inclusions during steel solidification is as follows [13]:

$$r \cdot \frac{dr}{dt} = \frac{M_{TiN} \cdot \rho_{Fe}}{100 M_{Fe} \cdot \rho_{TiN}} \cdot D_N \cdot (w_N - w_{eqN}) \quad (12)$$

r is the precipitation radius of TiN inclusions (in cm); t is solidification time; M_{TiN} is the molar mass of TiN (62 g/mol); M_{Fe} is the molar mass of steel (taken as 56 g/mol, Fe's atomic mass); ρ_{TiN} is the density of TiN inclusions (5.43 g/cm^3); ρ_{Fe} is the density of molten steel (7.07 g/cm^3); D_N is the diffusion coefficient of nitrogen (N) in molten steel; w_N is the mass fraction of N at the solidification front; w_{eqN} is the equilibrium mass fraction of N at the onset of TiN precipitation. By using the following equation, the relationship between the precipitation radius r of TiN inclusions and the cooling rate can be derived.

$$r = \sqrt{\frac{M_{TiN} \cdot \rho_{Fe}}{50 M_{Fe} \cdot \rho_{TiN}} D_N \cdot (w_N - w_{eqN}) \cdot \tau} \quad (13)$$

The calculation formula for the local cooling time, τ, is as follows:

$$\tau = \frac{T_L - T_S}{R_C} \quad (14)$$

The relationships between the precipitation radius, r, of TiN inclusions and the solid fraction, fs, were computed for Rc = 10, 5, 2, 1, and 0.5. The adopted range (0.5–10 K/s) encompasses all probable cooling rates [41–43]. As shown in Figure 16, the results indicate that the precipitation radius of TiN decreases with increasing cooling rate. At the minimum cooling rate of 0.5 K/s, the maximum radius reaches approximately 6 μm, whereas at the maximum rate of 10 K/s, it reduces to only 1.3 μm. When R_C > 2 K/s, the maximum radius remains below 2 μm, with minimal impact from further rate increases. Below 2 K/s, the radius increases significantly as the rate decreases. Therefore, controlling the cooling rate is

an effective approach to refine TiN inclusion sizes when the Ti and N contents in molten steel are fixed.

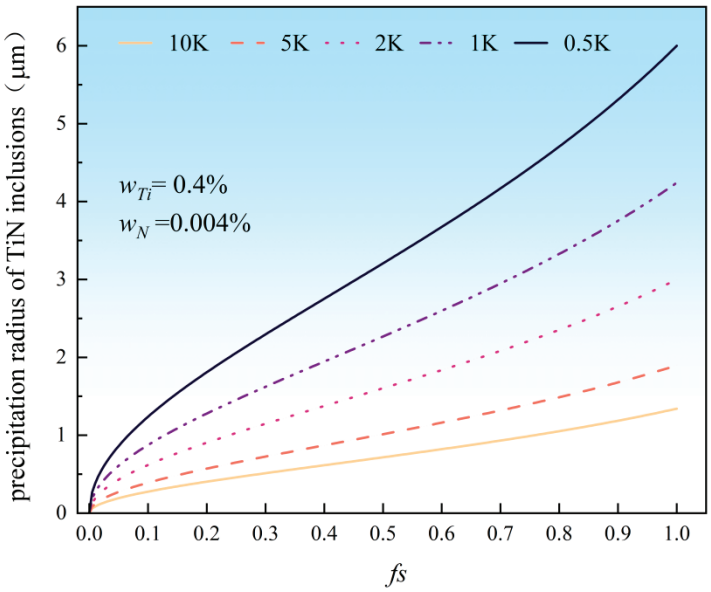

Figure 16. Relationship between TiN precipitation size and solid fraction under different cooling rates.

4. Conclusions

1. The primary inclusions in high-titanium steel consist of TiN, TiS, TiC and their composite forms. At the quarter-thickness position of the slab, inclusions demonstrate distinct size–composition correlations: small-sized inclusions (1–2 μm) are predominantly Ti (C,N) and TiN + TiS; medium-sized inclusions (2–10 μm) and large inclusions (>10 μm) are mainly TiS, TiN and their composite phases. Edge samples show TiN-rich characteristics, whereas interior and central regions exhibit increasing TiS content. The overall pattern reveals increasing TiN content with inclusion size growth. The inclusions in the central region of the slab are predominantly composed of TiN, TiS, and their composite phase TiN + TiS. The inclusion sizes are mainly distributed in the 2–10 μm range, exhibiting a distinct size–composition correlation: larger inclusions (greater than 5 μm) show higher TiN content, while the 2–5 μm TiS-TiN inclusions contain a relatively higher TiS composition. This size-dependent compositional variation demonstrates a progressive enrichment of TiN with increasing inclusion size.
2. At the quarter-thickness position of the slab, TiN inclusions primarily range between 2 and 10 μm, with a small number of larger inclusions exceeding 10 μm. In contrast, at the slab center, TiN inclusions are mainly 1–5 μm in size, with no large-sized TiN inclusions observed. Due to cooling rate effects, samples from the edge regions at both positions exhibit a higher proportion of smaller TiN inclusions, whereas interior samples show a predominance of larger-sized TiN inclusions. Within the interior regions of the steel slab, a substantial proportion of large-sized TiN inclusions persist, which pose significant detrimental effects on material performance. To address this critical issue, process optimization strategies such as enhanced cooling rates or reduced titanium content must be implemented to effectively suppress the formation of these deleterious large-scale TiN precipitates.
3. The number density of TiN inclusions at the center position of the slab is significantly lower than that at the quarter-thickness position. At both the quarter-thickness and center positions of the slab, the number density of TiN inclusions exhibits a gradual decrease from the edge to the interior regions in the samples. At the quarter-thickness

of the slab, the highest number density is 40.3 mm^{-2} and the lowest number density is 34.2 mm^{-2}. At the center of the slab, the highest number density is 41.3 mm^{-2} and the lowest number density is 13.4 mm^{-2}.

4. The calculation results demonstrate that in high-titanium steel containing 0.4% Ti, TiN inclusions begin to precipitate in the liquid phase; reducing the titanium content in the steel can effectively delay the precipitation of TiN. During solidification, TiN continuously precipitates with progressive size increases as solidification proceeds. Notably, the size of TiN inclusions decreases with increasing cooling rates. When the cooling rate is 0.5 K/s, the maximum size of TiN inclusions reaches 6 μm, whereas at a higher cooling rate of 10 K/s, the maximum size decreases significantly to 1.3 μm.

Author Contributions: Writing—original draft preparation, M.Z.; data curation, X.L.; formal analysis and software, Z.G.; Conceptualization, Y.S. All authors have read and agreed to the published version of the manuscript.

Funding: This work was supported by the Fundamental Research Funds for the Central Universities (grant number FRF-BD-23-02).

Institutional Review Board Statement: Not applicable.

Informed Consent Statement: Not applicable.

Data Availability Statement: The original contributions presented in this study are included in the article. Further inquiries can be directed to the corresponding author.

Conflicts of Interest: The authors declare no conflict of interest.

References

1. Mao, X.P.; Huo, X.D.; Sun, X.J.; Chai, Z. Strengthening mechanisms of a new 700 MPa hot rolled Ti-microalloyed steel produced by compact strip production. *J. Mater. Process. Technol.* **2010**, *210*, 1660–1666. [CrossRef]
2. Yin, X.; Sun, Y.H.; Yang, Y.D.; Bai, X.F.; Barati, M.; Mclean, A. Formation of inclusions in Ti-stabilized 17Cr austenitic stainless steel. *Metall. Mater. Trans. B* **2016**, *47*, 3274–3284. [CrossRef]
3. Zaitsev, A.I.; Baklanova, O.N.; Koldaev, A.V.; Grishin, A.V.; Rodionova, I.G.; Yashchuk, S.V.; Lyasotskii, I.V. Microstructure and property formation for high-strength low-carbon steels microalloyed with titanium and molybdenum. *Metallurgist* **2016**, *60*, 491–498. [CrossRef]
4. Xu, G.; Gan, X.L.; Ma, G.J.; Luo, F.; Zou, H. The development of Ti-alloyed high strength microalloy steel. *Mater. Des.* **2010**, *31*, 2891–2896. [CrossRef]
5. Kang, Y.; Mao, W.M.; Chen, Y.J.; Jing, J.; Cheng, M. Effect of Ti content on grain size and mechanical properties of UNS S44100 ferritic stainless steel. *Mater. Sci. Eng. A* **2016**, *677*, 211–221. [CrossRef]
6. Peng, Z.W.; Li, L.J.; Gao, J.X.; Huo, X.D. Precipitation strengthening of titanium microalloyed high-strength steel plates with isothermal treatment. *Mater. Sci. Eng. A* **2016**, *657*, 413–421. [CrossRef]
7. Medina, S.F.; Chapa, M.; Valles, P.; Quispe, A.; Vega, M.I. Influence of Ti and N contents on austenite grain control and precipitate size in structural steels. *ISIJ Int.* **1999**, *39*, 930–936. [CrossRef]
8. Gunduz, S.; Erden, M.A.; Karabulut, H.; Turkmen, M. The effect of Vanadium and Titanium on mechanical properties of microalloyed PM steel. *Powder Metall. Met. Ceram.* **2016**, *55*, 277–287. [CrossRef]
9. Park, J.H. Effect of inclusions on the solidification structures of ferritic stainless steel: Computational and experimental study of inclusion evolution. *Calphad* **2011**, *35*, 455–462. [CrossRef]
10. Chen, S.J.; Li, L.J.; Peng, Z.W.; Huo, X.D.; Sun, H.B. On the correlation among continuous cooling transformations, interphase precipitation and strengthening mechanism in Ti-microalloyed steel. *J. Mater. Res. Technol.* **2021**, *10*, 580–593. [CrossRef]
11. Shang, T.R.; Wang, W.L.; Kang, J.B.; Luo, S.; Zhu, M.Y. Precipitation behavior of TiN in solidification of 20CrMnTi under continuous casting conditions. *J. Mater. Res. Technol.* **2023**, *24*, 3608–3627. [CrossRef]
12. Fu, J.W.; Qiu, W.X.; Nie, Q.Q.; Wu, Y.C. Precipitation of TiN during solidification of AISI 439 stainless steel. *J. Alloys Compd.* **2017**, *699*, 938–946. [CrossRef]
13. Gui, L.T.; Long, M.J.; Zhang, H.D.; Chen, D.F.; Liu, S.; Wang, Q.Z.; Duan, H.M. Study on the precipitation and coarsening of TiN inclusions in Ti-microalloyed steel by a modified coupling model. *J. Mater. Res. Technol.* **2020**, *9*, 5499–5514. [CrossRef]

14. Nagata, M.T.; Speer, J.G.; Matlock, D.K. Titanium nitride precipitation behavior in thin-slab cast high-strength low-alloy steels. *Metall. Mater. Trans. A* **2002**, *33*, 3099–3110. [CrossRef]
15. Kim, Y.W.; Song, S.W.; Seo, S.J.; Hong, S.G.; Lee, C.S. Development of Ti and Mo micro-alloyed hot-rolled high strength sheet steel by controlling thermomechanical controlled processing schedule. *Mater. Sci. Eng. A* **2013**, *565*, 430–438. [CrossRef]
16. Shu, Q.F.; Visuri, V.V.; Alatarvas, T.; Fabritius, T. Model for inclusion precipitation kinetics during solidification of steel applications in MnS and TiN inclusions. *Metall. Mater. Trans. B* **2020**, *51*, 2905–2916. [CrossRef]
17. Michelic, S.K.; Loder, D.; Reip, T.; Ardehali Barani, A.; Bernhard, C. Characterization of TiN, TiC and Ti(C,N) in titanium-alloyed ferritic chromium steels focusing on the significance of different particle morphologies. *Mater. Charact.* **2015**, *100*, 61–67. [CrossRef]
18. Yang, J.; Wang, X.H.; Gong, Z.X.; Jiang, M.; Wang, G.C.; Huang, F.X. Precipitation thermodynamics analysis and control of titanium nitride inclusions in extra-low oxygen wheel steel. *Chin. J. Eng.* **2010**, *32*, 1138–1143.
19. Yan, W.; Shan, Y.Y.; Yang, K. Influence of TiN inclusions on the cleavage fracture behavior of low-carbon microalloyed steels. *Metall. Mater. Trans. A* **2007**, *38*, 1211–1222. [CrossRef]
20. Fu, J.C.; Zhu, J.; Di, L.; Tong, F.S.; Liu, D.L.; Wang, Y.L. Study on the precipitation behavior of TiN in the microalloyed steels. *Acta Metall. Sin.* **2000**, *36*, 801.
21. Liu, H.Y.; Wang, H.L.; Zheng, J.Q.; Li, H.Y.; Zheng, X.Y. Investigation of Ti inclusions in wire cord steel. *Ironmak. Steelmak.* **2011**, *38*, 53–58. [CrossRef]
22. Du, J.; Strangwood, M.; Davis, C.L. Effect of TiN particles and grain size on the charpy impact transition temperature in steels. *J. Mater. Sci. Technol.* **2012**, *28*, 878–888. [CrossRef]
23. Capurro, C.; Cicutti, C. Analysis of titanium nitrides precipitated during medium carbon steels solidification. *J. Mater. Sci. Technol.* **2018**, *7*, 342–349. [CrossRef]
24. Jin, Y.L.; Du, S.L. Precipitation behaviour and control of TiN inclusions in rail steels. *Ironmak. Steelmak.* **2016**, *45*, 224–229. [CrossRef]
25. Ma, W.J.; Bao, Y.P.; Zhao, L.H.; Wang, M. Control of the precipitation of TiN inclusions in gear steels. *Int. J. Miner. Metall. Mater.* **2014**, *21*, 234–239. [CrossRef]
26. Yan, W.; Shan, Y.Y.; Yang, K. Effect of TiN inclusions on the impact toughness of low-carbon microalloyed steels. *Metall. Mater. Trans. A* **2006**, *37*, 2147–2158. [CrossRef]
27. Tian, Q.R.; Wang, G.C.; Zhao, Y.; Li, J.; Wang, Q. Precipitation behaviors of TiN inclusion in GCr15 bearing steel billet. *Metall. Mater. Trans. B* **2018**, *49*, 1149–1164. [CrossRef]
28. Liu, D.M.; Song, S.Q.; Xue, Z.L.; Zietsman, J.; Qi, J.H.; Deng, Z.X. Formation of TiN Inclusions During Solidification of Titanium Micro-Alloyed Steel: Modeling With ChemAppPy. *Metall. Mater. Trans. B* **2023**, *54*, 382–394. [CrossRef]
29. Duan, H.j.; Zhang, Y.; Ren, Y.; Zhang, L.F. Distribution of TiN inclusions in Ti-stabilized ultra-pure ferrite stainless steel slab. *J. Iron Steel Res. Int.* **2019**, *26*, 962–972. [CrossRef]
30. Que, G.R.; Song, S.Q.; Nyembwe, A.; Xue, Z.L.; Qi, J.H.; Deng, Z.X. TiN inclusions distribution in the composite cross section of Titanium Micro-alloyed Steel slab: Thermo-chemical modeling and automatic statistic analysis. *J. Mater. Res. Technol.* **2023**, *26*, 5383–5392. [CrossRef]
31. Wang, B.; Xing, L.D.; Li, X.; Bao, Y.P.; Wang, M. Study on Inclusions Distribution Across the Thickness of Enameled Steel Slabs. *Metall. Mater. Trans. B* **2024**, *55*, 4432–4445. [CrossRef]
32. Gao, S.; Wang, M.; Guo, J.L.; Wang, H.; Zhi, J.G.; Bao, Y.P. Extraction, Distribution, and Precipitation Mechanism of TiN–MnS Complex Inclusions in Al-Killed Titanium Alloyed Interstitial Free Steel. *Met. Mater. Int.* **2021**, *27*, 1306–1314. [CrossRef]
33. Wang, H.; Qu, T.Q.; Liang, T.; Li, X.L.; Wang, D.Y.; Fan, L.; Zhang, Z.X.; Yang, Z.H. A new mathematical model for investigating solidification, solute transportation, and TiN precipitation in a micro-alloy steel containing Ti. *China Foundry* **2025**, *22*, 333–344. [CrossRef]
34. Choi, W.; Matsuura, H.; Tsukihashi, F. Effect of Non-metallic Inclusions in Fe-Al-Ti-O-N-S Alloy on Grain Size. *Metall. Mater. Trans. B* **2016**, *47*, 1851–1857. [CrossRef]
35. Li, M.; Matsuura, H.; Tsukihashi, F. Evolution of TiS and TiN in Fe-40 MassPctNi Austenitic Alloy During Heating at 1273 K (1000 °C). *Metall. Mater. Trans. B* **2019**, *50*, 2993–3001. [CrossRef]
36. Jin, P.; Shang, D.; Wang, G.; Xiao, Y.; Cao, L. Precipitation of TiS in Al–Ti Simultaneously Deoxidized Steel. *Steel Res. Int.* **2021**, *92*, 2000614. [CrossRef]
37. Shimahashi, M.; Muto, I.; Sugawara, Y.; Hara, N. The Role of Oxide Films on TiS and $Ti_4C_2S_2$ Inclusions in the Pitting Corrosion Resistance of Stainless Steels. *J. Electrochem. Soc.* **2013**, *160*, 262. [CrossRef]
38. Ozturk, B.; Matway, R.; Fruehan, R.J. Thermodynamics of inclusion formation in Fe-Cr-Ti-N alloys. *Metall. Mater. Trans. B* **1995**, *26*, 563–567. [CrossRef]
39. PAK, J.J.; Jeong, Y.S.; Hong, I.K.; Cha, W.Y.; Kim, D.S.; Lee, Y.Y. Thermodynamics of TiN Formation in Fe-Cr Melts. *ISIJ Int.* **2005**, *4*, 1106–1111. [CrossRef]

40. Cao, J.Q.; Li, Y.; Lin, W.M.; Che, J.L.; Zhou, F.; Tan, Y.F.; Li, D.L.; Dang, J.; Chen, C. Assessment of Inclusion Removal Ability in Refining Slags Containing Ce_2O_3. *Crystals* **2023**, *13*, 202. [CrossRef]
41. Wang, Y.; Chen, C.; Ren, R.J.; Xue, Z.X.; Wang, H.Z.; Zhang, Y.Z.; Wang, J.X.; Wang, J.; Chen, L.; Mu, W.Z. Ferrite formation and decomposition in 316H austenitic stainless steel electro slag remelting ingot for nuclear power applications. *Mater. Charact.* **2024**, *218*, 114581. [CrossRef]
42. Wang, Y.; Chen, C.; Yang, X.Y.; Zhang, Z.R.; Wang, J.; Li, Z.; Chen, L.; Mu, W.Z. Solidification modes and delta-ferrite of two types 316L stainless steels: A combination of as-cast microstructure and HT-CLSM research. *J. Iron Steel Res. Int.* **2025**, *32*, 426–436. [CrossRef]
43. Chen, L.; Wang, Y.; Li, Y.; Zhang, Z.; Xue, Z.; Ban, X.; Hu, C.; Li, H.; Tian, J.; Mu, W. Effect of Nickel Content and Cooling Rate on the Microstructure of as Cast 316 Stainless Steels. *Crystals* **2025**, *15*, 168. [CrossRef]

materials

MDPI

Article

The Influence of Heat Treatment Process on the Residual Ferrite in 304L Austenitic Stainless Steel Continuous Casting Slab

Zhixuan Xue [1], Kun Yang [2], Yafeng Li [3], Chaochao Pei [1], Dongzhi Hou [1], Qi Zhao [1], Yang Wang [1], Lei Chen [2], Chao Chen [1,*] and Wangzhong Mu [4,*]

[1] College of Materials Science and Engineering, Taiyuan University of Technology, Taiyuan 030024, China; 2024510282@link.tyut.edu.cn (Z.X.); 2024520357@link.tyut.edu.cn (C.P.); 2023000825@link.tyut.edu.cn (D.H.); zhaoqi0825@link.tyut.edu.cn (Q.Z.); wangyang0291@link.tyut.edu.cn (Y.W.)
[2] College of Mechanical Engineering, Taiyuan University of Technology, Taiyuan 030024, China; yangkun@tyut.edu.cn (K.Y.); chenlei839@163.com (L.C.)
[3] Xinzhou Comprehensive Inspection and Testing Center, Xinzhou 034000, China; 18003545064@163.com
[4] Department of Materials Science and Engineering, KTH Royal Institute of Technology, SE-100 44 Stockholm, Sweden
* Correspondence: chenchao@tyut.edu.cn (C.C.); wmu@kth.se (W.M.)

Abstract

This study investigates the distribution characteristics of residual ferrite in 304L austenitic stainless steel continuous casting slab and the impact of heat treatment processes on its content. Through optical microscopy (OM), thermodynamic calculation software (Thermo–Calc) and heat treatment experiments, it is found that the residual ferrite content along the thickness direction at the width center of the slab exhibits an "M"-shaped distribution—lowest at the edges (approximately 3%) and highest near the center (approximately 13%). Within the triangular zone of the slab, the residual ferrite content varies between 1.8% and 12.2%, with its average along the thickness direction also showing an "M"-shaped distribution; along the width direction, the average residual ferrite content is lower at the edge positions, while within the internal triangular zone, it ranges between 8% and 10%. The ferrite morphology changes significantly across solidification zones: elongated in the surface fine-grain zone, lath-like and skeletal in the columnar grain zone and network-like in the central equiaxed grain zone. Thermodynamic calculations indicate that the solidification mode of the 304L continuous casting slab follows the FA mode. Heat treatment experiments conducted across the entire slab thickness demonstrate effective reduction in residual ferrite content; the optimal reduction is achieved at 1250 °C with a 48 min hold followed by air cooling while preserving the original "M"-shaped distribution characteristic after treatment. Increasing the heat treatment temperature, prolonging the holding time and reducing the cooling rate all contribute to reducing residual ferrite content.

Keywords: 304L austenitic stainless steel; continuous casting slab; residual ferrite; thermodynamic calculations; heat treatment experiment

1. Introduction

As a typical grade of high-alloy steel, stainless steel exhibits excellent corrosion resistance and heat resistance, making it widely applicable in industrial fields and daily life [1–6]. Due to its outstanding corrosion resistance and mechanical properties, 304L austenitic stainless steel is commonly used in engineering sectors, such as petrochemicals, rail vehicles and aerospace [7–9]. The microstructure of austenitic stainless steel

produced via continuous casting typically features a ferrite–austenite duplex structure. The morphology and content of ferrite in the surface solidified structure of the cast slab can induce edge cracking during hot rolling [10–13]. Statistical evidence indicates that the presence of excessive ferrite (usually above 10%) adversely affects the corrosion resistance of cast slab [14–16]. When the ferrite content in 304L austenitic stainless steel is low, it essentially becomes a fully austenitic phase. This not only provides corrosion resistance but also ensures non-magnetic properties. Consequently, it is widely used in fields requiring non-magnetic interference, such as nuclear power, medical devices and mobile phone casings. The presence of the ferrite phase limits the application of 304L austenitic stainless steel [17,18]. Therefore, controlling the ferrite content in the continuous casting slab of 304L austenitic stainless steel is crucial [19–24].

In the conventional continuous casting process, where cooling is achieved through surface spray water cooling, the heat flow within the slab cross-section transfers unidirectionally along the thickness direction. This results in non-uniform cooling rate distribution across the slab thickness, leading to variations in ferrite content along this direction. The inhomogeneous distribution of residual ferrite across different regions of the slab will confer anisotropic mechanical properties and the formation of corrosion-susceptible zones (where ferrite-enriched areas are prone to selective corrosion). Therefore, research on ferrite distribution in different slab regions is critically important [25–29]. Numerous researchers have investigated ferrite content along the thickness direction in austenitic stainless steels. As early as 1984, Lindenberg et al. [30] first reported the inhomogeneous distribution of ferrite in stainless steel cast slab. Wolf et al. [31] found irregular ferrite distribution in 304 stainless steel slab. In 1995, Kim et al. [32] observed that ferrite content in 304 austenitic stainless steel slab exhibited an "M"-shaped distribution along the thickness direction: approximately 4% at the surface, reaching a maximum of 9% at 95 mm from the surface and decreasing to 6% at the slab center. Moreira dos Santos et al. [33] studied the formation and evolution of δ-ferrite during the hot processing of an 80-ton industrial AISI 304 austenitic stainless steel slab. Their research confirmed the "M"-shaped distribution of ferrite content along the thickness direction. After two subsequent hot rolling processes and one solution heat treatment, the average δ-ferrite content decreased following each treatment. Huang et al. [34,35] studied the δ-ferrite distribution in a billet and continuous cast strip. They found an "M"-shaped distribution of ferrite content along the thickness direction of the billet and a "W"-shaped distribution of ferrite content in the strip.

In summary, extensive research has demonstrated that ferrite content in 304 austenitic stainless steel cast slab follows an "M"-shaped distribution along the thickness direction. This pattern primarily arises from variations in composition, cooling rates and solidification modes across the slab cross-section. However, existing studies have predominantly focused on ferrite distribution at the width center of the slab, with limited research on ferrite content distribution at other positions. Chen and Cheng [36] investigated ferrite distribution at different positions across the cross-section of Fe-Cr-Mn stainless steel cast slab. They also observed an "M"-shaped distribution of ferrite content along the thickness direction in 304 stainless steel slab. Only Spacarotella et al. [37] examined the distribution of ferrite along the thickness direction at various positions across the entire cross-section of a 304 stainless steel slab, similarly identifying the characteristic "M"-shaped pattern.

Currently, heat treatment methods can be employed to regulate the ferrite content in austenitic stainless steel cast slab. Most researchers have focused on the changes in ferrite content under different heat treatment regimes. Nhung et al. [38] investigated the influence of temperature on δ-ferrite content in austenitic stainless steel welds. Specimens were held at 400 °C, 600 °C and 900 °C for 10 h. The study revealed that δ-ferrite content gradually decreased with increasing temperature, dropping from 23.5% in the as-welded state to

22% after holding at 400 °C for 10 h and further reducing to 11% after holding at 900 °C for 10 h. Kim et al. [39] explored the dissolution kinetics of δ-ferrite in 304 stainless steel strip specimens by varying annealing times within the temperature range of 1050–1200 °C. They found that δ-ferrite could generally be eliminated through prolonged homogenization heat treatment within this temperature range. Fukumoto et al. [40] studied the dissolution behavior of δ-ferrite in SUS304 continuous cast slab within the heat treatment temperature range of 1100–1200 °C. Specimens were heated for 20–120 min followed by water cooling. The results indicated that the δ-ferrite dissolution rate increased with rising temperature within the 1100–1200 °C range. Microstructural analysis showed a decreasing trend in δ-ferrite quantity, with its morphology transforming from vermicular to rod-shaped and spherical. Aghebatkheiri et al. [41] investigated the dissolution kinetics of δ-ferrite during homogenization of AISI 304 austenitic stainless steel. The study covered a temperature range of 1050–1250 °C and time spans of 1–12 h, with hourly sampling. The results demonstrated that δ-ferrite content decreased with increasing annealing temperature and time. Zargar et al. [42] used Thermo-Calc software to predict the "M"-shaped δ-ferrite content distribution along the thickness direction of continuously cast 304 austenitic stainless steel slab. A comparison between observations and calculations indicated that under rapid cooling conditions, reducing the cooling rate during solid-state transformation at the surface effectively decreased residual δ-ferrite. Li et al. [43] studied the hot deformation behavior of 301L stainless steel at 1000–1250 °C and strain rates of 0.1–50 s^{-1}. Diffusion annealing reduced δ-ferrite content from 12% to 0.67%, with δ-ferrite dissolution controlled by chromium and nickel diffusion, particularly evident at the γ/δ phase interfaces. The optimal diffusion annealing parameters were determined as 1300 °C for 10 min. As early as 1990, Wang et al. [44] also investigated changes in ferrite content in 316L stainless steel cast slab after heat treatment. They found that ferrite content decreased by nearly half after treatment while still maintaining the characteristic "M"-shaped distribution. However, most existing research has focused on laboratory-scale specimen heat treatment experiments. Subsequent studies on ferrite distribution within actual cast slab after industrial heat treatment have been scarce.

This study focuses on 304L austenitic stainless steel slab, investigating the morphological variations in ferrite along the slab thickness direction. The ferrite distribution in both the triangular zone of the slab and along the thickness direction at the width center of the cast slab is examined. Simultaneously, Thermo-Calc thermodynamic calculation software is employed to simulate the solidification process of the 304L cast slab. Based on the thermodynamic calculation results, various heat treatment processes are designed. Heat treatment experiments are then conducted across the entire slab thickness to investigate the reduction in ferrite content and the changes in ferrite distribution under different heat treatment regimes.

2. Materials and Methods

A batch of 304L continuous casting slab produced by a certain factory was selected, with a cross-section size of 200 mm × 1525 mm. Its composition is shown in Table 1. Samples were taken from both the triangular zone and the width center position of the slab. The metallographic method [45–47] was used to mechanically grind each sample sequentially using 400–2000 grit diamond sandpaper. Subsequently, polishing was performed using SiC polishing paste. The samples were etched with an aqueous HCl + $FeCl_3$ solution for approximately 2 min to reveal the ferrite structure. The ferrite content on the etched surface of each sample was determined using a ZEISS AX10 optical microscope (Precise Instrument Co., Ltd., Beijing, China.)at 100× magnification. To cover all areas of the sample surface, ferrite was observed and measured in at least 10 positions. The volume fraction of ferrite

in the selected positions was measured using IPP (version: Image-Pro-Plus 7.0) software, and the average value was calculated. Additionally, samples were taken from different positions at the slab center to observe the ferrite morphology; the sampling schematic is shown in Figure 1. The process flow of the metallographic method is shown in Figure 2.

Table 1. Main chemical components of 304L slab.

C	Si	Mn	P	S	Cr	Ni	N
0.0154	0.3763	1.795	0.0318	0.0014	18.01	8.01	0.0696

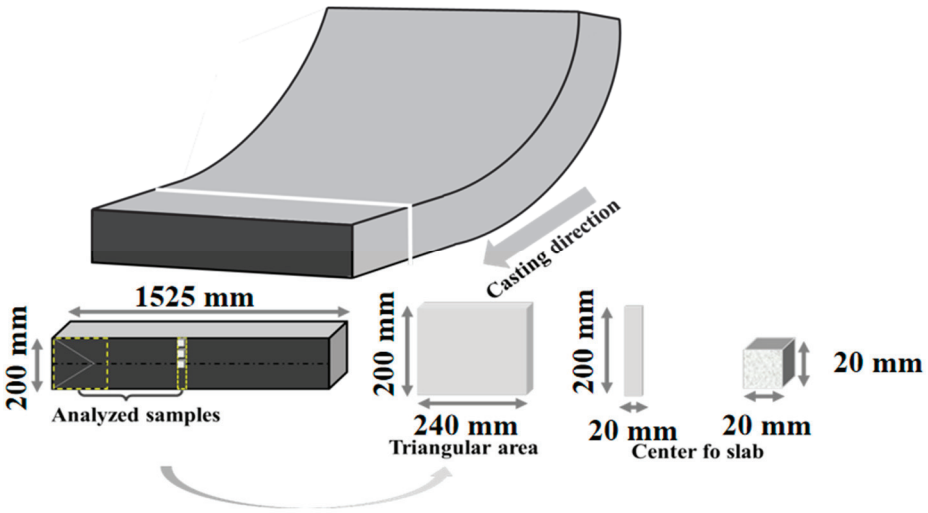

Figure 1. Schematic diagram of sampling of the continuous casting slab.

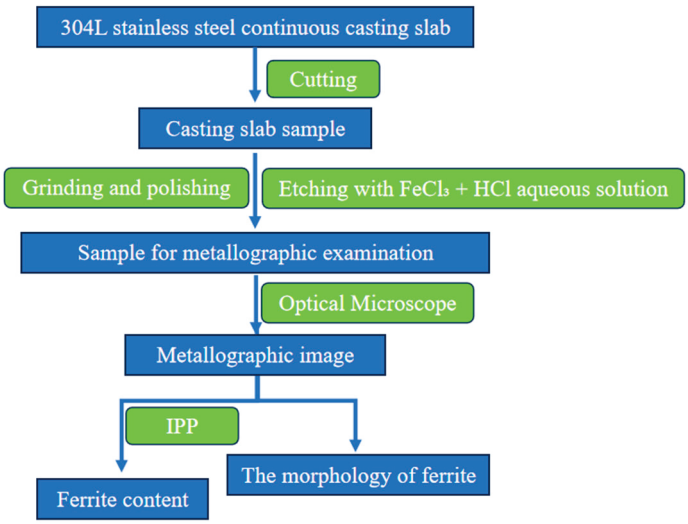

Figure 2. Metallographic process flow diagram.

To investigate the relationship between the solidification structure and the distribution of residual ferrite, the slab was subjected to macroscopic etching using an HCl + HNO_3 aqueous solution. The etching results of the slab are shown in Figure 3.

To investigate the equilibrium solidification process of the 304L continuous casting slab, the phase evolution during solidification from 1500 °C to 500 °C was calculated using Thermo-Calc (version: Thermo-Calc 2025a) software based on the composition in Table 1. Building upon these thermodynamic calculations, 20 mm × 20 mm × 200 mm specimens were extracted from the center of the 304L slab. These specimens were heated

in the BZ-4-13 muffle furnace (Kejing Material Technology Co., Ltd., Hefei, China) to four target temperatures (1000 °C, 1200 °C, 1250 °C and 1300 °C) and held for two sets of holding times (32 min and 48 min). After holding, rapid cooling was performed using either water cooling or oil cooling to obtain room-temperature microstructures. The specific experimental design is detailed in Table 2. Samples were taken from different positions of the heat-treated 304L slab to measure the residual ferrite content, following the same methodology described previously. Additionally, the through-thickness distribution of residual ferrite in the slab was measured under different heat treatment conditions.

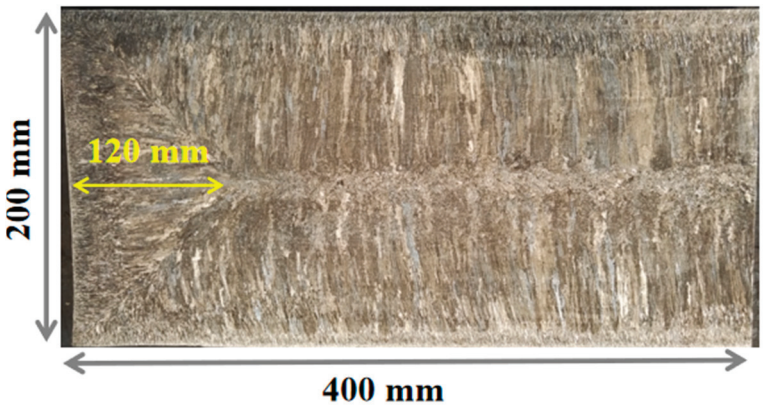

Figure 3. Macrostructure at the edge of 304L continuous casting slab.

Table 2. Heat treatment test scheme for 304L continuous casting slab.

	Holding Time	1000 °C	1200 °C	1250 °C	1300 °C
Water cooling	32 min	1	5	9	13
	48 min	2	6	10	14
Air cooling	32 min	3	7	11	15
	48 min	4	8	12	16

3. Results

3.1. Equilibrium Solidification Process of 304L Slab

To investigate the evolution of residual ferrite during the heating and rolling process of continuous casting slab, Thermo-Calc software was employed to calculate the phase transformation behavior of 304L stainless steel during solidification from 1500 °C to 500 °C, as shown in Figure 4. The results indicate the following: At 1462 °C, δ-ferrite begins to form in the liquid phase. When the temperature decreases to 1437 °C, austenite starts to precipitate in the liquid phase, while δ-ferrite content reaches its peak value of 85.1%. With further cooling, δ-ferrite content gradually decreases as austenite content increases. At 1432 °C, the liquid phase completely disappears, with δ-ferrite content at 82.3%. When the temperature drops to 1236 °C, δ-ferrite vanishes, leaving austenite as the sole constituent in the microstructure. 1437–1462 °C: L + δ dual-phase region. 1432–1437 °C: L + δ + γ three-phase region. 1236–1432 °C: δ + γ dual-phase region. 823–1236 °C: γ single-phase region. The solidification mode of austenitic stainless steels refers to distinct solidification sequences, typically categorized as A, AF, FA or F patterns based on the precipitation order of ferrite or austenite. The AF and FA modes specifically denote solidification processes where ferrite or austenite, respectively, serves as the primary phase for nucleation and growth. As illustrated in Figure 4, the solidification sequence follows L→L + δ→L + δ + γ→δ + γ→γ→γ + α + precipitates. This progression indicates that the solidification mode conforms to the FA (Ferritic-Austenitic) pattern in stainless steels.

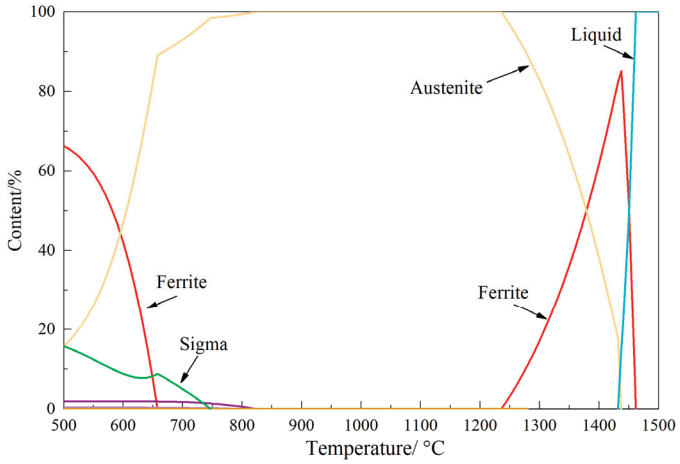

Figure 4. Equilibrium solidification process of the 304 stainless steel calculated by Thermo-Calc.

3.2. Morphology and Distribution of Residual Ferrite at the Mid-Width of Continuous Casting Slab

In the macrostructure shown in Figure 2, three primary regions are observed outside the triangular zone of the 304L slab: the surface fine-grain zone, columnar crystal zone and central equiaxed crystal zone. The morphology of ferrite along the thickness direction at the slab center is presented in Figure 5. Specifically, Figure 5a,c,e display ferrite morphology at 100× magnification in the surface fine-grain zone, columnar crystal zone and central equiaxed crystal zone, respectively. Figure 5b,d,f show corresponding ferrite morphology at 200× magnification.

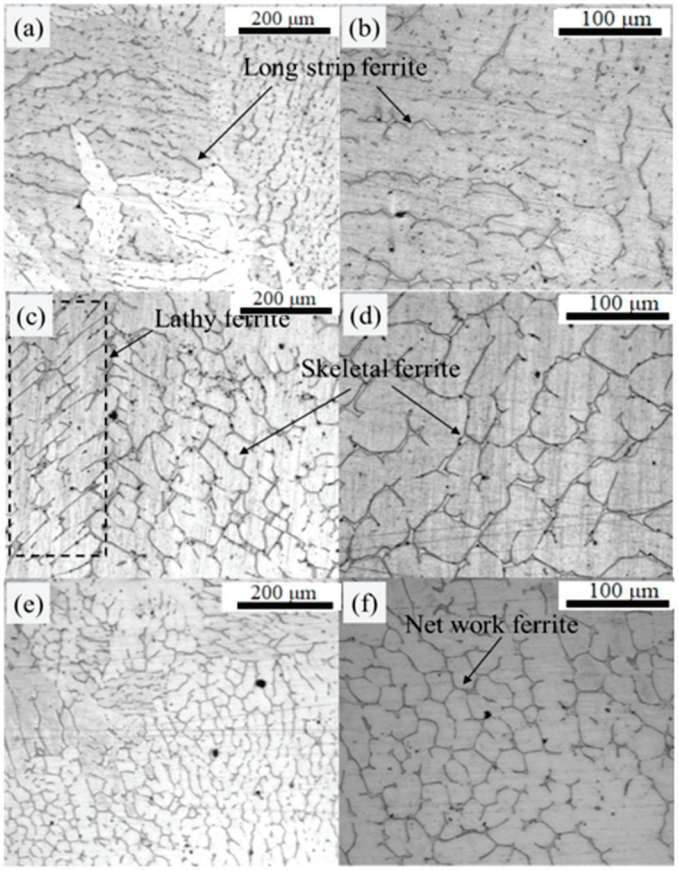

Figure 5. Ferrite morphology in different macrostructural regions of the slab: (**a**,**b**) Surface fine-grain zone; (**c**,**d**) Columnar crystal zone; (**e**,**f**) Central equiaxed crystal zone.

The solidification structure of the continuous casting slab is predominantly characterized by columnar crystals, with relatively small proportions of surface fine-grain and central equiaxed crystal zones. The central solidification structure exhibits normal morphology without defects such as shrinkage porosity or cavities. As shown in Figure 5a,b, long strip ferrite predominates in the surface fine-grain zone. These long strip ferrite structures display parallel alignment, with some containing fine secondary dendrites. The columnar crystal zone (Figure 5c,d) reveals both lathy and skeletal ferrite morphologies. These lathy and skeletal structures are retained due to incomplete transformation from ferrite to austenite under FA solidification mode [48]. In contrast, the central equiaxed crystal zone (Figure 5e,f) features a network-like ferrite structure enveloping austenite phases.

Further analysis of the ferrite content distribution along the thickness direction at the mid-width of the slab is presented in Figure 6. The ferrite distribution exhibits a distinct "M"-shaped profile at the slab center, with the lowest ferrite content of 3% observed near the slab edges and the highest content reaching 13% in the vicinity of the slab center. The ferrite content progressively increases from the slab surface to a depth of 80 mm but subsequently decreases toward the central region. Compared with the ferrite morphologies in Figure 5, significant variations are observed at the slab center. The formation of networked ferrite in the central equiaxed crystal zone may account for the reduced ferrite content in this region.

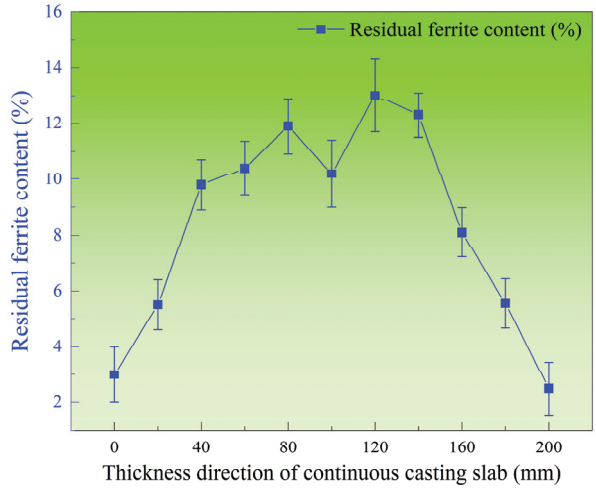

Figure 6. Distribution of residual ferrite in the thickness direction at the width center.

3.3. Distribution of Residual Ferrite in the Triangular Zone Region of Continuous Casting Slab

Table 3 presents the distribution of residual ferrite in the edge region of the 304L continuous casting slab. As shown in Table 3, the ferrite content exhibits significant variation within the slab. The minimum ferrite content of 1.8% occurs at the width edge, while the maximum value reaches 12.5% near the slab center. Residual ferrite content progressively increases along the through-thickness direction from the surface toward the center, followed by a moderate decrease at the central location.

The distribution of residual ferrite in the continuous casting slab was visualized through a three-dimensional representation, as shown in Figure 7. Analysis of Figure 7 reveals that residual ferrite content is relatively low near the slab edges and higher at the slab center. Within the triangular zone, ferrite content progressively increases from the width edge toward the center. A distinct ferrite content maximum occurs at the apex of the triangular zone, consistent with findings reported by Chen and Cheng [36] and Spacarotella et al. [37]. In regions outside the triangular zone, ferrite content gradually increases along the through-thickness direction from the slab edges toward the center. The distribution exhibits bilateral symmetry across the thickness direction. A ferrite content maximum

appears near the thickness center. Ferrite content shows a moderate decrease precisely at the thickness center. Overall, the distribution displays a pronounced "M"-shaped profile.

Table 3. Distribution table of residual ferrite in 304L continuous casting slab.

Thickness Width	10	20	40	60	80	100	120	140	160	180	200	220	240
10	4.8	5.2	3.7	2.7	2.4	2.6	2.8	2.2	2.6	2.0	3.1	2.6	2.6
20	5.4	7.1	9.0	10.7	9.6	8.9	8.2	8.0	7.0	5.3	6.7	7.0	7.5
40	2.5	8.7	6.9	9.8	8.9	9.8	10.3	10.2	9.5	8.7	9.0	8.8	10.8
60	2.0	9.7	10.4	9.8	11.1	11.1	11.6	10.8	10.6	9.9	10.9	9.2	11.8
80	1.9	10.0	10.8	11.0	10.6	10.4	10.7	12.5	11.8	12.4	11.2	11.3	12.4
100	1.8	9.8	11.1	10.8	10.3	11.5	12.2	9.6	9.1	9.5	8.3	10.9	11.2
120	1.8	9.1	9.7	11.2	11.3	11.0	11.2	12.4	11.6	11.7	12.6	12.2	12.3
140	2.0	9.9	10.2	9.7	11.4	11.6	11.6	11.7	11.5	10.9	10.7	11.7	10.7
160	2.3	8.9	9.2	10.2	10.2	9.9	9.8	10.7	10.2	9.4	10.1	8.7	10.0
180	3.9	7.4	8.0	8.6	9.9	8.7	8.0	9.2	8.9	8.1	6.6	8.8	8.4
200	5.0	4.0	3.7	3.2	3.3	2.4	2.7	2.2	2.7	3.2	2.3	2.6	3.2

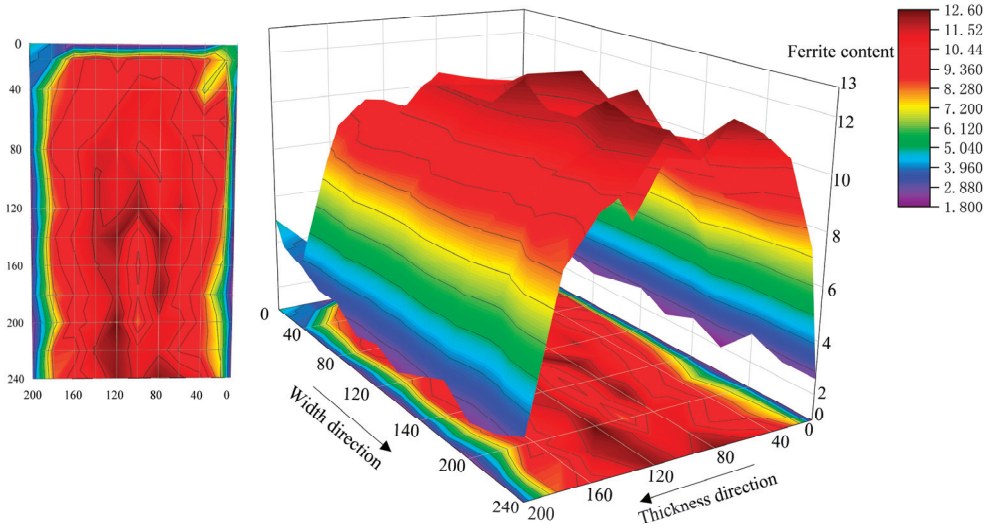

Figure 7. Three-dimensional distribution map of residual ferrite in 304L continuous casting slab.

To further analyze the distribution patterns of ferrite along the thickness direction at different width positions, Figure 8 shows the residual ferrite distribution along the thickness direction within the 0–120 mm range (inside the triangular zone) along the slab width. In the edge region along the width direction, the ferrite content is lower, exhibiting a "V"-shaped distribution. This may be related to the irregular shrinkage profile at the slab width edge shown in Figure 3. This phenomenon occurs because the slab edge undergoes solidification shrinkage during the solidification process and does not fully contact the mold, resulting in non-uniform cooling rates. In areas with severe solidification shrinkage, the excessive cooling rate leads to lower ferrite content. From the 20 mm width position to the end of the triangular zone, the ferrite distribution along the entire thickness direction consistently shows an "A"-shaped pattern. The ferrite content is relatively low in the edge regions along the thickness direction, while it remains relatively consistent from the 20 mm thickness position to the center of the thickness. Within this range, the ferrite content is maintained between 8% and 12%.

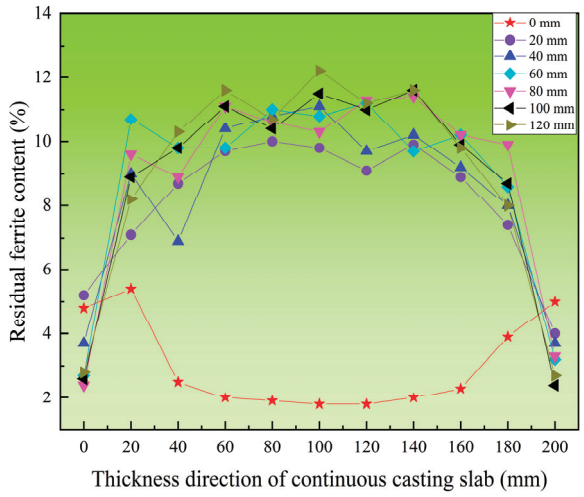

Figure 8. Distribution of residual ferrite along the thickness direction at different distances in the width direction of continuous casting slab (within the triangular area).

Figure 9 shows the residual ferrite distribution along the thickness direction within the 140–240 mm range (outside the triangular zone) along the slab width. In the region outside the triangular zone of the slab, it can be observed that the residual ferrite content at different positions along the width direction clearly exhibits an "M"-shaped distribution. Moreover, the residual ferrite content shows minimal variation across these positions. At the center of the slab thickness, a distinct reduction in ferrite content is evident.

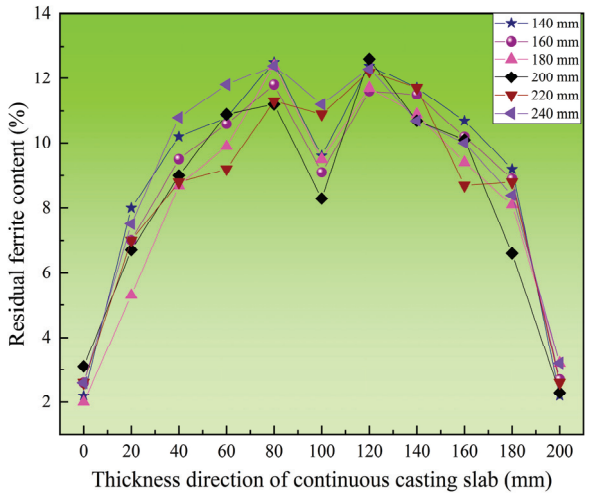

Figure 9. Distribution of residual ferrite along the thickness direction at different distances in the width direction of continuous casting slab (outside the triangular area).

Additionally, the average values and standard deviation of residual ferrite along both the width and thickness directions were calculated separately. Figure 10 illustrates the distribution of average residual ferrite content along the thickness direction in the triangular zone of the continuous casting slab. It can be observed that along the slab thickness direction, the residual ferrite distribution exhibits an "M"-shaped pattern similar to that observed at the width center of the slab. The lowest average residual ferrite content occurs at the edge of the thickness direction, measuring 3.02%. From the edge to a position 80 mm from the edge, the average ferrite content gradually increases, peaking at 11.8%. Subsequently, toward the slab center, the average ferrite content decreases to 9.1%.

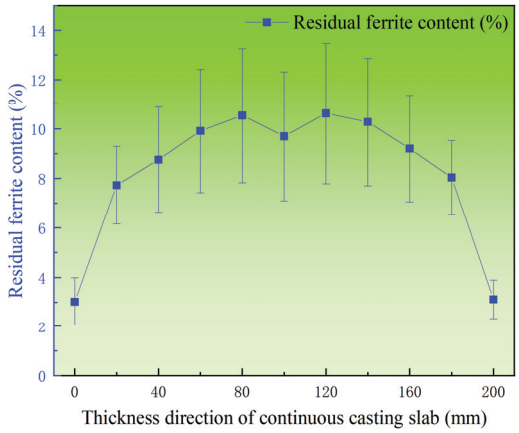

Figure 10. Distribution of average residual ferrite along the thickness direction of 304L continuous casting slab.

Figure 11 shows the distribution of average residual ferrite content along the width direction in the triangular zone of the continuous casting slab. It can be observed that along the slab width direction, the ferrite content remains relatively consistent within the slab interior, ranging between 8% and 10%, except at the edge, where the residual ferrite content is significantly lower at 3.04%.

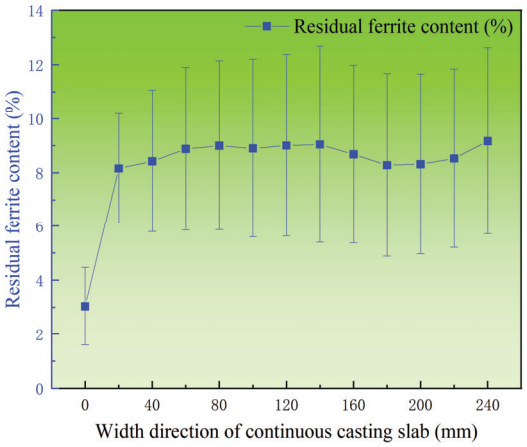

Figure 11. Distribution of average residual ferrite along the width direction of 304L continuous casting slab.

3.4. Distribution of Residual Ferrite in the Triangular Zone Region of Continuous Casting Slab

Additionally, eleven sampling points were selected across the entire thickness direction of the obtained continuous casting slab specimens for ferrite content measurement. The average ferrite content along the thickness direction was calculated from three repeated experimental measurements. Comparing the changes in average residual ferrite content before and after heat treatment, Figure 12 demonstrates that the residual ferrite in all heat-treated slabs decreased to varying degrees.

Figure 12 presents the average residual ferrite content for 16 sets of specimens after testing, with the original average ferrite content being 8.96%. The results reveal that under the same heat treatment temperature, specimens subjected to air cooling exhibit a more significant reduction in residual ferrite compared to water cooling. Under identical cooling conditions, extended holding times correspond to greater reductions in residual ferrite. Comparing the results across different temperatures, increasing the heat treatment temperature promotes the transformation of residual ferrite into austenite, thereby reducing ferrite content. Paradoxically, the reduction at 1300 °C was less pronounced than under

1250 °C holding conditions. The most substantial reduction occurred at 1250 °C, with the maximum decrease observed after 48 min of air cooling, reducing the ferrite content to 5.54% (a reduction of 3.42 percentage points). This phenomenon is explained by Thermo-Calc calculations (version: Thermo-Calc 2025a) (Figure 4) of phase evolution in 304L steel. The equilibrium microstructure at 1300 °C consists of high-temperature δ-ferrite and austenite, which is unconducive to residual ferrite transformation. δ-ferrite disappears at 1236 °C, and following further temperature reduction, it enters the fully austenitic phase region. Consequently, the most significant average ferrite reduction occurs following heat treatment at 1250 °C.

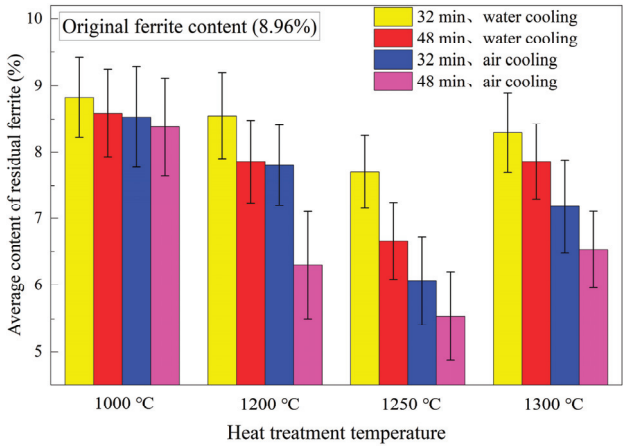

Figure 12. Average value of residual ferrite content after different heat treatment tests.

To investigate the effect of heat treatment on the residual ferrite distribution in continuous casting slab, a comparative analysis was conducted between four sets of specimens heat-treated at 1250 °C and the original specimens, as illustrated in Figure 13. The results demonstrate that after heat treatment at 1250 °C, the residual ferrite distribution in the slab remains heterogeneous and retains the original "M"-shaped pattern observed in the as-cast slab. Under identical cooling methods, the ferrite content in the slab after 48 min holding is generally lower than that after 32 min holding. When holding times are equivalent, air-cooled slabs exhibit lower residual ferrite content than water-cooled slabs. Notably, however, within the chill layer at the slab edge, water cooling induces a more pronounced reduction in residual ferrite content.

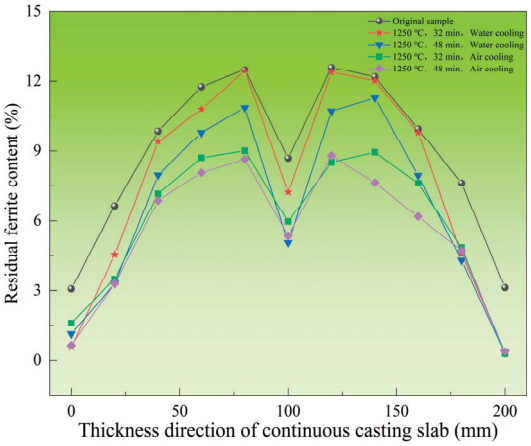

Figure 13. Comparison diagram of residual ferrite content between heat-treated sample and original sample of 304L continuous casting slab at 1250 °C.

3.5. Actual Precipitation Behavior of α-Ferrite

Thermo-Calc calculations in Figure 4 indicate that α-ferrite appears in the equilibrium phase structure when the temperature drops to approximately 600 °C. To verify whether α-ferrite increases during actual production processes, four specimen groups were subjected to prolonged holding at 600 °C followed by different cooling methods. The resulting changes in residual ferrite content (average reduction) are shown in Figure 14. The key findings are as follows. Contrary to thermodynamic predictions, residual ferrite showed no increasing trend after holding at 600 °C but actually decreased. The decreasing trend was more pronounced under air-cooling conditions. This demonstrates that no α-ferrite precipitation occurs under actual production cooling rates. The cooling process promotes transformation of residual δ-ferrite into austenite. Moderately slow cooling below 600 °C facilitates further residual ferrite transformation.

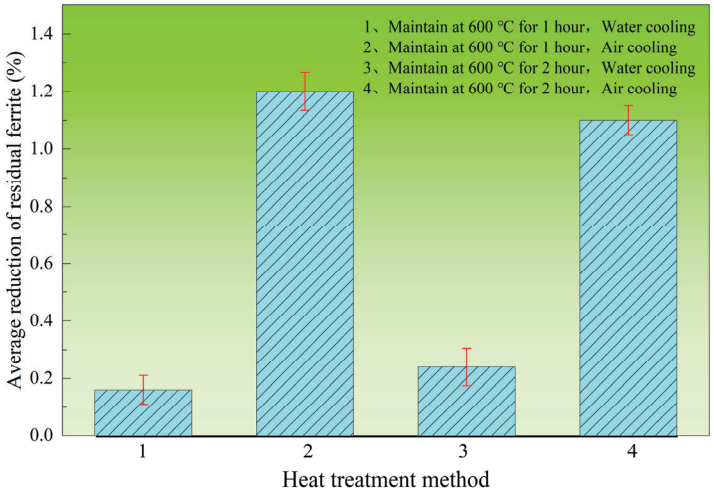

Figure 14. The changes in residual ferrite in 304L continuous casting slab were tested at 600 °C.

4. Discussion

4.1. Morphology and Distribution Mechanism of Residual Ferrite in Continuous Casting Slab

Based on Figure 5, it can be observed that the primary morphologies of residual ferrite in the slab include long strip, skeletal, lathy and network structures. Ferrite morphology is typically influenced by the solidification mode, cooling rate and macrostructure [49–54]. In this study, the solidification mode across the entire section of the 304L slab was consistently the FA mode. The formation of long strip ferrite at the slab edges is attributed to the high cooling rate within the edge chill layer. This high cooling rate promotes nucleation of both ferrite and austenite phases but suppresses ferrite growth, preventing it from developing into a complete skeletal structure, hence resulting in the long strip ferrite morphology at the slab surface. In the columnar dendritic zone of the slab, the predominant ferrite morphologies are lathy and skeletal. Within this zone, the cooling rate decreases, providing sufficient kinetic conditions for ferrite growth. Consequently, secondary dendrites can develop from the long strip ferrite, forming densely interconnected skeletal ferrite. In the central equiaxed grain zone, the ferrite primarily exhibits a network morphology. Here, ferrite nucleates extensively within the liquid phase, growing with an equiaxed grain morphology. As ferrite continuously transforms into austenite, the austenite/ferrite interface moves toward the ferrite side. Ultimately, continuous network ferrite forms along the austenite grain boundaries.

Based on the three-dimensional map of residual ferrite content in the triangular zone of the continuous casting slab, the high cooling rate in the chill layer at the slab edge suppresses ferrite growth, resulting in lower ferrite content. However, at the 0 mm width

position in the triangular zone, the ferrite distribution along the thickness direction exhibits a "V"-shaped profile, with higher levels on both sides and lower in the center. This occurs because solidification near the corner lags behind that at the center of the edge. The cooling rate at the corner is lower than at the center of the edge along the thickness direction. Consequently, at the 0 mm width position, ferrite on both sides (corners) has more time to grow, leading to higher ferrite content at the corners compared to the center. This creates the "V-shaped" ferrite distribution along the thickness direction. Between 20 mm and 120 mm in the slab width direction within the triangular zone, the cooling rate gradually decreases from the edge toward the center. This progressively enhances ferrite growth kinetics, causing ferrite content to increase steadily from the edge to the center, forming an "A"-shaped distribution. However, outside the triangular zone (width direction: 120~240 mm), the higher cooling rate at the edge inhibits the growth of high-temperature δ-ferrite, resulting in a lower ferrite content. As the distance from the surface toward the center increases, the cooling rate decreases. This leads to a gradual prolongation of the entire solidification and solid-state phase transformation process, while the ferrite dendrite arm spacing increases sharply. Concurrently, the extent of solid-state phase transformation weakens, causing a slight increase in room-temperature ferrite content. The decrease in ferrite content at the center is likely due to the sparse network-like ferrite structure formed there. The low cooling rate in the center allows more ferrite to transform into austenite, forming this sparse network-like ferrite structure, which ultimately reduces the ferrite content. Consequently, the ferrite content exhibits a distinct "M"-shaped distribution.

4.2. Mechanism of the Effect of Heat Treatment on Residual Ferrite Content and Distribution Throughout the Slab Thickness

During the heat treatment process throughout the entire thickness of the slab, the primary reaction occurring is the solid-state phase transformation of ferrite to austenite. This solid-state phase transformation is predominantly influenced by atomic diffusion distance. The heat treatment results show that the ferrite content decreased from the original 8.96% in the slab to varying levels, indicating that both heat treatment temperature and duration affect ferrite content. At 1100 °C, the temperature is relatively low, and the kinetic conditions for elemental diffusion are insufficient. Even with extended heat treatment time, the reduction in ferrite content remains limited. Thermodynamic calculations reveal that the temperature range of 1100–1236 °C corresponds to a single-phase austenite region. Holding within this range effectively promotes the transformation of ferrite to austenite. At 1250 °C, the thermodynamic results indicate that this temperature is no longer within the single-phase austenite region, and a small amount of ferrite phase may appear. However, due to its low content at this stage, ferrite remains metastable during heat treatment, while austenite persists as the primary stable phase. Additionally, the atomic diffusion rates at 1250 °C are higher than at 1200 °C. Consequently, the greatest reduction in ferrite content occurs under all tested conditions at 1250 °C. Specifically, under air cooling after holding at 1250 °C for 48 min—where atomic diffusion rates and diffusion time are maximized—the ferrite content decreases most significantly. At 1300 °C, thermodynamic calculations show ferrite content reaching as high as 20%. At this temperature, competing stability dynamics emerge between the two phases, with ferrite becoming more stable and less prone to transform into austenite. As a result, the net reduction in ferrite content is less substantial compared to that achieved at 1250 °C.

The heredity of the "M"-shaped distribution was also observed in the heat treatment results across the entire thickness of the slab. Under different holding times and cooling methods at 1250 °C, a distribution similar to the original slab's "M"-shaped pattern appeared consistently. This heredity of the "M"-shaped distribution is primarily related to the initial ferrite content and secondary dendrite arm spacing of the slab. In the edge region

along the slab thickness direction, the ferrite content remained similar across different holding times and cooling methods. This indicates that the transformation from ferrite to austenite was essentially complete under the conditions of 1250 °C, 32 min holding and water cooling. Further extending the holding time or reducing the cooling rate, while increasing the atomic diffusion distance, did not promote additional ferrite-to-austenite transformation. Consequently, only a short atomic diffusion distance is required to complete the solid-state phase transformation reaction at the slab edge. In contrast, within the central region (50–150 mm from the surface), the ferrite content decreased with prolonged holding time and reduced cooling rate. In this region (50–150 mm), the required diffusion distance for the solid-state phase transformation from ferrite to austenite increases. Here, extending the holding time and lowering the cooling rate effectively increases the atomic diffusion distance, thereby promoting the solid-state phase transformation. Under these conditions, the post-heat-treatment ferrite content mainly depends on the initial ferrite content.

The findings of this study provide theoretical guidance for steel manufacturers. Based on slab composition, manufacturers can first analyze the equilibrium solidification process using Thermo-Calc thermodynamic software. Below the δ-ferrite disappearance temperature during equilibrium solidification, maximizing heat treatment temperature and extending holding time effectively reduces residual ferrite content, whereby air cooling demonstrates superior efficacy over water cooling. Special attention should be given to the M-shaped ferrite distribution, particularly the bilateral ferrite peak zones along the slab centerline. Implementing dynamic intensive cooling in these critical regions suppresses ferrite coarsening.

5. Conclusions

1. This study investigated 304L austenitic stainless steel continuous casting slab. Along the thickness direction from surface to center, ferrite morphologies transition sequentially as long strip → skeletal/lathy → networked structures. In the width-center thickness direction, ferrite content varies within 3–13%, exhibiting an "M"-shaped distribution. Within the slab's triangular zone, ferrite content ranges from 1.8% to 12.2%. The average residual ferrite along the thickness direction shows an "M"-shaped distribution, while along the width direction, the average ferrite content is lower at the edges (3.04%) and remains relatively consistent (8–10%) within the slab interior.
2. Thermodynamic software calculations of the slab's equilibrium solidification process confirmed that the solidification mode of the 304L continuously cast slab follows the ferrite–austenite (FA) mode. Based on these thermodynamic calculations, heat treatment experiments were designed across the entire slab thickness. The results revealed that at a heat treatment temperature of 1250 °C, ferrite content decreased most significantly. Prolonged holding time and reduced cooling rate both facilitated further reduction in residual ferrite content. However, at 1300 °C (where the equilibrium microstructure consists of high-temperature δ-ferrite and austenite), the reduction in residual ferrite was less pronounced compared to the 1250 °C condition. Moreover, after heat treatment under various parameters, the ferrite distribution within the slab retained the original "M"-shaped profile observed in the as-cast slab.
3. Holding experiments at 600 °C confirmed no α-ferrite precipitation under actual cooling conditions. Moderately slow cooling below this temperature further promotes the transformation of high-temperature δ-ferrite into austenite.

Author Contributions: Conceptualization, K.Y., Y.W., L.C., C.C. and W.M.; methodology, Z.X., K.Y., Y.L., Y.W., L.C., C.C. and W.M.; software, Z.X. and W.M.; validation, Z.X. and C.P.; formal analysis, Z.X., K.Y. and Y.L.; investigation, Z.X., K.Y., Y.L., C.P., D.H., Q.Z., Y.W. and C.C.; resources, K.Y., Y.L. and L.C.; data curation, Z.X., Y.L., C.P., D.H. and Q.Z.; writing—original draft preparation, Z.X., C.P. and Y.W.; writing—review and editing, K.Y., L.C., C.C. and W.M.; visualization, Z.X., C.P., D.H., Q.Z. and Y.W.; supervision, K.Y., C.C. and W.M.; project administration, C.C.; funding acquisition, Z.X., D.H., C.C. and W.M. All authors have read and agreed to the published version of the manuscript.

Funding: This research was funded by the research project supported by the Applied Fundamental Research Programs of Shanxi Province, grant number 202303021221036; the Shanxi Scholarship Council of China, grant number 2022-040; the "Chunhui Plan" Collaborative Research Project by the Ministry of Education of China, grant number HZKY20220507; the Graduate Innovation Project of Shanxi Province; and the Undergraduate Innovation and Entrepreneurship Training Program of Shanxi Province, grant number 20250175.

Institutional Review Board Statement: Not applicable.

Informed Consent Statement: Not applicable.

Data Availability Statement: The original contributions presented in this study are included in the article. Further inquiries can be directed to the corresponding authors.

Conflicts of Interest: Author Yafeng Li is employed by the Xinzhou Comprehensive Inspection and Testing Center. The remaining authors declare that the research was conducted in the absence of any commercial or financial relationships that could be construed as a potential conflict of interest.

References

1. Lo, K.H.; Shek, C.H.; Lai, J.K.L. Recent developments in stainless steels. *Mater. Sci. Eng. R Rep.* **2009**, *65*, 39–104. [CrossRef]
2. Yang, S.; Ma, J.Y.; Chen, C.; Zhang, C.L.; Ren, J.Y.; Jiang, Z.H.; Fan, G.W.; Han, P.D. Effects of B and Ce Grain Boundary Segregation on Precipitates in Super Austenitic Stainless Steel. *Metals* **2023**, *13*, 326. [CrossRef]
3. Liu, Z.Q.; Wang, J.; Chen, C.; Tian, H.Y.; Han, P.D. Effect of boron on the solidification characteristics and constitutive equation of S31254 superaustenitic stainless steel. *Steel Res. Int.* **2024**, *95*, 2400050. [CrossRef]
4. Zhang, J.; Hu, Z.F.; Zhang, Z. EBSD parameter assessment and constitutive models of crept HR3C austenitic steel. *J. Iron Steel Res. Int.* **2023**, *30*, 772–781. [CrossRef]
5. Zhang, Y.; Liu, X.; Wang, C.J.; Liu, C. Effect of heat treatment on microstructure and mechanical properties of selective laser-melted PH13-8Mo stainless steel. *J. Iron Steel Res. Int.* **2024**, *31*, 945–955. [CrossRef]
6. Wang, Y.; Chen, C.; Ren, R.J.; Xue, Z.X.; Wang, H.Z.; Zhang, Y.Z.; Wang, J.X.; Wang, J.; Chen, L.; Mu, W.Z. Ferrite formation and decomposition in 316H austenitic stainless steel electro slag remelting ingot for nuclear power applications. *Mater. Charact.* **2024**, *218*, 114581. [CrossRef]
7. Dong, C.; Qu, S.; Fu, C.M.; Zhang, Z.F. Failure analysis of crevice corrosion on 304 stainless steel tube heat exchanger. *J. Iron Steel Res. Int.* **2023**, *30*, 1490–1498. [CrossRef]
8. Zhu, L.; Sun, C.Y.; Wang, B.Y.; Zhou, J. Cross wedge rolling deformation law and bonding mechanism of 304 stainless steel/Q235 carbon steel bimetallic shaft. *J. Iron Steel Res. Int.* **2024**, *31*, 2423–2437. [CrossRef]
9. Guo, X.W.; Ren, Z.K.; Wu, H.; Chai, Z.; Zhang, Q.; Wang, T.; Huang, Q.X. Effect of annealing on microstructure and synergistic deformation of 304/TC4 composite plates with corrugated interface. *J. Iron Steel Res. Int.* **2024**, 1–18. [CrossRef]
10. Kujanpaa, V.; Suutala, N.; Takalo, T. Correlation between solidification cracking and microstructure in austenitic and austenitic-ferritic stainless steel welds. *Weld. Res. Int.* **1979**, *9*, 55–76.
11. Rho, B.S.; Hong, H.U.; Nam, S.W. The effect of δ-ferrite on fatigue cracks in 304L steels. *Int. J. Fatigue* **2000**, *22*, 683–690. [CrossRef]
12. Wang, Q.Y.; Chen, S.H.; Lv, X.; Jiang, H.C.; Rong, L.J. Role of δ-ferrite in fatigue crack growth of AISI 316 austenitic stainless steel. *J. Mater. Sci. Technol.* **2022**, *114*, 7–15. [CrossRef]
13. Chen, S.H.; Wang, Q.Y.; Jiang, H.C.; Rong, L.J. Effect of δ-ferrite on Hot Deformation and Recrystallization of 316KD Austenitic Stainless Steel for Sodium-Cooled Fast Reactor Application. *Acta Metall. Sin.* **2024**, *60*, 367–376.
14. Wang, Z.G.; Gao, F.; Cao, G.M.; Tang, S.; Liu, Z.Y. Elemental inter-diffusions for the transformation of δ/M23C6/γ phases during heat treatment processes in heavy gage 316H-type austenitic stainless steel. *Metall. Mater. Trans. A* **2022**, *53*, 2652–2664. [CrossRef]
15. Dai, Z.X.; Jiang, S.L.; Ning, L.K.; Xu, X.D.; Li, S.; Duan, D.L. Effect of friction on corrosion behaviors of AISI 304 and Cr26Mo1 stainless steels in different solutions. *J. Iron Steel Res. Int.* **2023**, *30*, 2541–2556. [CrossRef]

16. Chen, S.H.; Wang, Q.Y.; Xie, A.; Rong, L.J. Corrosion behavior of δ-ferrite in AISI 316 austenitic stainless steel exposed to oxygen-saturated lead-bismuth eutectic at 550 °C. *Mater. Charact.* **2024**, *211*, 113930. [CrossRef]
17. Kumar, A.; Ganesh, P.; Sharma, V.K.; Manekar, M.; Gupta, R.K.; Singh, R.; Singh, M.K.; Mundra, G.; Kaul, R. Development of low-magnetic-permeability welds of 316L stainless steel. *Weld. J.* **2021**, *100*, 323–337. [CrossRef]
18. Bharani Chandar, J.; Lenin, N.; Rathinasuriyan, C. Exploring surface integrity Experimental investigation into abrasive waterjet deep hole drilling on ss 316L for biomedical applications. *J. Alloy. Metall. Syst.* **2024**, *8*, 100109. [CrossRef]
19. Myllykoski, L.; Suutala, N. Effect of solidification mode on hot ductility of austenitic stainless steels. *Met. Technol.* **1983**, *10*, 453–460. [CrossRef]
20. Ma, J.C.; Yang, Y.S.; Tong, W.H.; Fang, Y.; Yu, Y.; Hu, Z.Q. Microstructural evolution in AISI 304 stainless steel during directional solidification and subsequent solid-state transformation. *Mater. Sci. Eng. A* **2007**, *444*, 64–68. [CrossRef]
21. Fu, J.W.; Yang, Y.S.; Guo, J.J.; Ma, J.C.; Tong, W.H. Formation of a two-phase microstructure in Fe–Cr–Ni alloy during directional solidification. *J. Cryst. Growth* **2008**, *311*, 132–136. [CrossRef]
22. Fu, J.W.; Yang, Y.S.; Guo, J.J. Formation of a blocky ferrite in Fe–Cr–Ni alloy during directional solidification. *J. Cryst. Growth* **2009**, *311*, 3661–3666. [CrossRef]
23. Fu, J.W.; Yang, Y.S.; Guo, J.J.; Ma, J.C.; Tong, W.H. Formation of two-phase coupled microstructure in AISI 304 stainless steel during directional solidification. *J. Mater. Res.* **2009**, *24*, 2385–2390. [CrossRef]
24. Fu, J.W.; Yang, Y.S. Orientational dependence of lathy ferrite in Fe–Cr–Ni alloy during directional solidification. *Mater. Lett.* **2012**, *81*, 177–180. [CrossRef]
25. Lee, E.S.; Lee, J.M.; Kim, J.W. Improvement of surface quality for the HCR practice of 304 stainless steel slab. In Proceedings of the 58th Electric Furnace Conference and 17th Process Technology Conference, Orlando, FL, USA, 12–15 November 2000; pp. 867–873.
26. Kim, J.J.; Kim, S.K.; Kim, J.W.; Shim, S.D.; Lee, Y.D. Application of mold thermal monitoring system for improving slab surface quality at POSCO stainless steel works. In Proceedings of the 58th Electric Furnace Conference and 17th Process Technology Conference, Orlando, FL, USA, 12–15 November 2000; pp. 1009–1018.
27. Di, H.S.; Cui, G.Z.; Wang, G.D.; Liu, X.H. Hot Ductility of 304HC Stainless Steel and the Model of Resistance to Deformation. *Acta Metall. Sin.* **2003**, *16*, 97–103.
28. Hou, Z.B.; Cheng, G.G.; Wu, C.C.; Chen, C. Time-Series Analysis Technologies Applied to the Study of Carbon Element Distribution along Casting Direction in Continuous-Casting Billet. *Metall. Mater. Trans. B* **2012**, *43*, 1517–1529. [CrossRef]
29. Pang, J.C.; Qian, G.Y.; Pang, S.; Ma, W.H.; Cheng, G.G. Design of a submerged entry nozzle for optimizing continuous casting of stainless steel slab. *J. Iron Steel Res. Int.* **2023**, *30*, 2229–2241. [CrossRef]
30. Lindenberg, H.U.; Knackstedt, W.; Koehler, H.J.; Biesterfeld, W.; Unger, K.D.; Thielmann, R. Metallurgie des Stranggießens nichtrostender Stähle. *Stahl Eisen* **1984**, *104*, 227–234.
31. Wolf, M. Strand Surface Quality of Austenitic Stainless Steels: Part I—Macroscopic Shell Growth and Ferrite Distribution. *Ironmak. Steelmak.* **1986**, *13*, 248–257.
32. Kim, S.K.; Shin, Y.K.; Kim, N.J. Distribution of δ ferrite content in continuously cast type 304 stainless steel slab. *Ironmak. Steelmak.* **1995**, *22*, 316–325.
33. dos Santos, F.A.M.; Martorano, M.A.; Padilha, A.F. Delta ferrite formation and evolution during slab processing from an 80-ton industrial heat of AISI 304 austenitic stainless steel. *REM Int. Eng. J.* **2023**, *76*, 47–54. [CrossRef]
34. Huang, F.X.; Wang, X.H.; Wang, W.J. Characteristics of residual ferrite in solidification structure of austenitic stainless steel. *Iron Steel* **2012**, *47*, 69–73. [CrossRef]
35. Huang, F.X.; Wang, X.H.; Wang, W.J. Behavior of ferrite in AISI304 stainless steel strips. *Chin. J. Eng.* **2012**, *34*, 639–643. [CrossRef]
36. Chen, C.; Cheng, G.G. Delta-ferrite distribution in a continuous casting slab of Fe-Cr-Mn austenitic stainless steel. *Metall. Mater. Trans. B* **2017**, *48*, 2324–2333. [CrossRef]
37. Spaccarotella, A.; Ridolfi, M.R.; Picht, G.; Scheller, P.R. Control of δ-γ Transformation during Solidification of Stainless Steel slab in the Mould. *Steel Res. Int.* **2003**, *74*, 693–699. [CrossRef]
38. Nhung, L.T.; Nam, N.D.; Khanh, P.M. Effect of Temperature on δ-Ferrite Morphology of Carbon Steel and Austenitic Stainless Steel Welds. *Mater. Sci. Forum* **2021**, *1034*, 23–32. [CrossRef]
39. Kim, S.H.; Moon, H.K.; Kang, T.; Lee, C.S. Dissolution kinetics of delta ferrite in AISI 304 stainless steel produced by strip casting process. *Mater. Sci. Eng. A* **2003**, *356*, 390–398. [CrossRef]
40. Fukumoto, S.; Iwasaki, Y.; Motomura, H.; Fukuda, Y. Dissolution Behavior of δ-ferrite in Continuously Cast slab of SUS304 during Heat Treatment. *ISIJ Int.* **2012**, *52*, 74–79. [CrossRef]
41. Aghebatkheiri, F.; Mashreghi, A.R.; Hasani, S. Isothermal Kinetic Analysis of issolution of The Retained Delta Ferrite in AISI 304 Stainless Steel During Homogenization. *Int. J. Iron Steel Soc. Iran.* **2024**, *21*, 1–8. [CrossRef]
42. Zargar, T.; Sadeghi, F.; Kim, J.W.; Lee, J.S.; Heo, Y.U.; Yim, C.H. Kinetic model to investigate the effect of cooling rate on δ-Ferrite behavior and its application in continuous casting of AISI 304 stainless steel. *Metals Mater. Int.* **2022**, *28*, 2263–2276. [CrossRef]

43. Li, J.C.; Liu, Z.Y.; Wang, D.; Pan, J.X.; Zhao, M.Y.; Geng, S.L.; Cheng, Y.G. Hot Deformation Behavior of 301L Stainless Steel and Dissolution Behavior of δ-Ferrite During Heat Treatment. *Steel Res. Int.* **2023**, *94*, 2300181. [CrossRef]
44. Wang, X.G.; Dumortier, C.; Riquier, Y. Simulation of Solidification Process and Prediction of δ-ferrite Distribution in Continuously Cast Austenitic Stainless Steels slab. In Proceedings of the 6th International Iron and Steel Congress, Nagoya, Japan, 21–26 October 1990; pp. 705–712.
45. Niagaj, J.; Mazur, Ł. Review of methods for measurement of ferrite content in high alloyed steels and their welded joints. *Weld. Int.* **2014**, *28*, 345–353. [CrossRef]
46. Wang, Y.; Chen, C.; Yang, X.Y.; Zhang, Z.R.; Wang, J.; Li, Z.; Chen, L.; Mu, W.Z. Solidification modes and delta-ferrite of two types 316L stainless steels: A combination of as-cast microstructure and HT-CLSM research. *J. Iron Steel Res. Int.* **2025**, *32*, 426–436. [CrossRef]
47. Wang, Q.C.; Ren, Y.B.; Yao, C.F.; Yang, K.; Misra, R.D.K. Residual ferrite and relationship between composition and microstructure in high-nitrogen austenitic stainless steels. *Metall. Mater. Trans. A* **2015**, *46*, 5537–5545. [CrossRef]
48. Fu, J.W. *Study on Microstructure Formation and Evolution of Sub-Rapid Solidification Austenitic Stainless Steel*; Harbin Institute of Technology: Harbin, China, 2009.
49. Hull, F.C. Delta ferrite and martnesite formation in stainless steels. *Weld. J.* **1973**, *52*, 193.
50. Siegel, U.; Spies, H.-J.; Eckstein, H.-J. Effect of solidification conditions on the solidification sequence of austenitic chromium-nickel stainless steels. *Steel Res.* **1986**, *57*, 25–32. [CrossRef]
51. Scheller, P.R.; Flesch, R.; Bleck, W. Solidification Morphology and Microstructure Properties at Increased Cooling Rates for 18-8 Cr-Ni Stainless Steel. *Adv. Eng. Mater.* **1999**, *1*, 209–214. [CrossRef]
52. Padilha, A.F.; Tavares, C.F.; Martorano, M.A. Delta Ferrite Formation in Austenitic Stainless Steel Castings. *Mater. Sci. Forum* **2012**, *730*, 733–738. [CrossRef]
53. Saied, M. *Experimental and Numerical Modeling of the Dissolution of Delta Ferrite in the Fe-Cr-Ni System: Application to the Austenitic Stainless Steels*; Université Grenoble Alpes: Saint-Martin-d'Hères, France, 2016.
54. Chen, L.; Wang, Y.; Li, Y.F.; Zhang, Z.R.; Xue, Z.X.; Ban, X.Y.; Hu, C.H.; Li, H.X.; Tian, J.; Mu, W.Z.; et al. Effect of Nickel Content and Cooling Rate on the Microstructure of as Cast 316 Stainless Steels. *Crystals* **2025**, *15*, 168. [CrossRef]

materials

MDPI

Article

Statistical and ANN Modeling of Corrosion Behavior of Austenitic Stainless Steels in Aqueous Environments

Kwang-Hu Jung [1] and Seong-Jong Kim [2,*]

[1] Division of Cadet Training, Mokpo National Maritime University, Mokpo 58628, Republic of Korea; khjung@mmu.ac.kr
[2] Division of Marine Engineering, Mokpo National Maritime University, Mokpo 58628, Republic of Korea
* Correspondence: ksj@mmu.ac.kr; Tel.: +82-62-240-7226

Abstract

This study applies statistical approaches utilizing linear regression and artificial neural networks (ANNs) to predict the corrosion behavior of austenitic stainless steels (316L, 904L, and AL-6XN) under various environmental conditions. The environmental variables considered include temperature (30–90 °C), chloride ion concentration (20–40 g/L), and pH (2–6). Analysis of variance (ANOVA) confirmed that the input variables, including the Pitting Resistance Equivalent Number (PREN ranging from 24 to 45), significantly affect the critical pitting potential. The influence of the variables was ranked in the order: PREN, temperature, pH, and chloride ion concentration. A linear regression model was developed using significant factors and interactions identified at the 95% confidence level, achieving a predictive performance with R^2 = 0.789 for critical pitting potential. To predict potentiodynamic polarization curves, an ANN based on supervised learning with backpropagation was employed. The ANN model demonstrated a remarkably high predictive performance with R^2 = 0.972 in complex corrosion environments. The predicted polarization curves reliably estimated electrochemical characteristics such as corrosion current, corrosion potential, and pitting potential. These results provide a valuable tool for predicting and understanding the corrosion behavior of stainless steels, which can aid in corrosion prevention strategies and material selection decisions.

Keywords: corrosion prediction; austenitic stainless steel; linear regression; artificial neural network; pitting potential

1. Introduction

Austenitic stainless steels are widely used in various industries, including marine, offshore, chemical processing, and power generation, due to their excellent mechanical properties and corrosion resistance. However, under aggressive environment like seawater, these materials are susceptible to localized forms of corrosion such as pitting [1] and crevice corrosion [2]. Pitting corrosion can lead to catastrophic failures because it is difficult to detect and can propagate rapidly once initiated. Therefore, understanding and predicting the corrosion behavior of austenitic stainless steels is critical to ensuring the integrity and service life of structures and components made from these materials.

Traditional methods for assessing corrosion resistance involve experimental testing, such as potentiodynamic polarization measurements, which can be time-consuming and costly. These methods also require extensive laboratory work to evaluate the effects of various environmental factors like temperature [3,4], chloride ion concentration [5,6], and

pH [7]. While empirical models have been developed to estimate corrosion rates and surface corrosion potential, they often lack the ability to accurately predict corrosion behavior under complex environmental conditions due to the nonlinear and multifactorial nature of the corrosion process.

Recent advancements in computational techniques have opened new avenues for predicting material behavior [8,9]. Statistical methods such as linear regression have been employed to establish relationships between input variables and corrosion responses. However, linear models may not capture the complex interactions and nonlinearities inherent in corrosion phenomena. Artificial neural networks (ANNs), with their ability to model complex nonlinear relationships, offer a promising alternative. ANNs have been successfully applied in various fields of materials science and engineering to predict properties and behaviors based on input parameters [10–14].

Several studies have explored the use of ANNs for corrosion prediction. Ji et al. [15] developed an ANN model to predict corrosion rates of steel in dynamic environment, demonstrating improved accuracy over traditional empirical models. Akhlaghi et al. [16] utilized ANNs to estimate the pitting corrosion of steels, considering factors such as soil characteristics and pipe type of buried transmission pipelines.

The Pitting Resistance Equivalent Number (PREN) is a widely accepted parameter used to estimate the pitting corrosion resistance of stainless steels based on their chemical composition, particularly the contents of chromium, molybdenum, and nitrogen. However, PREN alone does not account for environmental factors that significantly influence corrosion behavior. Incorporating environmental variables into predictive models is essential for a more accurate assessment of corrosion risk.

In this study, statistical models were developed using linear regression and artificial neural networks to predict the pitting potential and polarization curves of austenitic stainless steels (316L, 904L, and AL-6XN) under various environmental conditions. By considering factors such as temperature, chloride ion concentration, pH, and PREN, we seek to establish reliable predictive tools that can aid in material selection and corrosion prevention strategies. The linear regression model will help identify the significant factors and their linear relationships with the pitting potential, while the ANN model will capture the nonlinear behaviors and interactions among the variables to predict the entire polarization curve.

This study involves conducting potentiodynamic polarization tests to generate experimental data across a full factorial design of experiments, ensuring that all combinations of factors and levels are considered. Statistical analysis, including analysis of variance (ANOVA), is performed to evaluate the significance of each factor and interaction. The models are then validated using separate datasets to assess their predictive performance.

By integrating statistical methods and machine learning techniques, this study contributes to the advancement of predictive corrosion modeling and provides valuable insights into the corrosion mechanisms of austenitic stainless steels under diverse conditions.

2. Materials and Methods

2.1. Materials and Specimen Preparation

In this study, the stainless steels used were STS 316L, 904L, and AL-6XN, with their chemical compositions provided in Table 1. For stainless steels, the Pitting Resistance Equivalent Number (PREN), which indicates resistance to localized corrosion based on chemical composition, can be calculated using Equation (1) [14]. To quantify the corrosion characteristics of each stainless steel as variables, the PRENs were applied; the PRENs of 316L, 904L, and AL-6XN are 24, 34, and 45, respectively. Each specimen was machined to

dimensions of 20 mm × 20 mm, polished up to #600 grit SiC abrasive paper, cleaned with distilled water, and stored in an oven.

$$PREN = \%Cr + 3.3\%Mo + 16\%N \quad (1)$$

Table 1. Chemical composition (wt.%) for steels.

Material	PREN	C	Si	Mn	Ni	Cr	Mo	Cu	N	Fe
316L	24	0.019	0.58	1.07	10.23	16.76	2.03	0.3	-	Bal.
904L	34	0.02	0.64	1.53	24	19.27	4.21	1.3	0.04	Bal.
AL-6XN	45	0.016	0.63	0.28	23.8	21.7	6.6	0.19	0.21	Bal.

2.2. Potentiodynamic Polarization Test

Potentiodynamic polarization tests were conducted to evaluate the electrochemical properties of each specimen under various experimental variables. A three-electrode corrosion cell was configured using a working electrode (specimen with an exposed area of 1.36 cm^2), a reference electrode (Ag/AgCl sat. KCl), and a counter electrode (platinum mesh of 20 mm × 20 mm size). Polarization was performed at a 1.67 mV/s scan rate, starting from −0.25 V vs. the open-circuit potential (OCP) up to a maximum of 1.2 V, after an initial stabilization period of 1800 s.

2.3. Statistical Approach

To obtain the training, validation, and test data for the ANN model, a full factorial model with four factors at three levels was designed. It includes experiments for all combinations of factors and levels [17]. This approach allows for the detection of main effects and interactions, enabling the derivation of regression equations with high reliability for various combinations of levels [18]. The full factorial design used in this study is presented in Tables 2 and 3. To adjust the levels of each factor, the Cl^- ion concentration was controlled using NaCl, and the pH was adjusted using hydrochloric acid. Each factor level was normalized to a value between 0 and 1 using Equation (2).

$$X = (x - x_{min})/(x_{max} - x_{min}) \quad (2)$$

Table 2. Experimental independent factor and their levels.

Factors	Unit	Level (Normalized Value)		
PREN (A)		24 (0)	34 (0.5)	45 (1)
Temperature (B)	°C	30 (0)	60 (0.5)	90 (1)
Cl^- concentration(C)	g/L	20 (0)	30 (0.5)	40 (1)
pH (D)		2 (0)	4 (0.5)	6 (1)

Table 3. Full factorial design matrix and experiment results.

Exp. No. (PREN)			Factor			$E_{corr.}$, V	E_{pit}, V	E_{range}, V
			Temp., °C	Cl^-, g/L	pH			
1 (24)	28 (34)	55 (45)	30	20	2	0.072	0.354	0.282
2 (24)	29 (34)	56 (45)	30	20	4	−0.029	0.279	0.308
3 (24)	30 (34)	57 (45)	30	20	6	−0.043	0.265	0.308
4 (24)	31 (34)	58 (45)	30	30	2	−0.085	0.277	0.362
5 (24)	32 (34)	59 (45)	30	30	4	−0.07	0.272	0.342
6 (24)	33 (34)	60 (45)	30	30	6	−0.081	0.309	0.39
7 (24)	34 (34)	61 (45)	30	40	2	−0.098	0.225	0.323

Table 3. *Cont.*

Exp. No. (PREN)			Factor			$E_{corr.}$, V	E_{pit}, V	E_{range}, V
			Temp., °C	Cl^-, g/L	pH			
8 (24)	35 (34)	62 (45)	30	40	4	−0.066	0.285	0.351
9 (24)	36 (34)	63 (45)	30	40	6	0.034	0.357	0.323
10 (24)	37 (34)	64 (45)	60	20	2	−0.13	0.152	0.282
11 (24)	38 (34)	65 (45)	60	20	4	−0.062	0.213	0.275
12 (24)	39 (34)	66 (45)	60	20	6	−0.118	0.146	0.264
13 (24)	40 (34)	67 (45)	60	30	2	−0.167	0.13	0.297
14 (24)	41 (34)	68 (45)	60	30	4	−0.116	0.065	0.181
15 (24)	42 (34)	69 (45)	60	30	6	−0.108	0.11	0.218
16 (24)	43 (34)	70 (45)	60	40	2	−0.117	0.091	0.208
17 (24)	44 (34)	71 (45)	60	40	4	−0.114	0.085	0.199
18 (24)	45 (34)	72 (45)	60	40	6	−0.295	0.123	0.418
19 (24)	46 (34)	73 (45)	90	20	2	−0.149	0.029	0.178
20 (24)	47 (34)	74 (45)	90	20	4	−0.157	0.065	0.222
21 (24)	48 (34)	75 (45)	90	20	6	−0.134	0.081	0.215
22 (24)	49 (34)	76 (45)	90	30	2	−0.166	0.043	0.209
23 (24)	50 (34)	77 (45)	90	30	4	−0.149	0.034	0.183
24 (24)	51 (34)	78 (45)	90	30	6	−0.114	0.055	0.169
25 (24)	52 (34)	79 (45)	90	40	2	−0.164	0	0.164
26 (24)	53 (34)	80 (45)	90	40	4	−0.107	0.015	0.122
27 (24)	54 (34)	81 (45)	90	40	6	−0.148	0.034	0.182

Here, x is the normalized value and x_{max} and x_{min} are the maximum and minimum values of each level. In the full factorial design with four factors at three levels, a total of 81 (3^4) experiments were required. To ensure the reliability of each test result, experiments were performed in duplicate. The influence and significance of each factor and level were evaluated through analysis of variance (ANOVA) at a 95% confidence level [19]. Statistical analysis of the full factorial design and data was conducted using Minitab® 19 software (Minitap, LLC, State College, PA, USA).

2.4. ANN

ANN method employing the backpropagation algorithm for supervised learning was utilized. Figure 1 illustrates the general structure of the neural network, which is a multilayer perceptron (MLP) consisting of an input layer, hidden layers, and an output layer. The activation functions used for each hidden layer were the sigmoid and hyperbolic tangent (tanh) functions. The data were divided into training, validation, and test sets at ratios of 80%, 10%, and 10%, respectively, and were randomly partitioned in each training process. The design and implementation of the neural network were carried out using Python 3.7 and the TensorFlow 2.0 library. The cost function for training process was the mean squared error (MSE) as shown in Equation (3). Here, n is the number of outputs in the training set, $X(t)$ is the actual value of the data, and $X'(t)$ is the predicted value from the model. For the optimization of the cost function, the Adam (Adaptive Moment Estimation) algorithm, known for its superior performance, was employed.

$$\frac{1}{n}\sum_1^n \left(X(t) - X'(t)\right)^2 \quad (3)$$

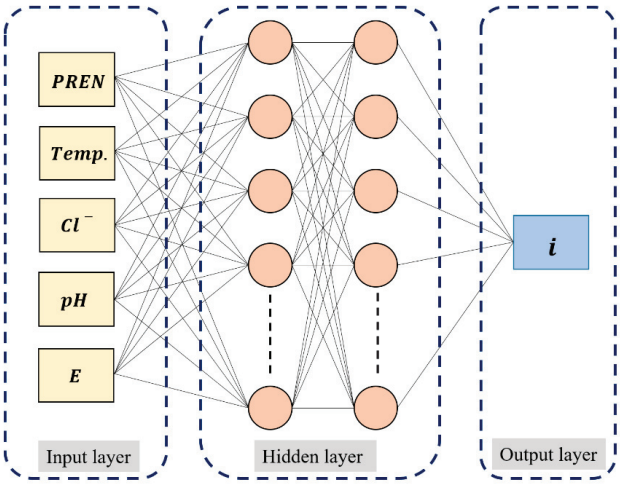

Figure 1. Schematic diagram for ANN architecture used for modeling polarization curves.

3. Results and Discussion

3.1. Potentiodynamic Polarization Curves

Figure 2 presents the polarization curves corresponding to specific factor levels to observe the impact of factor levels on changes in pitting behavior. In each graph, the levels of other factors are held constant except for the specific factor being varied. The critical pitting potentials obtained from each polarization curve, along with the current densities at each potential, were used as training data for linear regression and ANN. Generally, the polarization curves were divided into an anodic region where current density increases with rising potential, a plateau region of constant current density, and a region of rapid current density increase above a certain potential [20]. This behavior allows for the distinction of activation, passive, and passive breakdown regions in the anodic polarization as the potential increases [14,20]. The pitting corrosion can be predicted by comparing the pitting potential with the corrosion potential. Alloys with more noble pitting potentials typically exhibit higher pitting resistance [14,20]. On the other hand, the pitting potential is located in a less noble direction than the corrosion potential or is similar to it, the material is more susceptible to pitting corrosion. In the polarization test results corresponding to the full factorial design presented in Table 3, all pitting potentials were located in a more noble direction than the corrosion potentials, showing varying pitting potentials depending on the factor levels. As shown in Figure 2a,b, the polarization curves exhibited clear differences according to the levels of the pitting resistance equivalent number (PREN) and temperature. In contrast, Cl^- concentration and pH did not showed significant differences with changes, as depicted in Figure 2c,d. This indicates that while each factor and its levels influence the polarization characteristics, the degree of their impact varies.

3.2. Significance of Input Variables

In a four-factor model, the maximum interaction can extend up to the fourth order (term). As the order is more increases, the fit of the model to the data improves. However, the complexity of interpreting the model also increases significantly, and overfitting to the data may occur [17,21]. Therefore, the model should include appropriate orders and interactions based on the coefficients of determination (R^2) and significance of each term [22,23]. Table 4 shows the coefficients of determination corresponding to the maximum interaction orders in the full factorial model. The linear model without interactions exhibited a R^2 of 0.789 and an adjusted R^2 of 0.777. Models with second-order (quadratic) interactions or higher showed very high R^2 of 0.97 or above. The model with fourth-order (quaternary)

interactions had a R^2 of 0.996, indicating a fit close to 1. Considering the R^2 and the ease of interpretation, the model was designed to include second-order interactions.

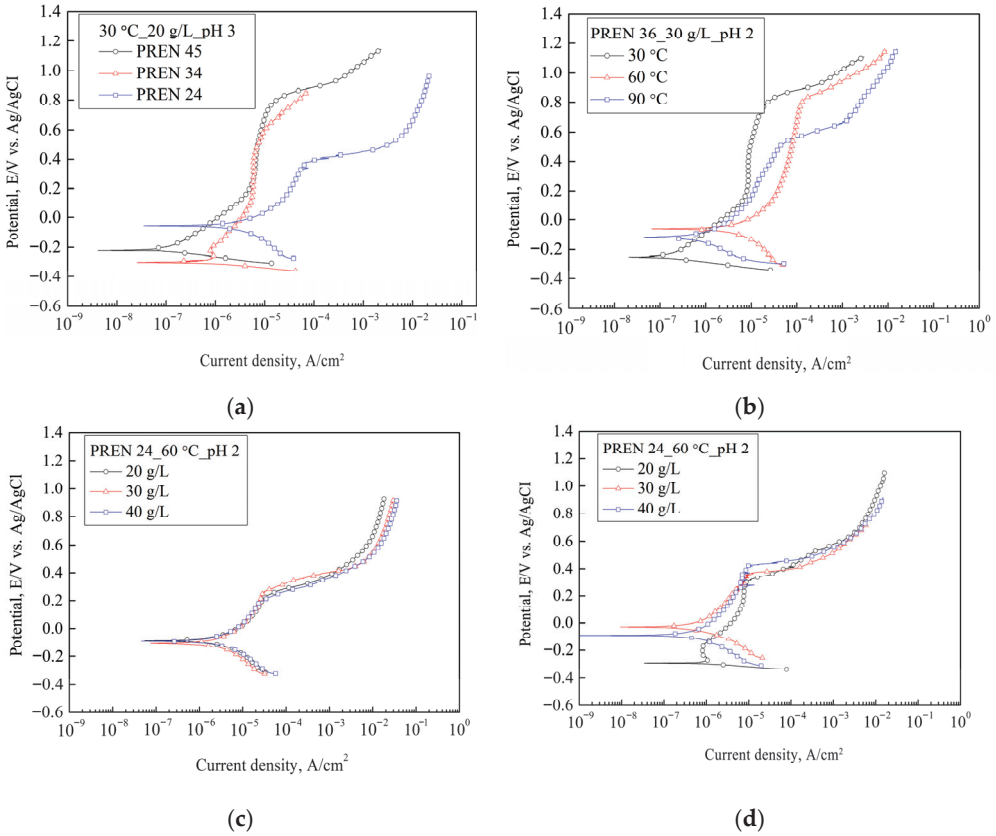

Figure 2. Potentiodynamic polarization curves with variable (**a**) PREN, (**b**) temperature, (**c**) Cl^- concentration, (**d**) pH.

Table 4. Coefficient of determination according to the interaction term of the multiple linear regression model.

Term	R^2	Adjusted-R^2
Linear	0.789	0.777
Quadratic	0.973	0.966
Cubic	0.993	0.989
Quaternary	0.996	0.993

Table 5 presents the analysis of variance (ANOVA) results for significant factors at the 95% confidence level. ANOVA [24–27] represents the dispersion of characteristic values as the sum of squares (SS) and decomposes this total sum into sums attributable to experimental factors, identifying those factors that have a particularly large effect compared to the error term. The total sum of squares can be divided into the sum of squares due to deviations of each process variable and the sum of squares due to error. The percentage contribution of each process variable's sum of squares to the total sum of squares indicates the contribution of that variable to the overall dispersion of characteristic values. Additionally, the F-value, defined as the ratio of the mean square (MS) of a process variable to the mean square of the error, indicates the importance of that process variable relative to the error.

Table 5. Result of ANOVA on the full factorial design.

Source	DF	Adj SS	Adj MS	F-Value	*p*-Value
Model	15	19.5002	1.30001	272.54	0.000
Blocks	1	0.0000	0.00004	0.01	0.926
Linear	6	15.8551	2.64252	554.00	0.000
A	2	10.0457	5.02287	1053.03	0.000
B	2	5.6797	2.83987	595.37	0.000
D	2	0.1296	0.06480	13.59	0.000
2-Way Interactions	8	3.6450	0.45563	95.52	0.000
A·B	4	3.5707	0.89267	187.15	0.000
A·D	4	0.0744	0.01859	3.90	0.005
Error	146	0.6964	0.00477		
Total	161	20.1966			
R^2				Adjusted-R^2	
96.55%				96.20%	

Here, the mean square is defined as the sum of squares of each factor divided by its degrees of freedom (DF). The most critical value in ANOVA is the *p*-value, which determines the significance of factors at the 95% confidence level, using 0.05 as the criterion. If the *p*-value is 0.05 or less, the factor is considered significant at the 95% confidence level, meaning that the levels of that factor have a significant effect on changes in the response variable. In the case of blocks, the *p*-value was 0.926, indicating that the block effect was not significant. This implies that repeated experimental values at the same level do not affect the model interpretation. Based on the ANOVA results, factors that satisfy the confidence level and their influences were identified in the full factorial design.

Figures 3 and 4 present Pareto charts illustrating the influence and significance of each input factor. The Pareto chart represents the contribution of each factor to the total contribution rate and can be calculated using Equation (4) [24]. In ANOVA at the 95% confidence level (red dashed line in Figure 3), factors A, B, D, and interactions A·B, B·D, A·D were found to be significant. The order of influence was identified as A (PREN), B (Temperature), C (pH), and D (Cl^- ion concentration). This result is consistent with the polarization curves shown in Figure 2. The Cl^- concentration increased from the minimum level (20 g/L) to the maximum level (40 g/L), the pitting potential showed an average decrease of about 30 mV. This suggests that the critical Cl^- concentration causing a sharp decrease in pitting potential is considered to be below 20 g/L. According to the literature by other researchers, Malik et al. [25] reported a decrease of 200–300 mV in the pitting potential of 316L stainless steel as the chloride ion concentration increased from 100 to 5000 ppm. Leckie and Uhlig [26] observed a decrease of 100 mV in the pitting potential of 18-8 stainless steel over a range of 0.1–1.0% chloride concentration. Ramana et al. [27] reported a decrease of about 40–60 mV in pitting potential with changes in chloride ion concentration from 17,500 to 70,000 ppm at various levels of temperature (20–60 °C) and pH (1.23–5.0). As the pH decreased from the maximum level (pH 6) to the minimum level (pH 2), the pitting potential showed an average decrease of about 64 mV. In acidic environments, a decrease in pH shifts the pitting potential in the less noble direction. However, it has been confirmed through other studies that the degree of this shift does not show a significant difference [25,27,28]. Thus, the changes in pitting potential with variations in chloride ion concentration and pH were consistent with the results reported in other studies.

$$P_i = \left(\frac{a_i^2}{\sum_{i \neq 0} a_i^2} \right) \times 100\% \quad (4)$$

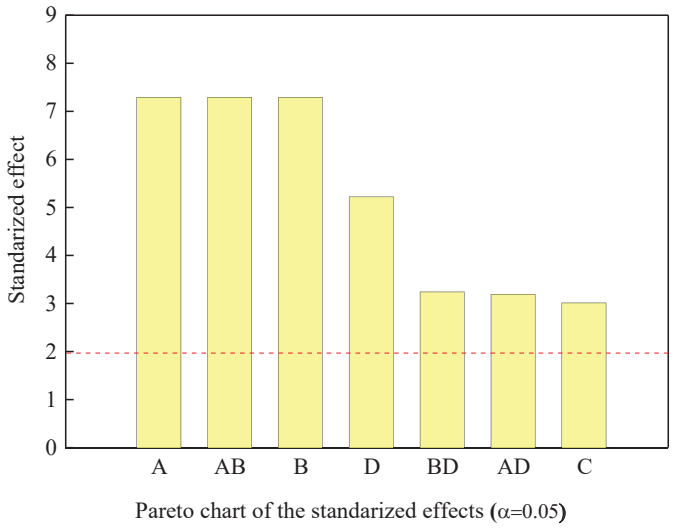

Figure 3. Pareto chart of the standardized effects of significant factors and interaction on critical pitting potential.

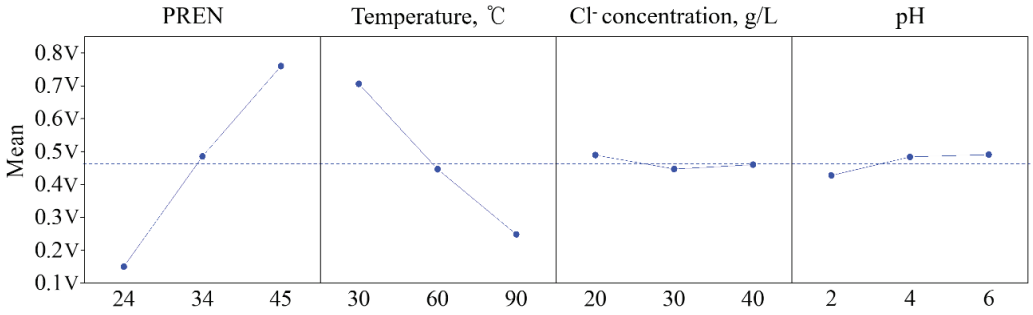

Figure 4. The main effect plots for the mean of critical pitting potential values.

3.3. Prediction of Pitting Potential Using Mathematical Regression Model

Through ANOVA, a regression equation was derived comprising factors and interactions that significantly influence the pitting potential. The first-order polynomial linear model (multiple-linear regression) consisting of four independent variables (x) and a dependent variable (y) can be expressed as Equation (5).

$$y_i = B_0 + \Sigma_{j=1}^{k} \cdot x_{ij} i = 1, 2, \cdots n \quad (5)$$

Here, β_0 and β_i are the bias and weights of the mathematical model, and x_{ij} are the input variables for each term. Table 6 presents the mathematical regression model capable of producing continuous results, along with its coefficient of determination, excluding terms for specific factor levels. The coefficient of determination for the regression model did not show significant differences depending on the inclusion of second-order or higher interactions. Instead, the linear regression model exhibited a higher coefficient of determination, indicating that a linear relationship between factor levels and pitting potential is more appropriate.

Figure 5 illustrates the probability plot between the actual and predicted data. In the probability plot, the green dotted line represents the 95% confidence interval, and the blue dashed line represents the 95% prediction interval. The confidence interval serves as a criterion for assessing the uncertainty of the regression function based on statistically limited data or data with many residuals [29]. The prediction interval serves as a criterion for assessing the uncertainty of new data values in a curve affected by noise [30]. In other words, the confidence and prediction intervals represent the probabilistic reliability

between the actual and predicted values. This confirms the high reliability and significance of predicting the pitting potential under complex environmental conditions of the factors.

Table 6. Regression models and their determination coefficient for critical pitting potential.

Term	Regression Model		
	R^2	R^2-Adjust	R^2-Prediction
Linear	$E_{pit} = 0.381 + 0.6085A - 0.458B - 0.031C + 0.063D$		
	0.779	0.774	0.76
Quadratic	$E_{pit} = 0.355 + 0.5890\ A - 0.4017\ B - 0.064\ D - 0.036\ A \cdot B + 0.0753\ A \cdot B - 0.0767\ B \cdot D$		
	0.783	0.768	0.756

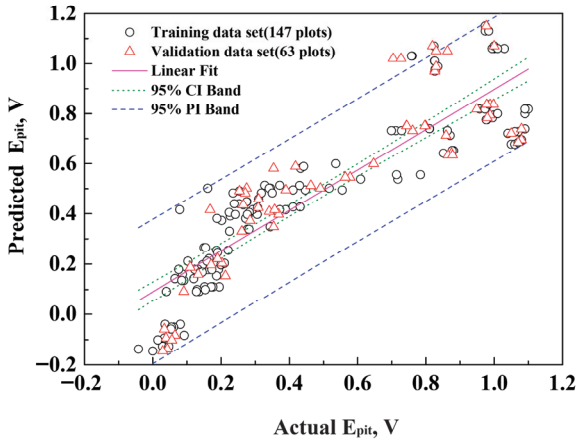

Figure 5. Comparison of actual and predicted values for critical pitting potential: training data set: 147 plots, validation data set: 63 plots.

3.4. Prediction of the Polarization Curve Using ANN

The linear functions modeled through full factorial design and analysis of variance demonstrated considerable reliability in predicting the pitting potential. However, there are limitations in modeling dynamic behaviors such as nonlinear polarization curves. ANN are highly suitable techniques for modeling data with nonlinear structures. Therefore, polarization curves at each factor level were predicted using an ANN model. Generally, ANN can perform accurate predictions with wide and deep architectures [31,32]. However, computational time and cost increase, and overfitting to the training data may occur. Therefore, selecting the optimal activation function and neuron architecture suitable for the type and complexity of the data is necessary. In previous studies on predicting dynamic polarization curves in complex environments, Hu et al. [30] used an ANN model consisting of a single hidden layer (sigmoid function) with 5 inputs and 50 neurons, and an output layer with 2 neurons. Kamrunnahar et al. [33] used a model with 7 inputs, triple hidden layers (tangent sigmoid function) consisting of 100, 100, and 50 neurons, and an output layer with 4 neurons. Wang et al. [34] employed a model with 5 inputs, double hidden layers (tangent sigmoid function) with 35 and 35 neurons, and an output layer with 4 neurons. As such, since the optimal activation function and number of neurons in hidden layers depend on the type and complexity of the data, it is very difficult to specify them. Therefore, the optimal ANN structure must be selected through numerous trials and errors. To select the optimal activation function and number of nodes suitable for the data type, activation functions such as sigmoid and tanh were used, and the ANN model was validated across various combinations.

$$sigmoid\ activation\ function: \ f(x) = \frac{1}{1+e^{-x}} = \frac{e^x}{e^x+1}$$

$$\textit{hyperbolic tangent activation function}: \ f(x) = \frac{e^{x} - e^{-x}}{e^{x} + e^{-x}}$$

Figure 6 shows R^2 of 0.9 or higher among various ANN structures. The R^2 tended to increase with the number of neurons. However, it plateaued beyond 60 neurons. Therefore, considering computational cost, an optimal number of 60 neurons was selected. Additionally, the overall structure employing sequential activation functions specifically sigmoid and tanh in a 5-60-60-1 architecture exhibited the highest R^2 of 0.972.

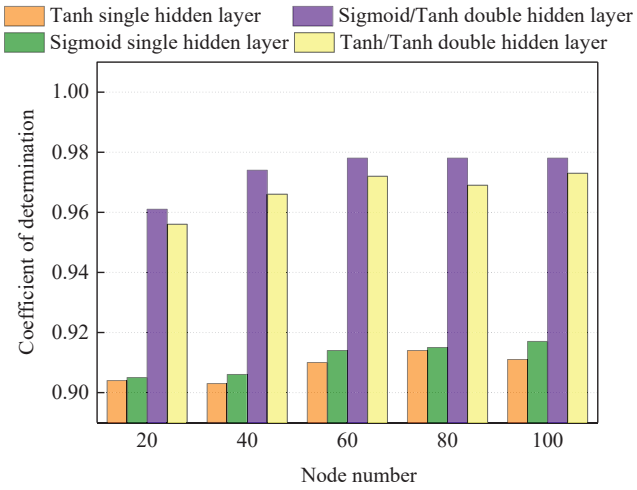

Figure 6. R^2 of ANN model with different activation functions and node numbers.

Figure 7 presents a comparison between actual and predicted values for 53,964 training data points, 5995 validation data points, and 6661 test data points. In the graph, the fit line (blue solid line) represents a perfect 100% agreement between actual and predicted data. Overall, the data points were distributed along the fit line, with coefficients of determination R^2 of 0.975, 0.968, and 0.908 for the training, validation, and test sets, respectively.

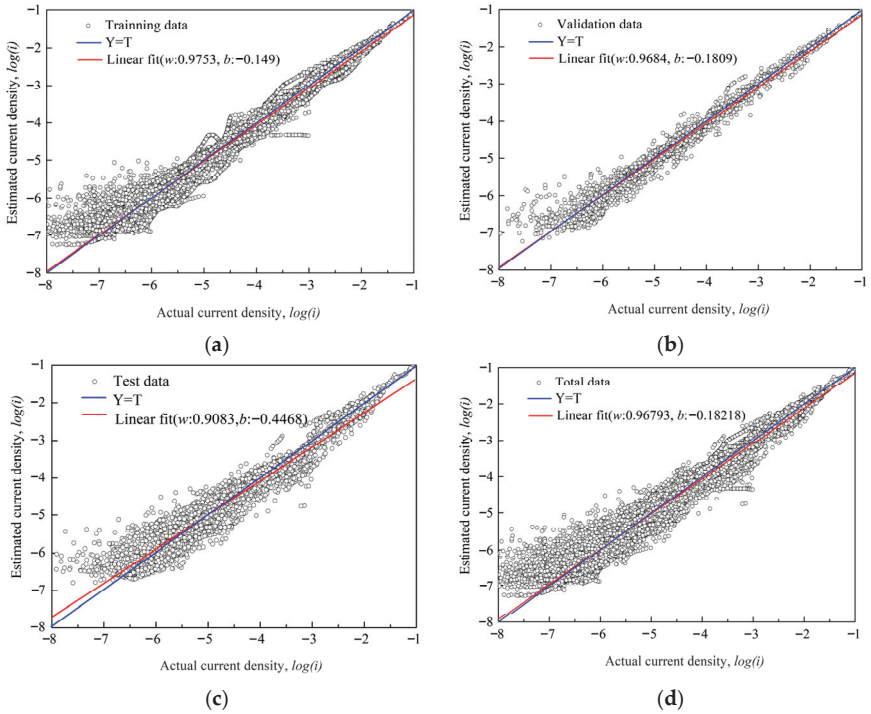

Figure 7. Comparison of actual and ANN predicted values for *log(i)*: (**a**) training data set: 53,964 plots (**b**) validation data set: 5995 plots (**c**) test data set 6661 plots, (**d**) total data set: 66,602 plots.

In Figure 7a,b, the points showed relatively high dispersion at low current densities; however, in the current density regions above 1×10^{-6} A/cm^2 where passive regions and pitting behavior occur in each polarization test—the dispersion was relatively close to the fit line.

Figure 8 compares the actual and predicted curves under test conditions included in the ANN training process to verify the training, validation, and test data. The ANN exhibited a very high degree of fit to the training data. The experimental and predicted curves were very similar in shape and matched very accurately in characteristic values such as OCP.

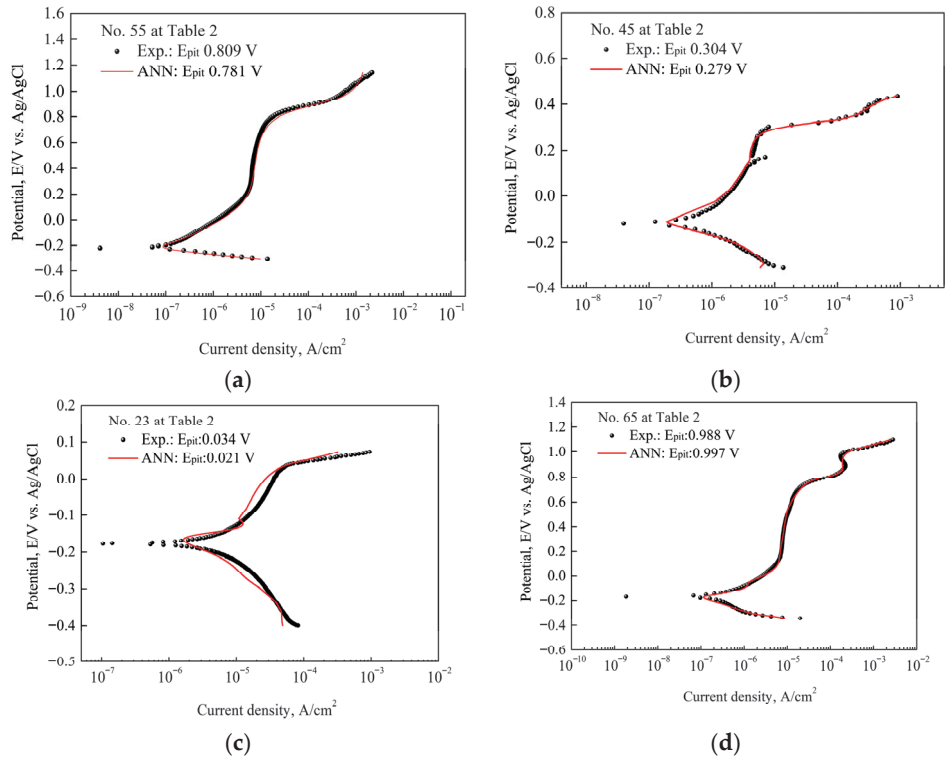

Figure 8. Experimental and ANN predicted polarization curves for some training data sets. These conditions are included in Table 3.

Figure 9 compares the experimental and predicted curves for new test conditions not included in the ANN model training. In Figure 9d, a slight deviation occurred between the two curves; however, the overall behavior and the prediction of the critical pitting potential showed a considerable tendency to match. Considering the inherent flexibility and complexity of electrochemical polarization tests, the predictive performance is judged to be of a fairly high level of reliability. Additionally, excluding the pitting resistance equivalent number (PREN), only 27 environmental variables were provided for each material, which can be considered data for some limited environments. It is anticipated that if the ANN model is trained with data from various levels, it could exhibit very high predictive performance.

In the experimental polarization curves, metastable pitting points were observed in Figures 8b and 9c, and in some experimental data, two distinct pitting stages appeared in Figures 8d and 9a,b. These features are typical of stainless steels due to their multiphase microstructures and varying electrochemical behavior. By contrast, the ANN-predicted curves smooth out such fluctuations and sharp transitions, since the model is data-driven and relies on pattern recognition rather than capturing electrochemical mechanisms. As a result, ANN predictions reproduce overall polarization trends; nevertheless, they do not

adequately reflect localized phenomena such as metastable pit initiation, phase-dependent breakdown, or passivity loss. Although oversimplified representation is a limitation of machine learning approaches, it also emphasizes their complementary role in providing reliable general trends of corrosion behavior.

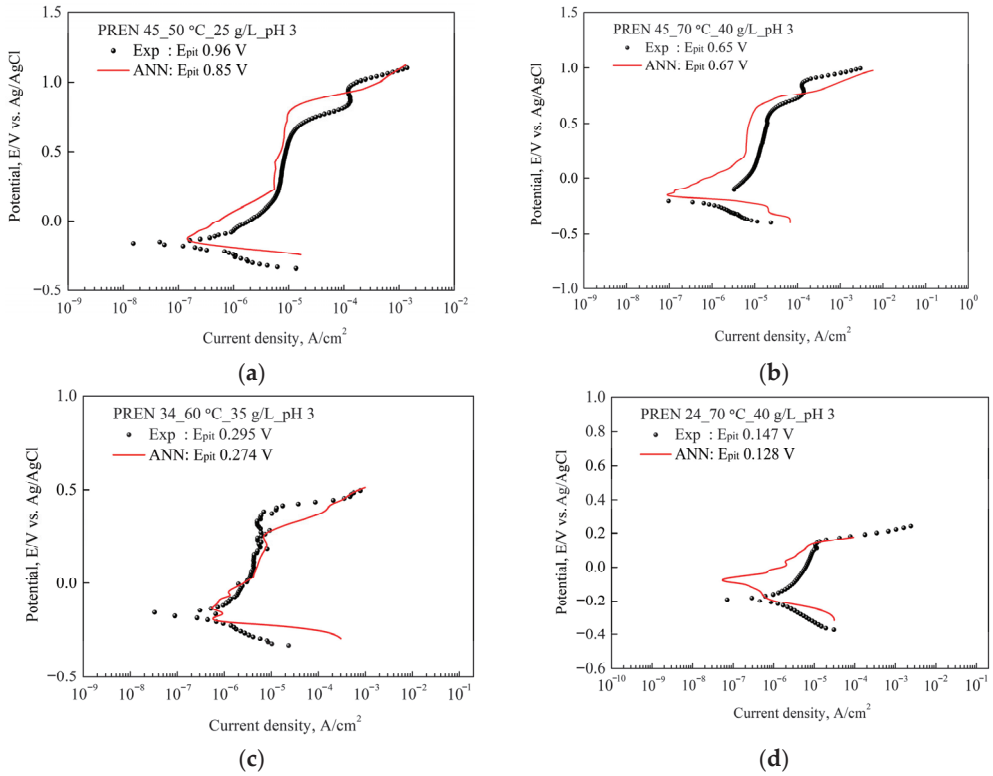

Figure 9. Experimental and ANN predicted polarization curves. These conditions are not included in Table 3 and the pitting potential. These results confirm the predictive performance of the ANN for the dynamic behavior of flexible and complex relationships like electrochemical polarization.

These findings confirm the predictive performance of the ANN for the dynamic behavior of electrochemical polarization under complex conditions. In addition, the applicability of the proposed methodology extends to the pitting corrosion examined in this study. Because both the regression and ANN models are fundamentally data-driven, they can be adapted to analyze other localized corrosion mechanisms, such as crevice corrosion or stress corrosion cracking. This flexibility highlights the potential of the approach as a versatile tool in corrosion prediction. Nevertheless, several limitations must be acknowledged. The present work was performed under controlled laboratory conditions and focused exclusively on pitting corrosion, which restricts direct extrapolation to other corrosion forms or complex field environments. Furthermore, uniform corrosion and microbiologically influenced corrosion may involve additional chemical or biological factors that are not fully represented by polarization data and thus may require further refinement of the model and broader datasets.

4. Conclusions

In this study, statistical approaches utilizing linear regression and ANN were applied to predict the pitting potential and polarization curves of austenitic stainless steels (316L, 904L, and AL-6XN) under various environmental variables, including temperature, Cl^- ion concentration, and pH.

The ANOVA confirmed that each input variable PREN ranging from 24 to 45, temperature from 30 to 90 °C, Cl^- ion concentration from 20 to 40 g/L, and pH from 2 to 6 had a significant effect on the critical pitting potential. The influence order was determined to be PREN, temperature, pH, and Cl^- ion concentration.

A linear regression model was established using significant factors and interactions identified at the 95% confidence level from ANOVA. The linear regression model exhibited a considerable predictive performance (R^2 = 0.789) in forecasting the critical pitting potential.

To predict potentiodynamic polarization curves, an ANN based on supervised learning with backpropagation was employed. The ANN model demonstrated a remarkably high predictive performance (R^2 = 0.972) for polarization curves in complex corrosion environments. The polarization curves predicted by the ANN model showed significant reliability in estimating electrochemical parameters such as corrosion current, corrosion potential, and pitting potential.

The results provide a valuable tool for predicting and understanding the corrosion behavior of stainless steels and are expected to contribute to decision-making in corrosion prevention and material selection in the future.

Author Contributions: Conceptualization, K.-H.J. and S.-J.K.; methodology, K.-H.J.; software, K.-H.J.; validation, K.-H.J.; formal analysis, K.-H.J.; investigation, K.-H.J.; resources, S.-J.K.; data curation, K.-H.J.; writing—original draft preparation, K.-H.J.; writing—review and editing, K.-H.J. and S.-J.K.; visualization, K.-H.J.; supervision, S.-J.K.; project administration, S.-J.K. All authors have read and agreed to the published version of the manuscript.

Funding: This research received no external funding.

Institutional Review Board Statement: Not applicable.

Informed Consent Statement: Not applicable.

Data Availability Statement: The original contributions presented in this study are included in the article. Further inquiries can be directed to the corresponding author.

Conflicts of Interest: The authors declare that there are no conflicts of interest.

Abbreviations

The following abbreviations are used in this manuscript:

ANN	Artificial Neural Network
PREN	Pitting Resistance Equivalent Number
ANOVA	Analysis of Variance
OCP	Open Circuit Potential

References

1. Zhao, J.; Cheng, C.Q.; Cao, T.S. Effect of Chemical Passivation Treatment and Flow on the Corrosion of 304 Stainless Steel in Hydrochloric Acid Solution. *Corros. Sci. Technol.* **2015**, *14*, 273. [CrossRef]
2. Lee, Y.H.; Kim, Y.H.; Kim, H. Crevice Corrosion Resistance of Stainless Steels in Natural Sea Water with Different Post Welding Treatment. *Corros. Sci. Technol.* **2003**, *2*, 219–224.
3. Xuan, J.; Xu, L.; Bai, S.; Zhao, T.; Xin, Y.; Zhang, G.; Li, L. Influence of Temperature on Corrosion Behavior, Wettability, and Surface Conductivity of 304 Stainless Steel in Simulated Cathode Environment of Proton Exchange Membrane Fuel Cells. *Int. J. Hydrogen Energy* **2021**, *46*, 22920–22931. [CrossRef]
4. Lei, L.; Sun, Y.; Zheng, K.; Wang, X.; He, P.; Liu, Y.; Jiang, Y. A Comparative Study on the Critical Pitting Criteria of a Super Ferritic Stainless Steel at Different Temperatures in Chloride or Bromide Solution. *Corros. Sci.* **2021**, *183*, 109311. [CrossRef]
5. Abdelfatah, A.; Raslan, A.M.; Mohamed, L.Z. Corrosion Characteristics of 304 Stainless Steel in Sodium Chloride and Sulfuric Acid Solutions. *Int. J. Electrochem. Sci.* **2022**, *17*, 220417. [CrossRef]

6. Huttunen-Saarivirta, E.; Isotahdon, E.; Que, Z.; Lindgren, M.; Mardoukhi, A.; Jorcin, J.B.; Wegrelius, L. Pitting Corrosion on Highly Alloyed Stainless Steels in Dilute Sulphuric Acid Containing Sodium Chloride. *Electrochim. Acta* **2023**, *457*, 142404. [CrossRef]
7. Kan, B.; Wu, W.; Yang, Z.; Zhang, X.; Li, J. Effects of Hydrostatic Pressure and pH on the Corrosion Behavior of 2205 Duplex Stainless Steel. *J. Electroanal. Chem.* **2021**, *886*, 115134. [CrossRef]
8. Jiménez-Come, M.J.; González Gallero, F.J.; Gómez, P.Á.; Matres, V. Prediction and Detection of Localised Corrosion Attack of Stainless Steel in Biogas Production: A Machine Learning Classification Approach. *Materials* **2025**, *18*, 1057. [CrossRef]
9. Dong, Z.; Zhang, M.; Li, W.; Wen, F.; Dong, G.; Zou, L.; Zhang, Y. Development of a Predictive Model for Carbon Dioxide Corrosion Rate and Severity Based on Machine Learning Algorithms. *Materials* **2024**, *17*, 4046. [CrossRef]
10. Song, H.; Ahmad, A.; Ostrowski, K.A.; Dudek, M. Analyzing the Compressive Strength of Ceramic Waste-Based Concrete Using Experiment and Artificial Neural Network (ANN) Approach. *Materials* **2021**, *14*, 4518. [CrossRef] [PubMed]
11. Kuppusamy, Y.; Jayaseelan, R.; Pandulu, G.; Sathish Kumar, V.; Murali, G.; Dixit, S.; Vatin, N.I. Artificial Neural Network with a Cross-Validation Technique to Predict the Material Design of Eco-Friendly Engineered Geopolymer Composites. *Materials* **2022**, *15*, 3443. [CrossRef]
12. Kolesnyk, V.; Peterka, J.; Alekseev, O.; Neshta, A.; Xu, J.; Lysenko, B.; Hrbal, J. Application of ANN for Analysis of Hole Accuracy and Drilling Temperature When Drilling CFRP/Ti Alloy Stacks. *Materials* **2022**, *15*, 1940. [CrossRef]
13. Huang, G.; Guo, Y.; Chen, Y.; Nie, Z. Application of Machine Learning in Material Synthesis and Property Prediction. *Materials* **2023**, *16*, 5977. [CrossRef]
14. McGuire, M.F. *Stainless Steels for Design Engineers*; ASM International: Novelty, OH, USA, 2008.
15. Ji, C.H.; Wang, H.; Chen, Q.; Ma, X.; Cai, Y. Corrosion Behavior Prediction for Hull Steels under Dynamic Marine Environments by Jointly Utilizing LSTM Network and PSO-RF Model. *Ocean Eng.* **2024**, *300*, 117371. [CrossRef]
16. Akhlaghi, B.; Mesghali, H.; Ehteshami, M.; Mohammadpour, J.; Salehi, F.; Abbassi, R. Predictive Deep Learning for Pitting Corrosion Modeling in Buried Transmission Pipelines. *Process Saf. Environ. Prot.* **2023**, *174*, 320–327. [CrossRef]
17. Durakovic, B. Design of Experiments Application, Concepts, Examples: State of the Art. *Period. Eng. Nat. Sci.* **2017**, *5*, 421–439. [CrossRef]
18. Farooq, M.A.; Nóvoa, H.; Araújo, A.; Tavares, S.M. An Innovative Approach for Planning and Execution of Pre-Experimental Runs for Design of Experiments. *Eur. Res. Manag. Bus. Econ.* **2016**, *22*, 155–161. [CrossRef]
19. Jankovic, A.; Chaudhary, G.; Goia, F. Designing the Design of Experiments (DOE)–An Investigation on the Influence of Different Factorial Designs on the Characterization of Complex Systems. *Energy Build.* **2021**, *250*, 111298. [CrossRef]
20. Jones, D.A. *Principles and Prevention of Corrosion*; Macmillan: New York, NY, USA, 1992.
21. Mathews, P.G. *Design of Experiments with MINITAB*; ASQ Quality Press: Milwaukee, WI, USA, 2005.
22. Zhong, K.; Meng, Q.; Sun, M.; Luo, G. Artificial Neural Network (ANN) Modeling for Predicting Performance of SBS Modified Asphalt. *Materials* **2022**, *15*, 8695. [CrossRef]
23. Nafees, A.; Javed, M.F.; Khan, S.; Nazir, K.; Farooq, F.; Aslam, F.; Vatin, N.I. Predictive Modeling of Mechanical Properties of Silica Fume-Based Green Concrete Using Artificial Intelligence Approaches: MLPNN, ANFIS, and GEP. *Materials* **2021**, *14*, 7531. [CrossRef] [PubMed]
24. dos Santos, T.C.; Gomes, D.P.P.; Bonomo, R.C.F.; Franco, M. Optimisation of Solid State Fermentation of Potato Peel for the Production of Cellulolytic Enzymes. *Food Chem.* **2012**, *133*, 1299–1304. [CrossRef]
25. Malik, A.U.; Kutty, P.M.; Siddiqi, N.A.; Andijani, I.N.; Ahmed, S. The Influence of pH and Chloride Concentration on the Corrosion Behaviour of AISI 316L Steel in Aqueous Solutions. *Corros. Sci.* **1992**, *33*, 1809–1827. [CrossRef]
26. Leckie, H.P.; Uhlig, H.H. Environmental Factors Affecting the Critical Potential for Pitting in 18–8 Stainless Steel. *J. Electrochem. Soc.* **1966**, *113*, 1262–1267. [CrossRef]
27. Ramana, K.V.S.; Anita, T.; Mandal, S.; Kaliappan, S.; Shaikh, H.; Sivaprasad, P.V.; Khatak, H.S. Effect of Different Environmental Parameters on Pitting Behavior of AISI Type 316L Stainless Steel: Experimental Studies and Neural Network Modeling. *Mater. Des.* **2009**, *30*, 3770–3775. [CrossRef]
28. Ruijini, G.; Srivastava, S.C.; Ives, M.B. Pitting Corrosion Behavior of UNS N08904 Stainless Steel in a Chloride/Sulfate Solution. *Corrosion* **1989**, *45*, 874–882. [CrossRef]
29. Dodge, Y. *The Concise Encyclopedia of Statistics*; Springer: New York, NY, USA, 2008.
30. Hu, Q.; Liu, Y.; Zhang, T.; Geng, S.; Wang, F. Modeling the Corrosion Behavior of Ni-Cr-Mo-V High Strength Steel in the Simulated Deep Sea Environments Using Design of Experiment and Artificial Neural Network. *J. Mater. Sci. Technol.* **2019**, *35*, 168–175. [CrossRef]
31. Islam, N.; Huang, W.; Zhuang, H.L. Machine Learning for Phase Selection in Multi-Principal Element Alloys. *Comput. Mater. Sci.* **2018**, *150*, 230–235. [CrossRef]
32. Géron, A. *Hands-On Machine Learning with Scikit-Learn, Keras, and TensorFlow: Concepts, Tools, and Techniques to Build Intelligent Systems*; O'Reilly Media: Sebastopol, CA, USA, 2019.

33. Kamrunnahar, M.; Urquidi-Macdonald, M. Prediction of Corrosion Behavior Using Neural Network as a Data Mining Tool. *Corros. Sci.* **2010**, *52*, 669–677. [CrossRef]
34. Wang, C.; Li, W.; Wang, Y.; Xu, S.; Yang, X. Chloride-Induced Stray Current Corrosion of Q235A Steel and Prediction Model. *Constr. Build. Mater.* **2019**, *219*, 164–175. [CrossRef]

materials

MDPI

Article

Formation of Akaganeite in Atmospheric Corrosion of Carbon Steel Induced by NaCl Particles in an 85% RH Environment

Haigang Xiao [1,*], Hongbo Zhang [1], Yan Guo [1], Hongduo Hao [1], Hao Chang [1] and Ying Li [2]

[1] Xi'an Thermal Power Research Institute Co., Ltd., Xi'an 710032, China; zhanghongbo@tpri.com.cn (H.Z.); guoyan@tpri.com.cn (Y.G.); haohongduo@tpri.com.cn (H.H.); changhao@tpri.com.cn (H.C.)
[2] Institute of Metal Research, Chinese Academy of Sciences, Shenyang 110016, China; liying@imr.ac.cn
* Correspondence: haigang001@126.com; Tel.: +86-029-82002217

Abstract

Akaganeite is the most destructive corrosion product in a rust layer, and it accelerates the corrosion rate of steel in certain atmospheres. Until now, considerable controversy has existed regarding the conditions required for its formation and its mechanism of formation. In this work, the formation of akaganeite in the specific corrosion process, which was atmospheric corrosion induced by NaCl deliquescence, was investigated through simulated experiments in a laboratory setting. Stereoscopic microscopy and scanning electron microscopy were employed to characterize the morphologies of the corrosion products, which could illuminate the morphological features of the electrolyte induced by the NaCl particles. The constituents of rust in a single droplet were analyzed by micro-Raman spectroscopy, and the components of the corrosion phases on a macroscopic scale were analyzed by XRD. The results indicate that the deliquescence of NaCl particles caused droplets to form around them, and atmospheric corrosion occurred in each droplet independently. Akaganeite can form during atmospheric corrosion induced by NaCl particles in the early stage within 12 h. The initial corrosion products, lepidocrocite and magnetite, increase the amount of akaganeite formed. The amount of salt deposited also plays an essential role in the formation of akaganeite on a macroscopic scale.

Keywords: akaganeite; atmospheric corrosion; salt

1. Introduction

Steel exposed to marine atmospheres suffers from severe atmospheric corrosion [1–7]. The composition of a rust layer determines its protective ability [6–9], and specifically, the presence of akaganeite (β-FeOOH) in the rust layer is considered one of the essential reasons for deteriorative corrosion [10–14]. However, the conditions required for its formation and its mechanism of formation in atmospheric corrosion have not yet been clarified [15,16]. Atmospheric corrosion occurs on metals within the cover of an electrolyte layer, which is an electrochemical corrosion process [17–19]. Electrolytes can form on or arrive at a metal surface by two main modes, direct deposition and sorption [20]. The formation mode of the electrolyte layer determines the features of the liquid film and subsequently influences the formation process of the corrosion products. Due to the high levels of airborne NaCl and humidity in marine atmospheres, atmospheric corrosion in these environments is frequently induced by the deliquescence of salt deposited on the surface of steel, which is a type of sorption. Thus, our investigation of the formation process and conditions of akaganeite formation in this specific process could not only elucidate the mechanism

of akaganeite formation but also allow great advances in corrosion protection methods for steel.

Deliquescence is the absorption of water vapor from a moist environment by a soluble salt to generate a liquid electrolyte. It occurs because the vapor pressure of a saturated aqueous salt solution is less than the vapor pressure of pure water [21]. Deliquescence occurs at a specific relative humidity, which is referred to as the deliquescence relative humidity, and for NaCl, that humidity is 75%. J. Weissenrieder [22] observed the fast deliquescence of NaCl crystallites at high relative humidity, and corrosion began in the droplets containing NaCl solution. Shengxi Li [23] investigated the effect of salt crystal size on atmospheric corrosion and suggested that only NaCl particles greater than 45–100 μm in diameter induced corrosion. Chunling Li [24] characterized the morphologies of corrosion products formed on weathering steel from deposited salt exposed to high-humidity environments by SEM and found that the corrosion products were essentially nodular. According to previous studies, a droplet forms around the NaCl particle in humid environments, and corrosion occurs under the droplet. Compared to the complete steel surface, the electrolyte formed by deliquescence is discontinuous and corrosion reactions proceed independently in every isolated droplet. In contrast, during direct deposition, a continuous and thick liquid film forms on the metal surface but dries out under certain environment conditions. Thus, trends in the changes in the chloride concentration and the thickness of the electrolyte layer are different in the corrosion processes induced by different electrolyte formation modes. Furthermore, according to previous studies on the conditions of akaganeite formation, sufficiently high chloride concentration [15,25,26] and oxygen supply throughout the thin liquid film to oxidize green rust [13,26–28] are required for akaganeite formation. Therefore, the formation conditions for akaganeite may be different in the two modes, and investigation of the akaganeite formation process during NaCl particle-induced atmospheric corrosion is necessary.

Until now, very few studies focused on the constituents of the corrosion products formed during NaCl particle-induced atmospheric corrosion have been published. Shengxi Li [29] identified, for the first time, the corrosion products formed on carbon steel under NaCl droplets that formed through the deliquescence of pre-deposited NaCl particles upon exposure to high humidity. They found that corrosion began under the NaCl droplets, and then lepidocrocite (γ-FeOOH) and a type of green rust formed first. This green rust was converted to lepidocrocite and magnetite (Fe_3O_4) as corrosion progressed. J. Forsberg [30] utilized time-resolved in situ X-ray spectroscopy to investigate the initial stage of atmospheric corrosion induced by deposited salt and detected a chloride-containing phase. To the best of our knowledge, the formation of akaganeite during atmospheric corrosion induced by NaCl deliquescence has not been reported previously.

Considering the factors mentioned above, the formation of akaganeite in NaCl particle-induced atmospheric corrosion has not been studied, although those conditions may be important for its formation. Additionally, the parameters that influenced this process have not been illuminated.

In the present work, the formation mechanism of akaganeite during the deliquescence process of salt deposits on steel surfaces was investigated. Samples with pre-deposited salt were exposed to a high-humidity environment (85%) to simulate the atmospheric corrosion process induced by the deliquescence of NaCl particles. Stereoscopic microscopy and SEM were employed to characterize the morphological features of the corrosion products formed in these samples. The constituents of rust in a single droplet were analyzed by micro-Raman spectroscopy, and the components of the corrosion phases over a macroscopic region were analyzed by XRD. Through the in situ Raman spectroscopy, the formation process of corrosion products was detected during the early stages of corrosion (within 12 h).

The parameters that influenced the formation of akaganeite during deliquescence were investigated by analyzing the results of simulated experiments carried out under different parameters. Furthermore, the role of initial corrosion products in the formation of akaganeite during deliquescence was also discussed.

2. Materials and Methods

2.1. Material

Samples of carbon steel Q235, which is square-shaped, with dimensions of 10 mm, 15 mm, and 5 mm, were employed in this work. The composition (wt. %) of Q235 includes C (0.176), S (0.023), P (0.019), Mn (0.57), Si (0.233), and Cu (0.033), with Fe composing the remainder. The samples were wet-polished to 1000-grade emery paper, cleaned with 95% ethanol under ultrasonication, rinsed with distilled water, dried, and stored in a moisture-free desiccator prior to use. The corrosion solution was prepared from analytically pure sodium chloride and distilled water.

2.2. Characterization of the Iron Rust Phases

To investigate the morphological features of the corrosion products formed during atmospheric corrosion induced by NaCl deliquescence, optical and SEM analyses were carried out. A Zeiss Stemi 508 (Zeiss, Jena, Germany) equipped with an Axiocam 105 Color microscopic camera (Zeiss, Jena, Germany) was utilized to obtain optical micrographs of the corrosion products formed on the samples after corrosion tests at 6.3 times and 50 times magnification. Microscopic observations were carried out using an SEM (INSPECT F50) (FEI, Eindhoven, The Netherlands) equipped with a secondary electron detector and energy-dispersive X-ray diffraction (EDX) (FEI, Eindhoven, The Netherlands). The acceleration voltage for SEM-EDX experiments was 20 kV.

Micro-Raman spectroscopy was used to analyze the constituents of the corrosion products on a microscopic scale. Micro-Raman analysis was performed on a LabRam HR800 (Horiba) Raman spectrometer (Villeneuve-d'Ascq, France)with a He-Ne gas laser (excitation wavelength 632.8 nm) coupled to a Leica microscope (Leica, Wetzlar, Germany) to focus the beam on a 1 μm diameter area, and the optical video microscope allowed for simultaneous optical imaging during Raman measurements. Raman spectra were collected in a backscattering geometry. The laser power focused through a 50× objective lens with a numerical aperture of 0.5. A 200 μm aperture and 1800 g/mm diffraction grating were used in the system. The maximum laser power was 25 mW. Because iron-containing compounds can be heated with focused laser radiation, neutral laser density filter D1 was used in order to reduce the laser power by 10 times. Thus, the laser power was 2.5 mW. A total accumulation time of 30 s was used.

Since XRD analysis allows to obtain information from corrosion products in an approximately 1 mm × 10 mm area, this technique was performed directly on the rusted steel plate to characterize the rust phases on a macroscopic scale. XRD measurements were performed with a Rigaku-D/max 2500 PC diffractometer (Rigaku, Tokyo, Japan) equipped with a Cu X-ray tube. A current of 300 mA and a voltage of 50 kV were set as the tube settings. The XRD data were collected over a 2θ range of 10° to 40° with a step size of 0.02° because the characteristic diffraction peaks for the relevant phases are in this range. The crystalline phases present in the rust formed on steels were identified from XRD patterns using the JCPDS database (Corrosion Phases 65/24988*) and Jade 5.0 software (Version number 5.0).

2.3. The Simulated Experiment Procedures

The salt particles were deposited on the sample surfaces by dispersing sodium chloride solution and evaporating the solvent. To enhance the spreadability and evaporation rate of the solution, a mixture of 50% alcohol and 50% NaCl solution was employed to wet the surfaces of the samples. After wetting the surface with 0.1 mL of the alcohol/NaCl mixture by pipette, the samples were dried in an oven at 60 °C. After ten minutes, the solvent evaporated, and crystalline salt was deposited on the surface of the steel. The amount of salt deposited was controlled by the concentration of NaCl in the solution. Considering that the salinity in real marine atmospheres can reach 1500 mg $m^{-2}d^{-1}$ according to ISO 9223 [31], the amounts of deposited salt in this study were 194.8 mg/m^2 and 1948 mg/m^2, and the concentrations of NaCl solution employed were 0.01 mol/L and 0.1 mol/L.

The samples with pre-deposited salt particles were exposed to an environment at 30 °C and 85% RH, and the conditions were maintained by a constant temperature and humidity test chamber (LRHS-101-LH) manufactured by Shanghai Linpin Instruments Co. Ltd. (Shanghai, China). After exposure to the high-humidity environment for 12 h and 24 h, samples were removed from the chamber and dried by cold wind to halt the corrosion reaction. Then, the corrosion products formed on the surfaces of the samples were characterized by each analysis technique.

3. Results and Discussion

3.1. Morphological Features of the Electrolytes Formed During Atmospheric Corrosion Induced by NaCl Deliquescence

Optical microscopy images of the corrosion products formed on the surface with 194.8 mg/m^2 of deposited NaCl after different periods during atmospheric corrosion induced by NaCl particle deliquescence are shown in Figure 1. Figure 1a shows the surface of samples after 194.8 mg/m^2 of salt was deposited. The images suggest some corrosion products formed during the salt deposition process, but the surface of the samples was flat and did not bulge. As shown in Figure 1b, discontinuous and nodular corrosion products formed on the surface of the metals, but regions without droplets were clean after 12 h of exposure to a high-humidity environment. After 24 h, corrosion products were distributed discontinuously on the metal surface. Figure 2 shows the optical observation of the corrosion results for samples with 1948 mg/m^2 of deposited NaCl after different periods of exposure during atmospheric corrosion induced by NaCl particle deliquescence. The morphologies of the corrosion products in these samples were similar to those of the samples with 194.8 mg/m^2 of NaCl.

Figure 3 shows the SEM images of the corrosion products formed after different durations of atmospheric corrosion induced by NaCl particle deliquescence. The EDS results presented in Figure 4 show that NaCl particles were detected on the surface of the samples after the salt deposition process. After 12 h of exposure to high humidity, the locations with pre-deposited salt particles had corroded. The edges of the corrosion products were round, and the corrosion products on the steel surfaces were clustered spheres. The morphologies of the corrosion products in simulated experiments confirmed that crystalline NaCl dissolved in droplets in high humidity due to deliquescence. Corrosion began in each droplet. Figure 5 shows the SEM images of samples with 1948 mg/m^2 pre-deposited salt, which are similar to those with 194.8 mg/m^2 of NaCl. The EDS results are presented in Figure 6.

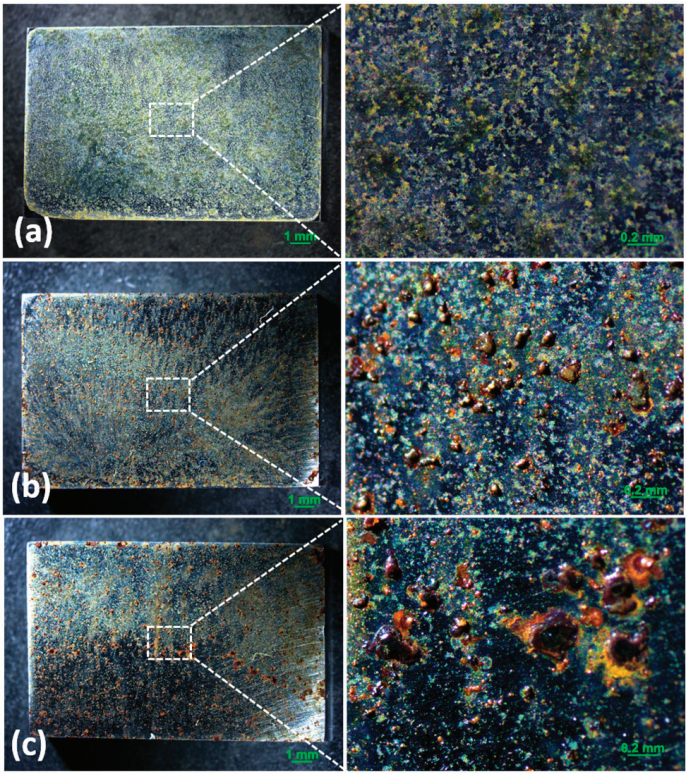

Figure 1. Optical images of the morphology of (**a**) samples with 194.8 mg/m^2 of deposited salt, (**b**) samples with 194.8 mg/m^2 of deposited salt exposed to high humidity for 12 h, and (**c**) samples with 194.8 mg/m^2 of deposited salt exposed to high humidity for 24 h.

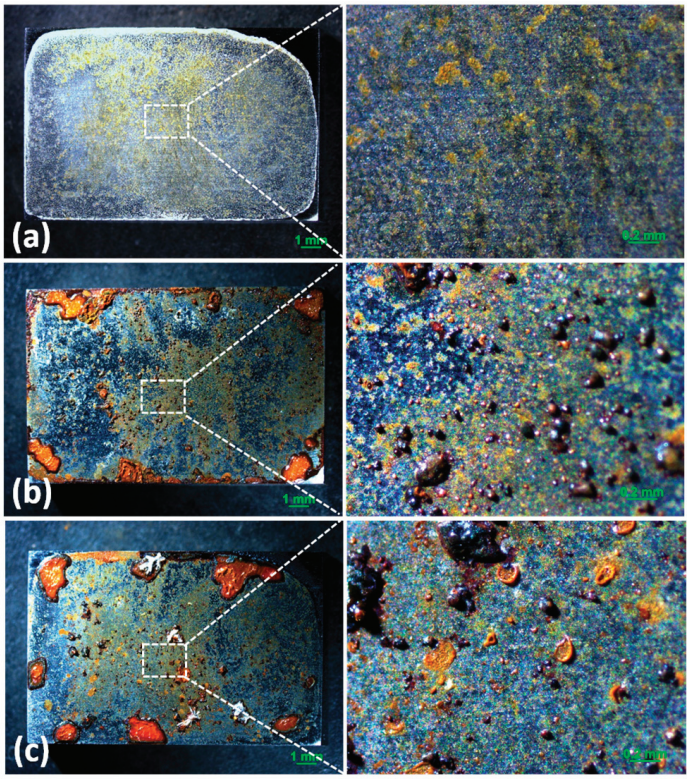

Figure 2. Optical images of the morphology of (**a**) samples with 1948 mg/m^2 of deposited salt, (**b**) samples with 1948 mg/m^2 of deposited salt exposed to high humidity for 12 h, and (**c**) samples with 1948 mg/m^2 of deposited salt exposed to high humidity for 24 h.

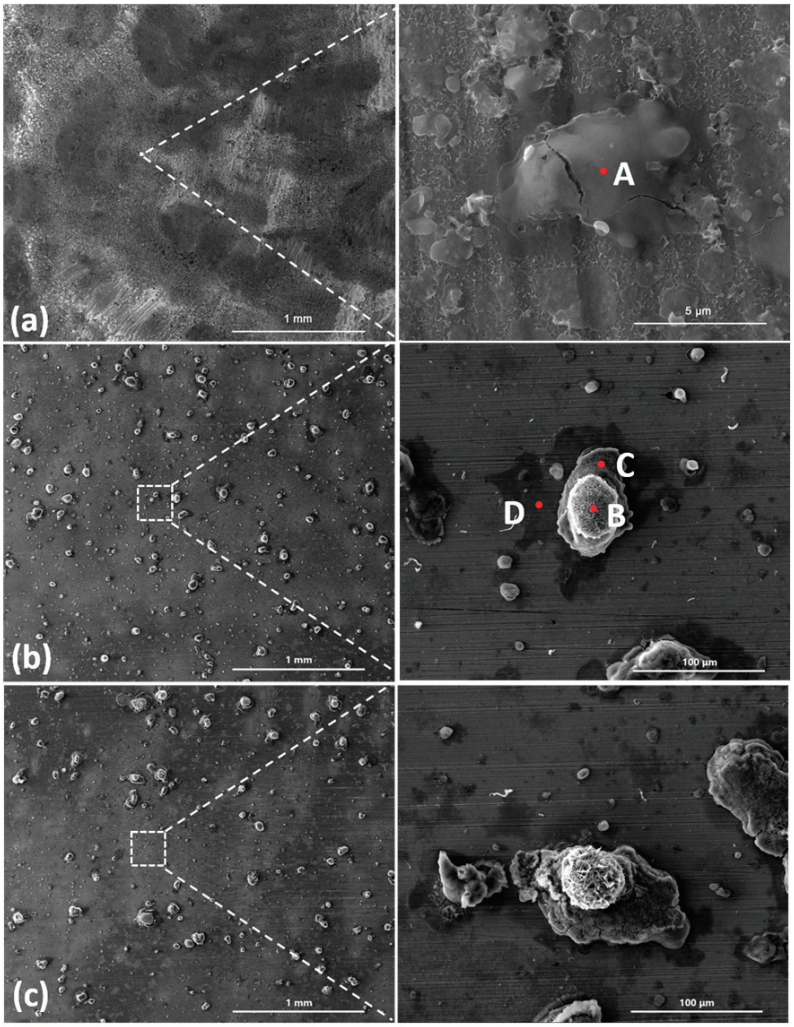

Figure 3. SEM micrographs of (**a**) samples with 194.8 mg/m^2 of deposited salt, (**b**) samples with 194.8 mg/m^2 of deposited salt exposed to high humidity for 12 h, and (**c**) samples with 194.8 mg/m^2 of deposited salt exposed to high humidity for 24 h.

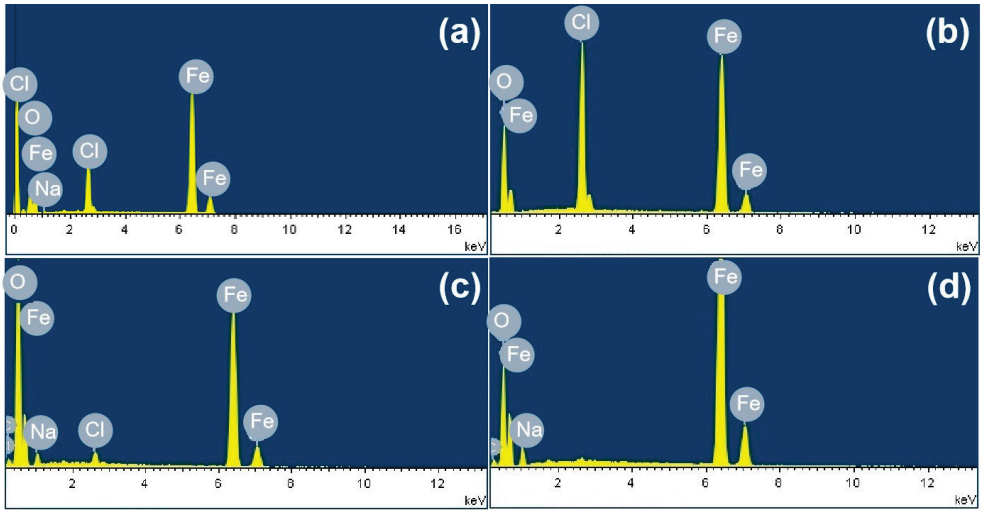

Figure 4. Elemental analysis of the rust layer: (**a**) elemental distribution at point A in Figure 3a, (**b**) elemental distribution at point B in Figure 3b, (**c**) elemental distribution at point C in Figure 3b, and (**d**) elemental distribution at point D in Figure 3b.

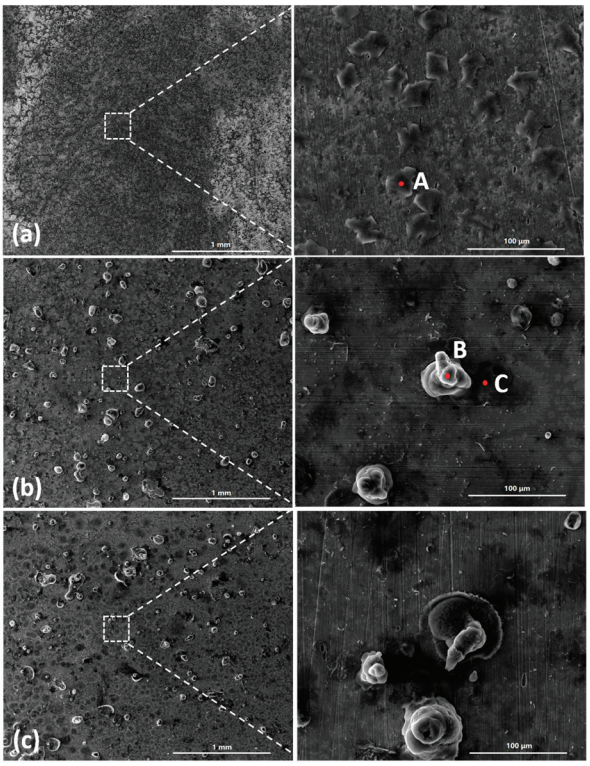

Figure 5. SEM micrographs of (**a**) samples with 1948 mg/m^2 of deposited salt, (**b**) samples with 1948 mg/m^2 of deposited salt exposed to high humidity for 12 h, and (**c**) samples with 1948 mg/m^2 of deposited salt exposed to high humidity for 24 h.

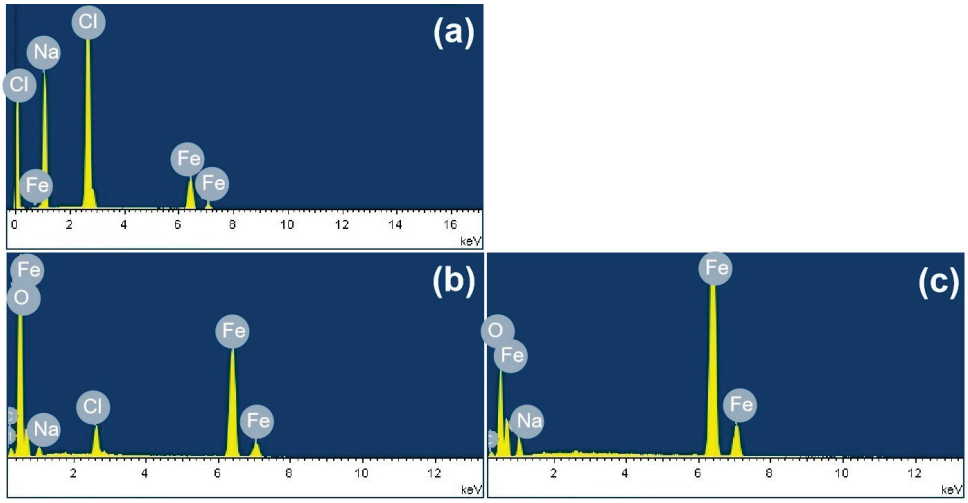

Figure 6. Elemental analysis of the rust layer: (**a**) elemental distribution at point A in Figure 5a, (**b**) elemental distribution at point B in Figure 5b, and (**c**) elemental distribution at point C in Figure 5b.

Based on the SEM observations of samples with NaCl particles and relevant EDS results, the NaCl particles deposited on the surfaces of the metals after evaporation of the NaCl solution were isolated. When the relative humidity of the surrounding environment exceeded the deliquescence point, droplets formed around the NaCl particles due to deliquescence. Corrosion occurred, and corrosion products formed in each droplet. Therefore, after the solvent was evaporated from the electrolyte, the corrosion products were spherical, and clusters were observed. The optical microscopy images and SEM observations also demonstrated that the electrolytes formed during atmospheric corrosion induced by NaCl deliquescence were discontinuously dispersed on the surfaces. In the atmospheric

corrosion process induced by precipitation, a continuous electrolyte film formed on the surface of the metals, and the soluble substances could migrate into the solution. As a result, corrosion products formed on the whole surface of the metal as a rust layer. However, the corrosion process in each droplet induced by the deliquescence of NaCl is independent and was not influenced by other droplets. The morphological features of the electrolyte are different from those of atmospheric corrosion induced by precipitation [32].

The morphological features of the electrolyte can influence the corrosion process. On one hand, the features affect the concentration of chloride in the solution. During deliquescence, a small quantity of water forms around a salt particle, and a concentrated solution film forms. The driving force for deliquescence is the difference between the vapor pressure of a saturated aqueous salt solution and the vapor pressure of pure water. As the droplet begins to form, the droplet is saturated with chloride. As deliquescence progresses, more water joins the droplet, and the concentration of chloride decreases. Thus, the magnitude of the driving force decreased as the concentration of NaCl in the solution decreased. Consequently, the volume of a stable droplet depends on the amount of NaCl particles pre-deposited and the relative humidity of the environment. Initially, the volume of the electrolyte is limited, and the concentration of chloride stays relatively high in the droplet. Corrosion reactions occurred in each droplet because they were small and rich in chloride. On the other hand, the small volume of droplets also guarantees sufficient oxygen supply from the surrounding environments during the corrosion process. Therefore, the morphology of the electrolyte induced by NaCl particles makes corrosion in an environment with a high concentration of chloride and a sufficient oxygen supply possible [32].

3.2. Constituents of Corrosion Products Formed in Single Droplet

As discussed in the previous section, atmospheric corrosion induced by NaCl particle deliquescence produced a large number of isolated corrosion regions, which were micrometers in size. To characterize the constituents of the corrosion products formed in single droplets during this process, micro-Raman analysis was conducted. Since some corrosion products formed during the NaCl deposition process, the constituents of these phases were studied in advance. Then, the newly generated products could be determined by comparing the variations in the constituents during the deliquescence of NaCl particles.

Figure 7 shows the optical images of the surface of the steel with 194.8 mg/m^2 of salt deposited and the micro-Raman analysis results for five representative points. The Raman spectra are named according to the number of points labeled on the optical images. From the comparison with the reference spectra of iron oxyhydroxides and oxides in the references [33–36], the peaks in points 2 and 4 were found to correspond to those of lepidocrocite (which is considered to be the initial corrosion product) at 255 and 380 cm^{-1}, which was also detected in [37,38]. In points 1, 3, and 5, no obvious corrosion products were detected. Similar results were observed on the surface with 1948 mg/m^2, lepidocrocite was detected at points 6 and 8, and no products were formed at the other points. Lepidocrocite was the only corrosion product formed during the salt deposition process. No akaganeite was obtained on the metal surfaces during the salt deposition process.

Then, micro-Raman analysis was carried out on the sample that had been exposed to an environment with 85% RH for 12 h with 194.8 mg/m^2 of pre-deposited salt. Figure 8a,b display a cluster of corrosion products on the steel surface, with the Raman spectra from the different points labeled in the optical image. After 12 h of exposure in a high-humidity environment, newly formed peaks were detected via Raman spectroscopy at several locations, notably at 390 cm^{-1}, 680 cm^{-1}, and 725 cm^{-1}. According to references [33–36], the peak at 680 cm^{-1} in Figure 8a,b corresponds to magnetite. Referring to multiple litera-

ture sources [33–36], the characteristic Raman peaks of akaganeite typically occur around 300 cm^{-1}, 387 cm^{-1}, 413 cm^{-1}, and 725 cm^{-1}. Therefore, we speculate that the peaks detected at 390 cm^{-1} and 725 cm^{-1} may be attributed to the formation of akaganeite. Although the peak around 300 cm^{-1} is not observed in Figure 8a,b, its absence may be due to the strong absorption of laser radiation by magnetite or the small amount of akaganeite itself. At points 2, 3, 5, 6, and 9, based on the position of the newly added peak, it is speculated that akaganeite may have formed. In addition, akaganeite was absent in the peripheral region. Figure 9 displays the surface with 1948 mg/m^2 of salt deposited and the associated Raman spectra. In this case, magnetite was detected at all five points, and akaganeite may have also formed.

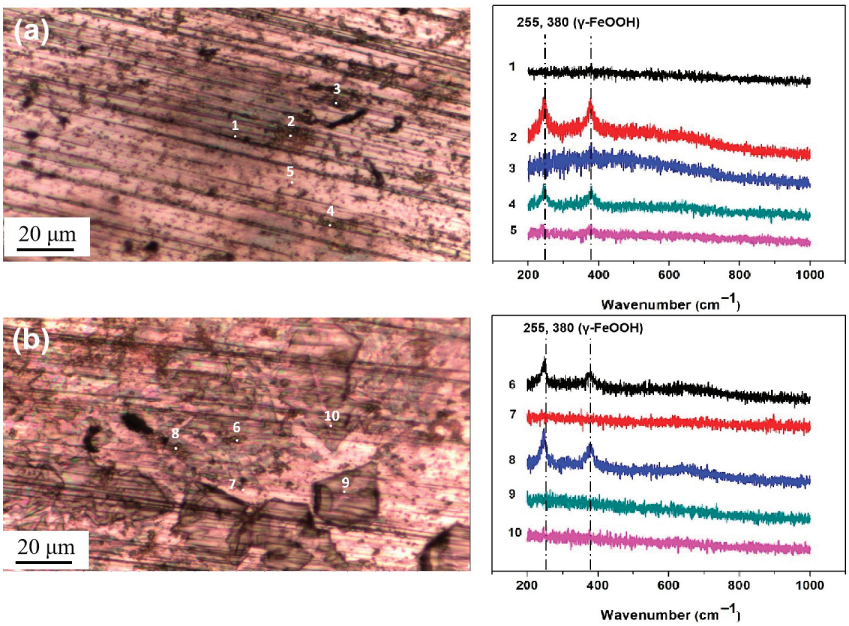

Figure 7. Micro-Raman spectra from different locations on the surface of the steel after salt deposition: (**a**) 194.8 mg/m^2; (**b**) 1948 mg/m^2.

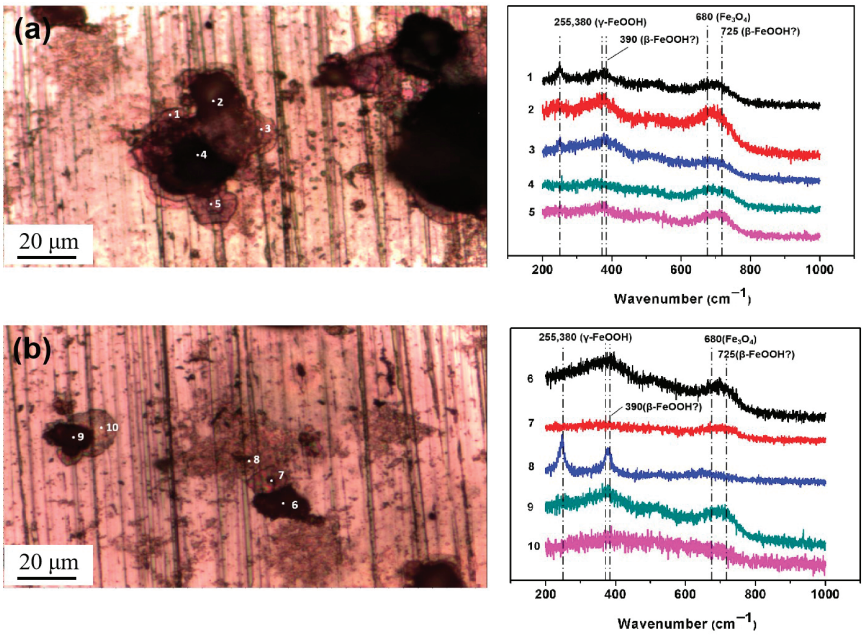

Figure 8. Micro-Raman spectra from different locations on the surface of the steel with 194.8 mg/m^2 of deposited salt that was exposed to a high-humidity environment for 12 h. (**a**) Position 1; (**b**) Position 2.

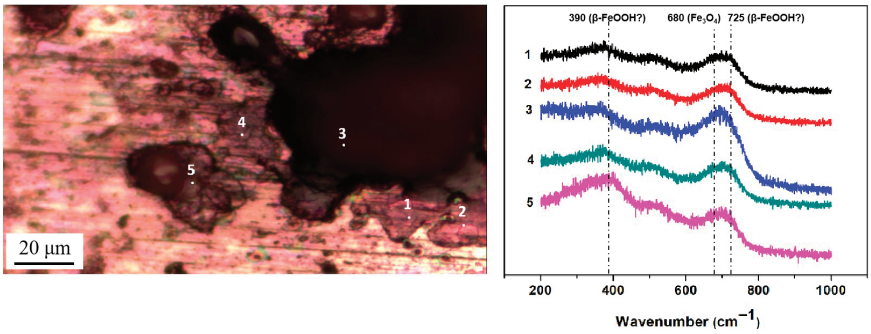

Figure 9. Micro-Raman spectra from different locations on the surface of steel with 1948 mg/m^2 of deposited salt that was exposed to a high-humidity environment for 12 h.

The results indicate that new corrosion products formed on the carbon steel surface under both salt deposition conditions (194.8 mg/m^2 and 1948 mg/m^2) after the deposited salt underwent hydrolysis in a high-humidity environment. Although spectral peaks potentially corresponding to akaganeite were detected at specific locations, its presence could not be conclusively confirmed due to a low concentration or interference from other compounds.

3.3. Parameters That Influenced the Formation of Akaganeite During Deliquescence

In the laboratory experiments, some initial corrosion products formed during the salt deposition process. The influence of the initial atmospheric corrosion products was investigated by comparison to the laboratory experiments. In group one, samples were immersed in 0.3 mol/L NaCl solution for 12 h prior to the formation of the initial corrosion products on their surface. The samples in this group were referred to as group one. In group two, samples without this treatment were employed. All these samples were subjected to the salt deposition process and exposed to a high-humidity environment for 12 h. The samples in this group were referred to as group two. Meanwhile, to analyze the effects of salt deposition, 194.8 mg/m^2 and 1948 mg/m^2 of salt were deposited in each group.

The SEM observations of the corrosion products formed on the group one substrates are displayed in Figure 10. Figure 10a,c show the initial morphologies of the surfaces after 194.8 mg/m^2 and 1948 mg/m^2 of salt had been deposited, respectively. Figure 10b,d depict the morphologies of the corrosion products formed during the deliquescence process. The EDS results are presented in Figure 11. After 12 h, raised corrosion products were formed on the steel surface, which indicated the formation of droplets due to deliquescence. The sizes of the raised corrosion products formed on the samples with initial corrosion products were larger than those on the samples without initial corrosion products.

In the previous section, the micro-Raman results suggest the possible presence of a small amount of akaganeite in each droplet. The relative amount of akaganeite was correlated with the corrosion rate [14]. Thus, it is necessary to macroscopically characterize the constituents of corrosion products. Figure 12 shows the XRD patterns of samples with different initial conditions. To compare the amount of akaganeite formed over a large area, XRD was utilized to characterize the constituents of corrosion. This technique collected the diffraction information in an area approximately 1 mm × 10 mm in size. Compared to micro-Raman spectroscopy, XRD could elucidate the constituents of the corrosion products macroscopically. The top three XRD peaks for akaganeite are 11.840°, 26.627°, and 35.150° according to JCPDS (042-1315). The top three XRD peaks for magnetite are 30.095°, 35.422°, and 62.515° according to JCPDS (019-0629). The top three XRD peaks for lepidocrocite are 14.136°, 27.080°, and 36.342° according to JCPDS (008-0098) [32]. Figure 12a,b show the XRD patterns of samples without initial corrosion products with salt amounts of

194.8 mg/m^2 and 1948 mg/m^2 being deposited, respectively. However, the intensity of the diffraction peaks was too low to assign to any specific corrosion products. In group one, to clarify the phases newly generated during deliquescence, the initial corrosion products formed by pretreatment were characterized by XRD prior to exposure to the high-humidity environment. In addition, the constituents of the initial corrosion products formed by the pretreatment were determined to be lepidocrocite and magnetite, as shown in Figure 12c. After 12 h of exposure to the high-humidity environment, the components of the samples with 194.8 mg/m^2 of salt did not change, and no peak indicative of akaganeite appeared. The identities of the constituents were not determined from XRD analysis due to the small amount of each constituent present. However, akaganeite was clearly formed on the macroscopic scale on the sample with 1948 mg/m^2 of deposited salt.

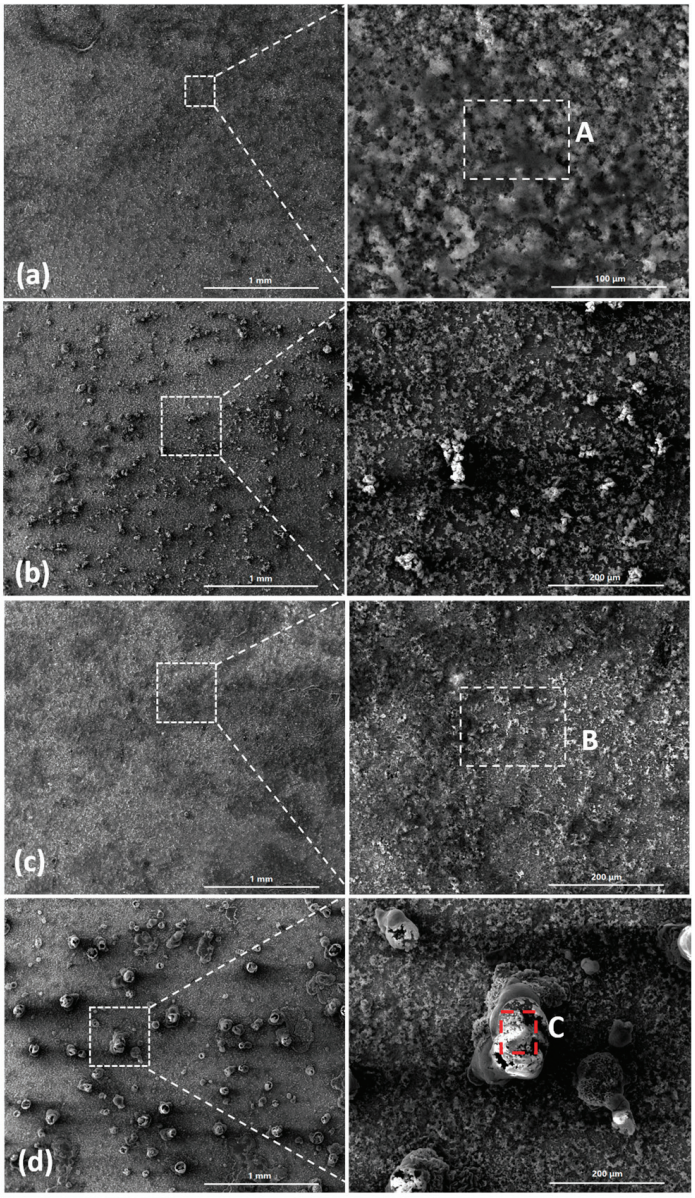

Figure 10. SEM observations of (**a**) samples with initial corrosion products and 194.8 mg/m^2 of deposited salt; (**b**) samples with initial corrosion products and 194.8 mg/m^2 of deposited salt exposed to an RH = 85% environment for 12 h; (**c**) samples with initial corrosion products and 1948 mg/m^2 of deposited salt; and (**d**) samples with initial corrosion products and 1948 mg/m^2 of deposited salt exposed to an RH = 85% environment for 12 h.

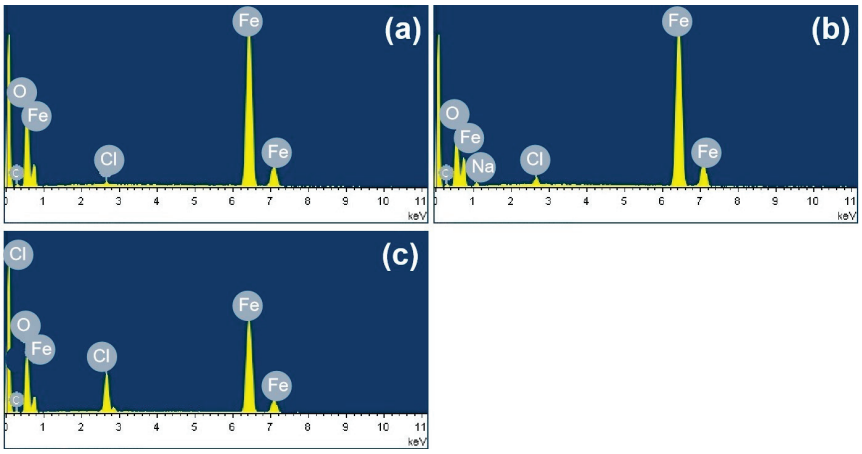

Figure 11. Elemental analysis of the rust layer: (**a**) elemental distribution of area A in Figure 10a, (**b**) elemental distribution of area B in Figure 10c, and (**c**) elemental distribution of area C in Figure 10d.

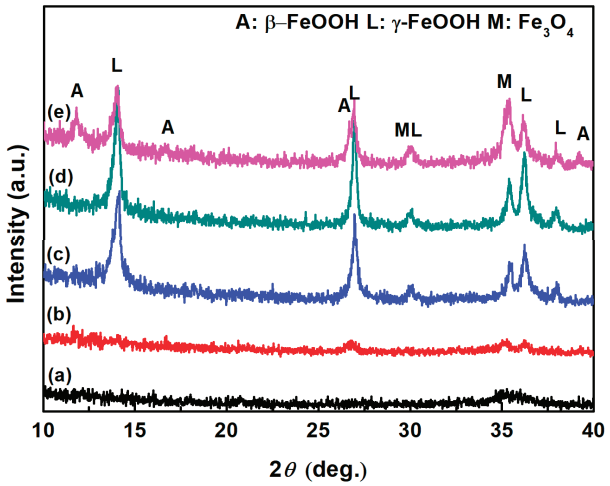

Figure 12. XRD patterns of the rust layer formed on (a) samples with 194.8 mg/m^2 of deposited salt exposed to high humidity for 12 h, (b) samples with 1948 mg/m^2 of deposited salt exposed to high humidity for 12 h, (c) samples with initial corrosion products formed by the pretreatment, (d) pretreated samples with 194.8 mg/m^2 of deposited salt exposed to high humidity for 12 h, and (e) pretreated samples with 1948 mg/m^2 of deposited salt exposed to high humidity for 12 h.

Combined with the test results of the micro-Raman analysis and XRD, the results demonstrated that akaganeite could form during the deliquescence of NaCl. High concentrations of chloride and Fe^{2+} are necessary for the formation of akaganeite [25]. Since akaganeite is a product of green rust [32], oxygen is also required as an oxidant. In each droplet, the Fe^{2+} generated by the corrosion reactions accumulated, and its concentration became quite high since the droplets were isolated and substances could not migrate. The high concentrations of oxygen and chloride satisfy the required conditions for akaganeite formation, and akaganeite was therefore formed.

In previous studies, researchers [13] suggested that akaganeite is formed during the dry periods of wet–dry cycles, and it is the product of a type of green rust. In the drying process, as the electrolyte evaporates, the concentration of chloride in the liquid increases. Additionally, the reduction in the thickness of the liquid film was beneficial for the transportation of oxygen. Both of these changes promote the formation of akaganeite. In atmospheric corrosion induced by deliquescence, the conditions are similar to those of the drying process in wet–dry cycles. The results of this study proved that akaganeite can form during atmospheric corrosion induced by deliquescence during the early stage

of corrosion (within 12 h). For the formation of akaganeite in cases with a continuous electrolyte film, an excess of salt deposited per area above the critical value was essential to guarantee the requisite high concentration of chloride in the solution. However, in atmospheric corrosion induced by deliquescence, corrosion reactions occurred in each droplet. The volumes of the droplets were correlated with the size of the NaCl particles. As a result, the concentration of chloride in each droplet was high regardless of the amount of salt deposited on the steel surface. In each droplet, the concentration of chloride was not dependent on the total salt deposited. Thus, the formation process and required conditions are different for different corrosion processes. In this case, the formation conditions and stage of akaganeite production are different from those of direct deposition.

The results also indicated that both the amount of salt deposited per area and the initial corrosion products influence the amount of akageneite formed. In atmospheric corrosion induced by deliquescence, the size and amount of NaCl particles determined the amount of electrolyte formed by deliquescence. A higher amount of deposited salt resulted in more electrolytes being generated. Thus, corrosion occurred over a larger area, which increased the number of places where akageneite was formed. As a result, macroscopic akaganeite could not be detected in the samples with less deposited salt.

To the best of our knowledge, the influence of the initial corrosion products on the formation of akaganeite has not previously been investigated [32]. In addition, we suggest that the initial corrosion products have two major effects. On one hand, the existence of lepidocrocite and magnetite vary the surface states and change the wettability of the surfaces. Capillary condensation may occur due to the porous nature of the corrosion products. On the other hand, lepidocrocite could participate in the corrosion process and be reduced to Fe^{2+}, which is the starting material for akaganeite formation. Therefore, the presence of the initial corrosion products had a substantial impact on the formation of akaganeite.

4. Summary

Raman spectroscopy and XRD have been employed to study the formation mechanism of akaganeite in the initial stage of atmospheric corrosion induced by the deliquescence of NaCl particles. Several conclusions can be drawn from the results.

In high-humidity environments, the deliquescence of NaCl particles induces the formation of droplets, and atmospheric corrosion initiated quickly under the droplets. Morphologically, the electrolytes formed under these conditions were isolated and discontinuous, which guaranteed high concentrations of chloride in the droplets and sufficient oxygen supply from the surrounding environment. Additionally, these two characteristics facilitate the formation of akaganeite. In the simulated experiments, Akaganeite can form during atmospheric corrosion induced by NaCl particles within 12 h. The initial corrosion products, lepidocrocite and magnetite, increased the amount of akaganeite formed, and the amount of salt deposited played an essential role in the formation of akaganeite on the macroscopic scale.

Therefore, in marine atmospheric environments, promptly removing the deposited salts from steel surfaces and reducing salt accumulation can prevent the formation of akaganeite during deliquescence process.

Author Contributions: Conceptualization, H.X. and Y.L.; Methodology, H.X.; Validation, H.Z., Y.G. and H.H.; Formal analysis, H.X. and Y.L.; Investigation, H.X. and H.C.; resources, H.X.; Data curation, H.X.; Writing—original draft, H.X.; Writing—review & editing, H.X.; Project administration, H.X.; Funding acquisition, H.X. All authors have read and agreed to the published version of the manuscript.

Funding: This research was funded by the Natural Science Basic Research Program of Shaanxi (Program No. 2024JC-YBQN-0469).

Data Availability Statement: The original contributions presented in this study are included in the article. Further inquiries can be directed to the corresponding author.

Conflicts of Interest: Authors Haigang Xiao, Hongbo Zhang, Yan Guo, Hongduo Hao, and Hao Chang are employed by the Xi'an Thermal Power Research Institute Co., Ltd. The remaining authors declare that the research was conducted in the absence of any commercial or financial relationships that could be construed as a potential conflict of interest.

References

1. Corvo, F.; Betancourt, N.; Mendoza, A. The influence of airborne salinity on the atmospheric corrosion of steel. *Corros. Sci.* **1995**, *37*, 1889–1901. [CrossRef]
2. Corvo, F.; Haces, C.; Betancourt, N.; Maldonado, L.; Véleva, L.; Echeverria, M.; De Rincón, O.T.; Rincon, A. Atmospheric corrosivity in the Caribbean area. *Corros. Sci.* **1997**, *39*, 823–833. [CrossRef]
3. Ma, Y.T.; Li, Y.; Wang, F.H. The effect of beta-FeOOH on the corrosion behavior of low carbon steel exposed in tropic marine environment. *Mater. Chem. Phys.* **2008**, *112*, 844–852. [CrossRef]
4. Ma, Y.; Li, Y.; Wang, F. Corrosion of low carbon steel in atmospheric environments of different chloride content. *Corros. Sci.* **2009**, *51*, 997–1006. [CrossRef]
5. Ma, Y.; Li, Y.; Wang, F. Weatherability of 09CuPCrNi steel in a tropical marine environment. *Corros. Sci.* **2009**, *51*, 1725–1732. [CrossRef]
6. Cai, S.; Ji, H.; Li, M.; Zhao, Z.; Gao, Z.; Zhu, F. Corrosion Mechanism and Simulation of Q235 Steel in Typical Marine Atmospheric Environment. *Mater. Corros.* **2025**, *76*, 1199–1217. [CrossRef]
7. Surnam, B.Y.R.; Ma, X.; Pedrazzini, S.; Bilsland, C.; Kootab, Z.S. Atmospheric Corrosion of Weathering and Mild Steels in the High Salinity Environment of Mauritius. *Surf. Interface Anal.* **2025**, *57*, 619–629. [CrossRef]
8. Paterlini, L.; Brenna, A.; Ceriani, F.; Gamba, M.; Ormellese, M.; Bolzoni, F. Atmospheric Corrosion of Different Steel Types in Urban and Marine Exposure. *Materials* **2024**, *17*, 6211. [CrossRef]
9. Wu, W.; Zhu, L.; Chai, P.; Liu, N.; Song, L.; Liu, Z.; Li, X. Atmospheric corrosion behavior of Nb- and Sb-added weathering steels exposed to the South China Sea. *Int. J. Miner. Metall. Mater.* **2022**, *29*, 2041–2052. [CrossRef]
10. Kamimura, T.; Hara, S.; Miyuki, H.; Yamashita, M.; Uchida, H. Composition and protective ability of rust layer formed on weathering steel exposed to various environments. *Corros. Sci.* **2006**, *48*, 2799–2812. [CrossRef]
11. Yamashita, M.; Maeda, A.; Uchida, H.; Kamimura, T.; Miyuki, H. Crystalline rust compositions and weathering properties of steels exposed in nation-wide atmospheres for 17 years. *J. Jpn. Inst. Met.* **2001**, *65*, 967–971. [CrossRef]
12. Kamimura, T.; Nasu, S.; Tazaki, T.; Kuzushita, K.; Morimoto, S. Mossbauer spectroscopic study of rust formed on a weathering steel and a mild steel exposed for a long term in an industrial environment. *Mater. Trans.* **2002**, *43*, 694–703. [CrossRef]
13. Nishimura, T.; Katayama, H.; Noda, K.; Kodama, T. Electrochemical behavior of rust formed on carbon steel in a wet/dry environment containing chloride ions. *Corrosion* **2000**, *56*, 935–941. [CrossRef]
14. Hara, S.; Kamimura, T.; Miyuki, H.; Yamashita, M. Taxonomy for protective ability of rust layer using its composition formed on weathering steel bridge. *Corros. Sci.* **2007**, *49*, 1131–1142. [CrossRef]
15. Morcillo, M.; Gonzalez-Calbet, J.M.; Jimenez, J.A.; Diaz, I.; Alcantara, J.; Chico, B.; Mazario-Fernandez, A.; Gomez-Herrero, A.; Llorente, I.; de la Fuente, D. Environmental Conditions for Akaganeite Formation in Marine Atmosphere Mild Steel Corrosion Products and Its Characterization. *Corrosion* **2015**, *71*, 872–886. [CrossRef]
16. Morcillo, M.; Chico, B.; Alcántara, J.; Díaz, I.; Simancas, J.; de la Fuente, D. Atmospheric corrosion of mild steel in chloride-rich environments. Questions to be answered. *Mater. Corros.* **2015**, *66*, 882–892. [CrossRef]
17. Hoerle, S.; Mazaudier, F.; Dillmann, P.; Santarini, G. Advances in understanding atmospheric corrosion of iron. II. Mechanistic modelling of wet–dry cycles. *Corros. Sci.* **2004**, *46*, 1431–1465. [CrossRef]
18. Hayashida, S.; Takahashi, M.; Deguchi, H.; Tsuchiya, H.; Hanaki, K.; Yamashita, M.; Fujimoto, S. Structure of Corrosion Product Formed on Carbon Steel Covered with $NiSO_4$-Added Resin Coating under Sulfuric Acid Mist Environment Containing Chloride. *Mater. Trans.* **2021**, *62*, 781–787. [CrossRef]
19. Zafar, F.; Bano, H.; Wahab, M.F.; Corvo, F. Mild steel corrosion behavior in a coastal megacity relevant to China Pakistan economic corridor. *NPJ Mater. Degrad.* **2023**, *7*, 37. [CrossRef]
20. Schindelholz, E.; Kelly, R.G. Wetting phenomena and time of wetness in atmospheric corrosion: A review. *Corros. Rev.* **2012**, *30*, 135–170. [CrossRef]
21. Schindelholz, E.; Risteen, B.E.; Kelly, R.G. Effect of relative humidity on corrosion of steel under sea salt aerosol proxies: II. $MgCl_2$, artificial seawater. *J. Electrochem. Soc.* **2014**, *161*, C460. [CrossRef]

22. Weissenrieder, J.; Leygraf, C. In Situ Studies of Filiform Corrosion of Iron. *J. Electrochem. Soc.* **2004**, *151*, B165. [CrossRef]
23. Li, S.X.; Hihara, L.H. Atmospheric corrosion initiation on steel from predeposited NaCl salt particles in high humidity atmospheres. *Corros. Eng. Sci. Technol.* **2010**, *45*, 49–56. [CrossRef]
24. Li, C.L.; Ma, Y.T.; Li, Y.; Wang, F.H. EIS monitoring study of atmospheric corrosion under variable relative humidity. *Corros. Sci.* **2010**, *52*, 3677–3686. [CrossRef]
25. Refait, P.; Remazeilles, C. On the formation of beta-FeOOH (akaganeite) in chloride-containing environments. *Corros. Sci.* **2007**, *49*, 844–857.
26. Xiao, H.; Ye, W.; Song, X.; Ma, Y.; Li, Y. Evolution of Akaganeite in Rust Layers Formed on Steel Submitted to Wet/Dry Cyclic Tests. *Materials* **2017**, *10*, 1262. [CrossRef]
27. Refait, P.; Genin, J.M.R. The mechanisms of oxidation of ferrous hydroxychloride beta-$Fe_2(OH)_3Cl$ in aqueous solution: The formation of akaganeite vs. goethite. *Corros. Sci.* **1997**, *39*, 539–553. [CrossRef]
28. Xiao, H.; Ye, W.; Song, X.; Ma, Y.; Li, Y. Formation process of akaganeite in the simulated wet-dry cycles atmospheric environment. *J. Mater. Sci. Technol.* **2017**, *34*, 1387–1396. [CrossRef]
29. Li, S.; Hihara, L.H. In situ raman spectroscopic study of NaCl particle-induced marine atmospheric corrosion of carbon steel. *J. Electrochem. Soc.* **2012**, *159*, C147. [CrossRef]
30. Forsberg, J.; Hedberg, J.; Leygraf, C.; Nordgren, J.; Duda, L.C. The Initial Stages of Atmospheric Corrosion of Iron in a Saline Environment Studied with Time-Resolved In Situ X-Ray Transmission Microscopy. *J. Electrochem. Soc.* **2010**, *157*, C110. [CrossRef]
31. *ISO 9223:1992*; Corrosion of Metals and Alloys Corrosivity of Atmospheres—Classication. ISO: Geneva, Switzerland, 1992.
32. Xiao, H.; Ye, W.; Song, X.; Wang, Y.; Ma, Y.; Li, Y. Determination of the key parameters involved in the formation process of akaganeite in a laboratory-simulated wet-dry cyclic process. *Corros. Sci.* **2017**, *128*, 130–139. [CrossRef]
33. Ohtsuka, T.; Tanaka, S. Monitoring the development of rust layers on weathering steel using in situ Raman spectroscopy under wet-and-dry cyclic conditions. *J. Solid State Electr.* **2015**, *19*, 3559–3566. [CrossRef]
34. Cambier, S.M.; Verreault, D.; Frankel, G.S. Raman investigation of anodic undermining of coated steel during environmental exposure. *Corrosion* **2014**, *70*, 1219–1229. [CrossRef] [PubMed]
35. Morcillo, M.; Wolthuis, R.; Alcántara, J.; Chico, B.; Díaz, I.; De La Fuente, D. Scanning Electron Microscopy/Micro-Raman: A Very Useful Technique for Characterizing the Morphologies of Rust Phases Formed on Carbon Steel in Atmospheric Exposures. *Corrosion* **2016**, *72*, 1044–1054. [CrossRef]
36. Li, S.; Hihara, L.H. A Micro-Raman Spectroscopic Study of Marine Atmospheric Corrosion of Carbon Steel: The Effect of Akaganeite. *J. Electrochem. Soc.* **2015**, *162*, C495–C502. [CrossRef]
37. Hiller, J. Phasenumwandlungen im rost. *Mater. Corros.* **1966**, *17*, 943–951. [CrossRef]
38. Misawa, T.; Asami, K.; Hashimoto, K.; Shimodaira, S. The mechanism of atmospheric rusting and the protective amorphous rust on low alloy steel. *Corros. Sci.* **1974**, *14*, 279–289. [CrossRef]

materials

MDPI

Article

Study on Multi-Factor Coupling Fatigue Properties of Weathering Steel Welded Specimens

Shuailong Song [1,2], Guangchong Qin [2], Tao Lan [2,*], Zexu Li [2], Guangjie Xing [3] and Yanchen Liu [1,2]

[1] School of Civil Engineering, Qingdao University of Technology, 777 Jialingjiang East Road, Huangdao District, Qingdao 266520, China; ovossl@163.com (S.S.); yanzhao3255@163.com (Y.L.)
[2] CSSC International Engineering Co., Ltd., 1 North Courtyard, Shuangqiao Middle Road, Chaoyang District, Beijing 100121, China; qinguangchong@126.com (G.Q.); lizexu@csic602.com.cn (Z.L.)
[3] School of Civil Engineering, Xian University of Architecture & Technology, No. 13 Yanta Road, Beilin District, Xi'an 710055, China; xingguangjie@cmhk.com
* Correspondence: mailto:qd_lantao@163.com; Tel.: +86-136-9356-8577

Abstract

Environmental factors significantly affect the fatigue performance of weathering steel welded components in high-altitude, low-temperature corrosive environments. This study conducted multi-factor-coupled constant-amplitude fatigue tests on Q500qENH weathering steel V-groove welded joints and built an equivalent finite element model using test data to explore key influencing factors under multi-condition coupling. Results show that stress level most significantly affects fatigue performance, followed by corrosion duration, then ambient temperature, with influences decreasing in turn. Analyzing 18-day cyclic immersion corrosion morphology predicts 21-year outdoor corrosion in plateau regions, providing a reliable method for long-term exposure prediction. Finite element simulations confirm that low temperatures improve slightly corroded specimens' fatigue performance by 20%, but damage accumulates before optimal service. This study offers key parameters for safe design of high-altitude weathering steel welded components.

Keywords: Q500qENH weathering steel; high-altitude low-temperature corrosion; fatigue test; crack propagation; fatigue life degradation mechanisms; scanning electron microscopy

1. Introduction

The western plateau region of China is characterized by pronounced annual and diurnal temperature variations [1], abundant summer rainfall, and intense solar radiation, all of which adversely affect the service life of steel bridges in high-altitude areas [2,3]. Compared with traditional coated steel, weathering steel incorporates corrosion-resistant alloying elements (e.g., Cu, P, Mo, Cr, Ni) [4], whose corrosion products and morphological characteristics depend significantly on alloy composition and atmospheric conditions [5]. In corrosive environments, this weathering steel forms a double-layered rust structure [6]: the outer layer is a porous iron oxide layer (with compounds like FeO and Fe_2O_3), while the inner layer is a dense amorphous FeOOH protective film. This process facilitates forming a protective passive film on the steel surface, which effectively prevents the underlying alloy from further corrosion [7]. This film effectively isolates the uncorroded steel substrate from further contact with corrosive media, significantly reducing ongoing corrosion rates [8,9]. Thus, over a 100-year service life, the adoption of uncoated weathering steel can reduce coating costs by more than 6.00%, rendering it an increasingly preferred material in bridge construction [10].

Corrosion reduces the cross-sectional area of weathering steel, and induces stress concentrations at pits, thereby degrading fatigue performance. For instance, Zhang et al. [11] conducted fatigue tests on corroded Q345NH weathering steel, finding 22.60% to 38.30% degradation in fatigue strength compared to uncorroded specimens. When environmental temperatures fall below the material's ductile-to-brittle transition threshold, further cooling reduces steel plasticity, diminishing alloy ductility and shortening fatigue life. Notably, Zhang et al. [12] performed high-cycle fatigue tests on Q500qENH weathering steel across temperatures from 19.85 °C to −60.15 °C. Their research revealed that within this range, decreasing temperatures cause metal atoms to enter lower-energy states, increasing dislocation migration resistance and cold brittleness. This enhances resistance to plastic deformation while paradoxically extending fatigue life. Within a certain range, an increase in the metal's resistance to plastic deformation can extend its fatigue life; if the resistance to plastic deformation becomes excessively strong, it may lead to increased brittleness, thereby shortening the metal's fatigue life. The extension of fatigue life typically requires the metal to release stress concentration through localized plastic deformation under cyclic loading. Excessive resistance to plastic deformation may inhibit this stress release, instead accelerating crack initiation.

In the application scenarios of weathering steel materials, welding of weathering steel components is frequently required. Although the introduction of corrosion-resistant alloying elements can enhance the corrosion resistance of weathering steel, some of these elements are affected by high welding temperatures, causing the microstructure to gradually deteriorate the weldability of weathering steel. During the welding process, this leads to segregation of alloying elements and gradient differences in cooling rates [13], resulting in defects such as lack of fusion and porosity in weathering steel components. The surface of the weld seam exhibits a highly irregular state, with each irregularity forming a notch. Each notch has both a local and global effect, as the number of notches influences the number of cracks triggered. Consequently, this causes a reduction in the fatigue life of the welded joint specimens [14]. After welding, the cooling process inevitably generates welding residual stresses in the weld zone. These stresses may induce stress concentration effects between the weld zone and the base material zone, further promoting crack initiation and propagation. Therefore, when monotonic stress is applied to welded joint specimens in fatigue testing, the location of maximum stress is prone to occur in the transition zone between the weld seam and the base material [15]. Zhang [16] conducted a comparative study on the fatigue performance of Q345NH weathering steel base metal, butt joints, and cruciform joints. The results showed that welding materials and welding process parameters exert a significant influence on the fatigue performance of weathering steel. The toughness degradation of weld metal was identified as the primary factor leading to reduced fatigue life of joints. Liao et al. [17] conducted fatigue crack growth tests on Q345qD bridge steel and its butt welds across multiple temperature zones (room temperature, −20.15 °C, and −60.15 °C). The results demonstrated that while decreasing environmental temperature reduced the crack growth rate in base metal, the weld joint region exhibited a significant increase in crack growth rate with temperature reduction due to the coupled effects of microstructural inhomogeneity and residual stresses. This reveals the unique evolution mechanism of fatigue damage in welded joints under low-temperature environments.

In summary, this study investigates crack propagation in V-groove welded joints of Q500qENH weathering steel under plateau low-temperature corrosive environments using an orthogonal experimental design including temperature, corrosion duration, and stress level. Constant-amplitude fatigue tests were conducted on V-groove welded joints specimens combined with SEM fractographic analysis to elucidate the damage evolution mechanisms governing crack initiation, propagation paths, and fracture characteristics. An

initial-defect-containing finite element model was established based on experimental data to simulate crack propagation processes and validate life prediction accuracy. This work provides theoretical support for safety assessment of welded weathering steel structures in plateau regions, offering significant implications for enhancing structural reliability under extreme environmental conditions.

2. Experimental Design

To investigate the variation patterns of fatigue life in weathered steel specimens with V-groove welded joints affected by corrosion under high-altitude low-temperature environments, fatigue tests were conducted on corroded V-groove welded joint specimens of weathered steel based on orthogonal experimental design. The fatigue test results were calculated and summarized, followed by comparative analysis to identify the optimal combination of influencing factors for fatigue life.

2.1. Specimen Dimension Design and Parameters

This test utilized 16 mm thick Q500qENH weathering steel plates to prepare V-groove welded joint specimens, with geometric dimensions shown in Figure 1 and base metal chemical composition detailed in Table 1. To address the welding characteristics of this high-strength bridge steel, JWER60NHQ solid wire (GMAW) with a diameter of 1.20 mm and JWS60NHQ submerged arc welding wire (SAW) with a diameter of 4 mm were selected. The chemical compositions of both wires are specified in Table 2. Take the chemical compositions of the weathering steel base metal and weld metal (Tables 1 and 2) from the actual production data provided by the manufacturer. Before factory delivery of the specimens, follow the weld inspection methods for welded specimens specified in GB/T 11345-2023 [18], and conduct UF Union-PXUT-350BPLUS (Nantong City, Jiangsu Province, China) ultrasonic flaw detection on the welds of all weathering steel V-groove welded joint specimens in each group to avoid defects such as insufficient weld fusion. A hybrid welding method combining gas metal arc welding (GMAW) and submerged arc welding (SAW) was employed. The procedure strictly adhered to the technical requirements of: GB/T 985.1-2008 [19], and GB 50661-2011 [20]. The specific welding parameters of Q500qENH weathering steel V-groove welded joint specimens are presented in Table 3, including welding passes, welding current, welding voltage, and welding speed. Representative welded specimens were visually inspected, and the average weld toe transition radius of the specimen welds was found to be approximately 15 mm, with the weld toe reinforcement around 1.2 mm—both meet the geometric dimension requirements for welded specimen welds specified in GB 50661-2011 [20] (see Table 4). To ensure uniform exposure of the test specimens to the corrosive medium, a surface pretreatment was conducted prior to periodic immersion corrosion testing, following the national standard GB/T 16545-2015 [21]. The pretreatment involved a combination of grinding with an Dongcheng-DCSM02-100E (Nantong City, Jiangsu Province, China) angle grinder and immersion in an acetone solution to remove surface impurities and the dense oxide layer on the metal. After completing the above pretreatment, the standardized specimens were thoroughly dried, followed by dimensional measurement and systematic numbering (see Table 4 for details).

The specimen numbering adopts a four-level coding system: "test type-specimen form-corrosion cycle-parallel sample serial number". For example, the code "PV2-2" represents: the second parallel specimen (2) after 2 corrosion cycles (2) of V-groove welded joint specimen (V) in fatigue test (P). This coding system ensures traceability of test samples and scientific management of experimental data. The morphology of the finished V-groove welded joint specimens is shown in Figure 2a. Due to the limitation of polishing equipment, the production factory only polished some corroded specimens. Due to the shooting

conditions of the production factory, only two specimens from each group were taken for recording. The distribution of the base metal zone, heat-affected zone, and weld zone of the V-groove welded joint specimens is shown in Figure 2b.

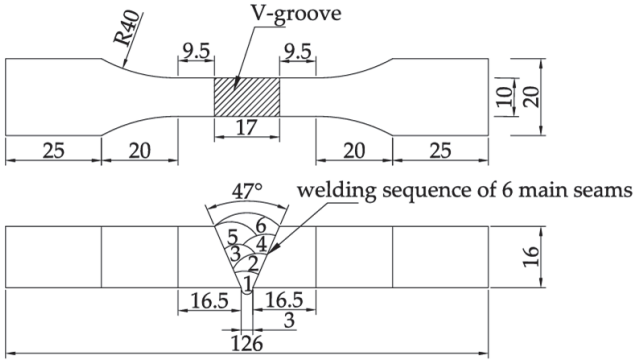

Figure 1. Weathering steel specimen with V-groove welded joint.

Table 1. Chemical composition of Q500qENH weathering-resistant steel.

Element/%	Si	C	Mn	S	P	Cr	Ni	Mo	Cu	V	Nb
Q500qENH	0.340	0.060	1.360	0.003	0.013	0.470	0.410	0.100	0.250	0.036	0.025

Note: Each element in the table is expressed in terms of mass fraction, where mass fraction = (mass of the target element/total mass of elements) × 100%.

Table 2. Chemical element content of welding electrode for Q500qENH weathering steel welded joint.

Element/%	Si	C	Mn	S	P	Cr	Ni	Mo	Cu
JWER60NHQ	0.360	0.050	1.130	0.002	0.008	0.360	0.550	—	0.340
JWS60NHQ	0.380	0.043	1.610	0.003	0.013	0.330	0.420	—	0.280

Note: Each element in the table is expressed in terms of mass fraction, where mass fraction = (mass of the target element/total mass of elements) × 100%.

Table 3. Welding parameters of V-groove welded joint specimens for Q500qENH weathering steel.

Groove Form	Welding Method	Welding Material	Welding Pass	Current/A	Voltage/V	Welding Speed/m·h^{-1}
V-groove	GMAW	JWER60NHQ	1	230	28	20
	GMAW	JWER60NHQ	2	280	31	20
	SAW	JWS60NHQ	3–6	610	30	24

Table 4. Fatigue test program.

Serial Number	Specimen Number	Weld Toe Reinforcement/mm	Weld Toe Radius/mm	D/d	T/°C	S/MPa
1	PV0-1	≤3	≥3	0	20	174
2	PV0-2			0	−20	232
3	PV0-3			0	−40	290
4	PV1-1			9	20	232
5	PV1-2			9	−20	290
6	PV1-3			9	−40	174
7	PV2-1			18	20	290
8	PV2-2			18	−20	174
9	PV2-3			18	−40	232

Note: The weld toe geometry of the weld falls within the above range, but it was not explicitly controlled as a test parameter.

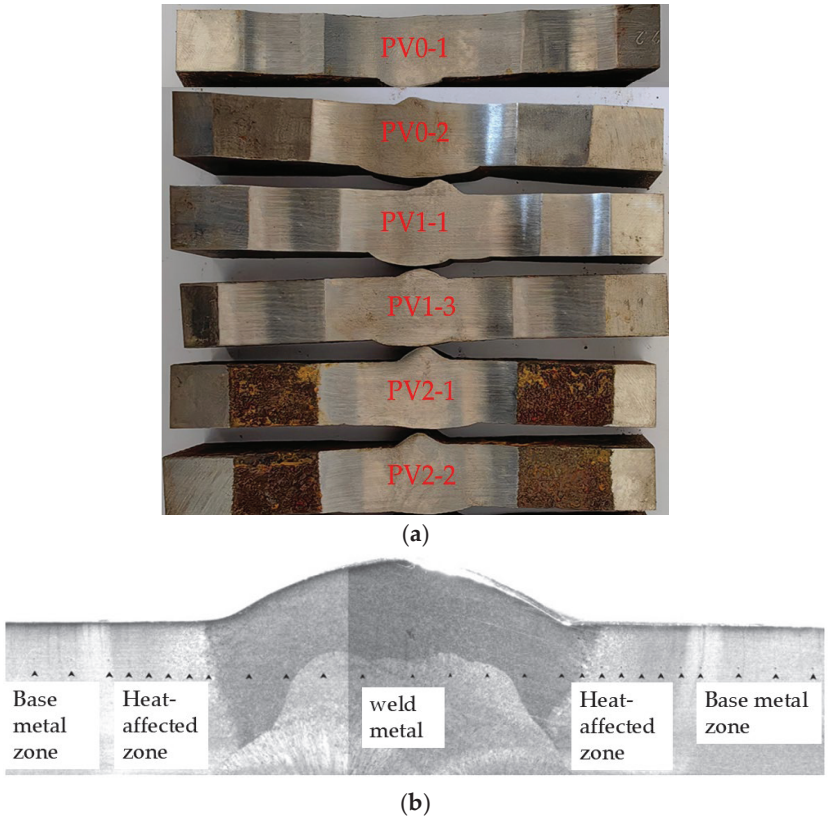

Figure 2. (**a**) V-groove welded joint specimens of weathering steel. (**b**) Morphology of V-groove.

2.2. Alternate Immersion Corrosion Test

This study employed a standardized periodic immersion corrosion test apparatus (Figure 3) to conduct cyclic immersion corrosion tests on three groups of fatigue specimens (nine in total) under three corrosion durations: 0 days (0 d), 9 days (9 d), and 18 days (18 d). The corrosion process was designed in accordance with: TB/T 2375-1993 [22], and GB/T 19746-2018 [23].

Figure 3. CHFL-360 (Wuxi City, Jiangsu Province, China) Cyclic immersion corrosion test chamber.

When simulating the corrosive environment of plateau regions using a sodium bisulfite ($NaHSO_3$) solution, periodic immersion corrosion tests were performed on weathering steel specimens via a dry-wet cyclic immersion method.

The requirements of TB/T 2375-1993 [22] were followed: when conducting periodic immersion corrosion tests via the dry-wet cyclic immersion method, the duration of each dry-wet cycle (including drying time and immersion time) was set to 60 ± 3 min—with the immersion time at 12 ± 1.5 min and the drying time at 48 ± 1.5 min [24]. During the corrosion test, the temperature in the cyclic immersion corrosion test chamber (Figure 3) was maintained at 45 ± 2 °C, and the relative humidity was maintained at 70 ± 5% RH.

In related work from the same group [25], cyclic immersion corrosion tests were conducted on Q500qENH weathering steel V-groove welded joint specimens using a sodium bisulfite ($NaHSO_3$) corrosion solution for durations of 0 days (0 d), 9 days (9 d), 18 days (18 d), and 27 days (27 d), and the corrosion rate of the corroded specimens was analyzed (see Figure 4a).

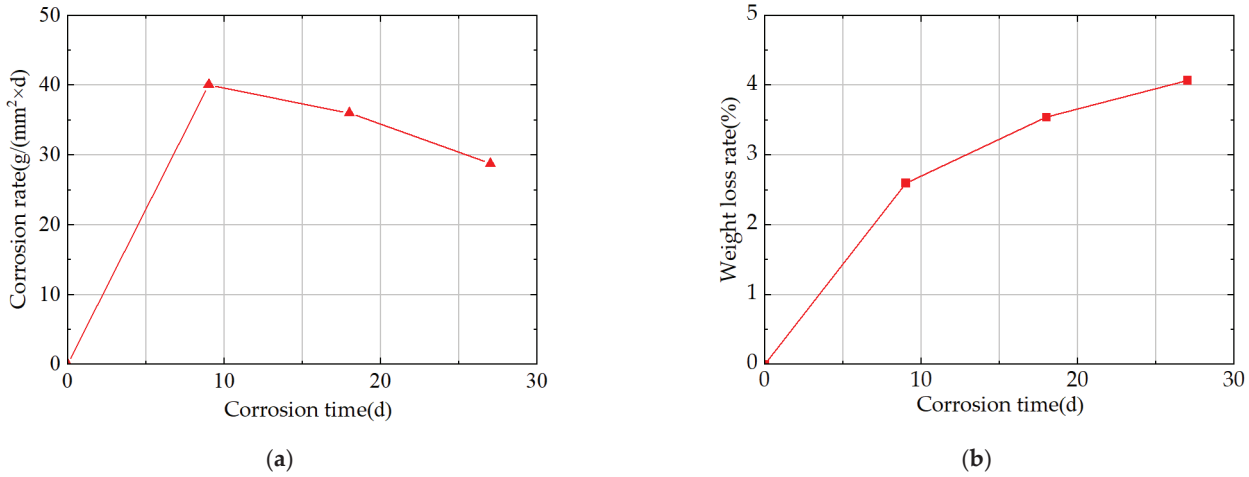

Figure 4. (**a**) Corrosion Rate of Q500qENH Weathering Steel V-Groove Welded Joint Specimens. (**b**) Weight loss rate of Q500qENH Weathering Steel V-Groove Welded Joint Specimens.

Results show that the specimens' corrosion rate peaks at 9 d; from 9 d to 27 d, the corrosion rate decreases with prolonged corrosion time and gradually stabilizes. Specifically, the corrosion rate at 18 d is 10.18% lower than that at 9 d, and the corrosion rate at 27 d is 20.00% lower than that at 9 d.

The variation in weight loss rate with corrosion time in integral welded joint specimens is shown in Figure 4b. For these integral specimens, the weight loss rate reaches 2.60% at 9 d; at this point, the rust layer on the specimens remains incompletely dense, leading to a relatively high corrosion rate and a nearly linear increase in mass loss. The weight loss rate of the integral specimens reaches 3.54% at 18 d, an increase of 0.94% compared with that at 9 d; at 27 d, it reaches 4.07%, with an increase of only 0.53% compared with that at 18 d.

This phenomenon can be explained as follows: as a dense protective rust layer gradually forms on the specimen surface, the contact area between the corrosive medium and the specimen surface decreases gradually, causing the corrosion rate to decline over time and ultimately resulting in a sublinear growth characteristic of weight loss rate with corrosion time.

For exploratory analysis, the 0–18 d period in cyclic immersion corrosion tests was treated as a complete corrosion cycle; the 0–9 d interval within this cycle was defined as the "early corrosion stage," and 9–18 d was defined as the "late corrosion stage." Such cyclic immersion corrosion tests were conducted to explore the variation law of fatigue performance of weathering steel V-groove welded joint specimens with corrosion time.

In SO_2-containing industrial atmospheres, weathering steel surfaces form corrosion products mainly consisting of α-FeOOH, γ-FeOOH, and small amounts of Fe_3O_4. The rust

layer initially forms with γ-FeOOH as the initial corrosion product. As corrosion proceeds, γ-FeOOH transforms into the more stable α-FeOOH, and the oxide film densifies [26].

In related work from the same group [25], $NaHSO_3$ solution was used as the corrosive medium to conduct cyclic immersion corrosion tests on Q500qENH weathering steel. XRD phase analysis of the rust layer was performed to reveal specific components: acicular γ-FeOOH, rose petal-like β-FeOOH, cotton ball-shaped α-FeOOH, and small amounts of Fe_3O_4. As corrosion time extends, γ-FeOOH converts to α-FeOOH. This similarity in phase evolution confirms that using $NaHSO_3$ solution in cyclic immersion tests simulates corrosion processes analogous to those in SO_2-containing plateau atmospheric environments.

Given the increasingly severe industrial pollution in the western plateau regions of China, such as the continuous rise in sulfur dioxide (SO_2) emissions in Sichuan and Qinghai provinces [27], it is recognized that harsh environmental conditions significantly reduce the corrosion resistance of weathering steel welded joint specimens. Accelerated tests under simulated harsh conditions were therefore performed. Thus, sodium bisulfite ($NaHSO_3$) solution with an initial concentration of $(1.00 \pm 0.05) \times 10^{-2}$ mol/L was used as the corrosive medium. Supplementary $NaHSO_3$ corrosive solution (concentration: 2.00×10^{-2} mol/L) was added daily, no more than twice, with each addition taking no more than two minutes to maintain the concentration of $NaHSO_3$ solution in the periodic immersion corrosion test chamber at $(1.00 \pm 0.05) \times 10^{-2}$ mol/L, and accelerated corrosion tests were performed on weathering steel fatigue specimens.

The concentration design is based on the following scientific rationale: firstly, the $NaHSO_3$ solution can form an effective electrochemical corrosion system with the weathering steel component, significantly accelerating the corrosion process; secondly, experimental measurements show that the pH value of this $NaHSO_3$ solution is 4.60 ± 0.20, which aligns well with the weakly acidic condensate environment (primarily composed of SO_2 hydration products) naturally formed on weathering steel component surfaces in plateau regions. This experimental design not only ensures that the electrochemical characteristics of the corrosion process match real-world conditions but also guarantees the similarity in morphology and composition of corrosion products. It thereby provides a reliable experimental foundation for studying the corrosion mechanisms of weathering steel in sulfur-polluted atmospheric environments in plateau areas.

It should be clarified that the applicability of the cyclic immersion corrosion tests conducted in this study—which use $(1.00 \pm 0.05) \times 10^{-2}$ mol/L $NaHSO_3$ solution as the corrosion medium—is limited to highly SO_2-enriched regions of western China (e.g., western Sichuan, eastern Qinghai).

The tests provide reference data for the corrosion behavior of 16 mm thick Q500qENH weathering steel V-groove welded joints in these regions; the corrosion morphology and rate trends they exhibit preliminarily reflect the long-term outdoor exposure characteristics of the material under such specific conditions.

It should be emphasized that these test results do not directly equate to the on-site corrosion behavior of Q500qENH weathering steel in all plateau regions or under all structural forms of components. In specific engineering applications, it is necessary to combine actual environmental parameters of the target region (e.g., SO_2 concentration, temperature, humidity) with structural characteristics of the components and conduct further targeted verification.

2.3. Fatigue Testing Protocol for Welded Specimens

Multiple parameters (e.g., corrosion time, stress level, temperature) influence the fatigue performance of Q500qENH weathering steel V-groove welded joint specimens.

Therefore, these three parameters are included in the fatigue test protocol for Q500qENH weathering steel V-groove welded joint specimens.

For multi-factor coupling test design, the variable control approach by Mehdi et al. [28] is referred to: gradient levels of key parameters (e.g., magnetic field intensity, purification time) are set to exploratively screen for optimal working conditions, providing references for the rational design of the "corrosion-low temperature-stress" multi-variables in fatigue tests of weathering steel. Herein, the orthogonal test design approach matches the requirements of multi-factor coupling test design. Given limited experimental resources, the $L_9(3^3)$ orthogonal experimental design is used to conduct exploratory analysis of key factors influencing the fatigue performance of specimens, evaluate the main effects of each parameter on fatigue life within a feasible experimental scope, and provide direction for subsequent confirmatory experiments.

This study focuses on the fatigue performance of weathering steel V-groove welded joint specimens and examines three primary influencing factors: corrosion duration (D), ambient temperature (T), and stress level (S). A three-factor, three-level test protocol is developed using the orthogonal experimental design method. The parameter levels of the three influencing factors (D, T, S) are presented in Table 4; this design enables systematic investigation of fatigue performance under coupled environmental and mechanical conditions.

The stress level (S) is defined as the maximum applied stress value in fatigue tests. Its three parameter levels are set as 0.30×, 0.40×, and 0.50× the yield strength. The yield strength data are taken from the same research group's literature [25], which comes from tensile tests at room temperature on 16 mm thick Q500qENH weathering steel V-groove welded joint specimens; the average yield strength of uncorroded specimens is 580.07 MPa (Table 5). A stress ratio (R) of 0.10 is maintained during the fatigue tests.

Table 5. Tensile mechanical properties of uncorroded 16 mm thick Q500qENH weathering steel v-groove welded joint specimens.

Sample Specimen Number	E/MPa	f_y/MPa	f_u/MPa	A/%	f_y/f_u	εu/%
PV0-1	207,610	580.07	683.48	18.18	0.85	9.59

In Table 5, E is used to denote elastic modulus; f_y for yield strength; f_u for ultimate tensile strength; A for percentage elongation after fracture; f_y/f_u for yield-to-ultimate strength ratio; and εu for ultimate strain.

The single-point fatigue testing method was adopted in this study, which is defined as testing one specimen per stress level. This fatigue testing method was combined with orthogonal experimental design to efficiently utilize limited specimens. A CIMACH GPS-200 (Changchun City, Jilin Province, China) high-frequency tensile-compressive fatigue testing machine equipped with a low-temperature environmental chamber and a liquid nitrogen tank was used to systematically evaluate the cryogenic fatigue performance of the specimens (Figure 5). The tests strictly simulated two typical cryogenic conditions (−20 °C and −40 °C), with loading procedures performed according to the experimental scheme outlined in Table 4. Two failure criteria were implemented as termination conditions: when the cycle count reached 2.00×10^6 cycles (i.e., two million cycles), or when the relative value of the specimen's elongation amount attained 3 mm. Through these experiments, complete fatigue life data for all specimens were successfully obtained (detailed in Table 6), providing a reliable comprehensive dataset for analyzing fatigue performance under cryogenic conditions. Each group of specimens was subjected to the specific test once.

(**a**) (**b**)

Figure 5. (**a**) Apparatus for low-temperature fatigue tests. (**b**) GPS-200 Fatigue testing clamp.

Table 6. Results of orthogonal design experiment.

Sample Specimen Number	D/d	T/°C	S/MPa	Fatigue Life/N
PV0-1	0	20	174	1,319,500
PV0-2	0	−20	232	332,700
PV0-3	0	−40	290	101,400
PV1-1	9	−40	174	2,000,000
PV1-2	9	20	232	2,000,000
PV1-3	9	−20	290	167,700
PV2-1	18	20	290	350,000
PV2-2	18	−20	174	2,000,000
PV2-3	18	−40	232	797,500

Note: PV1-1, PV1-2, and PV2-2 are 'run-out specimens'; the 2,000,000 fatigue loading cycles represent the test termination cycles of the specimens under the current stress level.

As shown in Table 6, some specimens did not fracture even after 2.00×10^6 loading cycles, which is primarily attributed to the lower applied stress levels and the beneficial effects of low-temperature conditions on the material's fatigue performance. For the weathering steel V-groove welded joint specimens that did not fully fracture, the fatigue loading was continued in the low-temperature fatigue testing apparatus under the same loading conditions as in the orthogonal experimental design until fracture occurred. Subsequently, the crack propagation morphology at the fracture surfaces of the specimens was characterized microscopically using a FEI Qunata600F (Hillsboro, OR, USA) scanning electron microscope (SEM).

The fatigue loading cycles of Specimen PV0-1 (T = 20 °C, S = 174 MPa) are reported as 1,319,500 cycles—fracturing before reaching the test termination cycle of 2.00×10^6 cycles. The fatigue loading cycles of Specimen PV1-1 (T = −40 °C, S = 174 MPa) are noted to reach the test termination cycle (2.00×10^6 cycles, no fracture), with the fatigue loading cycles increasing by ≥51.6% compared to the uncorroded group (PV0-1). Specimen PV2-2 (T = −20 °C, S = 174 MPa) is also confirmed to reach the test termination cycle (2.00×10^6 cycles). Comparison of these results confirms that under the matched stress of 174 MPa, mild/moderate corrosion (9 d, 18 d) significantly extends the fatigue loading cycles compared to no corrosion.

The fatigue loading cycles of Specimen PV0-2 (T = −20 °C, S = 232 MPa) are recorded as only 332,700 cycles. Specimen PV1-2 (T = 20 °C, S = 232 MPa) is confirmed to reach the test termination cycle (2.00×10^6 cycles), with its fatigue loading cycles increasing by ≥501% compared to the uncorroded group (PV0-2).

3. Orthogonal Experimental Analysis of Fatigue Life in Welded Specimens

Fatigue test results were analyzed using the $L_9(3^3)$ orthogonal experimental design, which incorporates range analysis and variance analysis as an exploratory approach. Orthogonal arrays were used to perform mathematical and statistical analysis of multiple influencing factors, and key factors affecting the fatigue performance of welded joints were preliminarily screened. The order of priority of the three influencing factors was determined from the orthogonal experimental design results, providing direction for subsequent confirmatory experiments.

3.1. Extreme Value Analysis Method

During the exploratory analysis, the range R_k for each influencing factor in the low-temperature fatigue test results (Table 7) was calculated to determine the optimal level combination of experimental factors.

$$R_k = \max[\overline{y}_{k1}, \overline{y}_{k2}, \ldots] - \min[\overline{y}_{k1}, \overline{y}_{k2}, \ldots] \quad (1)$$

Table 7. Range analysis results.

$\overline{y}_{kn}$	$\overline{y}_{k1}$	$\overline{y}_{k2}$	$\overline{y}_{k3}$	$\mathbf{Max}(\overline{y}_{kn})$	R_k
D	584,533	1,389,233	1,049,167	1,389,233	804,700
T	966,300	833,467	1,223,167	1,223,167	389,700
S	1,773,167	1,043,400	206,367	1,773,167	1,566,800

In the equation, (R_k) represents the range of the (k)-th factor, indicating the variation amplitude of fatigue life when the (k)-th factor changes. A larger R_k suggests that the factor has a greater influence on fatigue life and higher importance. And ($\overline{y}_{kn}$) denotes the average value of the experimental factor corresponding to the (n)-th level of the (k)-th factor, which is used to determine the optimal level combination for the (k)-th factor. The experimental results demonstrate a positive correlation between the parameter $\overline{y}_{kn}$ and the fatigue performance of specimens, where higher $\overline{y}_{kn}$ values indicate superior fatigue resistance. As shown in Table 7, the maximum average values of the experimental index for influencing factors D, T, and S are $\overline{y}_{D2}$, $\overline{y}_{T3}$, and $\overline{y}_{S1}$, respectively. Consequently, it can be inferred that the combination $D_2T_3S_1$ represents the most favorable factor configuration for enhancing the fatigue performance of the specimens.

Analysis of fatigue performance test results (Table 7) revealed that the calculated influence factors ranked as $R_S > R_D > R_T$ according to Formula (1), indicating distinct differences in the influence of each parameter on fatigue life of V-groove welded joint specimens. The research demonstrates that Q500qENH weathering steel V-groove welded joint specimens exhibited optimal fatigue performance under the following conditions: 9 d corrosion duration, −40 °C test temperature, and 174 MPa stress level. Parameter sensitivity analysis identified stress level (R_S) as the most influential factor on fatigue life, followed by corrosion duration (R_D), while environmental temperature (R_T) showed relatively minor effects. The initiation of metal fatigue cracks is affected by multiple factors, including alternating loads, surface conditions (such as surface defects and reduction in effective cross-sectional size), and environmental factors (such as temperature). Therefore, changes in the fatigue loading stress level and the gradual erosion of the specimen's effective cross-section by the corrosive solution will directly affect the stress state of the specimen, ultimately altering its ability to resist crack propagation. Metals have a brittle-ductile transition temperature line. In the fatigue test, the temperature conditions vary within the range of the brittle-ductile transition temperature line, and the fluctuation of

temperature conditions is small, which has little impact on the material properties of the specimen itself (such as brittleness and ductility) and is difficult to change the specimen's ability to resist crack propagation. Hence, the influence of the temperature conditions adopted in the test on the fatigue performance of the weathering steel V-groove welded joint specimens is lower than that of the loading stress level and corrosion time. These findings provide critical insights for parameter optimization of weathering steel welded structures in corrosion-fatigue environments, offering particularly valuable guidance for the design of welded structures subjected to alternating loads, such as railway vehicles and bridges.

3.2. Analysis of Variance

The analysis of variance method was used to process low-temperature fatigue test data to verify the accuracy of range analysis results. In the analysis of variance method, 9 specimens have a total of 8 degrees of freedom. The degrees of freedom (df) for corrosion duration (D), temperature (T), stress level (S), and error (e) were allocated in a balanced manner (see Table 8) to ensure no remaining degrees of freedom and meet the conditions of a saturated design.

Table 8. Analysis of variance results.

Influencing Factors	df	SS/$\times 10^{11}$	MSE/$\times 10^{11}$	F	Influence Contribution Degree
D	2	9.79	4.90	1.61	II
T	2	2.35	1.18	0.39	III
S	2	36.90	18.40	6.07	I
e	2	6.08	3.04	/	/
Total	8	55.10	/	/	/

Note: The large values of SS and MSE are due to the large numerical range of the fatigue life data (unit: cycles); the squaring of the data values during the calculation process results in the observed large numerical outcomes.

The specimen test results (Table 7) were used to calculate the sum of squared deviations (SS), degrees of freedom (df), mean squared error (MSE), and total sum of squared deviations (F_k) for the influencing factors (D), (T), (S), and the error term (e) [29,30]. The results of the sum of squared deviations (SS) and total sum of squared deviations (F_k) were compared, and an exploratory analysis was conducted on the key factors influencing the fatigue performance of Q500qENH weathering steel V-groove welded joint specimens.

The calculation formulas for the sum of squared deviations (SS) and mean squared error (MSE) are as follows:

$$SS_k = \frac{a}{m}\sum_{n=1}^{m}(\overline{y}_{kn} \times 3)^2 - \frac{1}{m}\left(\sum_{n=1}^{m}(\overline{y}_{kn} \times 3)\right)^2 \quad (2)$$

$$MSE_k = \frac{SS_k}{df} \quad (3)$$

$$F_k = \frac{MSE_k}{MSE_e} \quad (4)$$

In the formula, "a" represents the total number of influencing factors in the orthogonal test; "m" represents the number of orthogonal test runs.

For the quantitative analysis of Table 8 results, stress level is confirmed to exert the strongest regulatory effect on fatigue life (F_S = 6.07, accounting for 66.97% of the total SS), followed by corrosion duration (F_D = 1.61, accounting for 17.77% of the total SS), and ambient temperature exerts the weakest effect (F_T = 0.39, accounting for 4.26% of

the total SS). These results align with the range analysis (R_k: S = 1,566,800 > D = 804,700 > T = 389,700), further verifying the primary and secondary order of factor influences (Table 8).

The influence contribution degree of each factor on fatigue life was quantified using the sum of squared deviations (SS) and F-statistic: for stress level (S), SS = 36.90×10^{11} and $F_S = 6.07$; for corrosion duration (D), SS = 9.79×10^{11} and $F_D = 1.61$; for ambient temperature (T), SS = 2.35×10^{11} and $F_T = 0.39$. These values show the order of influence magnitude as S > D > T.

Exploratory range and variance analyses were conducted on the orthogonal experiment results, determining the primary and secondary order of factors affecting the steel's fatigue life as follows: stress level (S, R_S, with the highest influence contribution degree) > corrosion duration (D, R_D) > ambient temperature (T, R_T, with the lowest influence contribution degree).

Multifactor interaction analysis was conducted, confirming that under low-temperature conditions (−40 °C), extending the corrosion duration to 9 days combined with a lower stress level of 174 MPa yields the optimal fatigue performance for Q500qENH weathering steel V-groove welded joints, with the fatigue lifespan of the joints being significantly higher than that of other test groups.

This phenomenon is interpreted by the following mechanisms: first, a lower stress level (S, R_S) contributes to improving fatigue life to a certain extent; second, a shorter corrosion duration (D, R_D) helps remove initial defects on the specimen surface and enhance specimen integrity; finally, low temperature (T, R_T) induces internal metal atoms of the specimen to enter a low-energy state, increases the energy required for metal atom migration, and thereby inhibits crack propagation. The synergistic effect of these three factors effectively enhances the material's fatigue resistance.

4. Validation of Welding Finite Element Models

To obtain a comprehensive full-life analysis of fatigue crack initiation, propagation, and fracture, macroscopic and microscopic fractographic analysis were conducted on the fatigue fracture surfaces of the specimens based on fatigue crack propagation theory and scanning electron microscopy (SEM). For correlative analysis between microstructure and macroscopic properties, the multi-characterization combination method by Mehdi et al. [31] is referred to: techniques such as SEM, XRD, and Raman are used to quantify the material's microstructural characteristics (e.g., MXene interlayer spacing, defect density), the correlation between these characteristics and macroscopic properties (e.g., electrochemical stability) is then established, providing methodological references for the mechanism analysis of "rust layer structure–welding defects–fatigue life" in weathering steel.

The results of the orthogonal experimental design were analyzed, finding that ambient temperature has the lowest influence contribution degree on fatigue life, while stress level has the highest. Thus, analysis focuses on the fracture locations and macroscopic fracture surfaces of fatigue specimens with three different corrosion durations (0 d, 9 d, 18 d) under a stress level of 290 MPa, with the relevant results presented in Figures 6 and 7.

An exploratory study was conducted on the crack propagation mechanisms and fracture morphologies in the three primary regions of fatigue fracture (fatigue initiation zone, crack propagation zone, instantaneous fracture zone) to validate the intrinsic mechanisms of fatigue fracture.

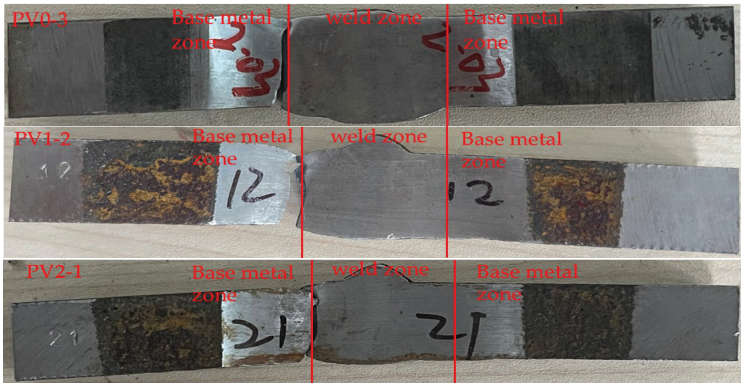

Figure 6. Location of specimen fracture surface.

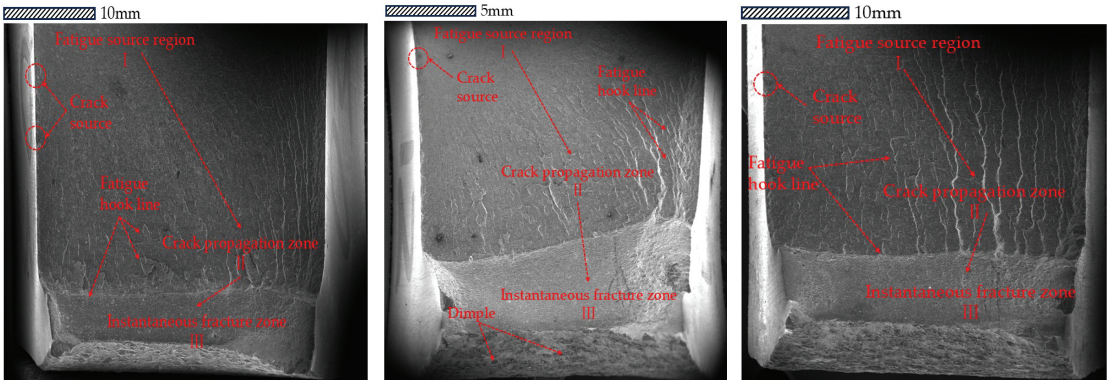

(**a**) (**b**) (**c**)

Figure 7. (**a**) Macroscopic morphology of fracture surface of PV0-3 fatigue specimens. (**b**) Macroscopic morphology of fracture surface of PV1-2 fatigue specimens. (**c**) Macroscopic morphology of fracture surface of PV2-1 fatigue specimens.

4.1. Macrofractographic Analysis of Fatigue Fracture Surfaces

The fatigue crack behavior of corroded weathering steel V-groove welded joint specimens is analyzed by combining the fatigue fracture theory of welded specimens and findings of corrosion morphology scanning.

In related work from the same group [32], the 3D surface roughness of corroded weathering steel V-groove welded joint specimens was obtained using a 3D laser scanner (as presented in Figure 8). An exploratory analysis of the influence mechanism of the corrosion factor on specimen crack initiation is conducted by combining the macroscopic fracture morphology of weathering steel V-groove welded joint specimens (as presented in Figure 7), and the crack initiation location is determined.

It is observed that fatigue cracks initiate at the weld toe-base metal interface, with crack sources near the specimen surface. This phenomenon is attributed to abrupt cross-sectional transitions at the weld–base metal interface—geometric discontinuity at the specimen's weld causes stress concentration at the weld toe-base metal interface.

For uncorroded specimens, their fracture surfaces are relatively smooth and flat, with fatigue source areas uniformly distributed. For V-groove welded joint specimens corroded for 9 days (9 d), surface pitting and fatigue cracks are observed; this phenomenon is attributed to pitting forming microscopic stress concentration points, which further induce crack initiation.

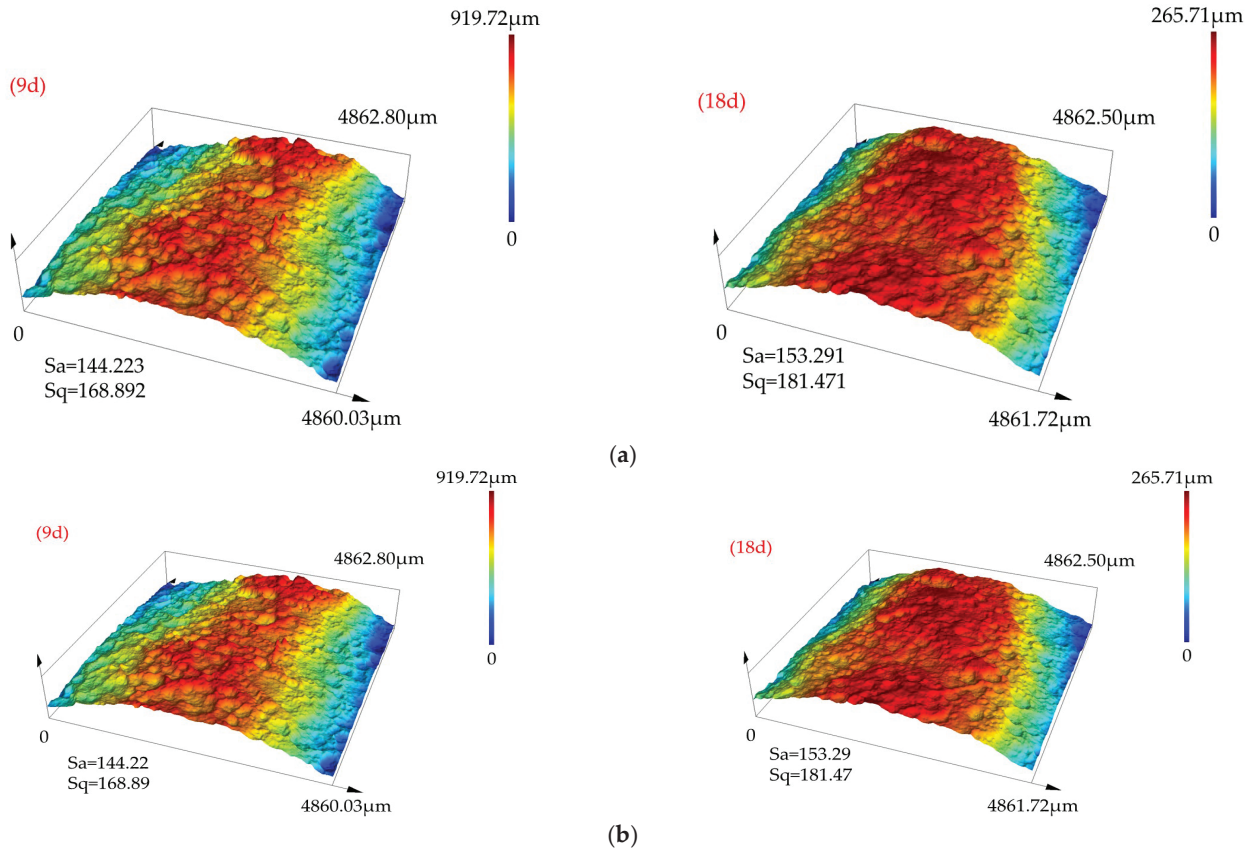

Figure 8. (**a**) Corrosion morphology of weld zone (WZ) in weathering steel V-groove welded joint specimens. (**b**) Corrosion morphology of base metal zone (BWZ) in weathering steel V-groove welded joint specimens.

For specimens corroded for 18 days (18 d), it is observed that as corrosion time extends, the pitting pit density on the specimen surface increases (as presented in Figure 8), and numerous obvious fatigue cracks exist in the crack propagation zone. When compared with the fracture morphology of specimens corroded for 9 d, synergistic effects between adjacent pits are observed—multiple pits act as simultaneous crack sources to jointly promote crack initiation. This indicates that as corrosion time extends, the specimen's crack propagation behavior has shifted from "single initiation" to "multi-crack synergistic propagation".

The propagation path of fatigue cracks is traced back to clarify their complete evolution process. It is observed that cracks first gradually penetrate along the transverse width of the specimen surface, then extend longitudinally along the specimen thickness direction until the specimens fracture. This propagation process is correlated with the coupling effect of continuous corrosion pitting evolution and cyclic loading to clarify the driving mechanism of crack path evolution.

4.2. Scanning Electron Microscopy (SEM) Fractographic Analysis of Fatigue Fracture Surfaces

To further investigate the mechanisms of crack initiation and propagation, a 10 mm cross-section near the fracture surface of the V-groove welded joint specimen was extracted using wire cutting. Subsequently, the fracture morphology of the specimen was characterized by Scanning Electron Microscopy (SEM) to elucidate the microstructural evolution during crack propagation under different corrosion cycles.

Scanning electron microscope (SEM) micrographs (as presented in Figure 9) are observed, and the distinct fracture characteristics are analyzed; an exploratory study is

conducted on the transition process of cracks from initiation to stable growth, as well as the interaction between corrosion-induced defects and crack trajectories.

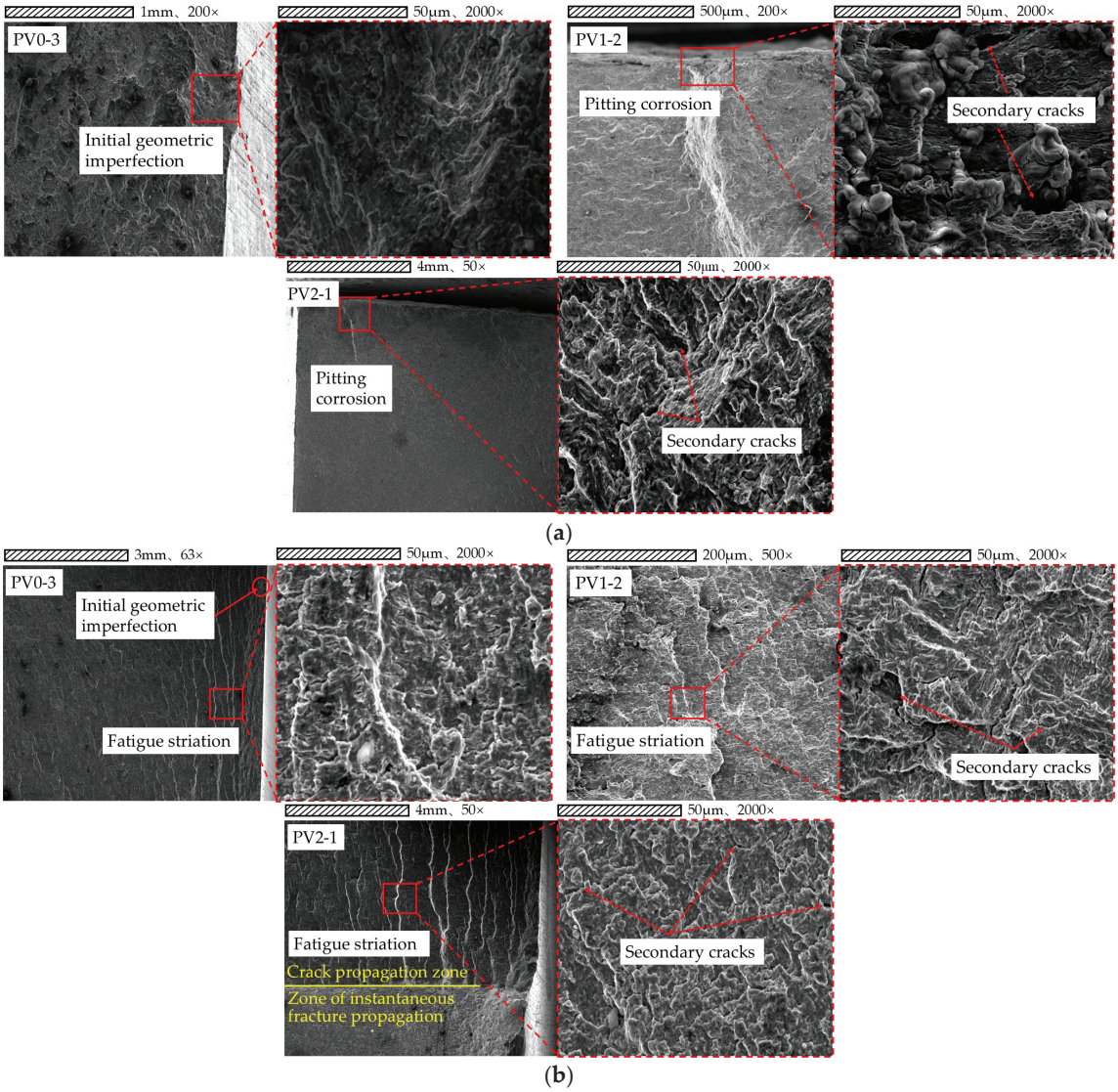

Figure 9. (**a**) Fatigue source region of PV0-3, PV1-2, and PV2-1 specimens. (**b**) Crack propagation zone of PV0-3, PV1-2, and PV2-1 specimens.

The scanning morphologies of corrosion pits and initial manufacturing defects (e.g., slag inclusions, gas pores) are compared: corrosion pits mostly appear as irregular depressions with corrosion products along their edges, while initial manufacturing defects mostly exhibit linear or tear-like traces.

Fatigue crack growth theory is applied to conduct macroscopic observations on the fracture surfaces of fatigue specimens, and it is confirmed that fatigue cracks typically initiate at stress concentration zones. Microscopic observations are performed, finding that numerous irregular fatigue striations exist in crack initiation zones, and secondary cracks associated with crack initiation are distributed on fracture surfaces—with the width direction of these secondary cracks consistent with the crack propagation direction.

The fatigue crack propagation origins of the specimens are traced, finding that fatigue cracks in uncorroded V-groove welded joints typically initiate at internal manufacturing defects such as slag inclusions and gas pores; in contrast, fatigue cracks in corroded V-groove welded joint specimens predominantly initiate at corrosion pits and tear ridges.

Microstructural analysis shows that the presence of corrosion pits causes stress concentration, which not only accelerates the crack initiation process but also reduces the resistance to corrosion-fatigue crack initiation and propagation in the pitted regions of the material. With prolonged corrosion exposure time, the increasing density of corrosion pits led to synergistic interactions between adjacent pits, thereby accelerating fatigue failure. The corrosion pits acted as critical stress concentrators that significantly reduced the fatigue life of welded joints by providing preferential sites for fatigue crack initiation and facilitating multi-site damage accumulation under cyclic loading conditions.

The microscopic morphology of fracture surfaces is analyzed, with typical fatigue fracture characteristics observed during crack propagation. In the crack propagation zone, it is identified that the metallic material at the crack tip undergoes significant plastic deformation and tearing, with the tearing direction perpendicular to the crack growth direction. When fatigue cracks propagate within single grains, their directional stability is observed; this stability is indicated to cause the material to form a series of parallel fatigue striations under cyclic stress.

The fatigue crack propagation process (as presented in Figure 9) is analyzed, confirming that fatigue cracks mainly initiate at stress concentration zones. V-groove welded joint specimens are observed using a scanning electron microscope (SEM), with irregular fatigue striations and secondary cracks aligned with the propagation direction identified in their crack origin regions. An investigation is conducted to determine two typical crack initiation modes: cracks in uncorroded specimens originate from internal defects (slag inclusions/gas pores), while cracks in corroded specimens originate from corrosion pits and tear ridges. Since the irregular geometry of corrosion pits generates significant stress concentrations—and the synergistic effect of these stress concentrations intensifies with prolonged corrosion exposure—corrosion pits become a critical factor accelerating crack initiation. It is recognized that the crack propagation zone exhibits features of polycrystalline materials, including orthogonal tear marks and multi-oriented fatigue striations; these features reflect the complex propagation paths induced by differences in grain orientation.

The above findings are synthesized to elucidate: as stress concentration sources, corrosion pits significantly reduce the fatigue life of welded joints by promoting multi-source damage accumulation. This conclusion provides important insights for exploring the fatigue failure mechanism of weathering steel welded joints under environmental-mechanical coupling effects.

5. Finite Element Modeling and Analysis of Welding Processes

The combined analytical approach based on ABAQUS (Version 2021) and FRANC 3D (Version 7.0) software is used to simulate the fatigue performance changes in weathering steel specimens affected by corrosion under low-temperature conditions.

First, fatigue performance analysis is conducted on the "PV0-3" specimen under the condition of maximum stress of 0.50 f_y (where f_y denotes yield strength, corresponding to 290 MPa). Then, the obtained fatigue life results of the model are compared with the fatigue test results of the specimen to verify the model's effectiveness. Finally, fatigue performance simulation is performed on the weathering steel specimen model under low-temperature conditions at different maximum stress levels.

An exploratory analysis is conducted on the influence mechanism of key factors on the fatigue performance of weathering steel V-groove welded joint specimens.

5.1. Model Parameter Optimization and Design

To more accurately reflect the material properties of the actual weathering steel specimens, establish the specimen model dimensions using the experimental specimen dimen-

sions. Using the linear elastic fracture mechanics approach, incorporate only the elastic phase parameters of the material into the specimen model simulation. Table 9 is taken from the same research group's literature [33], which contains the measured crack growth values of Q500qENH steel at −40 °C. T represents the ambient temperature; E denotes the elastic modulus; ρ stands for the density; μ indicates Poisson's ratio; C and m are the crack growth parameters in the Paris formula; and A refers to the percentage elongation after fracture. Figure 10 presents the stress–strain curve of weathering steel V-groove welded joint specimens at −40 °C.

Table 9. Test Results of Crack Propagation for Q500qENH Steel at −40 °C.

T/°C	E/MPa	ρ/ton·mm^{-3}	μ	C	m
−40	206,500	7.85×10^{-9}	0.30	6.97×10^{-12}	2.75

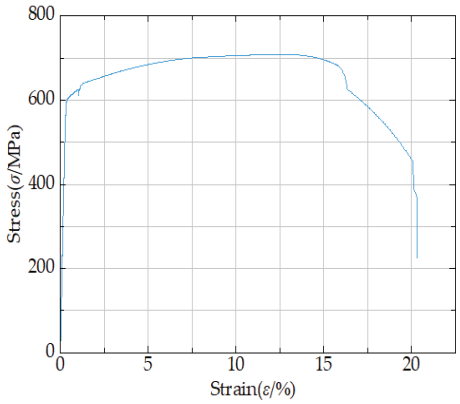

Figure 10. Stress–strain curve of weathering steel V-groove welded joint specimens at −40 °C.

Analyzing the scanning results of corrosion roughness for weathering steel V-groove welded joint specimens shows that most surface corrosion on the specimens appears as pitting pits. These pits weakly weaken the effective cross-section of the specimens. Thus, corrosion's influence on the specimens' elastic properties is not considered, and the elastic modulus remains unadjusted.

5.2. Static Analysis of Fatigue Specimen Model

To accurately simulate the mechanical response of fatigue specimens under actual service conditions, first, the geometric dimensions of weathering steel V-groove welded joint specimens are referred to, and a finite element model is established in ABAQUS software; detailed static stress analysis is then conducted on the specimens. Next, the specimen's finite element model is imported into FRANC 3D software, where it is divided into submodels. An initial crack is set in the submodel within FRANC 3D.

In this study, small specimens are used, and GB 50661-2011 [20] is strictly followed during the welding process; additionally, the weld zone is ground and polished after welding—these measures reduce the influence of welding residual stress on the specimens. Furthermore, this study aims to conduct an exploratory analysis of the key factors affecting the fatigue performance of V-groove welded joint specimens of Q500qENH weathering steel. The fatigue life results from finite element simulation are compared with those from fatigue tests; the error between the two does not exceed 10%. Thus, the influence of welding residual stress is not considered in the finite element simulation of this study.

As shown in the Paris Formula (5), the sensitivity of the finite element model to the Paris constants is expressed as follows: as C and m increase, the fatigue life of the finite element model decreases gradually.

$$dN = da/(C(\Delta K)^m) \quad (5)$$

Paris parameters are assigned to the submodel (as presented in Table 9), and crack propagation simulation is then performed. When the finite element model is established, boundary conditions where one end of the specimen model is fixed and the other end bears an axial equivalent concentrated load are adopted. The concentrated load value is taken as 0.50 times the yield strength (0.50 × 580.07 MPa) from Table 5, and the equivalent concentrated load (46,400 N) applied to the boundary of the specimen model is derived through cross-sectional dimension conversion. The mesh size of the specimen model for calculation is set to 1 mm (Figure 11a).

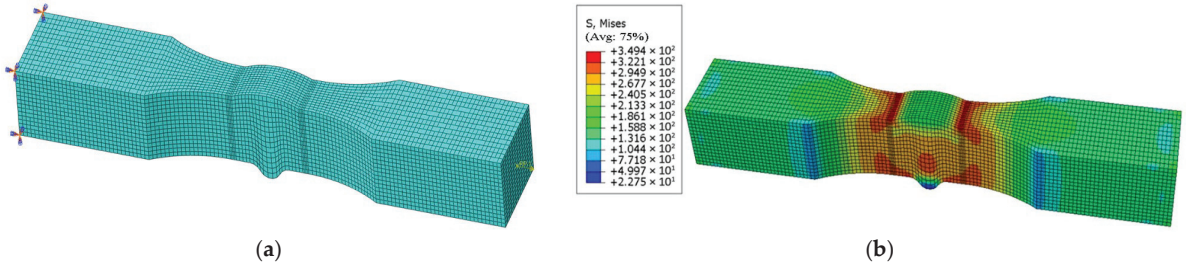

(**a**) (**b**)

Figure 11. (**a**) Mesh generation of PV0-3 specimen. (**b**) Static analysis of PV0-3 specimen.

Considering that mesh sensitivity affects the results of the specimen model, the stress nephogram of the calculation specimen model (Figure 11b) is compared with those of specimen models with mesh sizes of 2.00 mm (Figure 12b) and 0.50 mm (Figure 12d). The final results show that the stress result of the coarse-mesh model deviates by 1.69% from that of the calculation model (not exceeding 2.00%) and the stress result of the fine-mesh model deviates by 1.23% from that of the calculation model (also not exceeding 2.00%). It is confirmed that this result indicates the specimen model is mesh-insensitive and can achieve accurate numerical simulation.

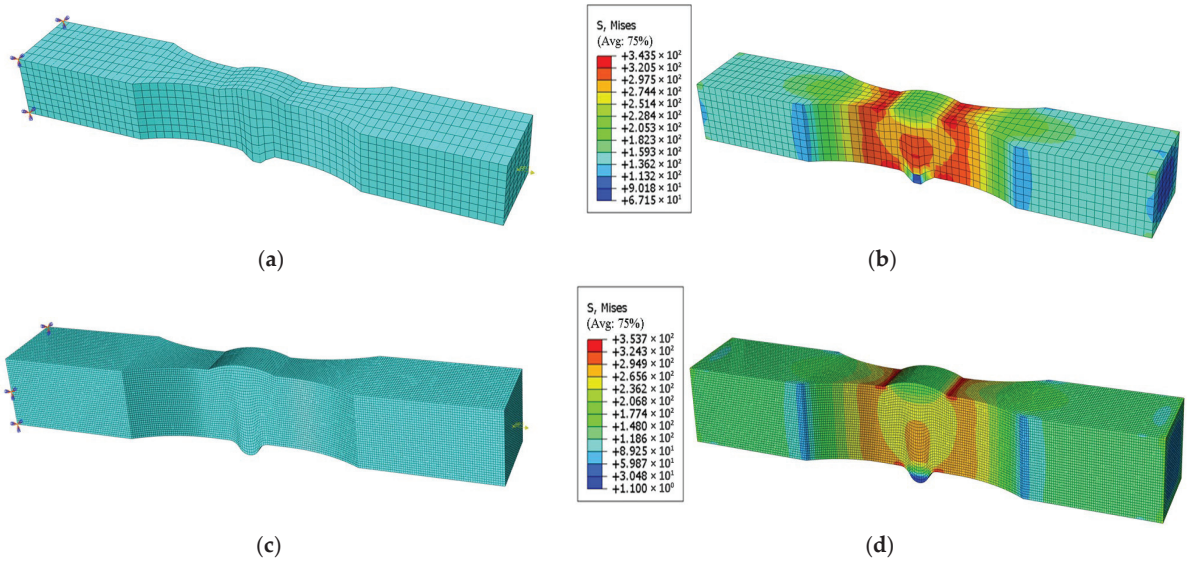

(**a**) (**b**)

(**c**) (**d**)

Figure 12. (**a**) Model of PV0-3 specimen with a mesh size of 2.00 mm. (**b**) Stress results of PV0-3 specimen model with a mesh size of 2.00 mm. (**c**) Model of PV0-3 specimen with a mesh size of 0.50 mm. (**d**) Stress results of PV0-3 specimen model with a mesh size of 0.50 mm.

Given that geometric discontinuities in the specimen shape tend to induce stress concentration effects, the mesh in the parallel section and weld zone of the calculation specimen model (as presented in Figure 11a) is locally refined, and the model is discretized using reduced-integration C3D8R hexahedral elements.

Numerical simulation results (Figure 11b) reveal significant stress concentration at the junction of the weld toe and base metal zone, with stress levels significantly higher than in other regions. Such stress concentration under cyclic loading may significantly reduce structural fatigue life and thus deserves special attention in engineering design.

5.3. Fatigue Crack Propagation Analysis in Test Specimens

5.3.1. Subdivision Modeling

The INP file exported from the ABAQUS global model was imported into FRANC 3D software, where an initial crack was inserted at the weld toe-base metal transition zone. Subsequently, the submodel shown in Figure 13 was extracted through mesh partitioning.

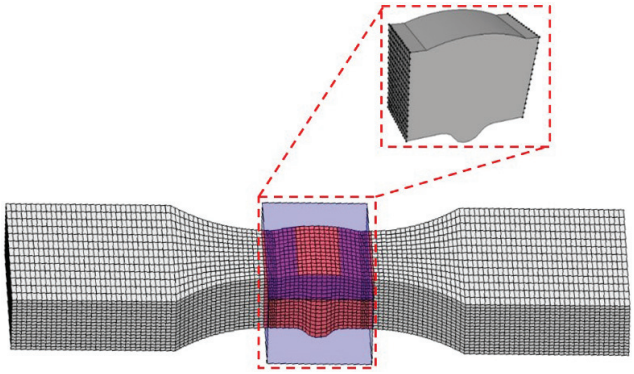

Figure 13. Subdivision process flowchart.

5.3.2. Introduction of Initial Crack

The static simulation results at −40 °C and the experimentally observed fracture locations are combined to determine the initial crack positions, and it is noted that fatigue cracks typically initiate at the junction of the weld toe and base metal. Initial cracks are introduced at the weld toe–base metal interface junction in the uncorroded model; in the corroded model, initial cracks are introduced at pitting locations near the interface of the weld toe and heat-affected zone (HAZ).

An elliptical crack configuration is adopted as the initial crack form for the V-groove welded joint specimen model. The crack dimensions are defined by the semi-minor axis length b (mm) and semi-major axis length c (mm) of the elliptical crack, and the aspect ratio is fixed at $b/c = 1$.

3D pitting morphology scans of weathering steel V-groove welded joint specimens corroded for 9 days and 18 days were conducted, as reported in the same research group's literature [32]; it is observed from the scanning results that in the specimen's base metal zone and weld zone: when the corrosion time reaches 9 days, pits gradually form a semi-elliptical shape; when the corrosion time reaches 18 days, the pit size increases significantly, dominated by local corrosion, and most pits connect with each other to form a penetrating state.

Given that most pits interconnect, it is difficult to divide hexahedral meshes accurately. To ensure effective meshing of the specimen model, the pit morphology is simplified by introducing a larger pitting pit at the weld toe-base metal junction of the specimen, thereby simplifying the simulation of crack propagation in corroded specimens. The 3D surface roughness scanning results in Figure 8 and the corrosion parameters in Table 10 are incorporated, and the pitting depth is set to 0.20 mm and the pitting width to 0.80 mm.

Table 10. Scanning results of corrosion morphology for Q500qENH weathering steel V-groove welded joint specimens.

D/d	Corrosion Depth/mm	Scanned Area	S_a/μm	S_q/μm	S_p/μm	S_v/μm	S_z/μm	Sdr/%
9	0.071	WZ	144.22	168.89	376.54	472.34	848.88	25.92
		BMZ	25.89	32.43	81.98	136.16	218.14	21.66
18	0.138	WZ	153.29	181.47	283.75	537.06	820.80	19.67
		BMZ	27.66	34.23	102.50	129.72	232.22	24.71

Note: WZ—Weld Zone; BMZ—Base Metal Zone.

The linear elastic mechanics method is adopted for crack propagation simulation. The specimen's thickness and width are combined, and with reference to the research conclusion by Zong et al. [34] (i.e., initial crack size should range from 0.10 mm to 0.50 mm), the initial crack size of the specimen model is determined to ensure the effectiveness of initial crack introduction and a sufficient crack propagation path.

With reference to the fatigue fracture analysis results of weathering steel V-groove welded joint specimens, it is noted that fatigue cracks typically occur at the junction of the base metal zone and weld toe. Therefore, the initial crack position of the model is set at the junction of the base metal zone and weld toe.

According to the specimen's thickness, both the initial crack width and depth of the uncorroded model are set to 0.40 mm. For the corrosion model, the influence of pitting pits on crack propagation is considered: a pitting pit is introduced at the junction of the base metal zone and weld toe, and an initial crack is introduced at the bottom of the pitting pit to simulate crack initiation induced by pitting-induced stress concentration. Given that the pitting pit has a depth of 0.20 mm and a width of 0.80 mm, both the initial crack width and depth of the corrosion model are set to 0.10 mm. This approach accounts for both geometric discontinuity effects in uncorroded conditions and localized stress concentration induced by corrosion pits, while maintaining consistency with established fracture mechanics principles for fatigue crack growth analysis.

For the uncorroded specimen model, the initial crack dimensions—where b denotes the semi-minor axis and c denotes the semi-major axis of the elliptical crack—are set with both b and c equal to 0.40 mm, and the crack front template radius is set to 10.00% of the initial crack size. The submodel mesh is then redefined (as presented in Figure 14a) to optimize mesh accuracy for subsequent crack propagation simulation.

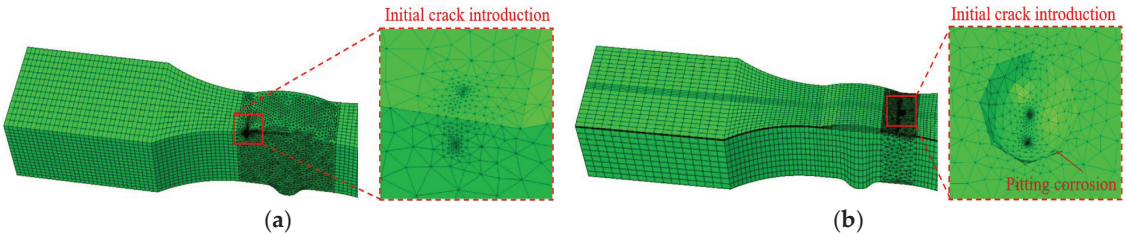

Figure 14. (**a**) Introduce initial cracks on the surface of the specimen model. (**b**) Initial crack initiated from the bottom of corrosion pit in specimen model.

The size of the initial crack directly affects the calculation of the stress intensity factor (SIF) and thus influences fatigue life prediction. For the Q500 weathering steel model, different initial crack sizes are introduced in the literature [33] from the same research group, including models that only vary the initial crack width c and models that only vary the initial crack depth b. Following the linear elastic fracture mechanics theory, the variation law of the model's fatigue life is analyzed. The results show that when the initial crack

width c increases by 0.10 mm, the model's fatigue life decreases by an average of 1.99%; when the initial crack depth b increases by 0.10 mm, the model's fatigue life decreases by an average of 3.28%.

The pit depth of the V-groove welded joint specimen in the finite element model was set to 0.20 mm, and the pit width was 0.80 mm. An initial crack with dimensions b = 0.10 mm and c = 0.10 mm was inserted at the bottom of the corrosion pit (Figure 14b).

Pit corrosion is the core inducement for crack initiation in corroded specimens. The parameters of the single pit introduced in this study are set according to the 3D roughness scanning results of the 5 mm × 5 mm area (depth = 0.20 mm, width = 0.80 mm).

A simplified analysis is conducted on specimens with pits: the width and depth of pits reduce the effective cross-sectional area of specimens, thereby decreasing their fatigue life. The single pit is treated as an approximation of the initial crack; its shape sensitivity is similar to that of the initial crack.

5.3.3. Static Analysis

On the ABAQUS finite element analysis platform, static analysis of the specimen is conducted, and the interaction integral method (M-integral) is used to calculate the stress intensity factors of the specimen model. During numerical simulation, an equivalent treatment method for mixed-mode cracking is introduced to address the mixed-mode crack issue in the model. The equivalent stress intensity factor ΔK_e [32] is employed to simulate three-dimensional crack propagation and further obtain the crack propagation characteristics.

Reference is made to the same-group literature [25], which conducts fatigue tests on 16 mm thick Q500qENH weathering steel V-groove welded joint specimens and investigates the critical value for the specimens' fatigue failure; from which it is observed that the specimens fail when the crack size reaches 56% to 77% of the specimen thickness (as shown in Figure 15). Thus, in this study, this proportion range is taken as a reference, and 75% of the specimen thickness is adopted as the critical failure size for simulating the crack propagation process of the specimen model.

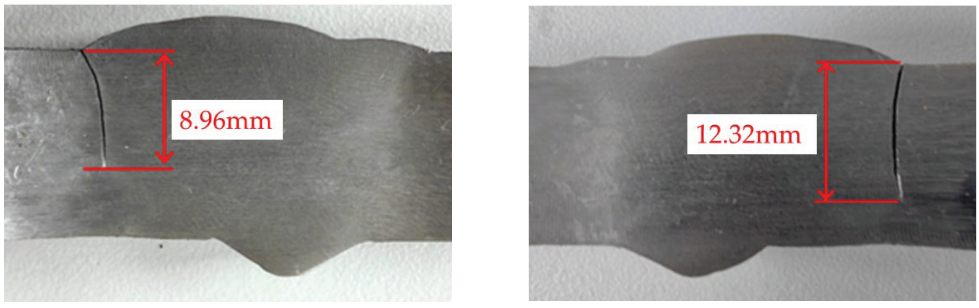

(**a**) (**b**)

Figure 15. (**a**) Crack on the front surface of V-groove welded joint specimen; (**b**) Crack on the back surface of V-groove welded joint specimen.

Paris' fatigue crack propagation theory is employed, and the equivalent stress intensity factor method is incorporated to predict the fatigue life (N).

5.4. Fatigue Test Results Validation

For the model, when its fatigue crack propagates to the failure state, the stress distribution is presented in Figure 16. The fatigue crack morphology of the failed model (Figure 17a) is compared with the fatigue test results of the specimen (Figure 17b), and it is confirmed that the crack propagation path and fracture location obtained from numerical simulation are highly consistent with the experimental observations.

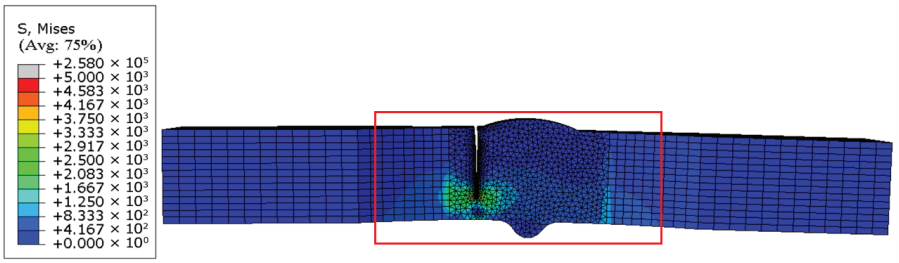

Figure 16. Numerical simulation of crack propagation loci in test specimens.

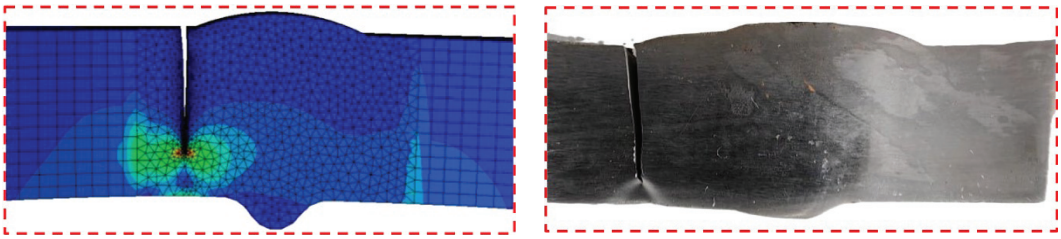

Figure 17. (**a**) Crack propagation simulation results of V-groove welded joint specimen model; (**b**) Crack propagation results of fatigue tests on V-groove welded joint specimens.

The effectiveness of introducing initial cracks at the weld toe–base metal interface for fatigue crack growth simulation is validated, and it is further confirmed that this method can accurately reflect the fracture behavior characteristics of actual specimens.

6. Fatigue Performance Simulation of Welded Joint Models

During the analysis of orthogonal test design results, it is identified that the influence of temperature on the specimens' fatigue life is weaker than that of corrosion duration and stress level; it is also identified that −40 °C (a low-temperature environment) is one of the conditions that enable the specimens to achieve optimal fatigue life.

To explore the effects of corrosion duration and stress level on the specimens' fatigue life under low-temperature conditions, crack propagation simulations are conducted on weathering steel V-groove welded joint specimens under −40 °C conditions.

The simulation results (Table 11) revealed the variations in fatigue life "N" and crack propagation length "*a*" of V-groove welded joint specimens under different stress levels. Specifically, the numerical simulation results in Table 11 were obtained by constructing a three-dimensional finite element model of Q500qENH weathering steel V-groove welded joint specimens using ABAQUS software. Material parameters were adopted from Table 9. A fully fixed boundary condition was applied to one side of the model, while cyclic loading was applied to the other side, consistent with the fatigue loading setup described in the fatigue test (as shown in Figure 11). Initial cracks were introduced into the specimen model using FRANC 3D, and crack propagation simulations were performed using the Paris equation. The simulation was stopped when the crack propagation depth reached approximately 75% of the specimen thickness. Key output parameters, including stress level, fatigue life, and crack propagation depth (Table 11), were extracted. Each set of specimens underwent three independent repeated simulations. The extracted results were averaged to reduce random errors, and the final values were rounded to two significant figures.

Table 11. Simulation of fatigue performance of v-groove welded joint specimens under −40 °C.

Exposure Period/d	Stress Level/MPa	Stress Amplitude ΔS/MPa	Fatigue Life/N	Crack Propagation Depth a/mm	logΔS	logN
0	174	156.60	6,496,247	11.56	2.20	6.81
	203	182.70	1,186,089	11.55	2.26	6.07
	232	208.80	418,499	11.54	2.32	5.62
	261	234.90	197,517	11.57	2.37	5.30
	290	261.00	109,308	11.77	2.42	5.04
18	174	156.60	8,581,337	11.55	2.20	6.93
	203	182.70	1,572,529	11.19	2.26	6.20
	232	208.80	820,672	11.04	2.32	5.72
	261	234.90	243,071	10.73	2.37	5.39
	290	261.00	144,222	10.98	2.42	5.16

Since the crack propagation life in the initial stage of fatigue simulation testing constitutes the predominant portion of the total fatigue life of the specimen model, the number of stress cycles required for the crack to propagate to its maximum length in the specimen model is adopted to represent its fatigue life. A comparison between the numerically simulated fatigue life results of the specimen model and the experimental fatigue life results obtained from physical testing (Table 12) reveals that the relative error between the two sets of fatigue life data falls within 10.00%. This close agreement indicates that the numerical simulation results are essentially consistent with the experimental results, thereby validating the accuracy of the crack propagation modeling in the finite element analysis.

Table 12. Experimental versus simulated fatigue life comparison.

Specimen Number	Experimental Temperature/°C	Stress Level/MPa	Fatigue Life/N	Simulated Fatigue Life/N	Relative Error
PV0-3	−40	290.00	101,400	109,271	7.76%
PV2-3	−40	232.00	797,500	820,672	2.91%

The fracture morphology and stress nephogram of the uncorroded specimen model (Figure 18) and the corroded specimen model (Figure 19) are analyzed, and it is found that the fatigue fracture of both types of specimen models occurs consistently at the junction of the weld toe and base metal interface. This characteristic is consistent with the results of low-temperature fatigue tests.

Regarding crack propagation behavior, the specimen models exhibited distinct directional characteristics: the crack width continuously expanded in the horizontal direction with increasing stress cycles, while the crack depth progressively increased in the longitudinal direction, ultimately leading to complete penetration of the model.

Furthermore, based on the fatigue life results of specimen models (Table 11), crack propagation length "*a*" versus cycle number "N" curves were established for both uncorroded (Figure 18) and corroded specimen models (Figure 19), as shown in Figure 20. These curves not only verify the reliability of the specimen models' fatigue life predictions but also provide compelling evidence for the validity of the crack propagation behavior analysis.

To ensure the reliability of the fatigue data, a detailed analysis of crack propagation behavior in V-groove welded joint specimens was conducted. As shown in Figure 20, a clear relationship between crack length (*b*) and the number of cycles (N) was established, highlighting the progression of fatigue damage under varying stress levels. This analysis focuses on the variation law of fatigue life of V-groove welded joint specimens of the new

Q500qENH weathering steel after being affected by corrosion. The results demonstrate that under non-corroded conditions, the fatigue life of the specimen model exhibits a significant decreasing trend with increasing stress levels (Figure 20a). Meanwhile, the crack growth rate continuously rises with increasing crack length, manifested as a monotonically increasing slope of the curve. As the specimen approaches failure, the curve slope tends toward infinity, indicating that the crack propagation process in V-groove welded joints exhibits a distinct acceleration characteristic—slow in the initial stage and rapid in the later stage until final fracture.

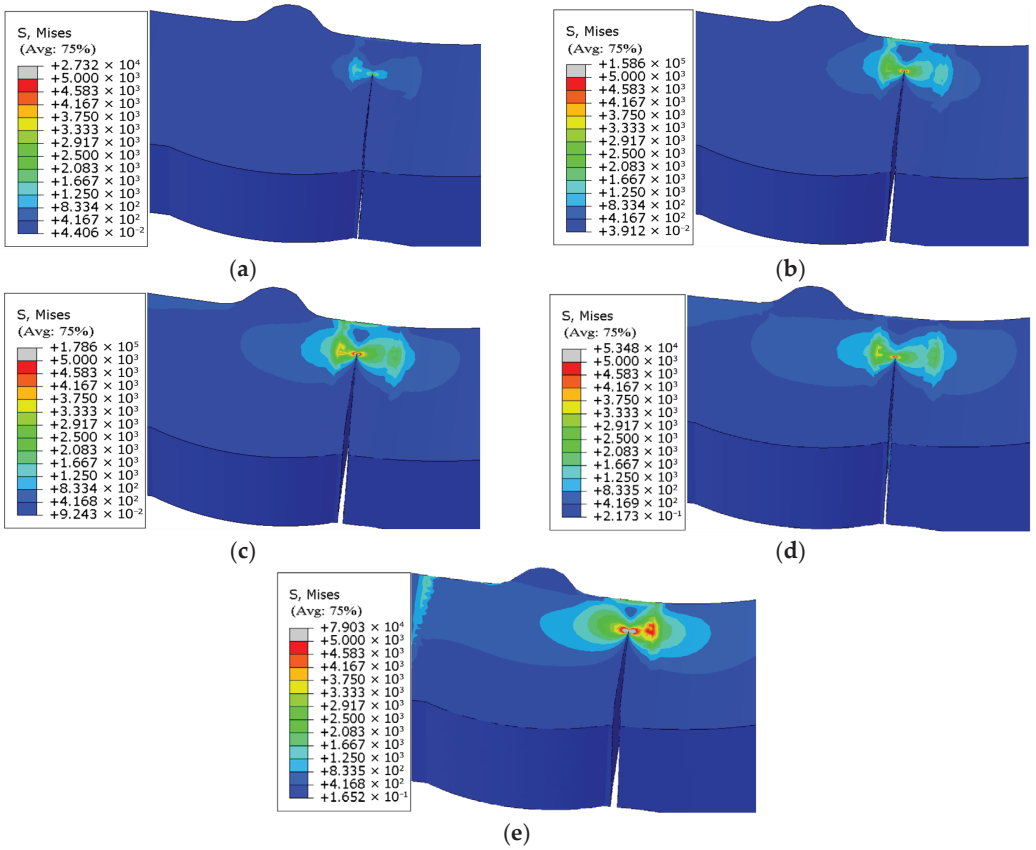

Figure 18. (**a**) Fracture morphology and stress cloud of uncorroded specimen under 174 MPa stress. (**b**) Fracture morphology and stress cloud of uncorroded specimen under 203 MPa stress. (**c**) Fracture morphology and stress cloud of uncorroded specimen under 232 MPa stress. (**d**) Fracture morphology and stress cloud of uncorroded specimen under 261 MPa stress. (**e**) Fracture morphology and stress cloud of uncorroded specimen under 290 MPa stress.

The crack propagation morphologies and evolution patterns of the specimen models in Figures 18–20 are compared, and it is found that the crack propagation modes simulated by the models—including crack initiation sites, propagation paths, and final fracture morphologies—all resemble the observations from low-temperature fatigue tests.

This indicates that integrating the collaborative analysis method of ABAQUS finite element software and FRANC 3D crack propagation simulation software can accurately simulate the fatigue crack initiation, propagation, and fatigue life results during the specimen's fatigue test. This method is used to conduct exploratory prediction of the fatigue life of weathering steel V-groove welded joint specimens.

To investigate the influence mechanism of environmental factors on the fatigue life of specimens, this study systematically analyzed the S-N curves (Figure 21) under low-temperature corrosive environments based on numerical simulation results. The findings demonstrate that under low-temperature conditions, the fatigue life of specimens exhibits a

significant increasing trend with the reduction in stress amplitude (ΔS). When the stress amplitude decreases from 182.70 MPa to 156.60 MPa, the fatigue life of uncorroded specimens increases by 447.70%, and that of specimens corroded for 18 days increases by 445.72%. Comparative analysis revealed that the fitted stress amplitude (ΔS) of corroded specimen models is generally higher than that of uncorroded specimens, indicating that mild corrosion environments can enhance the fatigue resistance of specimens with V-groove welded joints.

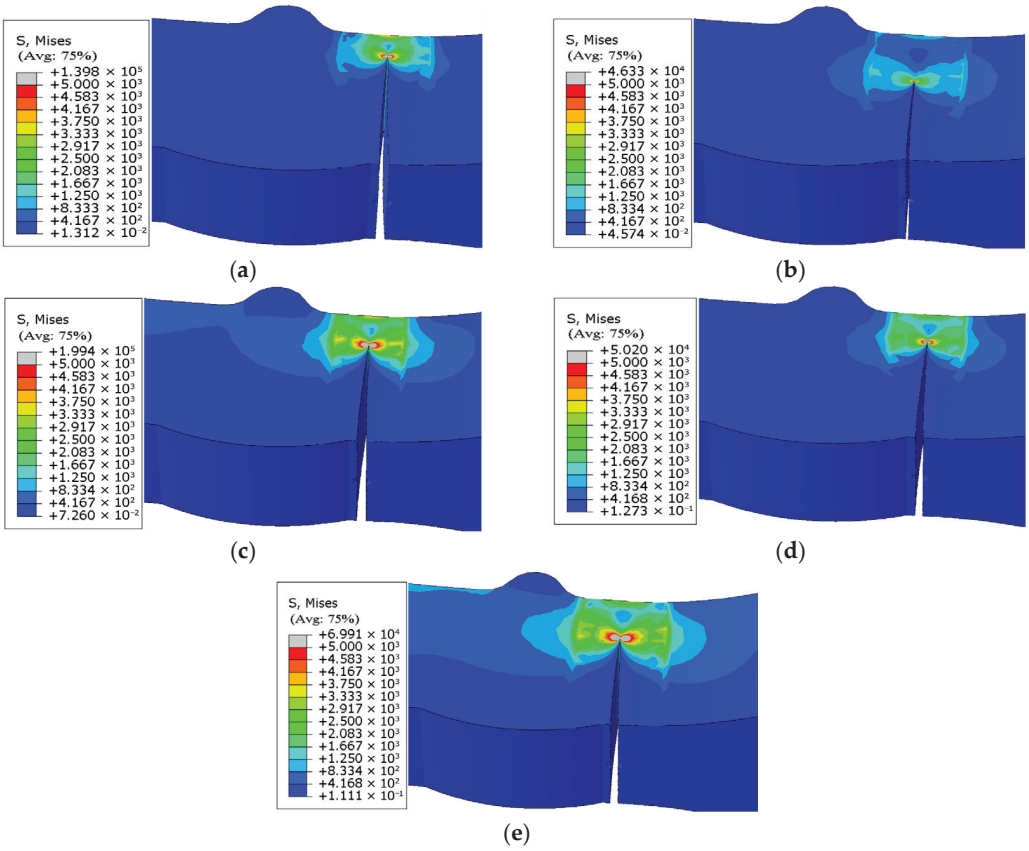

Figure 19. (**a**) Fracture morphology and stress cloud of corroded 18-day specimen under 174 MPa stress. (**b**) Fracture morphology and stress cloud of corroded 18-day specimen under 203 MPa stress. (**c**) Fracture morphology and stress cloud of corroded 18-day specimen under 232 MPa stress. (**d**) Fracture morphology and stress cloud of corroded 18-day specimen under 261 MPa stress. (**e**) Fracture morphology and stress cloud of corroded 18-day specimen under 290 MPa stress.

From the mathematical characteristics of the S-N curves, the fatigue fitting curves of corroded specimen models exhibit dual features: a decreased slope (reduced m-value) and an increased intercept, further confirming the enhancing effect of mild corrosion on the fatigue performance of V-groove welded joints in low-temperature environments. Mild corrosion forms tiny corrosion pits on the material surface; these pits disperse stress concentration and prevent its localization in a single area. Additionally, the corrosion pits from mild corrosion exhibit a passivation effect, so higher stress is required for crack initiation. Furthermore, mild corrosion removes minor surface defects (such as scratches, inclusions, etc.), which typically act as starting points of fatigue cracks. The analytical results are consistent with the low-temperature fatigue test data obtained through orthogonal experimental methods, jointly validating the improved low-temperature fatigue performance of Q500qENH weathering steel V-groove welded joint specimens under mild corrosion conditions. This study provides an important theoretical basis for fatigue assessment of welded structures in specialized environments.

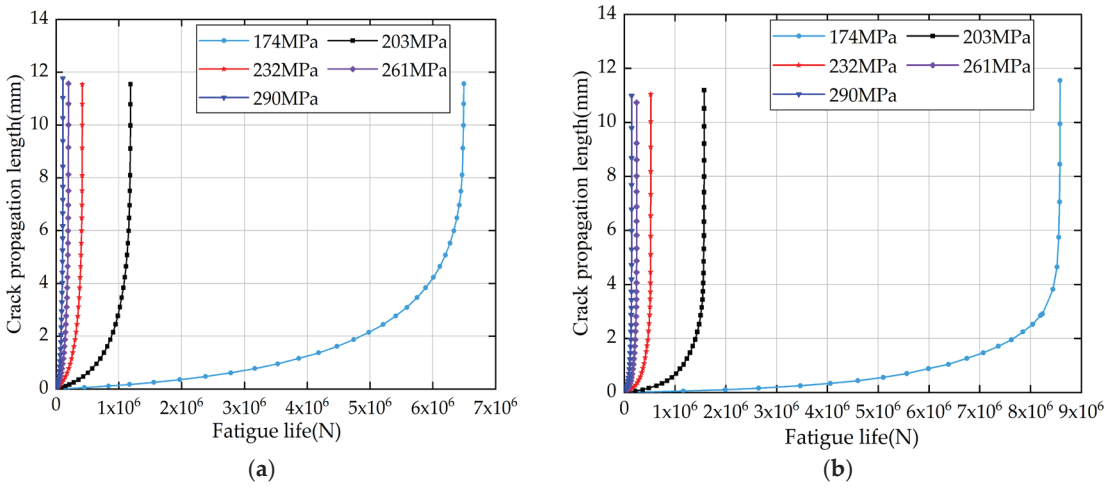

Figure 20. (**a**) Fatigue life curves of uncorroded specimens. (**b**) Fatigue life curves of corroded 18-day specimens.

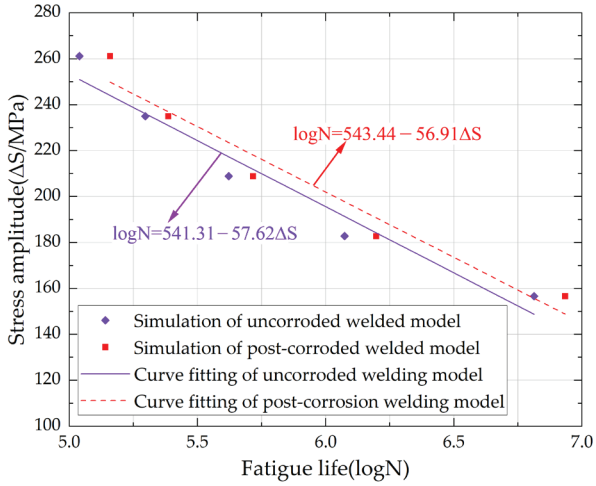

Figure 21. Simulation of S-N curves for low-temperature fatigue in corroded specimens.

The low-temperature fatigue test results are compared, and it is found that mild corrosion extends the fatigue life of Q500qENH weathering steel V-groove welded joint specimens. Under low-temperature conditions, specimens subjected to mild corrosion under the same stress level exhibit an approximately 20.00% higher fatigue life than uncorroded specimens.

Conclusions are derived from simulations and confined only to specific conditions: Q500qENH steel V-groove welded joints (16 mm thickness, GMAW-SAW hybrid welding), −40 °C low-temperature environment, and 2.00×10^{-2} mol/L $NaHSO_3$ corrosive medium. The conclusions should be additionally validated when extended to other steel grades, welding forms, or corrosive environments (e.g., marine atmospheric environments).

7. Discussion

An exploratory analysis is conducted on the equivalent conversion relationship between the indoor accelerated corrosion time and the actual plateau exposure corrosion time of weathering steel welded specimens under the same corrosion condition.

The same-group literature [32] reports that sodium bisulfite ($NaHSO_3$) corrosion solution is used to conduct cyclic immersion corrosion tests on Q500qENH weathering

steel V-groove welded joint specimens, and the corrosion test results are fitted to derive the relationship between corrosion depth and corrosion time (as shown in Equation (6)).

$$B = 0.02D^{0.620} \quad (6)$$

The definitions in Equation (6) are as follows: B denotes the corrosion depth and D denotes the indoor accelerated corrosion time.

Meanwhile, corrosion kinetics calculation methods are applied, the power function law [35,36] for conversion is integrated, and then the equivalent conversion relationship of corrosion time for Q500qENH weathering steel V-groove welded joint specimens in the Beijing area is derived (as shown in Equation (7)).

$$\log Y = -0.464 + 1.409 \log D \quad (7)$$

The definitions in Equation (7) are as follows: Y denotes the natural atmospheric exposure corrosion time and D denotes the indoor accelerated corrosion time.

The 18-day indoor accelerated corrosion time of Q500qENH weathering steel V-groove welded joint specimens is substituted into Equation (7), and it is obtained that the 18-day corrosion of the welded specimens corresponds to 20.17 years of outdoor exposure corrosion in the Beijing area. It is noted that this result indicates the damage degree of the welded specimens in the 18-day indoor accelerated corrosion test is equivalent to that of 20.17 years of natural atmospheric exposure in the Beijing area.

Reference is made to the findings of the same-group study [32], which states that the corrosion severity of steel in the Qinghai–Tibet Plateau is lower than that in the Beijing area. Exploratory conclusions are drawn from this study: in the Qinghai–Tibet Plateau, weathering steel specimens require at least 21 years of natural exposure corrosion to achieve a corrosion effect comparable to 18 days of laboratory cyclic immersion corrosion. However, this estimation does not fully account for the unique environmental factors of the plateau (e.g., extreme temperature fluctuations, strong ultraviolet radiation).

Equation (7) is used to equate the damage degree of welded specimens in indoor accelerated corrosion tests to that under outdoor atmospheric exposure corrosion in the Beijing area. The calculation results of this equation are treated as exploratory, and its equivalence scope is focused on the response law of the fatigue performance of welded specimens to corrosion, rather than on the precise equivalence of indoor and outdoor corrosion degrees.

The cyclic immersion corrosion method is adopted to conduct accelerated corrosion tests on weathering steel V-groove welded specimens, as the research cycle for outdoor exposure corrosion of steel is long. The purpose of the test is set to preliminarily explore the variation trend of the long-term outdoor corrosion behavior of weathering steel under the framework of similar conditions within a shorter indoor simulation time, rather than to obtain an exact "indoor–outdoor equivalence" relationship.

Accelerated corrosion tests for weathering steel specimens are designed to simulate the corrosion effects caused by outdoor exposure in specific environments. These tests are used to quickly grasp the basic laws of the actual corrosion behavior of V-groove welded joint components under long-term outdoor exposure and provide a practical application path for the research conclusions of this paper.

Its application scope is limited to Q500qENH weathering steel V-groove welded joints, high-altitude areas where temperature variation exceeds 40 °C and the minimum temperature can drop below −40 °C, and similar high-altitude sulfur dioxide-rich environments.

Fatigue test results based on orthogonal experimental design further reveal that, under natural corrosion conditions, Q500qENH weathering steel V-groove welded joints must

undergo a specific corrosion process to achieve optimal fatigue life enhancement in the low-temperature corrosive environment of the plateau. Notably, before reaching the optimal service state, the material is prone to damage accumulation effects.

The results demonstrate that Q500qENH weathering steel subjected to moderate pre-corrosion treatment can more effectively utilize its inherent corrosion-resistant properties, thereby significantly improving fatigue performance. This discovery provides important theoretical foundations and practical guidance for the engineering application of weathering steel in plateau environments.

8. Conclusions

Integrate the orthogonal experimental method and conduct high-cycle fatigue tests on V-groove welded joint specimens of corrosion-resistant weathering steel. Determine the optimal influencing factors on specimen fatigue life. Establish a finite element model to comparatively analyze the crack propagation mechanisms in fatigue specimens. Predict the fatigue life of the specimen model. The above lead to the following conclusions:

(1) High-cycle fatigue tests based on orthogonal experimental design revealed that stress level is the most dominant factor affecting the fatigue life of Q500qENH weathering steel V-groove welded joints, followed by corrosion duration and ambient temperature. Analysis of the orthogonal test results shows that when the maximum fatigue stress is 174 MPa, the optimal fatigue test conditions correspond to a corrosion time of 9 d and an ambient temperature of −40 °C, or a corrosion time of 18 d and an ambient temperature of −20 °C; when the maximum fatigue stress is 232 MPa, the optimal fatigue test conditions correspond to a corrosion time of 9 d and an ambient temperature of −20 °C; when the maximum fatigue stress is 290 MPa, the optimal fatigue test conditions correspond to a corrosion time of 18 d and an ambient temperature of 20 °C.

(2) High-cycle fatigue fracture surfaces based on SEM analysis revealed that stress concentration is the primary cause of fatigue crack initiation in V-groove welded joint specimens of Q500qENH weathering steel. The study confirmed that cracks in non-corroded specimens originated from internal defects (slag inclusions/porosity), whereas in corroded specimens, cracks initiated at corrosion pits and tear ridges. The synergistic effect of corrosion pits intensified with prolonged exposure time, promoting damage accumulation in the specimens and accelerating crack initiation.

(3) Finite element software was employed to establish a geometric model with initial cracks for simulation. Integrating fatigue test results, this study investigates Q500qENH weathering steel V-groove welded joint specimens under low-temperature conditions (−40 °C) and equivalent stress levels. The findings reveal that slight corrosion exposure can enhance fatigue life, though damage accumulation tends to occur before reaching optimal service performance. It is acknowledged that there are certain uncertainties in the numerical results of the model in this study, which mainly stem from the variability of material parameters, the simplification of boundary conditions, and the assumptions in the numerical model. The conclusions of this study are limited to applications only to specific materials and structural configurations similar to the specimens used. Further validation of the conclusions is required for other specimen types or different test conditions to avoid potential misinterpretation or misapplication.

Author Contributions: Conceptualization, G.Q. and Z.L.; Methodology, G.X. and Y.L.; Visualization T.L. and G.X. Software, S.S.; Validation, S.S., G.Q., T.L. and G.X.; Formal analysis, S.S. and Z.L.; Investigation S.S. and G.Q.; Resources, T.L.; Data curation, S.S. and Y.L.; Writing—original draft

preparation, S.S.; Writing—review and editing, T.L. All authors have read and agreed to the published version of the manuscript.

Funding: This research was funded by Ministry of Science and Technology of the People's Republic of China grant number 2022YFB3706400.

Institutional Review Board Statement: Not applicable.

Informed Consent Statement: Not applicable.

Data Availability Statement: The original contributions presented in this study are included in the article. Further inquiries can be directed to the corresponding author.

Conflicts of Interest: Authors Shuailong Song, Guangchong Qin, Tao Lan, Zexu Li, Guangjie Xing and Yanchen Liu were employed by the company CSSC International Engineering Co., Ltd. The remaining authors declare that the research was conducted in the absence of any commercial or financial relationships that could be construed as a potential conflict of interest.

References

1. Díaz, I.; Cano, H.; Lopesino, P.; De la Fuente, D.; Chico, B.; Jiménez, J.A. Five-year atmospheric corrosion of Cu, Cr and Ni weathering steels in a wide range of environments. *Corros. Sci.* **2018**, *141*, 146–157. [CrossRef]
2. Su, H.; Wang, J.; Du, J.S. Experimental and numerical study of fatigue behavior of bridge weathering steel Q345qDNH. *J. Constr. Steel Res.* **2019**, *161*, 86–97. [CrossRef]
3. Jia, P.W.; Ju, Y.D.; Akira, S. Effects of Water Jet Peening on Fatigue Properties of SPA-H and SPCC Steel. *Key Eng. Mater.* **2006**, *324–325*, 1229–1232. [CrossRef]
4. Morcillo, M.; Chico, B.; Díaz, I.; Cano, H.; De la Fuente, D. Atmospheric corrosion data of weathering steels. A review. *Corros. Sci.* **2013**, *77*, 6–24. [CrossRef]
5. Gorr, B.; Schellert, S.; Müller, F.; Christ, H.J.; Kauffmann, A.; Heilmaier, M. Current status of research on the oxidation behavior of refractory high entropy alloys. *Adv. Eng. Mater.* **2021**, *23*, 2001047. [CrossRef]
6. Yu, Y.; Zhang, X.; Hu, C.; Liu, L.; Wang, H. Fatigue Crack Growth Performance of Q370qENH Weathering Bridge Steel and Butt Welds. *Materials* **2024**, *17*, 6015. [CrossRef]
7. Shi, Y.; Yang, B.; Liaw, P.K. Corrosion-Resistant High-Entropy Alloys: A Review. *Metals* **2017**, *7*, 43. [CrossRef]
8. Morcillo, M.; Chico, B.; Díaz, I.; Cano, H.; De la Fuente, D. Weathering steels: From empirical development to scientific design, A review. *Corros. Sci.* **2014**, *83*, 6–31. [CrossRef]
9. McConnell, J.; Shenton, H.W., III; Mertz, D.; Kaur, D. Performance of Uncoated Weathering Steel Highway Bridges Throughout the United States. *Transp. Res. Rec.* **2014**, *2406*, 61–67. [CrossRef]
10. McConnell, J.; Shenton, H.W., III; Mertz, D.; Kaur, D. National review on use and performance of uncoated weathering steel highway bridges. *J. Bridge Eng.* **2014**, *19*, 04014009. [CrossRef]
11. Zhang, Y.; Zheng, K.F.; Zhu, J.; Lei, M.; Feng, X.Y. Research on corrosion and fatigue performance of weathering steel and High-Performance steel for bridges. *Constr. Build. Mater.* **2021**, *289*, 123108. [CrossRef]
12. Zhang, X.B.; Cui, C.; Zhang, Q.H.; Li, Y.P. Thermodynamic entropy based low-temperature fatigue life prediction for Q500qENH weathering steel in bridges. *Case Stud. Constr. Mater.* **2024**, *21*, e04029. [CrossRef]
13. Wang, Y.; Chen, C.; Yang, X.Y.; Zhang, Z.R.; Wang, J.; Li, Z.; Chen, L.; Mu, W.Z. Solidification modes and delta-ferrite of two types 316L stainless steels: A combination of as-cast microstructure and HT-CLSM research. *J. Iron Steel Res. Int.* **2025**, *32*, 426–436. [CrossRef]
14. Raffaella, S.; Luca, S. Proposal for kf effective notch factor estimation for life assessment of welded joint based on geometric parameters. *Eng. Fail. Anal.* **2024**, *157*, 107944.
15. Liang, Z.; Heng, L.; Yang, D.; Yao, C. Experimental and numerical study on fatigue damage evolution of Q690D welding details. *J. Constr. Steel Res.* **2024**, *212*, 108264.
16. Zhang, Y.; Zheng, K.; Heng, J.; Zhu, J. Corrosion-Fatigue Evaluation of Uncoated Weathering Steel Bridges. *Appl. Sci.* **2019**, *9*, 3461. [CrossRef]
17. Liao, X.W.; Wang, Y.Q.; Qian, X.D.; Shi, Y.J. Fatigue crack propagation for Q345qD bridge steel and its butt welds at low temperatures. *Fatigue Fract. Eng. Mater. Struct.* **2018**, *41*, 675–687. [CrossRef]
18. *GB/T 11345-2013*; Standardization Administration of the People's Republic of China. Non-Destructive Testing of Welds—Ultrasonic Testing—Techniques, Testing Levels and Assessment. Standards Press of China: Beijing, China, 2013.

19. *GB/T 985.1-2008*; General Administration of Quality Supervision, Inspection and Quarantine of the People's Republic of China, Standardization Administration of the People's Republic of China. Recommended Joint Preparation for Gas Welding, Manual metal Arc Welding, Gas-Shield Arc Welding and Beam Welding. Standards Press of China: Beijing, China, 2008.
20. *GB 50661-2011*; Ministry of Housing and Urban-Rural Development of the People's Republic of China. Code for Welding of Steel Structures. China Architecture & Building Press: Beijing, China, 2012.
21. *GB/T 16545-2015*; General Administration of Quality Supervision, Inspection and Quarantine of the People's Republic of China, Standardization Administration of the People's Republic of China. Corrosion of Metals and Alloys—Removal of Corrosion Products from Corrosion Test Specimens. Standards Press of China: Beijing, China, 2016.
22. *TB/T2375-1993*; Ministry of Railways of the People's Republic of China. Test Method for Periodic Immersion Corrosion of Weathering Steels for Railway Use. Standards Press of China: Beijing, China, 2003.
23. *GB/T 19746-2018*; General Administration of Quality Supervision, Inspection and Quarantine of the People's Republic of China, Standardization Administration of the People's Republic of China. Corrosion of Metals and Alloys—Alternate Immersion Test in Salt Solution. Standards Press of China: Beijing, China, 2018.
24. Wei, Z.J. The Research on Structure Property and Corrosion Behavior of Q450NQR1 High Strength Anti-Corrosion Steel. Master's Thesis, Northeastern University, Shenyang, China, 2019.
25. Wang, X.P. Research on the Weathering Resistance and Low Temperature Fatigue Performance of Q500QENH Weathering Steel After Corrosion in Industrial Atmospheric Environment. Master's Thesis, Southwest Jiaotong University, Chengdu, China, 2024. (In Chinese)
26. Zhao, W.; Yu, C.; Wang, Y.X. Evolution Law of Corrosion Product Films of Q345qDNH Bridge Weathering Steel in Simulated Industrial Atmospheric Environment. *Corros. Prot.* **2024**, *45*, 55–61.
27. Sharma, B.R.; Kuttippurath, J.; Patel, V.K.; Gopikrishnan, G.S. Regional sources of NH_3, SO_2 and CO in the Third Pole. *Environ. Res.* **2024**, *248*, 118–317. [CrossRef]
28. Mehdi, S.M.Z.; Abbas, S.Z.; Seo, Y.; Goak, J.C.; Lee, N. Enhancing Purity and Crystallinity of Carbon Nanotubes by Magnetically Assisted Arc Discharge and Thermal Purification and Their Field Emission Characteristics. *Surf. Interfaces* **2024**, *49*, 104442. [CrossRef]
29. Wang, L. Study on Weldability and Joint Fatigue Behavior of Al/Steel Dissimilar Metals Resistance Spot Welding. Ph.D. Thesis, Jilin University, Changchun, China, 2022. (In Chinese)
30. Zhang, L.M.; Zhang, D.; Wang, Z.Q.; Cong, Y.; Wang, X.S. Constructing a three-dimensional creep model for rocks and soils based on memory-dependent derivatives: A theoretical and experimental study. *Comput. Geotech.* **2023**, *159*, 105366. [CrossRef]
31. Mehdi, S.M.Z.; Abbas, H.G.; Ali, M.; Rizvi, S.B.H.; Choi, S.R.; Goak, J.C.; Seo, Y.; Kumar, S.; Lee, N. Enhanced Electrochemical Performance and Theoretical Insights of Ni-Intercalated Ti3C2Tx MXene. *Energy Environ. Mater.* **2025**, *8*, e12876. [CrossRef]
32. Xing, G.J. Experimental Study on Mechanical Properties of Welded Joints of Corroded Weathering Steel. Master's Thesis, Xi'an University of Architecture and Technology, Xi'an, China, 2024. (In Chinese)
33. Li, M.B. Study on Fatigue Performance of Welded Joints in Weather Resistant Steel Bridge Decks Under Multiple Coupling Effects. Master's Thesis, Xi'an University of Architecture and Technology, Xi'an, China, 2024. (In Chinese)
34. Zong, L. Investigation on Fatigue Crack Propagation and Life Prediction of Steel Bridges Based on Fracture Mechanics. Ph.D. Thesis, Tsinghua University, Beijing, China, 2015. (In Chinese)
35. Zhang, L.M.; Cong, Y.; Meng, F.Z.; Wang, Z.Q.; Zhang, P.; Gao, S. Energy evolution analysis and failure criteria for rock under different stress paths. *Acta Geotech.* **2021**, *16*, 569–580. [CrossRef]
36. Liang, C.F.; Hou, W.T. 8-Year Atmospheric Exposure Corrosion Study of Carbon Steel and Low Alloy Steel. *J. Chin. Soc. Corros. Prot.* **2005**, *25*, 1–6.

MDPI AG
Grosspeteranlage 5
4052 Basel
Switzerland
Tel.: +41 61 683 77 34

Materials Editorial Office
E-mail: materials@mdpi.com
www.mdpi.com/journal/materials

Academic Open
Access Publishing

mdpi.com

ISBN 978-3-7258-5704-3